University of Genoa

PhD program in Civil, Chemical and Environmental Engineering

Fluid Dynamics and Environmental Engineering

Cycle XXX

PhD Thesis

Fluid flow in the eye in the presence of intraocular lenses

Candidate: Peyman Davvalo Khongar
Supervisors: Rodolfo Repetto, Jan Oscar Pralits

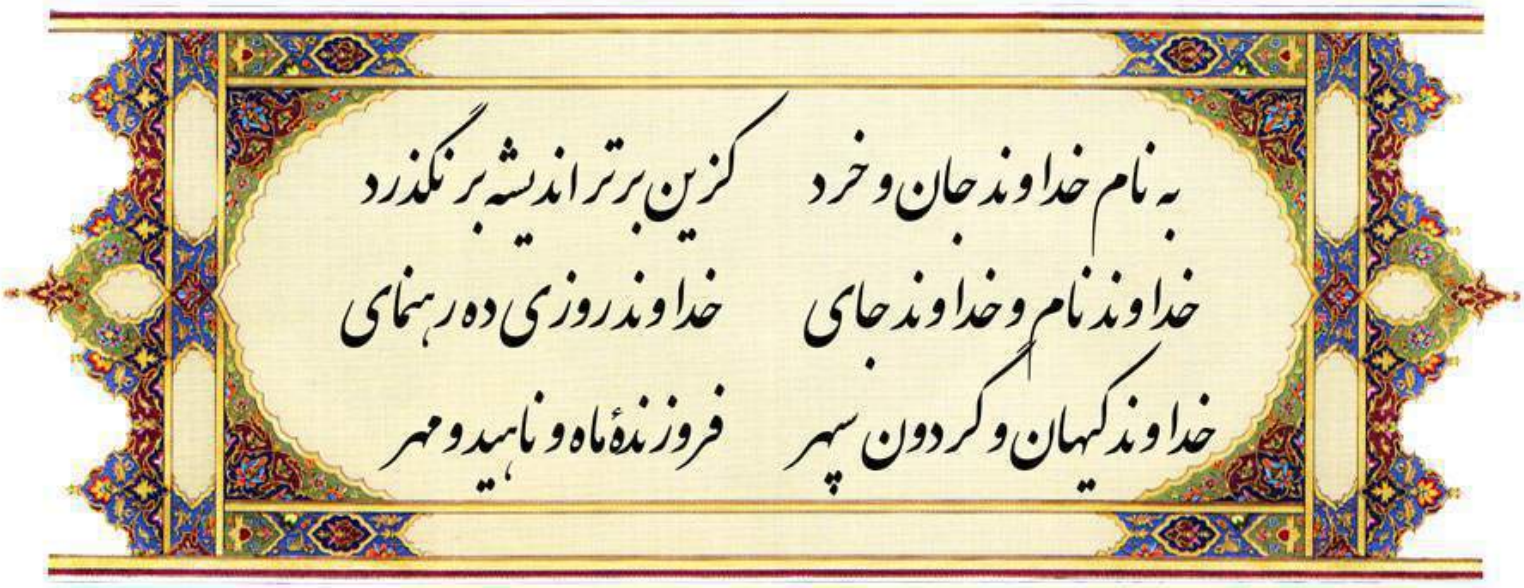
به نام خداوند جان و خرد
کزین برتر اندیشه برنگذرد
خداوند نام و خداوند جای
خداوند روزی ده رهنمای
خداوند کیهان و گردون سپهر
فروزندهٔ ماه و ناهید و مهر

تقدیم به پدر، مادر و خواهر عزیزم

Acknowledgements

Firstly, I would like to express my sincere gratitude to my supervisors Prof. Rodolfo Repetto and Prof. Jan Pralits for the continuous support of my PhD study and related research, for their patience, motivation, and knowledge.

I would like to thank Mr. Fred Wassenburg and Dr. Paolo Soleri from Ophtec BV. for supporting and providing me the opportunity to analyze their lenses during my research.

My sincere thanks also go to Prof. Franco Auteri and Prof. Anna Pandolfi from Polytechnico di Milano who provided me the opportunity to join them and develop the in–house code of chapter 7. Without their precious support, it would not be possible to develop this code.

I would like to also thank the professors and staff members of department of civil, chemical and environmental engineering (DICCA), particularly former PhD coordinator of fluid dynamics curriculum, Prof. Giovanna Vittori who is of the highest kind, quality, and order, supreme and an idol of a strong and intelligent woman.

A special acknowledgement goes to my friends and office colleagues of many years: Christina Isakova, Danele Lagomarsino, Davide Medicina, Duaa Telfah, Edoardo Alinovi, Francesco De Leo, Francesco Enrile, Francesco Ferrari, Gaetano Porcile, Hossein Darban, Irene Nepita, Masoud Ghaderi, Mariia Dvoriashyna, Rahim Atashipour and Stefano Putzu. Thank you for being with me all the way.

I would like to thank my family: my lovely parents and my sister for supporting me spiritually throughout this PhD and my life in general.

Last but not the least, Sasan Sodagar. My true friend, my true hero. It is so sad that you are not among us any more. You are near, even if I dont see you. You are with me, even if you are far away. You are in my heart, in my thoughts, in my life, always...

Contents

List of Figures

List of Tables

Summary of chapters

In this thesis we study with mathematical models the fluid dynamics of the anterior segment of the eye in the presence of intraocular lenses. In particular we consider two different phakic iris–fixated intraocular lenses, used for the correction of refractive errors, and an aphakic iris–fixated, used for cataract surgery. The ultimate goal of this thesis is to investigate whether the complications associated with the implantation of such lenses can be explained on the basis of mechanical laws and if mathematical modeling can help defining strategies to mitigate such complications. In the following we provide a short overview of the outline of the thesis and of the content of each chapter.

Chapter 1

In this chapter we first discuss the anatomy of the human eye. We briefly describe the main components of the eye and their functions in section 1.1. Since this thesis is focused on the fluid dynamics of aqueous humor, in section 1.2 we discuss the properties of the fluid and its main roles. We also outline the structure of the cornea, which is useful for better understanding corneal metabolism. Refractive errors and their correction options are discussed in section 1.3. Implantation of a phakic intraocular lens (pIOL) is one of those options that we discuss in more detail. In section 1.4 we discuss about cataract and its surgical options, and in particular, consider the cases in which an iris–fixated aphakic intraocular lens has to be adopted. Finally, in section 1.5 we discuss the aims of this thesis which, based on mathematical models, can be summarized as follows: improve our understanding of the characteristics of aqueous flow in the anterior chamber of the human eye (a) and metabolic species transport to the cornea (b), with and without the presence of a pIOL and the mechanical implications of implanting an iris–fixated cataract lens on the anterior or posterior surface of the iris (c).

Chapter 2

In this chapter we review the research works that have been done on aqueous humor flow in the anterior and vitreous chambers and nutrients transport to the cornea. We divide each section into two subsection, reviewing both the experimental and mathematical studies. In section 2.2 we identify the main mechanisms inducing aqueous flow in the anterior chamber: aqueous production at the ciliary processes and drainage at the trabecular meshwork, buoyancy–driven flow due to temperature differences across the anterior chamber, transient flow due to miosis (i.e. contraction of the pupil) and eye movements. In section 2.3 we focus on the studies of glucose, oxygen and lactate distribution to the cornea since these metabolic species control cell viabilities and influence the structural integrity of the cornea.

Chapter 3

In this chapter we describe the governing equations and the numerical methods used in the thesis. The chapter is divided in two main sections: fluid motion (3.2) and metabolic species delivery (3.3). In section 3.2 we first establish the governing equations of fluid motion. A temperature equation is added to these equations, when temperature gradients are essential in the modeling. We then discuss the numerical technique (the Finite Volume Methods (FVM)) that have been used to solve these equations. The mathematical formulation of this method is also introduced in this section. We then shortly introduce the OpenFOAM library and its solvers, which are used for solving the equations mentioned above using FVM. In section 3.3 we propose a mathematical model for the metabolic species delivery to the cornea. For solving this model we use the Finite Element Method (FEM) using COMSOL Multiphysics software, and the corresponding solvers are briefly described in this chapter.

Chapter 4

In this chapter we study aqueous flow in the anterior chamber, with and without the presence of an iris–fixated pIOL. We consider all flow mechanisms, mentioned in chapter 2. We mainly focus on investigating the main complications that are associated to the implantation of a pIOL: iris and corneal cell detachment and increase of the IOP. We also study a possible modification of the lens body, by considering the presence of one or more perforations in it, aimed at making the flow in the presence of the pIOL more similar to the physiological one. We used two different commercially available of iris–fixated pIOLs: the Artiflex and the Hydrophobic Artiflex. In section 4.2 and 4.3 we discuss the geometries used in the simulations. For the simulations we used OpenFOAM, and the boundary conditions and the solvers are discussed in section 4.4. In subsection 4.5.1 we present all results, related to the physiological case and in subsections 4.5.2 and 4.5.3 we show the results for the case when pIOLs are implanted. In each of these subsections we separately study the aqueous flow induced by mechanisms mentioned in chapter 2. The main conclusions of this chapter are: the presence of a pIOL changes the aqueous flow characteristics but the main hydrodynamic parameters (.e.g. maximum pressure and wall shear stress) remain within a clinically acceptable range (a) and a perforation in the lens body can be effective in avoiding excessive pressure growth in the case that the passage between the pIOL and the iris gets blocked (b).

Chapter 5

In this chapter we study metabolic species delivery to the cornea, taking into account of aqueous humor flow. In section 5.2 we discuss the idealized axisymmetric shapes of the anterior chamber and cornea, adopted in the simulations. For our analysis, we considered two main cases, metabolic species transport to the cornea when the eyelids are open (a) and closed (b). When the eyelids are open, the thermal flow and the flow generated by eye rotations are intense and we postulate that the aqueous humor is well-mixed in the anterior chamber. For this reason we lump the species transport across the anterior chamber into a boundary condition on the endothelium/anterior chamber interface. On

the other hand, when the eyelids are closed, the mechanisms that produce fluid flow are mainly the bulk production/drainage flow, discussed in chapter 2. Since this flow is very slow, for this case we also account for transport of metabolic species within the aqueous humor. In all cases we consider both absence and presence of a pIOL. We also consider a central hole in the body of the pIOL to investigate its effect on the transport of metabolic species to the cornea. The model is then solved numerically using COMSOL Multiphysics. In section 5.4.3 we present the boundary conditions used in our simulations. In section 5.5 we show the results of our simulations, both for the steady and unsteady cases. The main conclusions of this chapter are: the presence of a pIOL decreases glucose availability at the cornea in comparison to the physiological one (a) and the perforation of the lens might help to increase this availability (b).

Chapter 6

Iris–fixated aphakic IOLs, used in cataract surgery, can be implanted both on the posterior and anterior surface of the iris. In this chapter we study from the mechanical point of view whether one of these options is preferable to the other. The lens that has been used in this analysis is the Artisan Aphakia +30.0 D lens (aIOL). In section 6.2 we discuss the geometries that have been used in the simulations. Since in chapter 4 we show that the saccadic rotations generate the most intense aqueous flow among all mechanisms, we restrict our analysis to aqueous flow in the anterior and vitreous chambers induced by saccadic rotations of 10°, 20° and 30°. The boundary conditions and solver associated to the simulations are discussed in section 6.3. The main observables of the numerical simulations are the forces acting on the aIOL and the forces transmitted by the aIOL to the iris. The procedure used to calculate such forces is discussed in section 6.4. We consider two main cases in our analysis: the flow in the saccadic rotation in the presence of an aIOL on the anterior (a) and posterior (b) side of the iris and the corresponding results are shown in sections 6.5.1 and 6.5.2, respectively. Since throughout this chapter we consider the case in which vitrectomy is performed and the vitreous gel is replaced by aqueous humor, in both domains we consider that the fluid has the properties of aqueous. The model is then solved numerically using OpenFOAM. The main conclusion of this chapter is that implantation of the aIOL on the posterior surface of the iris could be potentially associated with a higher risk of lens dislocation, since the observed forces are higher.

Chapter 7

In this chapter we discuss the in–house code, developed for solving the Navier–Stokes equations, using a direction splitting method with immersed boundary treatment. In section 7.1 we discuss some of the benefits of this new method over traditional techniques. In section 7.2 and 7.3 we discuss the motivations for development of this code and the mathematical formulations of this method, respectively. Then in section 7.4 we introduce a series of benchmark cases and we compare the result of our code with OpenFOAM and other numerical works. The main conclusions of this chapter are: in our bechmark cases, the in–house code was in a very good agreement with OpenFOAM and other research works and in general, running serially, the in–house code is faster that OpenFOAM in

terms of computational time, in particular when mesh movements are involved in the simulations.

Chapter 1

Introduction

1.1 Anatomy of the eye

Eyes are complex optical systems which collect light signals form the environment and convert them into electro-chemical impulses in neurons. These signals are transmitted to the brain through complex neural pathways for the vision process. The eye has a nearly spherical shape and its antero-posterior and nasal-temporal lengths are about 24.2 mm and its superior-inferior length is usually slightly larger [6]. The inner part of the eye is divided into three regions called chambers: **anterior**, **posterior** and **vitreous chambers**. The anterior chamber is the space in the eye bounded anteriorly by the cornea and posteriorly by the iris and the central part of the lens. The posterior chamber is the region between the lens and the posterior side of iris. Finally the vitreous chamber is located in the back part of the eye and is bounded by the lens, the ciliary body and the retina and it is filled with the vitreous humor.

A sketch anatomy of the eye is shown in figure (1.1) and a short description of the main parts of the human eye is reported below:

- **Cornea**. The front part of the eye is covered by a transparent spherical shell called the cornea, which protects the eye and holds the structure together. The main purpose of the cornea is to help focusing the light as it enters the eye globe. The cornea is an avascular tissue i.e. it does not contain blood vessels or lymphatics.

- **Iris**. It is a colored muscular diaphragm, which regulates the amount of light entering the eye by adjusting the size of the pupil.

- **Pupil**. This is the opening of the iris that allows light to strike the retina. It appears black since no light is reflected from behind it. The size of the pupil determines how much light is let into the eye.

- **Eye lens**. It is a convex lens made of transparent jelly material, which is harder in the center than at the boundaries. It is held in position by the ciliary muscles. The cilliary muscles help in changing the curvature and focal length of the eye lens. the outermost layer of the lens is called **capsule** and the lens fibers form the bulk of the interior of the lens. With advancing age the lens often loses its transparency (cataract) and it is often replaced by an artificial intraocular lens.

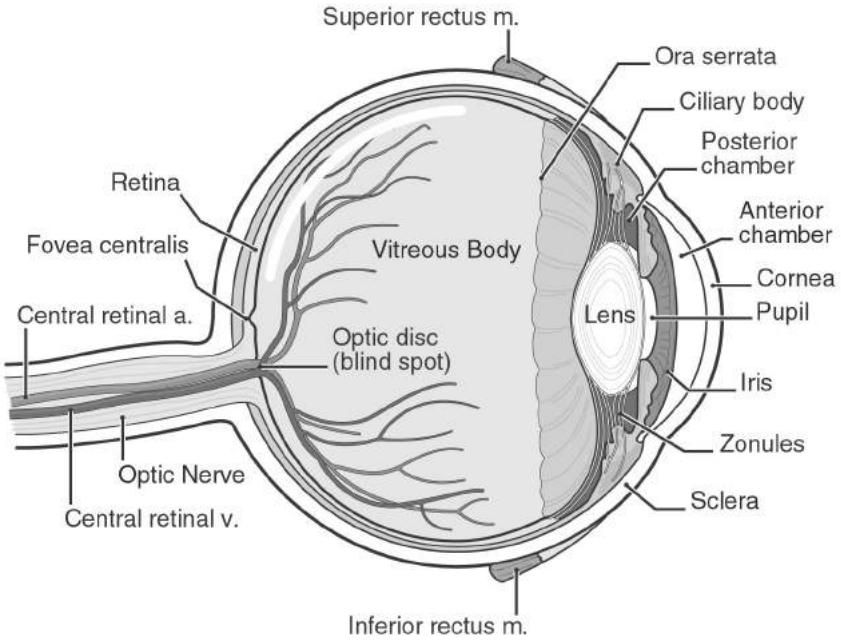

Figure 1.1: Cross-section of the human eye with an indication of its main components [34].

- **Retina**. The inner back surface of the eyeball is called the retina. It is a light sensitive semi-transparent membrane. When light falls on the retina's receptors they send electrical signals to the brain through the optic nerve. This process allows the vision.
- **Sclera**. The white outer external coat of the eye, which provides mechanical strength to the eye ball.
- **Ciliary body**. This is the part of the eye that includes the ciliary muscle, which controls the shape of the lens, and the ciliary epithelium, which produces the aqueous humor.
- **Aqueous humor**: Optically clear, slightly alkaline liquid that occupies the anterior and posterior chambers of the eye.
- **Vitreous humor**. It is the clear gel-like substance filling the central cavity of the eye.
- **Trabecular meshwork**. This is an area of eye tissue which is located at the angle between the cornea and the iris. The aqueous humor drains out of the eye through the trabecular meshwork via anterior chamber.
- **Schlemm's canal**. A modified capillary blood vessel in the eye that collects the aqueous humor from the trabecular meshwork and delivers it into blood vessels.
- **Optic nerve**. It consists of more than a million nerve fibers, that carry visual signals from the retina to the brain.

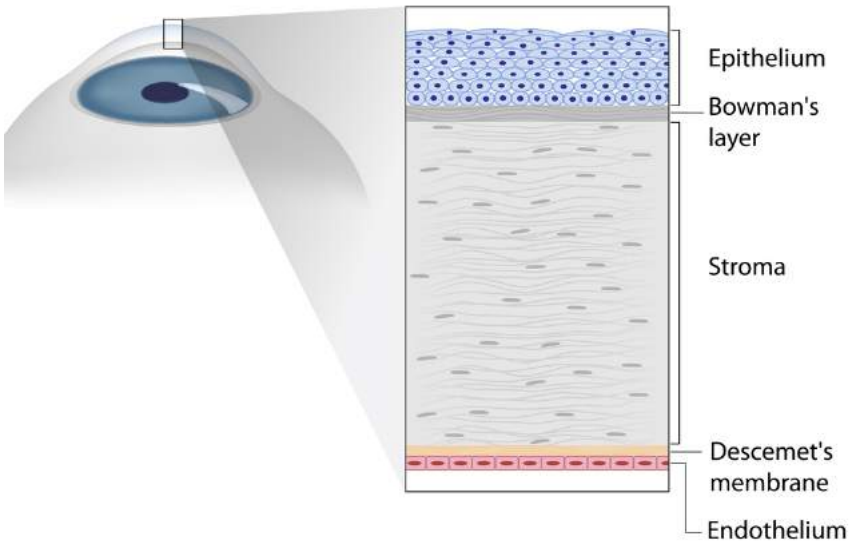

Figure 1.2: Schematic diagram of corneal layers [24].

1.2 Functionality and physiological properties of the aqueous humor and cornea

Aqueous humor is a transparent, watery fluid that contains 98% water and 2% of amino acids, electrolytes, ascorbic acid, glutathione and immunoglobulins [47]. The main functions of aqueous humor are to provide nutrients (including oxygen) to avascular tissues, such as the lens and the cornea, and removes their waste products. In addition, a balancing between aqueous production and resistant to drainage regulates the internal pressure of the eye, known as intraocular pressure (IOP). Aqueous humor is formed from blood by filtration, secretion, and diffusion through the ciliary body. It flows in the posterior chamber, passes through the pupil into the anterior chamber and is eventually drained out of the eye at the porous trabecular meshwork. From there it flows into the Schlemms canal, a ringlike passageway around the outer angle of the anterior chamber in front of the iris and enters the veins [47, 54].

Aqueous humor plays an important role in the health of human eye. As an example, if it does not flow through the drainage angle properly, IOP in the eye increases. This produces mechanical stresses on the optic nerve in the back of the eye that can damage the nerve fibers potentially leading to glaucoma.

In the present thesis we are mostly concerned with aqueous motion in the anterior chamber in relation to stresses the fluid can exert on the boundaries and also transport processes to the cornea. Aqueous motion in the anterior chamber can be induced by several mechanisms that will be described in detail in chapter 2.

In order to understand the nutrient transport from the aqueous to the cornea, it is useful to briefly recall the structure of the cornea itself. The human cornea has five layers [23]:

– **Epithelium**. This is the outermost layer of the cornea. It acts as a barrier to protect cornea, resisting the free flow of fluids from the tears, and prevents bacteria from reaching other layers.

- **Bowman's layer**. This is a very thin, smooth, non–regenerating layer between epithelium and stroma. The functionality of this membrane remains unclear [135].
- **Stroma**. The thickest layer of the cornea (90% of total corneal thickness) located behind Bowman's layer and in front of Descemet's membrane. The corneal stroma plays several roles within the eye. It is the main refracting lens and protects the inner contents of the eye [96]. It is also the load bearing structure of the cornea.
- **Descemet's membrane**. Under the stroma is Descemet's membrane, a thin but strong sheet of tissue that serves as a protective barrier against infection and injuries.
- **Endothelium**. This layer is the extremely thin, innermost layer of the cornea, which are essential in keeping the cornea clear. The primary task of this layer is to pump excessive fluid out of the stroma. Without this pumping action, the stroma would swell and cornea would loose its transparency. It also has the task of a barrier to deliver nutrients from the aqueous humor to the other corneal layer and pass the waste from other layer to aqueous. If too many endothelial cells die, corneal edema and blindness ensue, with corneal transplantation being the only available therapy.

A schematic diagram of corneal layers is shown in figure 1.2.

1.3 Refractive error and treatment

Sometimes, due to the changes in the shape of the eye or irregularity in the shape of cornea and natural lens, light can not focus on the retina properly and the resulting image is blurry. This problem is referred to as *refractive error*. It is categorized as **myopia**, **hyperopia**, **astigmatism**.

In myopic eyes, the eye ball is slightly longer than normal and the incoming light focuses in front of the retina, rather than directly on its surface. Myopic eyes have problems in focusing distant objects. On the other hand in hyperopic eyes the eye globe is slightly shorter than normal and the light rays focus behind the retinal surface, resulting difficulties with seeing near objects. Finally, astigmatism occurs when the cornea or the lens of the eye is irregular in shape. This irregularity causes light entering the eye to focus on two or more points, rather than at a single point. A small amount of astigmatism may cause headache, eye strain and blurry vision. Strong astigmatism can significantly disturb the vision. Figure 1.3 shows a comparison between normal eye and eyes with refractive errors.

Refractive errors may be corrected with eyeglasses, contact lenses or refractive surgery. The options regarding which method can be used depend on various considerations, involving eye health, refractive status and lifestyle. Corrective laser eye surgery is the most popular surgical option and consists in reshaping the curvature of the cornea [71, 128]. However, laser corneal ablation might not be an appropriate option for severe refraction errors and corneas with insufficient thickness [108, 128].

An alternative option, which is progressively gaining popularity, is the implantation of an intraocular lens (IOL) into the eye [89, 124]. There many types of IOLs designed for different purposes. Iris-fixated pIOLs, which are concerned with this work, were originally developed by Worst [137]. They are small, ultra-thin lenses that are implanted in the anterior chamber of the eye, in front of the pupil and are fixed to the iris through special

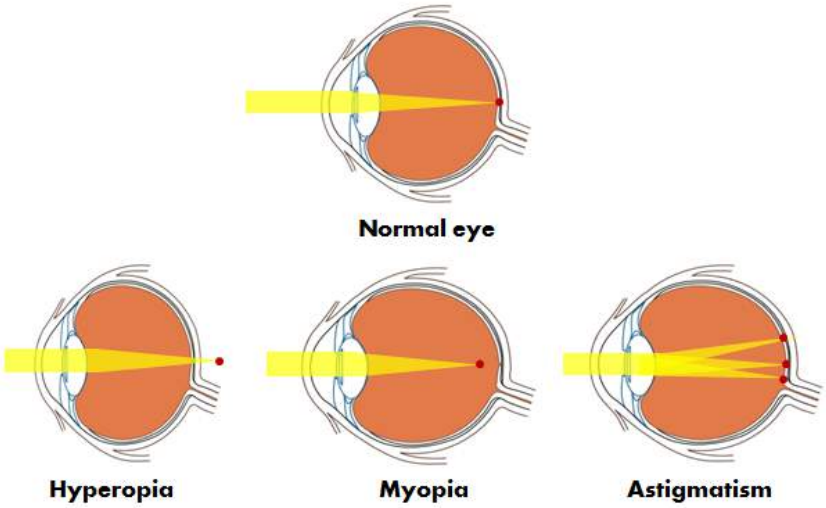

Figure 1.3: Normal eye and refractive errors.

claws. Very few complications are associated with implantation of such lenses. However, occasionally, patients can experience corneal endothelial cell loss, cataract formation, and secondary glaucoma [77]. In this thesis we consider two different iris-fixated pIOLs; the **Artiflex** and the **Hydrophobic Artiflex**.

1.4 Cataract and treatment

Cataract is a clouding of the eye crystalline lens, which leads to a decrease in vision and blindness (see figure 1.4 (a)). Cataract is typically associated with ageing and are causes in extreme case to 50% of blindness worldwide [103].

The most effective way of treating this problem is cataract surgery. The two main types of this surgery are Extracapsular Cataract Extraction (**ECCE**) and Intracapsular Cataract Extraction (**ICCE**). ECCE consists in removing almost the entire lens and leaving the elastic lens capsule intact. Then an intraocular lens (IOL) is placed in the capsule. Figure 1.4 summarizes the ECCE surgical procedure. On the other hand ICCE requires the removal of the lens and the surrounding lens capsule in one piece. After lens removal, an IOL with special haptics is implanted either in the anterior or posterior side of the iris. In this thesis we consider the **Artisan Aphakia** +30.0 D lens (aIOL), designed by Ophtec BV. This lens is commonly used in the ICCE cataract surgery. This aIOL can be implanted to the anterior or the posterior side of the iris after vitrectomy. This is possible as the lens optical properties remain unchanged upon reversal of the lens. In chapter 6 we study which option is more convenient from the mechanical point of view.

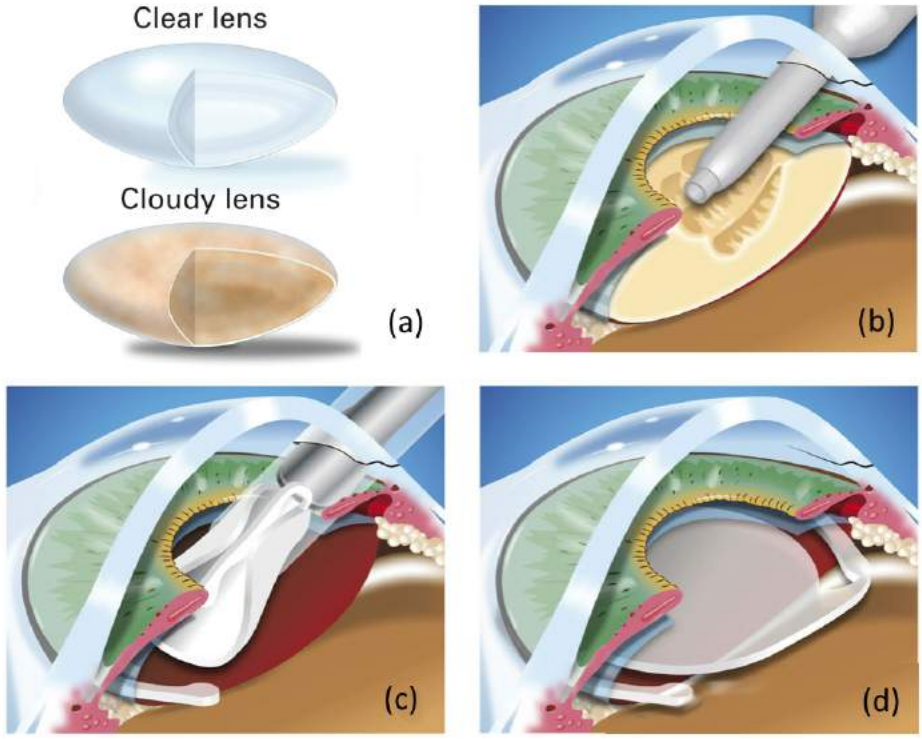

Figure 1.4: (a) normal and cloudy natural lens, ECCE surgery which (b) opaque natural lens is remove and the lens capsule remained intact. (c) a foldable IOL is implanted in the capsule. (d) the surgery is completed and IOL is placed [21].

1.5 Aims of this thesis

The proposed research work is aimed at improving our understanding of aqueous flow in the human eye, with and without the presence of an intraouclar lens. In this PhD thesis we try to provide answer to the following questions:

- *How and to what extend implantation of an iris–fixated intraouclar lens modifies aqueous humor flow in the anterior chamber of the human eye?*
- *If changes due to the presence an pIOL are observed, can these changes help explaining the possible occurrence of cell loss from the iris and cornea and contribute increasing the IOP?*
- *Can modifications in the pIOL design decrease the risk of the possible occurrence of the iris and corneal cell detachment and increase in the IOP?*
- *How and to what extend does implantation of an iris–fixated intraouclar lens modify nutrient delivery to the cornea?*
- *How and to what extend does the position of an Artisan aphakia lens affect the risk of lens displacement?*

These questions all provides a better understanding of the effect of IOLs in the eye using the mathematical tools, when many of the experimental researches failed to achieve this goal due to the complexity, costs and laws enforced by health agencies.

1.6 Structure of this thesis

In **chapter 2** we review the experimental and mathematical researches in the literature regarding the aqueous flow and nutrient delivery process to the cornea. We also describe the existing researches that studied the effect of intraocular lenses on the aqueous flow dynamics and nutrient transport to the cornea. In **chapter 3** we describe the mathematical equations and tools that have been used in order to answer the questions posed in section 1.5. Using these tools, in **chapter 4**, we study the different aqueous flow mechanisms described in chapter 2. In that chapter we consider two main configurations: flow in the anterior chamber without (a) and with (b) the presence of pIOLs. Furthermore we study the effect of design modification of the Hydrophobic Artiflex pIOL on aqueous flow. In **chapter 5** we study two different lens positioning of the Artisan aphakia pIOL: in the anterior (a) and posterior (b) sides of iris. In that chapter we analyse the possible lens dislocation risks that might occur in both configurations and compare them. Finally overall conclusions and future developments associated to this research work are given in **chapter 6**.

Chapter 2

Literature review

2.1 Introduction

This chapter provides a review of the researches that have been carried out regarding in the aqueous flow in the anterior chamber of the eye and nutrient delivery to the cornea. The chapter is divided by two main sections; *aqueous flow in the anterior chamber of the eye* (section 2.2) and *nutrient delivery of the cornea* (section 2.3).

2.2 Aqueous flow in the anterior chamber of the eye

As we discussed in chapter 1, section 1.2, aqueous humor is a transparent, watery fluid which is secreted by the cilliary body, flows along the posterior chamber, the anterior chamber through the pupil and eventually exits the eye through the trabecular meshwork and Schlemm's canal [74]. Aqueous humor is continually produced by the ciliary processes and its rate of production must be balanced by an equal rate of drainage. Changes in the production rate or the resistence to the outflow have strong effect on the IOP [5].

Two of the main functions of aqueous humor flow are to regulate the mean IOP (a) and deliver nutrients to the avascular tissue of cornea and natural lens (b) [47]. In this section we focus on the first of such roles and the second one will be discussed in section 2.3.

2.2.1 Experimental studies

In the early '90s, aqueous humor was considered a stagnant fluid [26]. However many important observations laid this misconception to rest. Seidel [127, 126] injected a dye from a reservoir through a cannula into the anterior chamber of the rabbit eye. When the reservoir was lowered, aqueous humor moved to the cannula and displaced the dye. On the other hand when reservoir was raised to create pressure over 15 mmHg (the mean normal IOP in man), the dye moved to the anterior chamber and appeared in the episcleral veins. In his work he concluded that the aqueous humor is continually produced and drained. Later Goldmann [49, 48, 50], by injecting fluorescein intravenously, observed that the dye enters the anterior chamber and is drained at the trabecular meshwork. These observations opened many new problems, such as identifying the rate of aqueous flow, changes in the flow due to different conditions and aqueous humor formation.

Goldmann [51] was the first to introduce a method to evaluate the aqueous flow rate. In his experiments he used fluorescein to calculate this flow rate. Later many researchers showed that the rate of aqueous humor flow varies according to a circadian rhythm, with different rates of flow during day and night time [75, 131, 112, 93]. Liu et al. [87] have shown that the rate of aqueous flow is reduced to 49% at night in comparison to day time.

In addition to the bulk aqueous flow, aqueous humor motion is also much affected by the temperature gradients and gravity in the anterior chamber. Ehrlich [33] was the first to observed that fluorescein injected systemically appeared in the anterior chamber of animal eyes in a centrally placed vertical line. Using this observation Türk [132] suggested this might be due to aqueous motion produced by the temperature gradient across the anterior chamber. Yeslin et al. [142] measured the temperature of the eyes of adult albino rabbits and showed consistent gradients from the anterior surface of the retina to the outer surface of the cornea. In their research they observed a temperature difference of $\approx 3°C$ across the cornea. Wyatt [138] experimentally demonstrated the existence of a buoyancy-driven flow in the anterior chamber by applying cooled or heated gel-packs to the lids.

Miosis can also induce aqueous flow in the anterior chamber. Miosis is the excessive constriction of the pupil. Dorairaj et al. [30] performed an experiment on the posterior chamber volume after using ultrasound images before and after pupil dilation. They showed that after pupil dilation, changes in the posterior volume of eye can occur. They also showed that iris motion has a small influence in the posterior volume. Later Yamamoto et al. [140] used particle image velocimetry (PIV) in order to measure the flow of aqueous humor through a laser iridotomy hole during miosis in rabbits. Assuming that during miosis in an eye with an iridotomy, the volumetric flux through the pupil is negligible compared to that through the iridotomy hole, one can consider that estimates of volumetric fluxes by Yamamoto et al. [140] could be similar to to the volumetric flux through the pupil in an eye without iridotomy.

Repetto et al. [118] experimentally investigated the fluid motion induced by sinusoidal and real large saccadic eye movements in a spheroid, mimicking the vitreous chamber. Using the particle image velocimetry technique, they measured the flow velocity field on the equatorial plane orthogonal axis of the rotation a spheroid representing a simplified model of vitreous chamber. In their work, vitreous humor was considered as a Newtonian fluid. Later Stocchino et al. [129] studied the dynamics of vitreous humor in a sphere with a small indentation experimentally. Their model was under prescribed sinusoidal oscillations. They showed that a complicated flow field develops that includes circulations close to the indentation. Bonfiglio et al. [16] performed an experimental setup, consisting of a Perspex model of the vitreous chamber as a sphere using artificial vitreous humor. They concluded that viscoelasticity of the fluid has a strong influence on flow characteristics.

Unfortunately there is no analogous experiment to study the motion in the anterior chamber of the eye.

2.2.2 Mathematical studies

Aqueous flow in the anterior chamber has been studied mathematically by many researchers. The first hydrodynamic model of aqueous flow in the posterior and anterior chambers was developed by Friedland [45]. In that model the geometry of the eye was simplified so that an analytical solution to the Stokes equations could be obtained and

applications to open angle and pupillary block glaucoma were discussed. The authors only considered the flow induced by the production/drainage mechanism. Later Canning et al. [20] using Boussinesq approximation and lubrication theory found an analytical solution of the aqueous flow due to buoyancy effects in the anterior chamber. In their model the effect of temperature distribution across the anterior chamber was considered. The geometry of the anterior chamber was simplified in order to be able to obtain a solution to the reduced Navier-Stokes equations. They also found an analytical solution to the bulk aqueous flow on a simplified axisymmetric geometry of anterior chamber. Their models was revisited by Fitt et al. [42] who concluded that buoyancy is the dominant mechanism among other physical mechanisms inducing flow in the anterior chamber. However they could not find an analytical solution for the flow motion in the anterior chamber due to eye movements.

Heys et al. [65] introduced a model of aqueous flow in the anterior and posterior chambers, taking to account the elasticity of the iris. In their model the flow was induced by the pressure difference between the posterior and anterior chambers and they did not take in to account of the temperature gradient across the chambers. Eye models such as those developed by Lagendijk [79], Scott [125], Okuno [100] and Amara [4] were able to predict temperature distribution in the eye. However in those models the aqueous humor was considered as a stagnant fluid. Heys et al. [64] provided a Boussinesq model of natural convection of aqueous humor in the anterior chamber of the eye. They also studied circulation pattern which governs the shape of the Krukenberg spindle (a distinctive vertical band of pigment on the posterior cornea surface that form in some pathologies). The authors solved the full Navier-Stokes and energy equations numerically. Villamarin et al. [133] modeled aqueous flow in the human eye using numerical tools. In their model the geometry of the anterior chamber was based on the anatomy of a real human eye and the flow in the trabecular meshwork and Schlemms canal has also been considered.

Recently [32] studied the aqueous flow in the posterior chamber of the eye and investigate its modification due to the presence of an iridotomy. They considered two aqueous flow mechanisms: aqueous production in the ciliary body and iris motion due to pupil constriction/dilation (miosis/mydriasis). They shown that the latter one can cause a significantly more intense flow. Unfortunately not much work has been done on the flow induced by miosis.

Much work has been done on the flow induced by eye rotations of vitreous chamber. David et al. [25] introduced an analytical viscoelastic model and a numerical Newtonian model of vitreous motion under sinusoidal oscillations. They simplified the vitreous chamber as a sphere and calculated the time-dependent fluid shear and the its maximum. They conclude that myopic eyes have a larger shear force exerted on them. Later Repetto [113] provided an analytical model of the dynamics of the liquefied vitreous induced by saccadic eye movements. The vitreous chamber was assumed as a weakly deformed sphere. Furthermore, he suggested that the irregularity in the shape of the vitreous chamber may significantly modify tangential stresses on the boundary in comparison to a sphere shape. Repetto et al. [116] investigated theoretically the effect of the domain shape in the flow induced by saccadic rotations by considering an idealized model. The geometry was assumed to be a sphere with a small indentation and the motion was prescribed by small-amplitude sinusoidal torsional oscillations. In their model the the vitreous humor was considered as a Newtonian fluid, representing the liquefied vitreous humor. Balachandran [7] performed a numerical study of drug dispersion in the liquid vitreous due to saccadic

eye movements. However, he did not present a comparison of his results with the experimental data and analytic solutions available in the literature. Later Abouali et al. [2] studied the flow dynamics of liquefaction vitreous due to saccadic movements numerically. They compared the wall shear stress on the retina for various saccade amplitudes. They also investigated the effect of variation in vitreous viscosity and the natural lens indentation size. Modarreszadeh et al. [97] performed numerical study of the human vitreous humor flow in the vitreous chamber. They considered vitreous humor as a viscoelastic substance in linear and non-linear viscoelastic regimes.

The effect of saccadic eye movements on the fluid dynamics in the anterior chamber was first studied numerically by Abouali et al. [1]. They concluded that shear stresses and velocity magnitudes created by the saccadic motion are much higher than those produced by buoyancy flow.

Very few researchers have investigated the effects of intraocular lens on flow field in the eye. Niazi et al. [99] studied the effect of an intraocular lens on the aqueous flow in the anterior chamber. Their studied was just restricted to the flow induced by the temperature gradient across the anterior chamber. Later Repetto et al. [114] extended their work and studied the effect of a phakic iris–fixated intraocular lens (pIOL) on the aqueous flow in the anterior chamber, accounting for all the main mechanisms that produce fluid motion. They concluded that the presence of a pIOL changes the aqueous flow dynamics significantly. However, these alterations are unlikely to be the cause of medical complications associated with pIOL use. Kawamorita et al. [72] performed simulations of aqueous humor flow in the posterior chamber with a phakic intraocular lens (ICL) with a central perforation. They suggest that the central hole in the ICL improves aqueous humor circulation to the anterior chamber. Later Fernandez et al. [40] studied the aqueous flow with the presence of two types of ICL, with and without an iridatomy and central hole in the body of the lens. They also consider the effect pupil diameter in their simulations.

2.3 Nutrient delivery of the cornea

2.3.1 Experimental studies

Corneal health requires proper oxygen and nutrient availability. It is known since a long time that oxygen is mainly delivered to the cornea from the atmosphere [41]. In mid '90s the rates of oxygen uptake in the cornea in a variety of animals have been studied by many researchers [12, 121, 27, 80]. In these works corneas were macerated and the cells were suspended in saline. The oxygen uptake of the resultant suspension was measured by the microrespirometer technique. Hill et al. [66] measured the oxygen flux across the anterior surface of the human cornea in vivo. Heald and Langham [62] calculated the oxygen solubility and diffusion coefficient through the whole rabbit cornea. Later Takahashi et al. [130] calculated the diffusion of oxygen in steer and rabbit corneas, using a newer micropolarographic technique. Maurice [92] calculated the oxygen consumption rates for the stroma, epithelium and endothelium. Later Freeman [43] and Freeman et al. [44] determined the oxygen consumptions of the individual layers of the rabbit cornea. Harvitt et al. [59] realized that the measurement of previous works on tear oxygen tension beneath contact lenses was lower than the previous mathematical model predictions. They developed a phosphorescence-based technique in order to calculate the

Rabbit aqueous humor lactate concentration		
Author	No. of rabbits	Lactate concentration (mg/dl)
Reddy et al. [111]	Pooled	83.7 posterior chamber=89.1
Riley [120]	10	89.1 ± 14.4
Laursen et al. [82]	42	55.8
Lamano et al. [58]	42	62.68 ± 9.50
Ruben et al. [122]	11	77.93±9.62
Bergmanson et al. [11]	10	55.26 ± 19.8

Table 2.1: Lactate concentration in the aqueous humor of the rabbit from different publications. The table is taken from Ruben et al.[122]

corneal oxygen consumption rate. They concluded that the corneal oxygen consumption rate for each layer calculated with their method was very similar to other previous works. Later Harvitt et al. [61] using the experiments of Harvitt et al. [60] showed that the low tear oxygen tension beneath contact lenses can be explained by acidosis effect under wearing contact lens. Bonanno et al. [15] performed noninvasive experiments to estimate the corneal oxygen consumption in human subjects.

Mclaren et al. [95] measured the concentration of oxygen in the aqueous humor without penetrating the eye. The authors used a scanning ocular fluorometer and measured the oxygen tension through the depth of the anterior chamber. Their experiments were done for different conditions of the eye; closed eyelids, open eyelids, with and without the presence of a PMMA contact lens.

Glucose and lactate distribution experiments in the cornea have not been as popular as oxygen experiments, owing to their complexity. Zurawski et al. [144] provided experimental results on cultured corneal cells glucose consumption under 155 mmHg oxygen tensions. The maximum glucose concentration was set to 5 mmol/l, which is less than the 6.9 mmol/l found in the normal eye. Myung et al. [98] measured the glucose diffusion coefficients of human, bovine, and porcine corneas in vitro. They used a modified blind well chamber apparatus (Boyden chamber).

Many works studied lactate concentration in the aqueous humor of the rabbit [111, 120, 82, 58, 122, 11]. Table 2.1 shows aqueous humor lactate concentration in these publications. Langham et al. [80] also showed that when rabbits eyelids are closed for 24 hours, the corneal lactate acid increases by 10% to 20% with respect to the open eyelid case. Ruben et al. [122] discussed the effect of PMMA in the aqueous humor lactate concentration in rabbit eyes. Based on their publication, one can conclude that lactate concentrations higher than 96 mg/dl (5.3 mM) should not be observed in the anterior chamber.

2.3.2 Mathematical studies

Fatt et al. [35] proposed a mathematical model for the steady-state distribution of oxygen and carbon dioxide in the cornea. Their model was tested for open and closed eyelids, with and without the presence of a contact lens. The proposed model is one-dimensional and the oxygen consumption rate was assumed constant. Later Fatt et al. [36] improved

this model by considering different oxygen consumption rates and oxygen transmissibility for the stroma, epithelium and endothelium layers. Fatt et al. [37] reexamined the oxygen tension distributions in the cornea using the experimental data from Freeman [43] and Freeman et al. [44]. Weissman et al. [134] calculated human corneal oxygen flux under different soft contact lenses. Later Fatt et al. [38] suggested that the oxygen tension under a gas permeable contact lens during closed eye wear will determine whether abnormal corneal swelling occurs and the oxygen level under such a lens is a unique function of the oxygen transmissibility rather than oxygen permeability or the lens thickness. Harvitt et al. [61] updated the previous models and included the acidification effect under contact wear to the models. Brennan [17] developed an 8-layer model for corneal oxygen distribution. He subdivided the 5 layers of cornea into regions, to avoid the previously observed prediction of negative oxygen concentrations in the stroma and epithelium. All models described above are one-dimensional. Later Alvord et al. [3] proposed a two-dimensional axisymmetric finite element analysis model for the corneal oxygen distribution, with and without contact lens. In that work different oxygen consumption functions (constant, step, monod kinetic, proportional and sigmoid) have been discussed. The coefficients of the sigmoidal function in their model was fit to Bonannos oxygen consumption rate versus oxygen tension [15] in vivo data.

Maurice [91] predicted glucose distribution at the epithelial layer. Using an electric circuit analogy [94] he calculated the glucose distribution in the cornea mathematically. Their work mainly focused on the effect of the intracorneal lenses on the glucose delivery to the cornea. They concluded that shape, depth, thickness and permeability of the lens can modify glucose availability at the cornea. Larrea et al. [81] modeled oxygen and glucose distribution before and after an intracorneal lens implantation using finite element analysis. Similar to all models mentioned above, their model did not consider the direct influence of oxygen consumption on glucose consumption. Chhabra et al [23] proposed a coupled reaction-diffusion model for corneal metabolism. Their model described the metabolic consumption of glucose and oxygen to produce lactic acid, hydrogen ion, bicarbonate ion, and carbon dioxide through Monod kinetics-based reactions for both aerobic and anaerobic pathways. The model was one-dimensional and also considered the corneal acidosis. Later Pinsky [107] adopted the same approach and proposed a three-dimensional model of metabolic species transport in the cornea, with a hydrogel intrastromal lens. He extrapolate the experimental data of Zurawski et al. [144] to the range of glucose concentration found in the normal cornea (6.9 mmol/l).

Chapter 3

Governing equations and numerics

3.1 Introduction

As discussed in chapter 2, section 2.2, aqueous motion in the anterior chamber can be driven by the following different mechanisms

- **Bulk flow induced by aqueous production/drainage**. Aqueous is produced at the ciliary processes and drained at the trabecular meshwork,
- **Buoyancy-driven flow** due to temperature differences across the anterior chamber,
- Transient flow due to **miosis** (i.e. contraction of the pupil),
- **Eye rotations**.

As we mentioned in chapter 1, section 1.5, one of the main aims of this work is to mathematically analyse the effect of an intraocular lens on the aqueous motion and its nutrient delivery to the cornea. In order to mathematically analyse these effects, the governing equations of motion should be formulated and a physical model for the transport and consumption of metabolic species should be written.

In section 3.2 we establish the governing equations of motion, the **Navier-Stokes** equations [9]. For the buoyancy-driven aqueous flow, the Navier-Stokes equations are accompanied by a thermal equation. In section 3.3 we also propose a mathematical model for the delivery of metabolic species to the cornea. Using these equations, with a set of proper boundary conditions, we can model aqueous motion and nutrient delivery in the anterior chamber and cornea. Since these equations in general are highly non linear partial differential equations and the domain of interest is complex, it is not possible to find an analytical solution. For this reason solving these equations requires numerical techniques, and they are discussed in subsection 3.2.1 and 3.3.1, respectively.

3.2 Fluid motion

The fundamental equations of fluid dynamics are based on the following universal laws of conservation:

- conservation of mass,

– conservation of momentum,

– conservation of energy.

The resulting equations, after applying the conservation of mass to a fluid flow is called the **continuity equation**. The conservation of momentum represents Newtons second law. Applying this law to a fluid flow results in a vector equation known as the **momentum equation**. The conservation of energy is the first law of thermodynamics and the resulting equation is called the **energy equation**. To close the system of equations, it is necessary to establish some relationships between fluid properties, which are called constitutive equations. For the Newtonian fluid the following relationship can be used to close the system:

$$\boldsymbol{\sigma} = -p\mathbf{I} + \mathbf{d}, \tag{3.1}$$

where p is the pressure, $\mathbf{I}$ is the identity tensor and $\mathbf{d}$ is the deviatoric part of the stress tensor and $\boldsymbol{\sigma}$ is the stress tensor.

Considering the above, the fluid motion for incompressible fluids is governed by the following equations

$$\frac{\partial \mathbf{u}}{\partial t} + (\mathbf{u} \cdot \nabla)\mathbf{u} + \frac{1}{\rho}\nabla p - \nu \nabla^2 \mathbf{u} - \mathbf{f} = \mathbf{0}, \tag{3.2a}$$

$$\nabla \cdot \mathbf{u} = 0. \tag{3.2b}$$

In the above equations, t is time, $\mathbf{u}$ denotes the velocity vector, p is the pressure, ρ is the density, ν the kinematic viscosity and $\mathbf{f}$ is a source term. ∇ is the divergence operator.

When we study the thermally induced flow, the constitutive equation is the Fourier's law

$$\mathbf{q} = -k\nabla T, \tag{3.3}$$

where $\mathbf{q}$ is the heat flux, k is the thermal conductivity of the fluid and T is temperature. Using the above equations in the energy equation we have

$$\frac{\partial T}{\partial t} + (\mathbf{u} \cdot \nabla)T - \frac{k}{\rho c_p}\nabla^2 T = 0, \tag{3.4}$$

where c_p is the specific heat at constant pressure. In equation (3.4) we have neglected the heat production due to mechanical energy dissipation, which is negligible in the present context [20]. We adopt the Boussinesq approximation, which is known to be very accurate for liquids undergoing small variations in temperature. In this approximation we neglect variations in the fluid density except in the gravitational forcing term and we neglect variations in the kinematic viscosity ν. In this case $\mathbf{f}$ in equation (3.2a) is the gravitational acceleration. In the gravitational term we assume that the aqueous humor density ρ has a small linear dependency on temperature and is independent of pressure, leading to

$$\rho = \rho_0[1 - \alpha(T - T_0)], \tag{3.5}$$

where ρ_0 is the fluid density at a reference temperature T_0 and α is the linear thermal expansion coefficient of the fluid. All aqueous properties in equations (3.2a-3.5) are presented in table A.1 in the Appendix.

3.2.1 Numerical tools and modeling

The Navier-Stokes equations can be solved analytically for some simple cases and under certain assumptions, existence and uniqueness of weak solutions are assured. Unfortunately there is no general theory for the solution of these equations. For this reason solving the Navier-Stokes equations requires numerical techniques. The development and use of such techniques belong to the field of computational fluid dynamics (CFD). There are many mathematical techniques that can be used in order to solve the Navier-Stokes equations numerically. In this work, depending on the problem, Finite Volume Methods (FVM), Finite Difference Methods (FDM) and Finite Element Methods (FEM) have been used.

3.2.1.1 Finite Volume Method using OpenFOAM

Although FDM and FEM are widely used in the numerical mathematics, FVM has gained popularity in discretization methods due to its high flexibility and has shown a prominent role in the simulation of fluid flow problems. FVM owns its flexibility to the fact that discretization is carried out directly in the physical space and no transformation between physical and the computational coordinate system is needed. Due to the nature of FVM, this technique is very convenient when simulating complex geometries.

In FVM, the physical domain of interest is discretized. This requires the subdivision of the domain into discrete non-overlapping cells that completely fill the computational domain to yield a grid or mesh system. The information of the mesh such as cell to cell relations, face to cell relations, geometric information of the surfaces, cell centroid and volume, face centroid, area and normal direction, etc should be stored as basic mesh information. Generally the solution of the equations will be saved at the centroid of cells.

In the finite volume discretization process, the equations are integrated over the elements and the Gauss theorem is applied to transform the volume integrals to surface integrals. Then the surface and volume integrals are transformed into discrete ones and integrated numerically through the use of integration points.

The conservation equations (3.2a-3.4) can be written in a general conservation equation [86]

$$\frac{\partial}{\partial t}(\rho\phi) + \nabla \cdot (\rho \mathbf{v}\phi) = \nabla \cdot (\Gamma^{\phi} \nabla \phi) + Q^{\phi}, \tag{3.6}$$

where $\mathbf{v}$ is the velocity, Γ^{ϕ} is the diffusion coefficient of ϕ and Q^{ϕ} is the production or consumption of ϕ within the control volume per unit volume. Equation (3.6) is general and can represent any of the conservation equations. Considering the steady-state form of this equation and integrating over an element C (see figure 3.1) we have

$$\int_{V_C} \nabla \cdot (\rho \mathbf{v}\phi) dV = \int_{V_C} \nabla \cdot (\Gamma^{\phi} \nabla \phi) dV + \int_{V_C} Q^{\phi} dV. \tag{3.7}$$

using the divergence theorem, the above equation becomes

$$\oint_{\partial V_C} (\rho \mathbf{v}\phi) \cdot d\mathbf{S} = \oint_{\partial V_C} (\Gamma^{\phi} \nabla \phi) \cdot d\mathbf{S} + \int_{V_C} Q^{\phi} dV, \tag{3.8}$$

where $d\mathbf{S} = \mathbf{n}dS$ is the surface element and $\mathbf{n}$ is the normal unit vector. $\oint_{\partial V_C}$ is the closed surface integral over the volume V_C. Using a Gaussian quadrature, the integrals at the

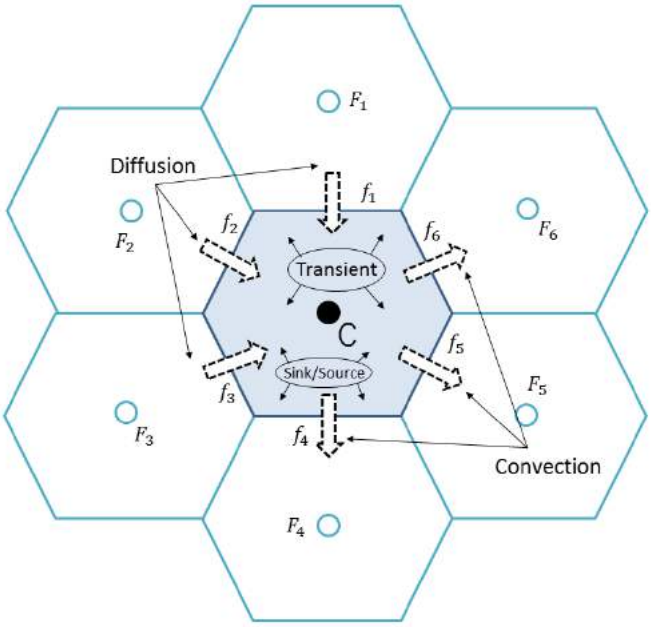

Figure 3.1: Schematic diagram of an element C surrounded by other elements $\{F_i\}_{i=1}^{6}$. $\{f_i\}_{i=1}^{6}$ are the face names of element C.

face f of the element becomes

$$\oint_{\partial V_C} (\rho \mathbf{v}\phi) \cdot d\mathbf{S} = \sum_{f}^{faces(V)} \sum_{ip}^{ip(f)} \Big(\omega_{ip} (\rho \mathbf{v}\phi)_{\mathbf{ip}} \cdot \mathbf{S_f} \Big), \tag{3.9}$$

$$\oint_{\partial V_C} (\Gamma^{\phi} \nabla \phi) \cdot d\mathbf{S} = \sum_{f}^{faces(V)} \sum_{ip}^{ip(f)} \Big(\omega_{ip} (\Gamma^{\phi} \nabla \phi)_{ip} \cdot \mathbf{S}_f \Big), \tag{3.10}$$

where ip is the integration point index, $ip(f)$ is the number of integration points along surface f and ω_{ip} is the weighing function and $\mathbf{S}_f$ is a vector along unit normal to surface f with the magnitude of area of surface f. In most cases, only one Gauss integration point is used which is located at the centroid of the face. This leads to a second order accuracy of the solution and low computational time [88]. Using one Gauss integration point ω_{ip} is one. Adopting a Gaussian quadrature integration, the volume integral of the source term is computed as

$$\int_{V_C} Q^{\phi} dV = \sum_{ip}^{ip(V)} \Big(\omega_{ip} Q^{\phi}_{ip} V \Big). \tag{3.11}$$

Similar to the previous case, using one Gauss integration point, located at the centroid of the element, the second order accuracy is assured and $\omega_{ip} = 1$. Finally using mid-point integration approximation and using one Gauss integration point for the faces and element, the semi-discrete steady state finite volume equation for element C will be

$$\sum_{f}^{nb(C)} \Big(\rho \mathbf{v}\phi - \Gamma^{\phi} \nabla \phi \Big)_f \cdot \mathbf{S}_f = Q^{\phi}_C V_C. \tag{3.12}$$

The right part of equation (3.12) represents the total flux over all faces of cell C and the left part represents the total volume flux of cell C. The Equation (3.12) is now ready to be transferred into an algebraic equation by expressing the face and volume fluxes in terms of the values of the variable at the neighbouring cell centers.

The face flux can be split into a linear and a nonlinear part in which the linear part is a function of ϕ values at the faces (i.e. ϕ_C and ϕ_F). Thus for all cell faces we have

$$\sum_{f}^{nb(C)} J_f = \sum_{f}^{nb(C)} \Big(J_f^C \phi_C + J_f^F \phi_F^f + J_f^N \Big), \tag{3.13}$$

where J_f^C and J_f^F are the linearization coefficients of face f and J_f^N is the nonlinear contribution. The volume flux is also linearised as

$$Q_C^\phi V_C = J_V^C \phi_C + J_V^N. \tag{3.14}$$

Substituting equation (3.13) and (3.14) in (3.12) yields the following algebraic relation

$$a_C \phi_C + \sum_{f}^{nb(C)} a_f \phi_{F_f} = b_C, \tag{3.15}$$

where

$$a_C = \sum_{f}^{nb(C)} J_f^C - J_V^C, \tag{3.16}$$

$$a_f = J_f^F, \tag{3.17}$$

$$b_C = J_V^N - \sum_{f}^{nb(C)} J_V^N. \tag{3.18}$$

These algebraic equations are then assembled into a global matrix and vectors which can be expressed as

$$\mathbf{A}\phi = \mathbf{b}, \tag{3.19}$$

where the unknown variable ϕ is defined at each interior element and at the boundary of the computational domain. This equation can be solved directly or iteratively. For the unsteady case additional time integration over the volume of the element in equation (3.6) is also needed, which depends on the temporal discretization scheme.

Open source Field Operation And Manipulation (OpenFOAM) is an open source finite volume C++ library for CFD, developted by OpenFOAM foundation and distributed exclusively under the GNU General Public Licence (GPL).[102] The primary usage of this library is the creation of executables (*applications*) to solve specific problems (*solvers*) or to manipulate data (*utilities*). OpenFOAM is also supplied with pre- and post-processing environments. The overall structure of OpenFOAM is shown in figure 3.2.

One important characteristic of OpenFOAM is its use of operator overloading that allows algorithms to be expressed in a simple way. As an example, the discretization of the transport equation for a scalar ϕ is given by

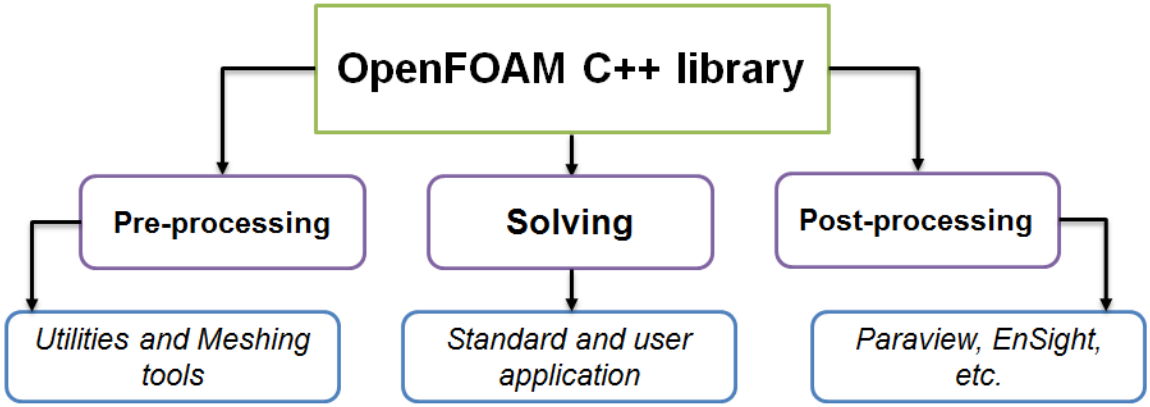

Figure 3.2: Schematic diagram of OpenFOAM structure.

$$\frac{\partial}{\partial t}(\phi) + \nabla \cdot (\mathbf{v}\phi) = \nabla \cdot (D^{\phi}\nabla\phi) + p\phi, \tag{3.20}$$

and can be coded in OpenFOAM as it is shown in figure 3.3.

```
(
    fvm::ddt(phi)
  + fvm::div(mDot, phi)
  - fvm::laplacian(Dphi, phi)
 ==
    fvm::Sp(P,phi)
);
```

Figure 3.3: Script for solving the simple transport equation 3.20 in OpenFOAM.

The namespaces **fvm::** and **fvc::** allow for the evaluation of a variety of operators, such as laplacian and divergence operators, implicitly and explicitly, respectively. These operators are used to construct the LHS and RHS of a system of equations representing the discretized form of equation (3.20) over each element in the mesh. Although the implementation seems simple, due to many reasons such as stability and consistency of the solution, many stability and correction algorithms for complex fluid flows should be used. There are many solvers defined in OpenFOAM in order to model complex fluid flows involving combustion and chemical reactions, multiphase flows and mass transfer, turbulence and heat transfer and etc. For the purpose of this work which invariably involves laminar flows, **simpleFoam**, **pimpleFoam**, **pimpleDyMFoam** and **buoyantBoussinesqSimpleFoam** have been used.

simpleFoam is a steady-state solver for incompressible, laminar or turbulent flow solver based on *Semi-Implicit Method for Pressure-Linked Equations* (SIMPLE) algorithm [104, 90], where the treatment of the non-linear effects of the velocity during the resolution are more important than the precise determination of the pressure field. In this algorithm an approximation of the velocity field is obtained by solving the momentum equation. The pressure gradient term is calculated using the pressure distribution from the previous iteration or an initial guess. The pressure equation is formulated and solved in order to

obtain the new pressure distribution. Finally, the velocities are corrected and a new set of conservative fluxes is calculated. As each iteration is equivalent to a pseudo time step, the properties are under relaxed in order to stabilize the method and improve convergence.

PimpleFoam is a large time-step transient solver for incompressible flows using the PIMPLE (merged PISO-SIMPLE) algorithm [68]. *PimpleDyMFoam* uses the same algorithm and also consider the dynamical motion of the domain. The PISO algorithm is suitable for transient simulations where it is necessary to fully solve the velocity-pressure coupling for each time step. The non-linear effects of the velocity are reduced setting small time steps characterized by Courant numbers below one. In transient compressible cases the error due to the non-linear effects of the velocity are more important because of the compressibility. Then the momentum equation is located in an outer loop named PIMPLE and the momentum balance is recalculated according to a number of PIMPLE iterations. The energy equation can be located in the PIMPLE loop or in the PISO loop. When a thermodynamic property (temperature, density or pressure) vary rapidly in time, the energy equation should be located inside the PISO loop in order to improve the pressure temperature coupling.

buoyantBoussinesqSimpleFoam is a steady-state solver for buoyant, turbulent flow of incompressible fluids using the Boussinesq approximation. This solver can be used when the temperature gradient in the domain is small. The flow is solved using the SIMPLE algorithm considering the buoyancy term [102].

For the simulations of chapter 4 and 6, the described finite volume approach using OpenFOAM has been considered.

3.3 Metabolic species delivery

As mentioned in chapter 1, section 1.5, one of the crucial tasks of aqueous humor is the transfer of its nutrients and oxygen to avascular tissues such as the natural lens and cornea. In this section we introduce a mathematical model for metabolic species delivery to the cornea. In this model the presence of aqueous humor has also been considered. We first briefly describe the corneal metabolism that will be used in the model later.

Corneal metabolism model

Glucose consumption from corneal cells occurs through two main pathways: aerobic (or tricarboxylic acid or Krebs cycle) and anaerobic (Embden-Meyerhof) glycolysis [39]. For the normal rabbit cornea, $\approx$ 15% of glucose breakdown is through aerobic glycolysis [119, 43]. Moreover, $\approx$ 10% of corneal glucose is supplied from glycogen and endogenous glucose [119], however in this work we have neglected this contribution.

In the glycosis one mole of 6-carbon glucose is converted first to 3-carbon pyruvate. Then, in the presence of oxygen, pyruvate is converted to acetyl-CoA and enters to Krebs cycle, resulting in the formation of carbon dioxide and, through the oxidative phosphorylation, water. This pathway is simplified as follows:

$$C_6H_{12}O_6 + 6O_2 \longrightarrow 6CO_2 + 6H_2O + energy. \tag{3.21}$$

In the aerobic respiration 6 moles of water and 6 moles of carbon dioxide are produced by the consumption of 1 mole of glucose with 6 moles of oxygen and the reaction produces 36 net moles of ATP [119, 43].

In the absence of oxygen, the pyruvate produced by glycolysis is converted to lactate and hydrogen ions. This pathway is called Embden-Meyerhof, and is simplified as follows:

$$C_6H_{12}O_6 \longrightarrow 2C_3H_5O_3^- + 2H^+ + energy. \tag{3.22}$$

In this path, for each mole of consumed glucose, two moles of adenosine triphosphate (ATP) are produced. Acidification of the cornea due to this reaction is buffered by bicarbonate ion to produce dissolved carbon dioxide.

In the majority of the corneal oxygen diffusion models, the effect of aerobic and anaerobic glycolytic pathways were neglected.

Transport equations

As described above, the metabolic pathways play crucial roles in supplying nutrient for cells of avascular tissues such as the cornea. This type of processes mainly involves oxygen and glucose consumption and lactate accumulation which they control cell viabilities and influence of the structural integrity of these tissues. As an example, accumulation of lactate ions due to lack of oxygen tension leads to oedema [85]. For this reason, we solely consider the three metabolic speicies of oxygen, glucose and lactate concentrations in our model.

When the eyelids are open, due to the temperature gradient across the anterior chamber, a buoyancy driven aqueous flow is generated that is significantly more intense than the production/drainage flow (see Repetto et al [115]). Eye movements are also capable of generating significant velocities in the aqueous. Due to these observations it is reasonable to assume that the aqueous humor is well mixed in the anterior chamber and, consequently, the concentration of species are constant in the anterior chamber. Therefore, lumping the effect of species transport across the anterior chamber into a boundary condition on the endothelium for solving the problem in the cornea is a sensible approach and a model for the aqueous humor flow can be neglected.

On the contrary, when the eyelids are closed, the temperature in the anterior chamber is approximately uniform and equal to body temperature and, as a result, the thermal flow vanishes. Therefore, the mechanisms that produce fluid flow will be restricted to: i) aqueous humor production at the ciliary processes and drainage at the the trabecular meshwork and ii) rapid eye movements which occurs at phases well separated in time by periods of rest. Since the production/drainage flow is very slow in this case we should not expect metabolic species concentrations to be constant throughout the anterior chamber. Thus, in order to study metabolic species delivery to the cornea in the case of closed eye lids, it is necessary to also account for transport within the aqueous humor.

When the eyelids are closed, buoyancy and gravity effects (whose effective direction is dictated by the patient's sleeping position) are negligible and flow is dominated by fluid motion through the pupil aperture [20, 42]. Since the Reynolds number is very small [42], and we are only interested in the presence of a steady flow, the Navier–Stokes equation can be reduced to the following Stokes equation

$$\frac{1}{\rho}\nabla p - \nu\nabla^2\mathbf{u} = \mathbf{0}, \tag{3.23a}$$

$$\nabla \cdot \mathbf{u} = 0. \tag{3.23b}$$

Transport of metabolic species in the aqueous is also affected by its motion and therefore is modelled with the following advection/diffusion equations

$$\frac{\partial c_i}{\partial t} + (\mathbf{u} \cdot \nabla) c_i - D_i^{aq} \nabla^2 c_i = 0, \qquad (i = O, G, L) \tag{3.24}$$

where $\mathbf{u}$ is the velocity vector of aqueous motion in the anterior chamber, calculated by solving equations (3.23a) and (3.23b). In the above equations, subscripts of $i = O, G$ and L refer to oxygen, glucose and lactate ion, respectively. c_i and D_i^{aq} are the concentration and diffusion coefficients of the corresponding metabolic species in aqueous, respectively. In our model the oxygen concentration c_O will be represented as $k_O p_O$ where k_O is henry's constant and p_O is the oxygen tension.

Chhabra et al. [23] proposed a three-dimensional metabolic model for the corneal layers. the coupled oxygen, glucose and lactate ion is governed by the following diffusion/reaction equations:

$$\frac{\partial c_i}{\partial t} - D_i^j \nabla^2 c_i + m Q_i^j = 0. \qquad (i = O, G, L) \tag{3.25}$$

In the above equations, indices of j refers to three corneal layers of endotheluim, stroma and epitheluim. Q_i^j $(i = O, G, L)$ refers to oxygen, glucose consumption and lactate production rate, respectively. m is 1 for oxygen and glucose and -1 for lactate ion equations. D_i^j refers to the diffusion coefficients of metabolic species for each corneal layer.

Reaction models

Considering equations (3.21) and (3.22), the metabolic consumption of glucose can be related to oxygen consumption and lactate production as follows

$$Q_G^j = \frac{Q_O^j}{6} + \frac{Q_L^j}{2}. \tag{3.26}$$

The above equation implies that each mole of glucose oxidation requires six moles of oxygen and each mole of anaerobic glycosis leads to the production of two moles of lactate ions.

In Chhabra et al. [23], for each layer of cornea, the dependency of Q_O^j on both p_O and c_G was modelled using a non-linear Monod kinetics. We modify the authors' approach and use a sigmoidal function to model the dependency of Q_O^j on p_O, as proposed by Alvord et al. [3]. This is because the sigmoidal function described in their work fits better with the in vivo experiments of Bonanno et al. [15].

This results in the use of the following expression for the oxygen consumption rate

$$Q_O^j = \frac{Q_{Omax}^j}{1 + e^{\frac{-(p_O - p_{crt})}{R}}} \frac{c_G}{c_G + K_G^O} \left(1 + 0.8 \frac{7.6 - pH}{K_{pH} + 7.6 - pH}\right). \tag{3.27}$$

The parameters appearing in the sigmoidal function are based on the experimental data of Bonanno et al. [15] and reported in table A.4 in the Appendix. The glucose Monod dissociation equilibrium K_G^O is considered equal to 0.4 mmHg, corresponding to an oxygen consumption rate of 93.75% of the saturation value at a glucose concentration of 6 mM [23]. The third term in the equation above (in brackets) refers to the reduction of pH

from the normal value of 7.6 due to the acidosis which is described in Chhabra et al. [23]. In the case of open eyelids the corneal pH is about 7.6 but, when the eyelids are closed, it decreases to approximately 7.39 [14]. In our model this effect has been considered. Lactate ion production rate is described by the following equation

$$Q_L^j = Q_{Lmin}^j(1 + \frac{K_O^L}{K_O^L + p_O})\frac{c_G}{c_G + K_G^L}, \tag{3.28}$$

where Q_{Lmin}^j is the minimum lactate ion production rate and varies by corneal layers. We note that K_O^L reflects how glycolysis shifts from aerobic respiration to anaerobic fermentation as oxygen tension falls. At low oxygen tension, the lactate ion production rate is assumed to be double compared to the minimum value Q_{Lmin}^j, whereas for high oxygen tension, the production rate tends to Q_{Lmin}^j. The shift constant K_O^L is evaluated equal to 2.2 mmHg, by assuming that at an oxygen tension of $p_O = 20$ mmHg, lactate ion production rate is 10% above its minimum possible value Q_{Lmin}^j. Finally, K_G^L is assumed to be equal to K_G^O. The above choice of the values of the parameters appearing in (3.28) follows the approach of Pinsky [107].

The values of the parameters that appear in the equations (3.24-3.28) are listed in tables A.3, A.4 and A.5 in the Appendix.

3.3.1 Numerical tools and modeling

3.3.1.1 Brief explanation of the Finite Element Method

The Finite Element Method (FEM) is one of the widely used numerical methods for the solution of differential equations together with FVM and FDM. One of the main reasons to the success of FEM is the flexibility of the formulation in which the properties of the discretization is controlled by the choice of of approximating the finite element spaces. Similar to FVM and FDM, the domain in which the numerical solution should be found is partitioned into a finite set of cells with disjoint interiors such that their union covers the whole domain. Then a local function space is defined on each cell and using these function spaces one can build the global function space. A cell together with a local function space and a set of rules for describing those local functions is called a finite element. The formal definition reads as follows: a finite element is a triple $(K, P(K), \Sigma)$, where

- K is the a closed bounded domain subset of $\mathbb{R}^d$ where $(d = 1, 2, 3, ...)$ with nonempty interior and piecewise smooth boundary,
- $P = P(K)$ is a finite dimensional function space on K,
- Σ is a set of degree of freedom

such that a function $v \in P(K)$ can be uniquely determined by Σ [143].

A finite element method is characterized by a weak formulation, a discretization method and solution algorithms. The weak form of differential equations is generally obtained by multiplication of the strong form of these equations with test functions in an appropriate space called *test space* and integrated over the domain. Using some rules such as Green identities, the order of the derivatives in some of the integral terms can be reduced. In this way these equations are no longer required to hold absolutely or well defined and have instead weak solutions only with respect to certain test functions.

Some of the variational formulation are the Galerkin method, the discontinuous Galerkin method, mixed methods which in the context of this work we use the first one.

3.3.1.1.1 Linear problem

Consider a general linear variational problem written in the following canonical form

Suppose that $a : V \times V^{'} \to \mathbb{R}$ and $f : V^{'} \to \mathbb{R}$. In this context V and V' are called the trial space and the test space, respectively. Find $u \in V$ such that

$$a(u, v) = f(v) \quad \forall v \in V'. \tag{3.29}$$

Thus we express the variational problem in terms of a bilinear form a and a linear form (functional) f. In the Galerkin method, finite-dimensional vector subspaces $V_n \subset V$ and $V'_n \subset V'$ are chosen and we have the following projected problem: find $u_n \in V_n$ such that

$$a(u_n, v_n) = f(v_n) \quad \forall v_n \in V'_n \in V'. \tag{3.30}$$

Reducing the problem (3.29) to (3.30) allows us to numerically compute the u_n as a finite linear combination of the basis vectors in V_n. Let us assume $\{\phi_i\}_{i=1}^n$ and $\{\phi'_i\}_{i=1}^n$ be basis of V_n and V'_n, receptively. Then

$$u_n = \sum_{j=1}^{n} U_j \phi_j. \tag{3.31}$$

Substituting $v = \{\phi'_j\}$ and (3.31) in equation (3.30) we have

$$a(\sum_{j=1}^{n} U_j \phi_j, \phi'_i) = \sum_{j=1}^{n} U_j a(\phi_j, \phi'_i) = f(\phi'_i) \quad (i = 1, ..., n). \tag{3.32}$$

This equation can be written as a linear system of equations $\mathbf{AU} = \mathbf{f}$ where

$$A_{ij} = a(\phi_j, \phi'_i), \tag{3.33}$$

$$f_i = f(\phi'_i). \tag{3.34}$$

The aim of Galerkin's method is the production of this linear system of equations which can be used to compute the solution.

3.3.1.1.2 Nonlinear problem

Nonlinear variational problems can written in the following canonical form: find $u \in V$ such that

$$F(u; v) = 0 \quad \forall v \in V', \tag{3.35}$$

where here $F : V \times V^{'} \to \mathbb{R}$ is a semi–linear form. Similar to the linear case, by choosing finite-dimensional vector subspaces $V_n \subset V$ and $V'_n \subset V'$ we have the following discrete form

$$F(u_n; v_n) = 0 \quad \forall v_n \in V'_n. \tag{3.36}$$

Let us again assume $\{\phi_i\}_{i=1}^n$ and $\{\phi_i'\}_{i=1}^n$ be basis of V_n and V_n', receptively and consequently $u_n = \sum_{j=1}^n U_j\phi_j$. Then the finite element solution u_n can be computed by solving a nonlinear system of equations $\mathbf{b}(\mathbf{U}) = \mathbf{0}$ where $\mathbf{b} : \mathbb{R}^\mathbf{n} \to \mathbb{R}^\mathbf{n}$ and

$$b_i = F(\sum_{j=1}^{n} U_j\phi_j; \phi_i') = 0 \quad (i = 1, ..., n). \tag{3.37}$$

To solve the nonlinear system (3.37) using Newtons method or some variant of Newtons method the Jacobian of $\mathbf{b}$ should be calculated. If the semilinear form F is differentiable in u we have

$$A_{ij}(u_n) = \frac{\partial b_i(\mathbf{U})}{\partial U_j} = \frac{\partial F(u_n; \phi_i')}{\partial U_j} = F'(u_n; \phi_i')\frac{\partial u_n}{\partial U_j} = F'(u_n; \phi_i')\phi_j = F'(u_n; \phi_i', \phi_j). \tag{3.38}$$

The Jacobian matrix A and b should be computed in each newton iteration and update $\mathbf{U}$ by

$$U^{k+1} = U^k - \delta U^k \quad (k = 1, ...,), \tag{3.39}$$

which δU^k is the solution of

$$A(u_n^k)\delta U^k = b(U^k) \quad (k = 1, ...,). \tag{3.40}$$

since for each fixed u_n, $a = F'(u_n; ., .)$ is a bilinear and $L = F(u_n, .)$ is a linear form, for each Newton iteration, we solve a linear variational problem of the following canonical form: find $\delta u \in V_{n,0}$

$$F'(u_n; \delta u, v_n) = F(u_n, v_n) \quad \forall v_n \in V_n'. \tag{3.41}$$

where $V_{n,0} = \{v - w : v, w \in V_n\}$. Discretization (3.41) as in the linear one will recover the linear system (3.40).

For the simulation of metabolic species delivery, COMSOL Multiphysics 4.3 has been used. This program is a cross-platform finite element analysis, solver and multiphysics simulation software. It allows conventional physics-based user interfaces and coupled systems of partial differential equations (PDEs). Similar to OpenFOAM, this software contains three main stages of pre-processing, solver and post-processing. However unlike OpenFOAM the domain of interest can be designed in the program itself. The solver can import or design 1D, 2D, 3D and 2D axisymmetric geometries and calculate the solution of desired equations corresponding to the dimension of the domain.

3.3.1.2 Finite Element Method using COMSOL Multiphysics

COMSOL Multiphysics has plenty of add-on modules for simulating designs and processes based on fluid flow, heat transfer, electromagnetics, structural mechanics, acoustics, and chemical engineering behavior. For the simulation of equations (3.23a) and (3.23b) the **Creeping Flow** option from *Fluid Flow* module has been used. The equations (3.24-3.28) have been written in **Transport of Diluted Species** option form *Chemical Species Transport* module. Note that all these equations can be written in their strong form and the program transfers these equations to their weak form. For the simulation of all equations *MUltifrontal Massively Parallel sparse direct Solver* (**MUMPS**) has been used.

This solver is specially useful for the solution of large sparse systems of linear algebraic equations on distributed memory parallel computers. For time dependent simulations, for time stepping, *Backward Differentiation Formula* (**BDF**) has been considered. BDF is a family of implicit methods of numerical integration of differential equations. They are multistep methods that approximate the derivative of a given function using information from already computed and in this way it increases the accuracy of the approximation.

For the simulations of chapter 5, we used COMSOL Multiphysics to solve the metabolic species model, described above.

Chapter 4

Mathematical models of aqeous flow in the anterior chamber in the presence of phakic iris-fixated intraocular lenses

4.1 Introduction

As discussed in chapter 2, section 2.2, aqueous motion in the anterior chamber can be driven by different mechanisms.

- Aqueous production at the ciliary processes and drainage at the trabecular meshwork, which in this work we refer to this flow as "**bulk flow induced by aqueous production/drainage**",
- **Buoyancy-driven flow** due to temperature differences across the anterior chamber,
- Transient flow due to **miosis** (i.e. contraction of the pupil),
- **Eye rotations** such as saccadic motions.

In this chapter we study these motions in the anterior chamber, with and without the presence of different phakic iris-fixated intraocular lenses (pIOL). Fluid motion will be studied numerically using OpenFOAM. We will see how and to what extend the implantation of pIOLs modify the aqueous humor flow in the anterior chamber. We also investigate whether these changes can help explaining the possible occurrence of iris and corneal cell detachment and increase of the presented IOP. Furthermore, we study a possible modification of the lens body aimed at making the flow in the presence of the pIOL more similar to the physiological one.

The present chapter is organized as follows. We first discuss the geometries adopted in the simulations in section 4.2 and 4.3. Then we will discuss the boundary conditions and the solvers used in the simulations in section 4.4. In section 4.5 we will present all results, related to the case in which no lens is presented in the anterior chamber (4.5.1) and in the presence of the two pIOLs considered (4.5.2 and 4.5.3). For each case, aqueous flow induced by mechanisms mentioned above will be described separately. In section 4.6

and 4.7 we will summarize the simulations and results, respectively. Finally, the main results conclusions of this chapter is given in section 4.8.

The results in this chapter have been published in a research paper [73].

4.2 Geometries

We limit our simulations to the anterior chamber and neglect the flow in the posterior chamber. Thus, in our simulations, the iris-lens channel represents the inlet section. For the anterior chamber we use the same idealized shape as in Repetto et al. [115], a cross-section of which is shown in figure 4.1. The geometry is axisymmetric and since our analysis is 3-dimensional, this geometry is revolved by 360 degrees around its axis of symmetry.

In our simulations we use two different types of pIOLs: the **Hydrophobic Artiflex** and the **Artiflex**. The geometry of the Hydrophobic Artiflex (figure 4.2 (b)) and Artiflex (figure 4.3 (b)) pIOLs have been provided by Ophtec BV. Both pIOLs consist of a lens and two haptics, which are used to fixate the pIOL to the iris. A three-dimensional view of the anterior chamber with the pIOLs implanted is shown in figures 4.2 (a) and 4.3 (a).

As it can be seen in figure 4.2 (b), the geometry of the body of the Hydrophobic Artiflex pIOL is axisymmetric. On the other hand for the Artiflex lens this symmetry is broken as shown in figure 4.3 (c). Moreover, the Artiflex pIOL is thicker than the Hydrophobic one, which might create very narrow region between the iris and the lens. For this reason the numerical results are very sensitive to the positioning of the Artiflex len in the anterior chamber. Since the exact position of the pIOL varies from implantation to implantation, for this lens we performed a parametric analysis by choosing a reference position of the lens and then slightly varying it.

We also study two modified configurations of the Hydrophobic Artiflex pIOL, obtained by generating holes across the lens body. The perforation of the intraocular lenses are already in use for implantation in the posterior chamber. In the first case the original pIOL design is modified by drilling a central round hole through the lens body, as shown in figure 4.2 (c). As a reference value for the diameter of the hole, we use the value adopted by Kawamorita et al. [72] for posterior chamber pIOLs, i.e. $d_{hole} = 0.36\ mm$. One of the main reasons for considering the possibility of adding holes in the pIOL is to avoid excessive IOP growth.

For the second setup we consider the case of two side holes through the lens body (see figure 4.2 (d)). The symmetry axes of the holes are parallel to the coordinate normal to the anterior surface of the lens and the diameters are, again, $d_{hole} = 0.36\ mm$.

In the present study we neglect the presence of the haptics for both lenses, which were shown by Repetto et al. [115] to have negligible influence on aqueous flow. Neglecting the haptics has two advantages. On the purely computational side it allows us to work with smaller meshes, thus significantly decreasing the computational time. This is particularly relevant for the case of unsteady simulations, which have a high computational cost (long computational time). Moreover, neglecting the presence of the haptics allows us to establish the role of the positioning of the lens on the fluid dynamics in the anterior chamber. In fact, by removing the haptics we can freely change the position of the lens within the anterior chamber. As it will be shown later in this chapter this will allow us to obtain relevant physical insight into the problem.

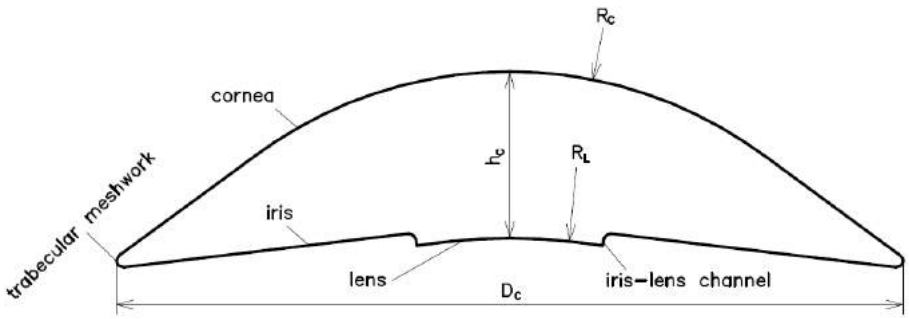

Figure 4.1: Cross section of the idealized anterior chamber.

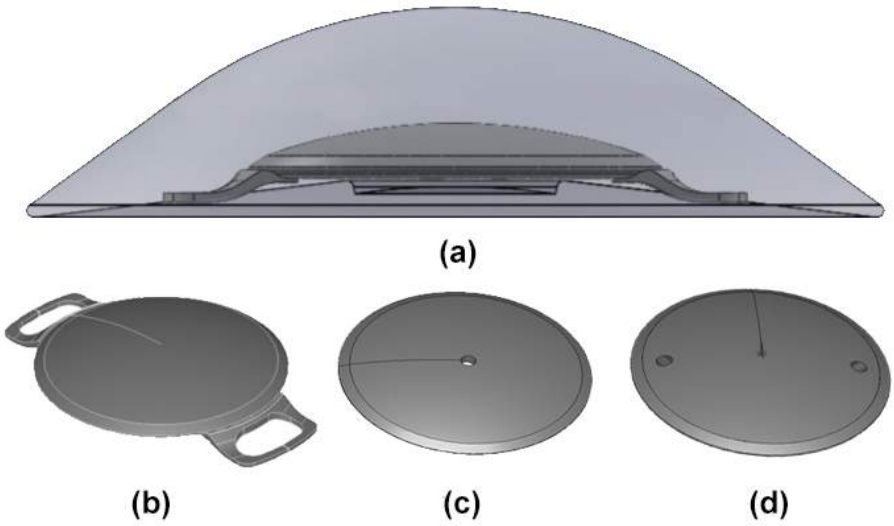

Figure 4.2: (a) Hydrophobic Artiflex pIOL positioned within the anterior chamber, (b) geometry of the Hydrophobic Artiflex consisting of a lens and two haptics. These haptics are used to fixate the Hydrophobic Artiflex to the iris. (c) Hydrophobic Artiflex with a central hole of radius 0.18 mm, (d) Hydrophobic Artiflex with two side holes of radius 0.18 mm.

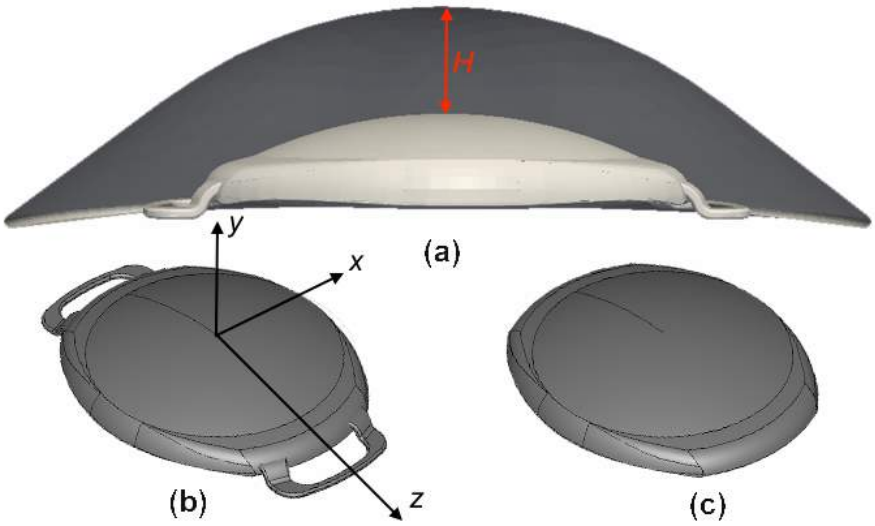

Figure 4.3: (a) Artiflex pIOL positioned within the anterior chamber. parameter H is the distance between the centre of the cornea and the centre of the lens surface (b) geometry of the Artiflex consisting of a lens and two haptics. The axis of coordinates is also should for further analysis. (c) Artiflex without haptics.

4.3 Positioning the pIOLs

In order to mimic the real lens implantation, we positioned the Hydrophobic Artiflex pIOL in the anterior chamber in such a way that its haptics coincide with the iris. Figure 4.4 shows the position of the pIOL on the iris. Due to the design of this lens, the distance between the tips of the haptics and the lens body is large (see figure 4.5). Thus after placing the pIOL, the gap between the iris and lens is large.

In order to choose a reasonable position for the numerical model, we first matched the position of the haptics of the Artiflex with the reference positioned Hydrophobic one. With this assumption, the distance H (see figure 4.2.a) between the centre of the cornea and the centre of the lens surface was $H_0 = 1.492\ mm$. Then by decreasing this value, we perform several parametric analysis. In particular, we write

$$H = H_0 - \alpha \qquad (\alpha \geq 0), \tag{4.1}$$

where H is the new distance between the centre of the cornea and the centre of the pIOL surface after varying the parameter α. Equation (4.1) shows that by increasing the value of α one displays the Artiflex pIOL towards the cornea.

We also analysed the effect of translating the lens by a distance β in the x–direction and by a distance γ in the z–direction, respectively.

Figure 4.6 represents a cross section orthogonal to the x-axis of the anterior chamber with the Artiflex in two different positions. Figure 4.6 (b) refers to the case in which $H = H_0$ and the lens body is almost intersecting with the iris, while figure 4.6 (a) shows the case in which lens has been translated by $\alpha = 0.06$ mm towards the cornea.

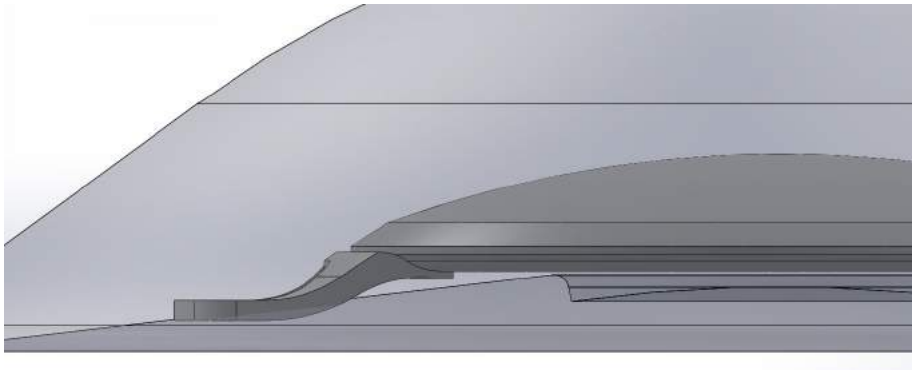

Figure 4.4: the Hydrophobic Artiflex pIOL positioned within the anterior chamber to the iris.

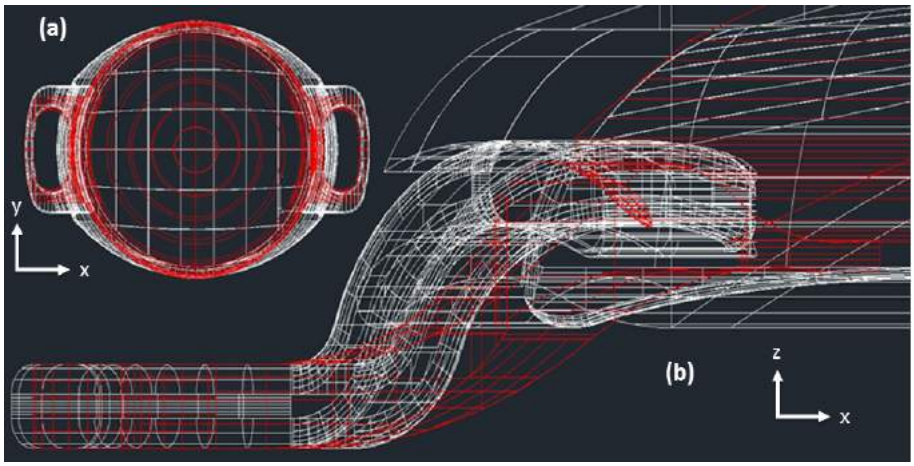

Figure 4.5: (a) $x - y$ plane projection of the Hydrophobic Artiflex (red) and Artiflex (white) pIOLs. (b) $x - z$ plane projection of both lenses. The haptics of pIOLs are matched.

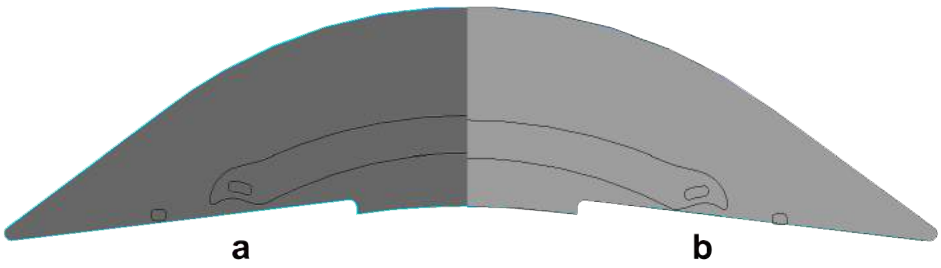

Figure 4.6: The Artiflex lens positioned with (a) $H = 1.432$ mm ($\alpha = 0.06$ mm); (b) $H = H_0 = 1.492$ mm ($\alpha = 0$ mm).

4.4 Boundary conditions and solvers

In order to study all of flow mechanisms discussed in chapter 2, section 2.2, numerically, we need to specify proper boundary conditions over different surfaces of the anterior chamber and the pIOL, if present. Furthermore, we used OpenFOAM in order to model all these flows and, depending on the type of the flow, a proper solver among those discussed in chapter 3, section 3.2, has been used. In this section we discuss the boundary conditions and OpenFOAM solvers adopted in the simulations. Figure 4.1 shows all the surfaces when boundary conditions have been imposed.

4.4.1 Bulk flow induced by aqueous production/drainage

In the numerical simulations related to this flow, the following boundary conditions have been considered:

- **Iris–lens channel.** This is the inlet surface. We impose a parabolic velocity profile, which corresponds to a flux across the patch equal to 5×10^{-11} m^3/s (see table A.1 in the Appendix). We note that this profile has a better performance that a uniform inlet velocity profile, which is locally incompatible with the no-slip condition on the lens and would produce localized numerical oscillations of the pressure at the inlet patch (in the region where this joins with the lens patch). On the other hand using a parabolic velocity profile, the velocity at the edges of the inlet patch is set to zero. As a result, the pressure distribution on the channel patch is smoother. We finally note that, owing to the very small thickness of the iris-lens channel, lubrication theory is expected to be valid here. According to this theory the velocity profile across the domain is parabolic. This justifies our choice of a parabolic velocity distribution at the entrance of the computational domain.
- **Trabecular meshwork.** This is the outlet surface. We impose zero pressure. We note that the pressure is defined up to a constant. In other words what matters is differences in pressure within the domain rather than the actual value of the pressure.
- **All other surfaces.** We assume that all other surfaces are solid walls and impose the so–called no–slip boundary condition.

The solution of this particular flow is found running the *simpleFoam* solver, which is discussed in Chapter 3, section 3.2.1.

4.4.2 Flow generated during miosis

For these simulations we impose the following boundary conditions:

- **Iris–lens channel.** This is the inlet surface. We impose an inflow flux variable in time, according to the law shown in figure 4.8.
- **Trabecular meshwork.** This is the outlet surface. We impose zero pressure.
- **All other surfaces.** We impose on all other surface the no–slip boundary condition.

The time–dependent numerical solution of this flow is found running the *pimpleFoam* discussed in Chapter 3, section 3.2.1.

4.4.3 Flow induced by buoyancy effects

For the simulations of the buoyancy driven flow, the following boundary conditions have been imposed:

- no-slip velocity boundary condition on all surfaces;
- prescribed temperature on the cornea ($T = 34\ ^\circ\text{C} = 307.15$ K);
- prescribed temperature on all other surfaces (37 °C = 310.15 K, approximately equal to body temperature).

The steady state numerical solution of this flow is found running the *buoyantBoussinesqSimpleFoam* discussed in chapter 3, section 3.2.1. As it was mentioned there this solver uses a semi-implicit method to iteratively solve the Navier-Stokes equations and the heat equation, making use of the Boussinesq approximation for modelling density variations due to temperature differences.

4.4.4 Flow induced by saccadic eye rotations

For the simulations regarding saccadic eye rotations, we impose the following boundary conditions:

- **All surfaces.** We impose on all other surface a velocity boundary condition associated to the saccadic motion discussed this chapter, section 4.5.1.3.

The time–dependent numerical solution is found, running the *pimpleDyMFoam* discussed in Chapter 3, section 3.2.1.

4.5 Results

In this section we show the results of the aqueous flow mechanisms discussed in the introduction of this chapter. For this results, boundary conditions and solvers described in section 4.4 have been used. For our simulations we consider two main cases: flow in the anterior chamber without (a) and with (b) the presence of a pIOL.

In order to asses the reliability of the numerical simulations we first performed careful convergence studies. Specifically, we run several simulations progressively increasing the mesh size.

4.5.1 Flow in the anterior chamber without the presence of a pIOL

In order to understand the effect of a pIOL on aqueous flow in the anterior chamber, we first need to study the flow in the physiological case, in the absence of the pIOL, which we will use a reference case.

4.5.1.1 Bulk flow induced by aqueous production/drainage

As it was discussed in chapter 2, section 2.2, aqueous humor produced by the ciliary body, enters the anterior chamber through the pupil, and is drained into the trabecular meshwork.

The pressure (a) and velocity magnitude (b) distributions on a diametral cross-section of the anterior chamber are shown in figure 4.7. As expected the flow is extremely regular (the Reynolds number is very small) and fluid particles are smoothly swept from the inlet section to the cornea–iris angle, where the outflow section is located. The velocity and pressure fields are axisymmetric and peak at the inlet section.

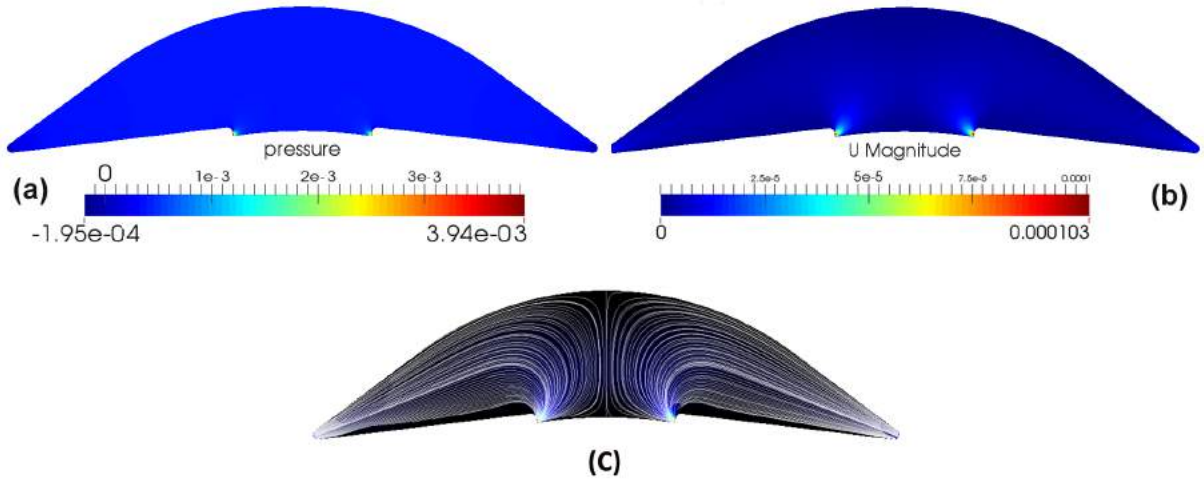

Figure 4.7: Pressure (a) and velocity magnitude (b) distribution over a diametral cross-section of anterior chamber without a pIOL. Streamlines of the flow is shown in (c). Maximum pressure: $p_{\max} = 3.94 \times 10^{-3}$ Pa. Maximum velocity magnitude: $u_{\max} = 10.3 \times 10^{-5}$ m/s.

Flow generated during miosis

During pupil contraction (miosis), flow is generated from the posterior to the anterior chamber of the eye. This flow is much more intense than the bulk flow due to production–drainage of aqueous described in the previous section, but it lasts a short time, typically less than 1 s. In order to be able to quantify such a flow. This information is not presently available.

Owing to the lack of information concerning the flux during miosis we refer in the following to measurements taken be Yamamoto et al. [139] on rabbit eyes. The authors performed a laser iridotomy on a rabbit eye and measured with the Particle Image Velocimetry technique (PIV) the flux through the iridotomy. If we assume that the flux through the iris–lens channel is negligible compared to that through the hole in the iris, the flux through the iridotomy hole is a good approximation of the total flux from the posterior to the anterior chambers during miosis.

Yamamoto et al. [139] measured a maximum velocity $u_{\max}$ equal to 9.39 mm/s through the laser iridotomy hole, which had a diameter d_{LI} of approximately 0.56 mm. The duration of the jet T_{jet} from was approximately equal to 0.66 s, which is the average duration of miosis in humans after light stimulation [101]. Based on the above considerations the

authors assumed the following time law for the flux Q through the iridotomy

$$Q(t) = \pi \frac{d^2}{4} u_{\max} \cos\left(\frac{\pi t}{2T_{\text{jet}}}\right), \tag{4.2}$$

where t is time.

We have modified the above expression by adding a ramp, of duration 0.1 s, during which the velocity grows from 0 to $u_{\max}$, which is aimed at avoiding numerical artefacts during the very initial stage of the simulation. The assumed flux $Q(t)$ is shown in figure 4.8.

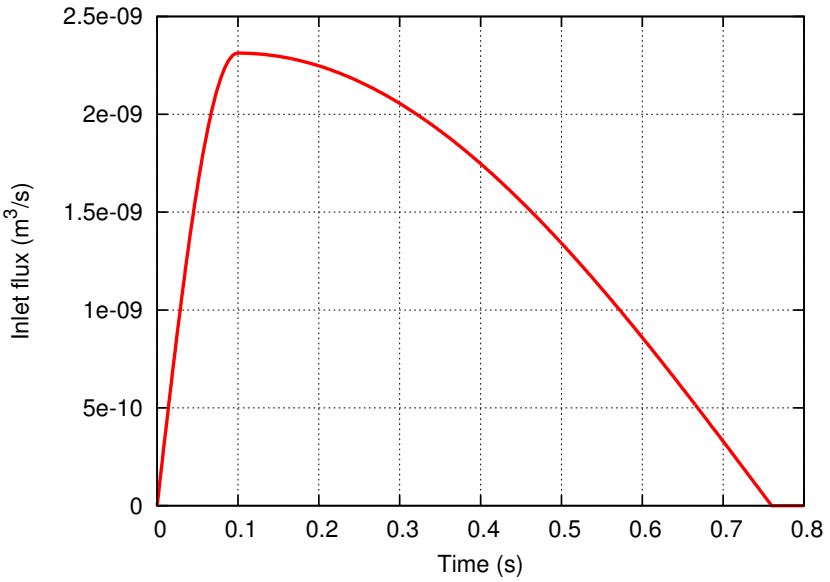

Figure 4.8: Flux from the posterior to the anterior chamber of the eye generated during miosis. The intensity of the flux is based on the measurements by Yamamoto et al. [139] on rabbit eyes.

Results from this simulation in terms of inlet pressure will be shown and compared with the case in which the Hydrophobic Artiflex lens is implanted in the anterior chamber in section 4.5.2.

4.5.1.2 Flow induced by buoyancy effects

In this section we study the motion induced in the anterior chamber by a temperature difference between the cornea and the posterior part of the chamber.

As we discussed in chapter 2, section 2.2, this flow has been studied by several authors analytically [e.g. 20], numerically [e.g. 64] and experimentally [e.g. 140]. These studies have demonstrated that a buoyancy driven flow is generated by temperature differences across the anterior chamber. Specifically, since the inner surface of the cornea is typically colder than body temperature, fluid particles close to the cornea move down and, for continuity, particles close to the iris (which is approximately at body temperature) move up. In normal conditions this flow is much more intense than that produced by production/drainage of the aqueous. Owing to this observation we neglect in the simulations presented in this section the very slow flow induced by aqueous production/drainage.

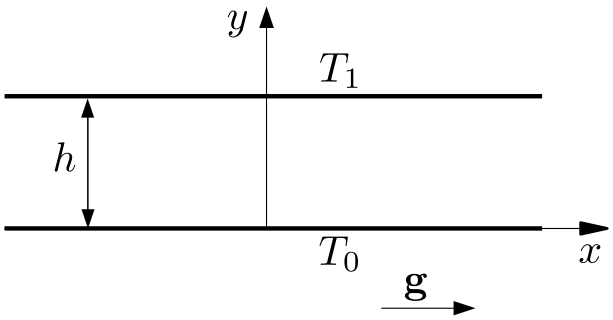

Figure 4.9: Sketch of the domain for the analytical solution of a simple buoyancy driven flow.

In order to validate the numerical code we run a numerical simulation for a case in which an analytical solution of the problem can be found.

Let us consider two parallel, infinitely long plates arranged in a vertical position. Let x be a Cartesian co–ordinate parallel to the plates and y one orthogonal to them. We assume that gravity acts in the positive x–direction (see figure 4.9). Finally, we assume a two-dimensional flow in the $x - y$ plane.

The governing equations, adopting the Boussinesq approach to treat the effect of density changes induced by temperature, are given below:

$$\rho_0 \left(u_t + uu_x + vu_y\right) = -p_x + \rho_0 \nu (u_{xx} + u_{yy}) + \rho_0 g[1 - \alpha(T - T_0)], \tag{4.3a}$$

$$\rho_0 \left(v_t + uv_x + vv_y\right) = -p_y + \rho_0 \nu (v_{xx} + v_{yy}), \tag{4.3b}$$

$$u_x + v_y = 0, \tag{4.3c}$$

$$T_t + uT_x + vT_y = \frac{k}{\rho_0 c_p}(T_{xx} + T_{yy}), \tag{4.3d}$$

where ρ_0 is the baseline density (at a given temperature), u and v are the x and y components of the velocity, p is pressure, T is the absolute temperature, ν is the kinematic viscosity, α the thermal expansion coefficient of the fluid, k its thermal conductivity and c_p its specific heat at constant pressure.

We seek a unidirectional solution such that $\mathbf{u} = [u(y), 0]$ and $T_x = 0$. In this case the above equations simplify to

$$-\frac{p_x}{\rho_0} + \nu u_{yy} + g[1 - \alpha(T - T_0)] = 0, \tag{4.4a}$$

$$p_y = 0, \tag{4.4b}$$

$$u_x = 0, \tag{4.4c}$$

$$T_{yy} = 0. \tag{4.4d}$$

The system of PDEs (4.4a-d) can be easily solved to obtain

$$T = T_1 + \eta y, \qquad \eta = \frac{T_0 - T_1}{h}, \tag{4.5a}$$

$$u = \frac{g\alpha\eta}{6\nu} y \left(y - \frac{h}{2}\right)(y - h), \tag{4.5b}$$

$$p = \rho_0 g \left[1 - \frac{\alpha}{2}\left(T_1 - T_0\right)\right] x + c, \tag{4.5c}$$

where c is a constant that can determined by specifying the value of the pressure at a point.

In figure 4.10 we show comparisons between the analytical solution and the numerical solution obtained using OpenFoam. In the figure we plot the velocity profile (a), the dynamic pressure profile (b) and the temperature profile (c) across the gap thickness. Analytical functions are plotted with a solid blue curve and numerical results with red circles. In all cases we find excellent agreement.

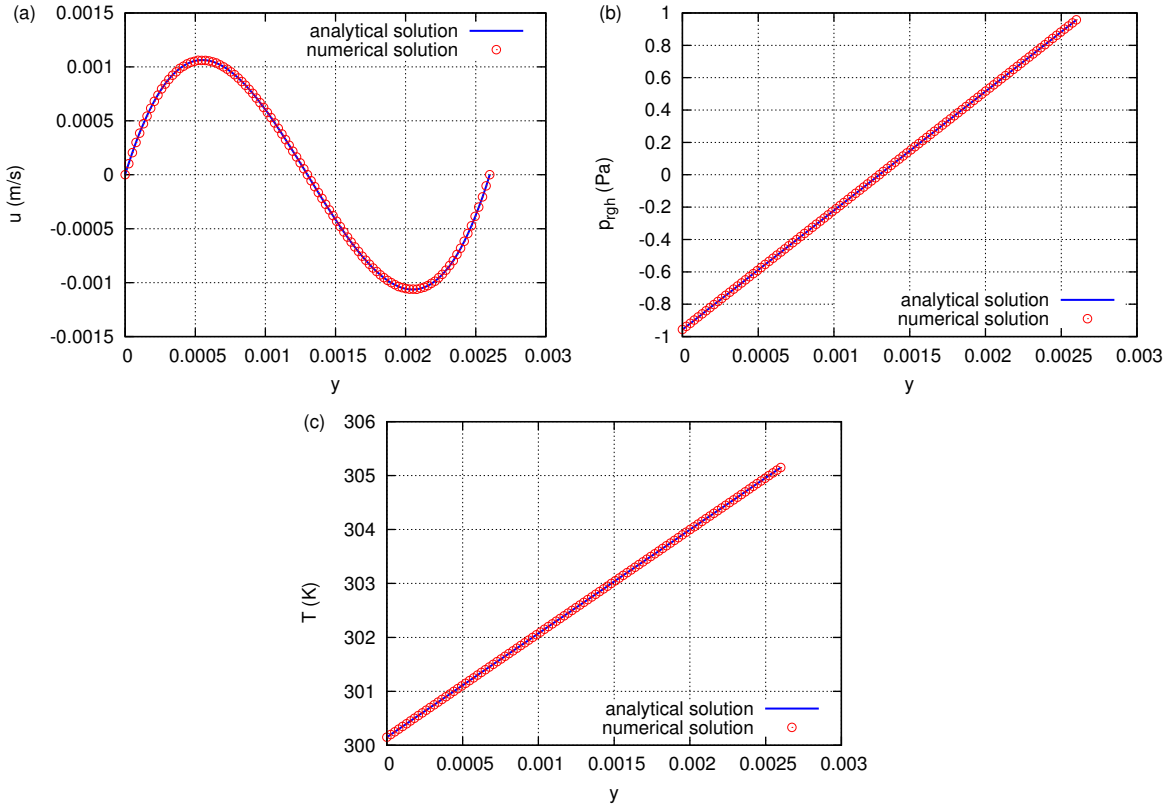

Figure 4.10: Comparison between theoretical and numerical results for the buoyant flow between two infinitely long parallel plates. (a) u, (b) p_{rgh}, (c) T versus y. $h = 0.0026$ m, $\Delta T = 3$ K, $\alpha = 3 \cdot 10^{-4}$ K^{-1}, $\nu = 7.5 \cdot 10^{-6}$ m^2/s.

We now consider the case of the flow in the anterior chamber.

In figure 4.11 (b) we also show colour maps of the vertical velocity component on various vertical cross–sections. Positive values correspond to downward velocity (gravity acts in the x positive direction). As expected particles close to the cornea move down and particles in the back of the domain move up. The maximum streaming velocity is significantly higher than that due to the production/drainage flow (approximately two orders of magnitude), which justifies our neglecting the latter flow.

In figure 4.11 we show streamlines of the flow (c) and also colour maps of the temperature (d) and of the velocity magnitude (a) on various horizontal planes. As predicted by previous investigations the flow is essentially two–dimensional and approximately take place on vertical planes.

In figure 4.12 we show the map of the wall shear stress (WSS) on the cornea and iris. The corneal wall shear stress approximately peaks in the centre of the cornea. The

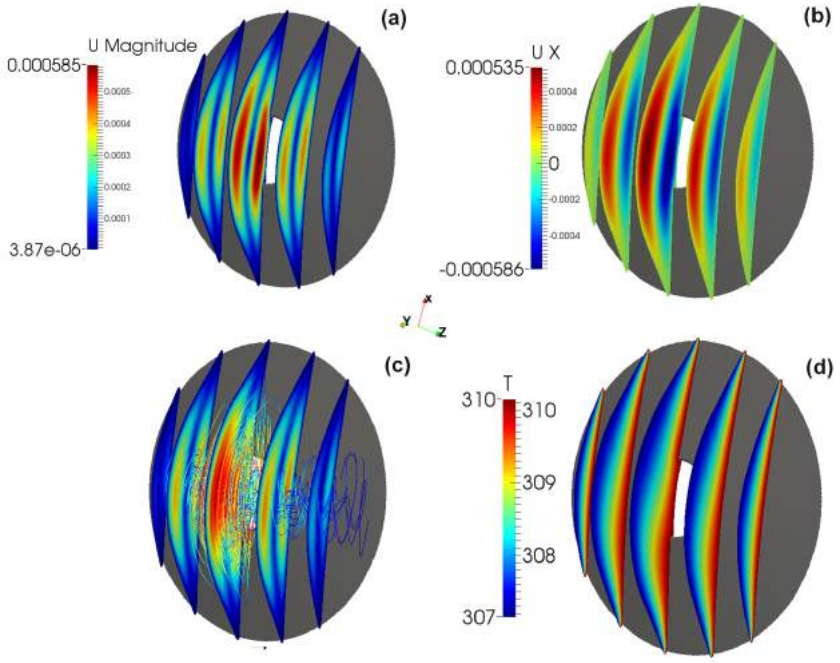

Figure 4.11: Colour maps of (a) the velocity magnitude (b) vertical velocity component (d) temperature on various vertical crosssections. (c) Streamlines of the flow. Gravity in all images is in the negative x–direction.

maximum wall shear stress on the iris appears near to edges of iris-channel surfaces.

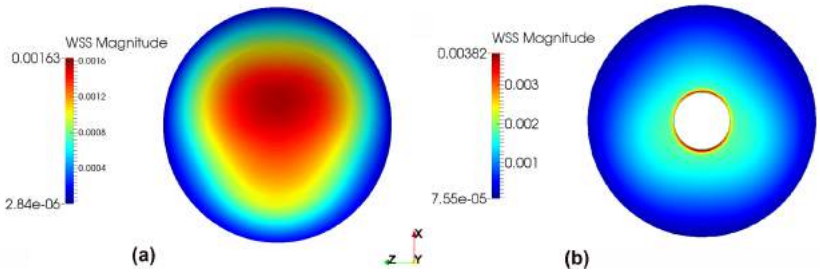

Figure 4.12: Colour map of the wall shear stress on (a) the cornea (b) the iris.

4.5.1.3 Flow induced by saccadic eye rotations

In this section we study the motion induced in the anterior chamber by rotations of the eye bulb. We neglect the bulk flow and the thermally driven flow discussed discussed in previous subsections because they both generate significantly smaller velocities and pressures than those generated during eye rotations.

We note that, owing to the highly unsteady nature of the flow, in order to attain convergence in the simulations very small time steps have to be adopted ($\approx 10^{-6}$ s). This implies that the computational time required for modelling a saccadic rotation is very long (of the order of a week on a 16 CPU computer, with the same spatial mesh as adopted in the simulations presented in the previous sections).

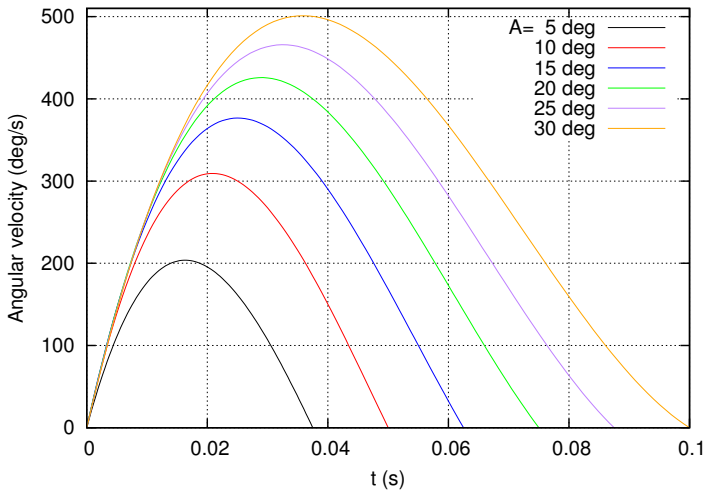

Figure 4.13: Examples of saccadic eye movements as predicted by the equation proposed by Repetto et al. [118], based on the metrics of eye movements reported in [10]. The figure shows the eye angular velocity versus time for different amplitudes A of the saccade.

We consider saccadic eye rotations as they are frequent and fast eye movements that are known to produce significant flow of the aqueous humor in the anterior chamber [1].

We model saccadic rotations using the law proposed by Repetto et al. [118], according to which the dependency of the eye angular velocity on time is expressed by a fourth order polynomial. The coefficients of this polynomial function are computed on the basis of measurements of real eye rotations reported in Becker et al. [10]. Saccadic rotations have been modelled in the same way by Abouali et al. [1] in their numerical simulations.

In figure 4.13 we show the angular frequency of the eye versus time for saccadic rotations of different amplitudes. Saccades are characterized by:

i) a very high initial angular acceleration (up to 30000 deg/s^2);

ii) a somewhat less intense deceleration that is nevertheless capable of inducing a very efficient stop of the movement;

iii) a peak angular velocity that rises in proportion to the saccade amplitude up to a saturation value ranging between 500 and 600 deg/s;

iv) a very short duration.

In the following we consider eye rotations in the counterclockwise direction about the z–axis. Moreover we focus on a saccadic rotation of 10 deg of amplitude.

In figure 4.14 we show contour plots of the velocity magnitude on a diametral cross–section of the anterior chamber for different time steps. Black arrows indicate the velocity vector fields. As can be seen in this figure, a thin boundary layer forms at the walls of the domain. We note that the time $t = 0.02s$ is close to the instant at which the maximum angular velocity is attained. At that time large values of the wall shear stress are expected to be associated. We can also estimate the thickness δ of the boundary layer at time t (valid for short times), which can be obtained as $\delta \sim \sqrt{\nu t}$, with ν the fluid kinematic viscosity.

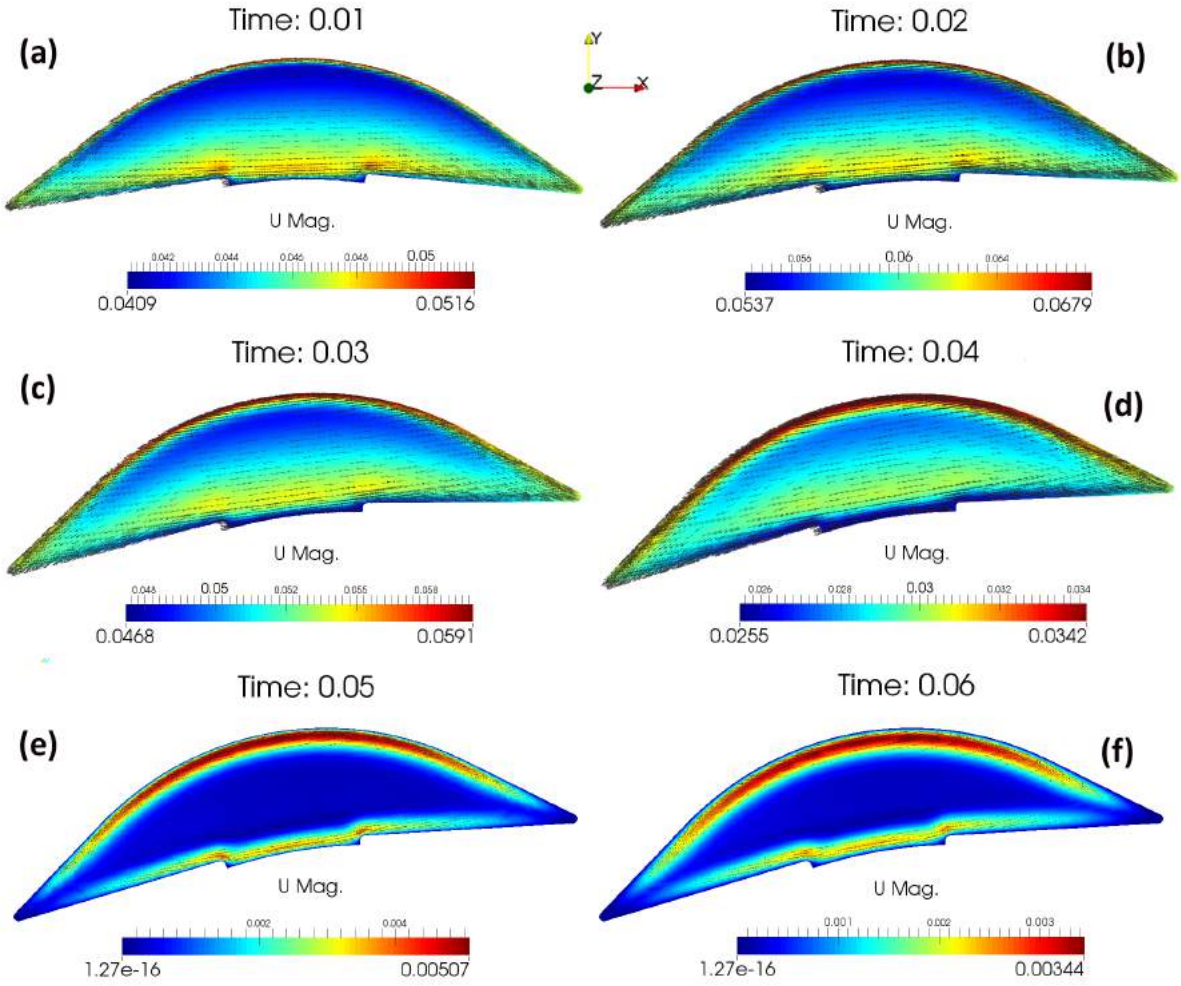

Figure 4.14: Velocity magnitude profile on a diametral cross–section of the anterior chamber for different time steps for saccadic motion of 10 degrees amplitude. The arrows indicate the velocity vector fields.

The flow field shown in figure 4.14 (e) is relative to the time $t = 0.05$, at which the eye movement has already stopped (see figure 4.13, red curve). At this time the flow field is characterized by a counterclockwise circulation, which is progressively dissipated over long times.

The maximum wall shear stress on the cornea, which is the main observable of interest for this application, has been computed and is reported in figure 4.25, where the results obtained are compared with those relative to the presence of the Hydrophobic Artiflex lens in the anterior chamber. We note that the time evolution of the wall shear stress agrees closely (both qualitatively and quantitatively) with that obtained numerically by Abouali et al. [1].

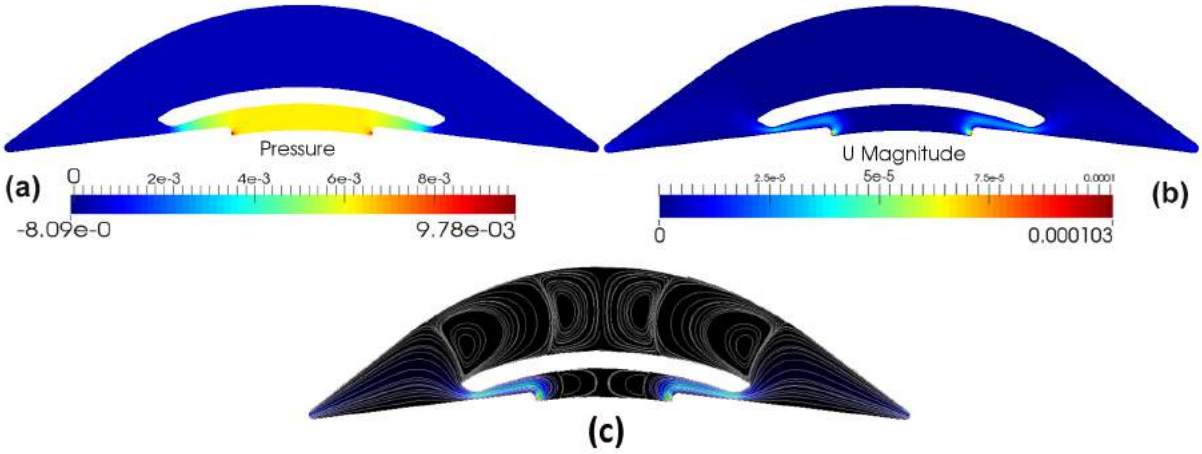

Figure 4.15: Pressure (a) and velocity magnitude (b) distribution over a diametral cross-section of anterior chamber a pIOL. Streamlines of the flow is shown in (c). Maximum pressure: $p_{\max} = 9.78 \times 10^{-3}$ Pa. Maximum velocity magnitude: $u_{\max} = 10.3 \times 10^{-5}$ m/s.

4.5.2 Flow in the anterior chamber with the presence of a Hydrophobic Artiflex pIOL

4.5.2.1 Bulk flow induced by aqueous production/drainage

4.5.2.1.1 Effect Hydrophobic Artiflex pIOL in the aqueous flow

In figure 4.15 we show the pressure (a) and velocity magnitude (b) distributions on a diametral cross-section of the anterior chamber with the presence of the Hydrophobic Artiflex pIOL. Figure 4.15 (c) shows the streamlines of the flow and considering the velocity magnitude, very slow circulations anterior to the lens can be seen. This is due to the presence of the pIOL that forces the aqueous flow toward the regions near to the trabecular meshwork. The presence of the Hydrophobic Artiflex pIOL slightly increases the pressure underneath of the lens in comparison to the reference case.

4.5.2.1.2 Effect of a single central hole perforation on the body of the pIOL

In figure 4.16 we show the pressure (a) and velocity magnitude (b) distributions on a diametral cross-section of the domain through the hole. As expected the pressure is maximum underneath the pIOL, whereas the velocity peaks within the hole. The maximum velocity $u_{\max}$ is approximately equal to 10.3×10^{-5} m/s, which gives a Reynolds number Re of the flow within the hole equal to $\approx 4.9 \times 10^{-4}$ (with $Re = u_{\max} d_{\text{hole}}/\nu$). The Reynolds number being very small, the flow is dominated by viscous effects and no jet is generated at the exit of the hole.

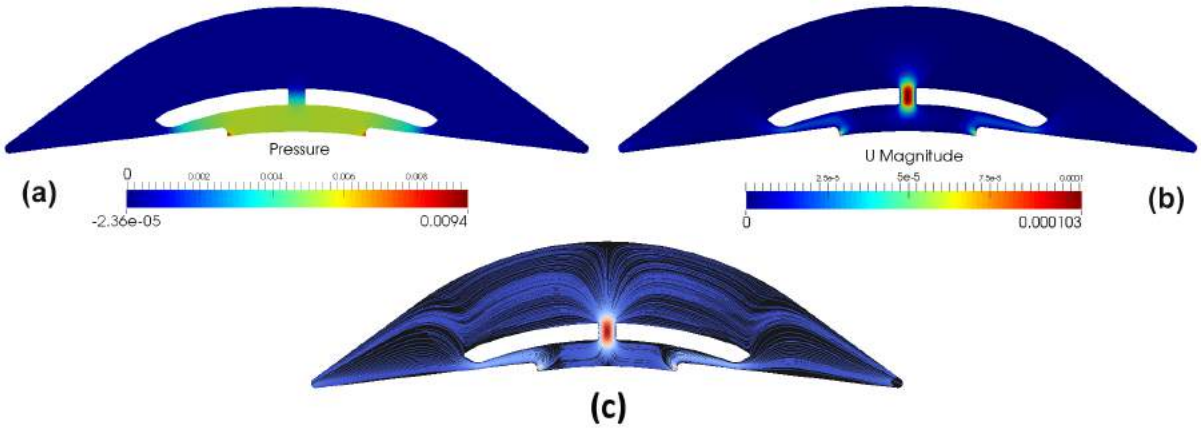

Figure 4.16: Pressure (a) and velocity magnitude (b) distribution over a diametral cross-section of anterior chamber with a pIOL with central hole. Streamlines of the flow is shown in (c). Maximum pressure: $p_{\max} = 9.40 \times 10^{-3}$ Pa. Maximum velocity magnitude: $u_{\max} = 10.3 \times 10^{-5}$ m/s.

The streamlines corresponding to the flow are shown in figure 4.16 (c). As expected as a consequence of the low values of the Reynolds number the streamlines follow closely the shape of the domain and no regions of detached flow are found.

Figure 4.17 shows the values of the pressure drop across the domain in different cases. In particular, we consider the case in which the pIOL is not present in the anterior chamber (no pIOL) and the cases of the pIOL without the hole (pIOL) and with central hole (using different hole diameters). It appears that, with a hole of 0.36 mm (which is the largest tested), the pressure is only slightly lower than without the hole. We also remark that all the pressure drops shown in the figure are tiny compared the IOP (which is approximately equal to 2600 Pa).

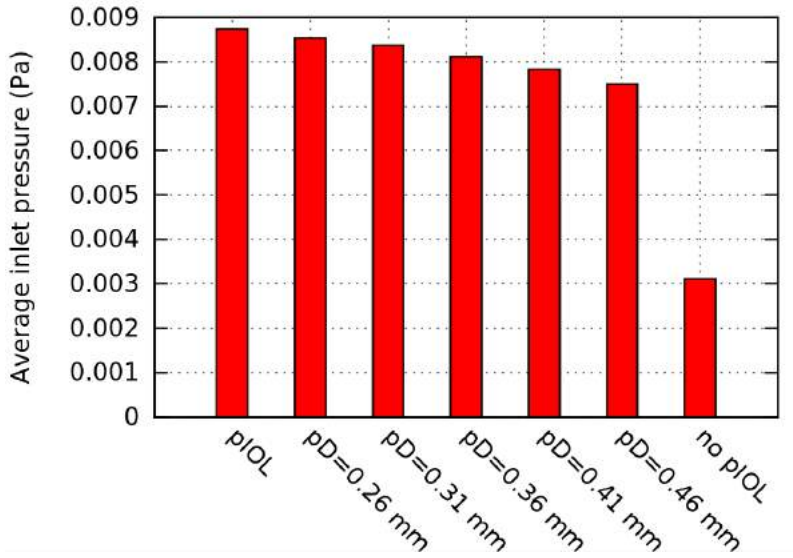

Figure 4.17: Pressure drop between the inlet and outlet sections in different conditions. Leftmost bar: pIOL normally places. Rightmost bar no pIOL. All other bars: pIOLs with central holes with different diameters.

Various hole diameters have been tested but we note that holes larger than 0.36 mm might lead to optical problems. The numerical simulations suggest that approximately 10% of the total flux flows through the reference hole, while the rest still passes in the gap between the pIOL and the iris. Figure 4.18 shows the flux ratio through the hole as a function of hole diameter.

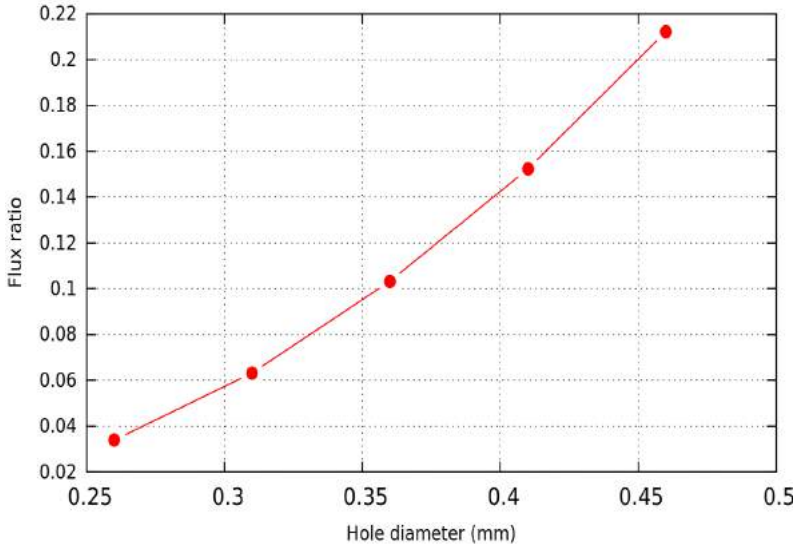

Figure 4.18: Flux ratio through the hole versus the hole diameter.

4.5.2.1.3 Effect of plugging the iris-pIOL channel

As it is mentioned before one of the main reasons for considering the possibility of adding a hole in the pIOL is to avoid excessive IOP growth, in particular in the case in which the

space between the pIOL and the iris gets plugged. We remark that this is an unlikely event, if the pIOL is properly placed in the anterior chamber. Closure of the passage between the pIOL and the iris can potentially occur either as a consequence of cell deposition or because the iris moves forward with ageing. In both cases the result is that the aqueous humor produced in the posterior chamber cannot flow into the anterior chamber through the pupil.

In this section we modify the geometry considered by artificially sealing the passage between the pIOL and the iris and considering a pIOL with a central hole. Aim of these simulations is to investigate whether the presence of a hole in the pIOL can avoid excessive pressure build up in the case of blockage of the normal aqueous pathway.

We have modified the geometry in two different ways: in the first case we have introduced an impermeable cylinder under the pIOL and in the second case we have displaced the iris anteriorly until it got in contact with the pIOL (the position of which was held fixed). In both cases the results are very similar; we therefore discuss just the first case in the following.

In figure 4.19 we show contours of the velocity magnitude and streamlines over a diametral cross-section through the hole. The passage between the pIOL and the iris has been blocked with and impermeable cylinder. In figure 4.19 (c) we plot the corresponding streamlines. As expected, the velocity attains relatively large values at the hole and the fluid is almost stagnant in the peripheral region under the pIOL.

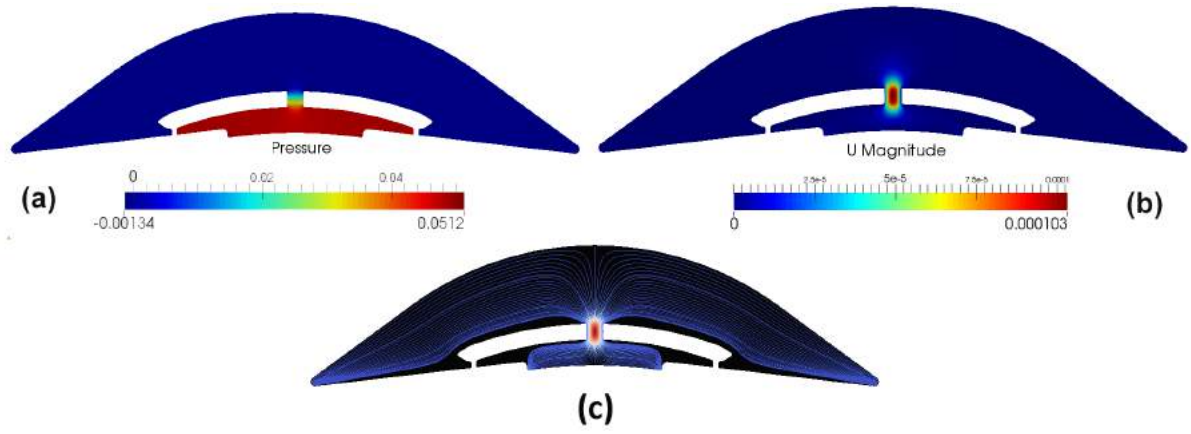

Figure 4.19: Pressure (a) and velocity magnitude (b) distribution over a diametral cross-section through the hole. Streamlines of the flow is shown in (c). The passage between the pIOL and the iris has been blocked with and impermeable cylinder. Maximum pressure: $p_{\max} = 5.12 \times 10^{-2}$ Pa. Maximum velocity magnitude: $u_{\max} = 9.63 \times 10^{-4}$ m/s.

The numerical simulation shows that, in the case in which the passage under the pIOL has been blocked, the average inlet pressure is about 0.05 Pa, which is 5.7 times more than in normal conditions in which there is no hole in the lens and the aqueous can freely flow between the pIOL and the iris. Even in this case, however, the pressure drop across the domain still assumes very small values compared to the IOP (too small for being clinically relevant). This implies that a perforation in the pIOL with a diameter 0.36 mm allows aqueous flow from the posterior to the anterior chamber without generating dangerous high pressures, even in the extreme case in which the passage between the pIOL and the iris is completely blocked.

4.5.2.1.4 The effect of two lateral perforations on the body of the pIOL

We consider in this section another geometry of the lens, consisting of two lateral perforations introduced in the body of the pIOL. Results showing the pressure and velocity distribution in this case are presented in figure 4.20. The results are shown on a diametral cross-section of the domain that passes through the holes. The flow is evidently not axisymmetric in this case.

In this case the pressure drop and the velocities through the holes are slightly smaller than in the case of a central hole. The general picture is, however, substantially the same as in the case of a single central perforation.

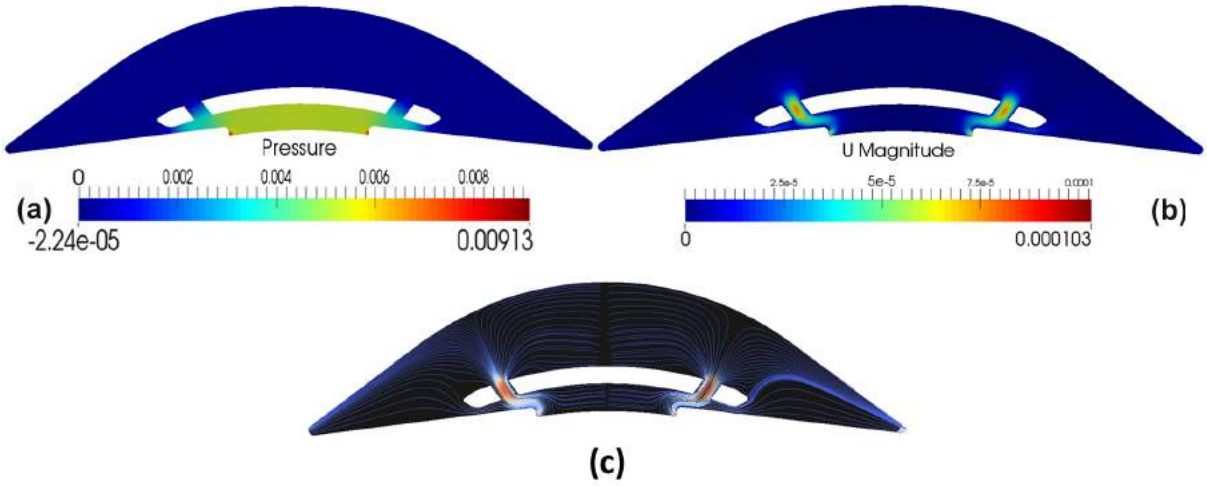

Figure 4.20: Pressure (a) and velocity magnitude and streamlines (b) distribution over a diametral cross-section for the case of two side holes. Streamlines of the flow is shown in (c). Maximum pressure: $p_{\max} = 9.13 \times 10^{-3}$ Pa. Maximum velocity magnitude: $u_{\max} = 10.3 \times 10^{-5}$ m/s.

4.5.2.2 Flow generated during miosis

In figure 4.21 we plot the average inlet pressure versus time. The green curve is relative to the case in which there is no pIOL in the anterior chamber and the blue line refers to the pIOL without a hole. The red line describes the case of the pIOL with a central hole and, finally, the black line the case of pIOL with a hole in which the passage between the pIOL and the iris is sealed. All curves have a similar trend, with the maximum of the pressure occurring at the time at which the flux peaks. The values of the pressure are, in this case, significantly higher than in the case considered in section 4.5.1.1 and 4.5.2.1, but still far too small to be of clinical significance.

Yamamoto et al. [139] performed numerical simulations of the flow through a laser iridotomy hole during miosis and argued that the jet passing through the hole may produce levels of the wall shear stress on the cornea large enough to cause corneal endothelium cell damage and loss, especially in those with shallow anterior chambers. A similar mechanism could take place in the case of a pIOL with a central hole as, also in this case, a jet is generated at the outlet of the hole that points towards the cornea. Kaji et al. [69] also performed invitro experiments of corneal cell detachment, exposing porcine corneal endothelial cells to a controlled level of wall shear stress (0.01–1 Pa). They observed

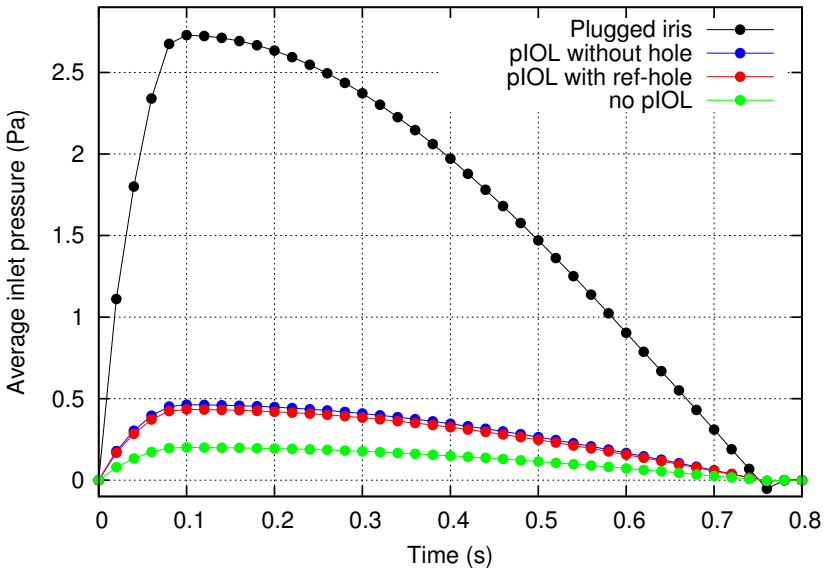

Figure 4.21: Spatially averaged inlet pressure as a function of time during miosis.

that the number of detached corneal endothelial cells increases with the shear stress. In particular, significant increase of cell detachment rate was observed at 0.03 Pa after 1–hour attachment and at 0.1 Pa after 3–hour attachment. It is reasonable, however, to expect that these values underestimate the wall shear stress required to induce cell detachment from the cornea invivo. It is, therefore, unlikely that the shear stress levels predicted by the numerical model might produce cell damage on the iris.

We find that the maximum wall shear stress on the central cornea is equal to $\approx 6.19 \times 10^{-5} Pa$ in the case of the pIOL with the hole and grows to $2.17 \times 10^{-3} Pa$ if we consider the extreme case in which the passage between the pIOL and the iris gets blocked and all the fluid has to flow through the hole in the pIOL. These values seem to remain small enough to avoid any risk of cell detachment from the cornea [69]. We finally note that laser iridotomy, besides being beneficial in order to avoid the risk of pressure increase in the case of flow blockage, would also decrease significantly the maximum wall shear stress on the iris.

4.5.2.3 Flow induced by bouyancy effects

We now consider the buoyancy driven flow induced by thermal effect in the presence of a pIOL. In this work we did not account for heat transport through the lens. We note, however, that theoretical predictions based on the lubrication theory show that the maximum aqueous velocity decreases as the thermal diffusion coefficient of the lens increases [114]. Therefore, the results obtained in the present analysis and shown below represent an upper limit for the fluid velocity in the anterior chamber. Since we are mostly interested in conditions that might increase the walls shear stress on the cornea and iris this choice is conservative.

In figure 4.22 (b) we show colour maps of the vertical velocity component on various vertical cross–sections. Positive values correspond to downward velocity (gravity acts in the positive x–direction). This is the analogous of figure 4.11 (b), which was obtained for the case without intraocular lens. In fact the two figures are directly comparable, since

the same parameter values and boundary conditions have been used in the two cases. As can be seen in figure 4.22 (c) it appears that placement of the lens in the anterior chamber significantly modifies fluid flow. Specifically, in this case the flow is much more three–dimensional. Particles in the central part of the domain and anterior to the lens move down. Fluid flow at the sides of the lens is mostly directed upwards and very little flow takes place behind the lens.

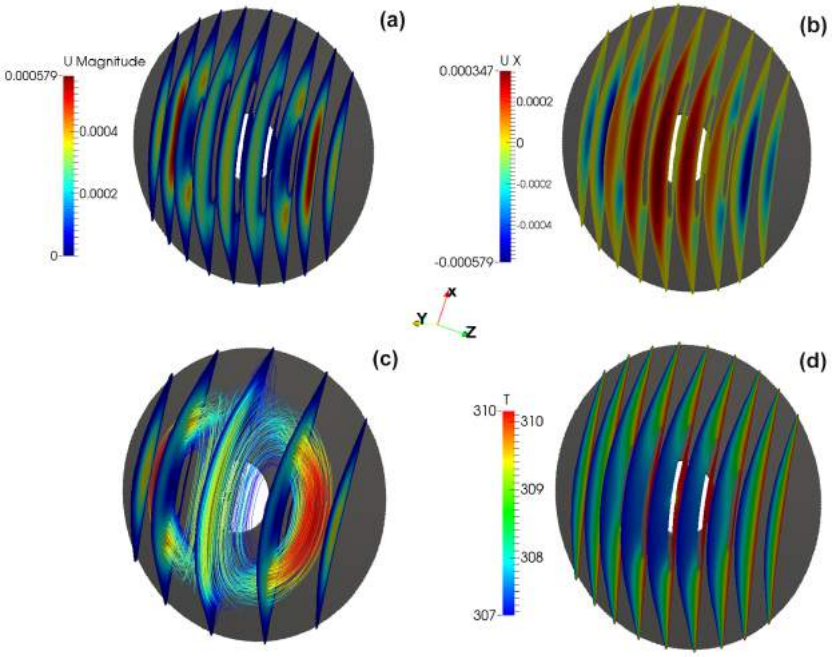

Figure 4.22: Colour maps of (a) the velocity magnitude (b) vertical velocity component (d) temperature on various vertical crosssections. (c) Streamlines of the flow. Gravity in all images is in the negative x–direction.

The colour maps of the temperature and of the velocity magnitude on various horizontal planes are reported in figure 4.22 (d) and (a) respectively. The figure confirms that most of the circulation takes place in front and on the sides of the intraocular lens, and the flow behind the lens is quite weak. We note, however, that even if the structure of the velocity field is significantly modified by the presence of the lens, the maximum values of the velocity is approximately the same as in the absence of lens.

Changes in the flow field have also consequences on the wall shear stress distribution on the cornea, as it is shown in figure 4.23 (a). The maximum wall shear stress in this case is slightly smaller than in the absence of the lens.

Finally, we show in figure 4.23 (b) the wall shear stress distribution on the iris. This peaks at the sides of the lens, where there is a relatively intense upward directed flow, and in correspondence of the constriction between the intraocular lens and the iris. The maximum is approximately twice as large as on the cornea for normal lens placement. We note, however, that all values of the wall shear stress found in this section are too small to be clinically relevant.

We note that, the presence of the central hole in the pIOL body has very little influence on the velocity field and temperature distribution. In fact the flow through the hole in this case is very small ($\approx 3.6 \times 10^{-13}$ m^3/s), much smaller than the flow produced at the

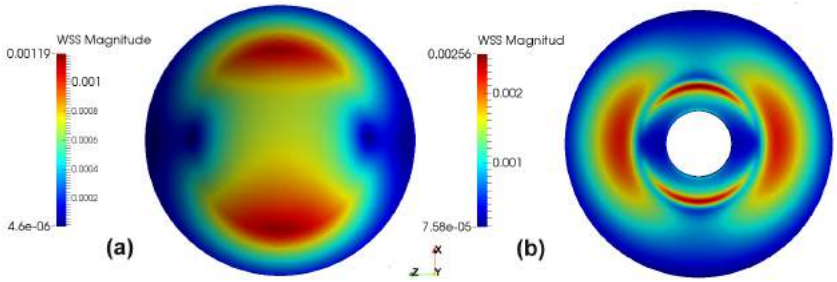

Figure 4.23: Colour map of the wall shear stress on (a) the cornea and (b) the iris.

ciliary processes. The wall shear stress distribution and magnitude is very similar to that obtained in the absence of the central hole in the pIOL. In conclusion, a perforation in the pIOL has very little influence on the thermal flow.

4.5.2.4 Saccadic motion with the presence of a pIOL

In figure 4.24 we show contour plots of the velocity magnitude on a diametral cross–section of the anterior chamber with the presence of a pIOL at different time steps for the saccadic motion of 10 degrees amplitude. This figure can be compared directly with figure 4.14. The results are qualitatively similar to those obtained in the absence of the intraocular lens. However, due to the small gap between the lens and iris, less flow moves toward the region underneath of the pIOL.

We also performed this study for the case of lens with central hole. The results are qualitatively and quantitatively very similar to those obtained in the case of the non perforated pIOL.

In figure 4.25 we plot the time evolution of the maximum (in space) wall shear stress on the cornea for different cases. Specifically, we consider the case in which there is no pIOL in the anterior chamber (black curve), the case of pIOL without perforation (blue curve) and the case of perforated pIOL (red curve). It appears that the time evolution of the wall shear stress is very similar in all cases. The maximum value attained corresponds to the case in which there is no pIOL in the anterior chamber. In the figure, the green line corresponds to the maximum value of the wall shear stress in the case of the buoyancy driven flow. This value is found to be much smaller than that generated during eye rotations.

We can therefore conclude that a perforation in the pIOL has negligible influence on the flow induced by eye rotations.

4.5.3 Flow in the anterior chamber with the presence of the Artiflex pIOL

In the present subsection we show the results of the flow in the anterior chamber with the presence of the Artiflex pIOL. As discussed in section 4.2 this lens is not axisymmetric and is thicker that the Hydrophobic Artiflex pIOL. We note here that we do not show the results for the flow generated by miosis since the results are qualitatively and quantitatively very similar to those obtained in the case of the Hydrophobic Artiflex pIOL.

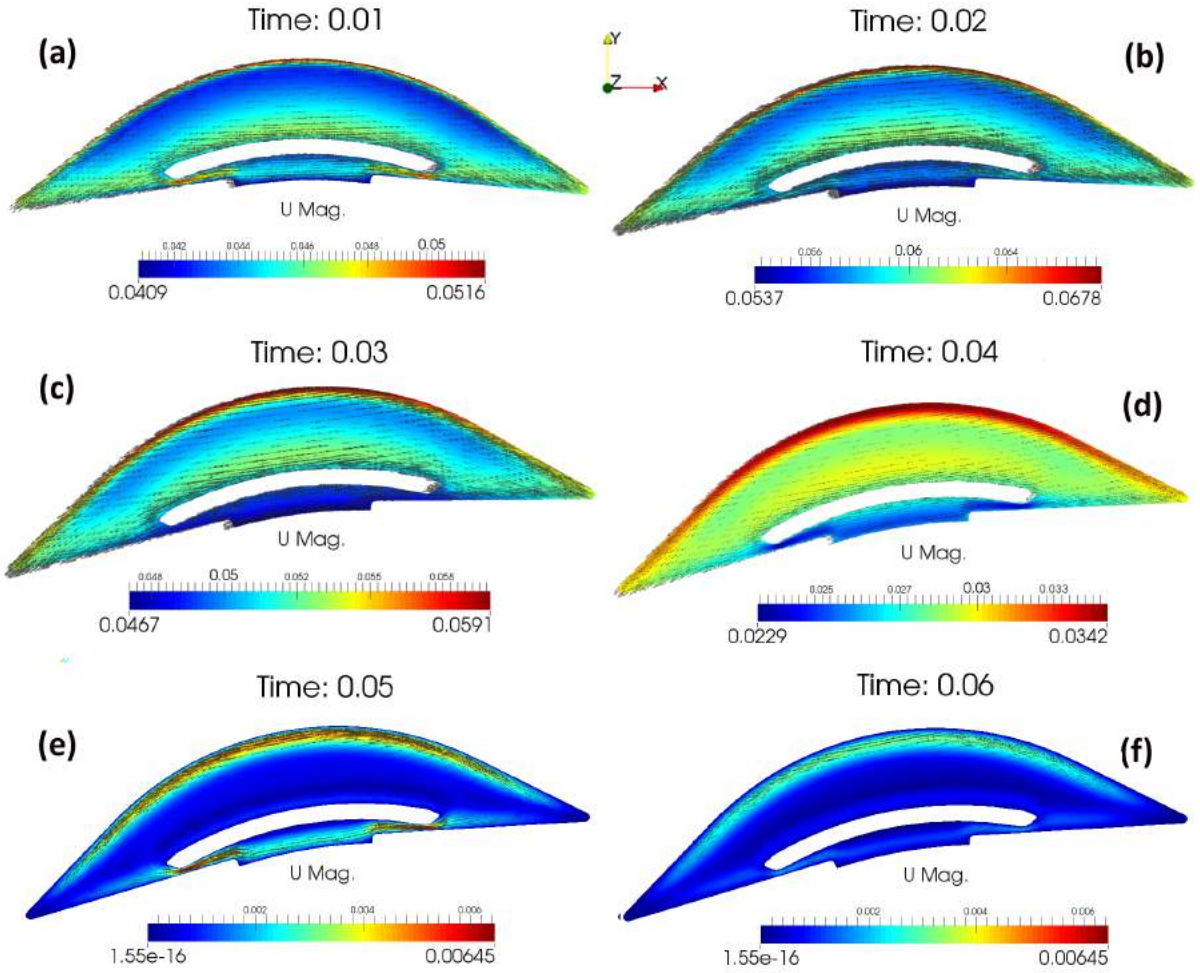

Figure 4.24: Velocity magnitude profile on a diametral cross–section of the anterior chamber with the presence of Hydrophobic Artiflex pIOL, for different time steps for the saccadic motion of 10 degrees amplitude. The arrows indicate the velocity vector fields.

4.5.3.1 Bulk flow induced by aqueous production/drainage

4.5.3.1.1 Changing the axial distance between the pIOL and cornea

Maps of the pressure, velocity and wall shear stress on the cornea and iris for the case in which $\alpha = 0.06$ mm are presented in figure 4.26. Since the gap between the iris and lens is very small, the mesh in this narrow region is carefully refined. As one could expect, due to the small gap, that the pressure underneath of the lens is higher (approximately twice as big) compared to what we found in the previous case, in the presence of the Hydrophobic Artiflex. However, the pressure still remains much smaller than the intraocular pressure and the pressure increase induced by the Artiflex has no clinical significance.

The aqueous humor velocity peaks underneath the lens and is almost zero in the central region of the domain, anterior of the Artiflex. As a consequence the wall shear stress on the iris is higher compared to that on the cornea. The maximum WSS on the iris is anyway within a clinically acceptable range.

Figure 4.27 (a) and (b) show the variation of average inlet pressure and the maximum

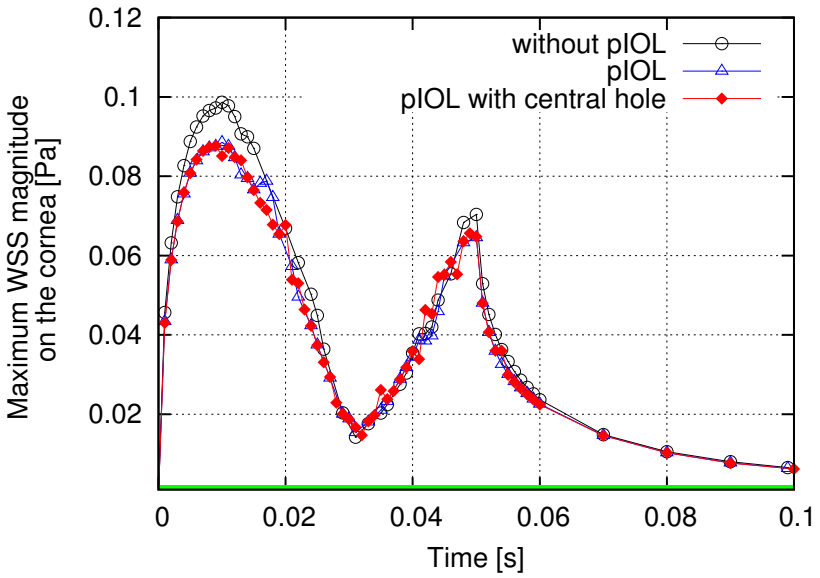

Figure 4.25: Time evolution of the maximum (in space) wall shear stress on the corneal endothelial cells. Black curve: no lens in the anterior chamber; blue curve: presence of the normal intraocular lens; red curve: presence of the intraocular lens with central hole; green line: value of the wall shear stress generated by the thermally driven flow.

WSS on the iris for different values of α. We recall that parameter α (introduced in section 4.3) is a parameter, specifiling the position of the pIOL with respect to the iris: the higher the value of α, the closer the lens get to the cornea and consequently, is displaced away from the iris, creating more space underneath the lens and thus decreasing the blockage effect. As a consequence the pressure and maximum WSS on the iris both decrease. In all cases the values of the average inlet pressure and maximum WSS on the iris are below what could be considered clinically relevant.

4.5.3.1.2 Offset positioning with respect to the axial direction

In this section results are presented for cases in which the lens has been positioned at an offset distance of β in the x–direction and γ in the z–direction, with respect to the y-axis (see section 4.2, figure 4.3). Moreover, for each value of β and γ the combined effect of varying α has also been analysed.

In figure 4.28 (a) and (b) results are presented for the average inlet pressure and maximum WSS on the iris for different values of α and β. As shown in these plots, changing the position of lens in the x–direction has a minor effect.

Similarly, in figure 4.29 (a) and (b) we show the effect of varying α and γ. Again we find that changing the position of the lens in the z–direction has a small effect in terms of pressure in the anterior chamber.

4.5.3.2 Flow induced by bouyancy effects.

In figure 4.30 (b) we show colour maps of the vertical velocity component on various vertical cross–sections for the case of $H = 1.432$ mm ($\alpha = 0.06$ mm). Gravity acts in the negative x–direction. The flow characteristics are similar to those obtained in the case of

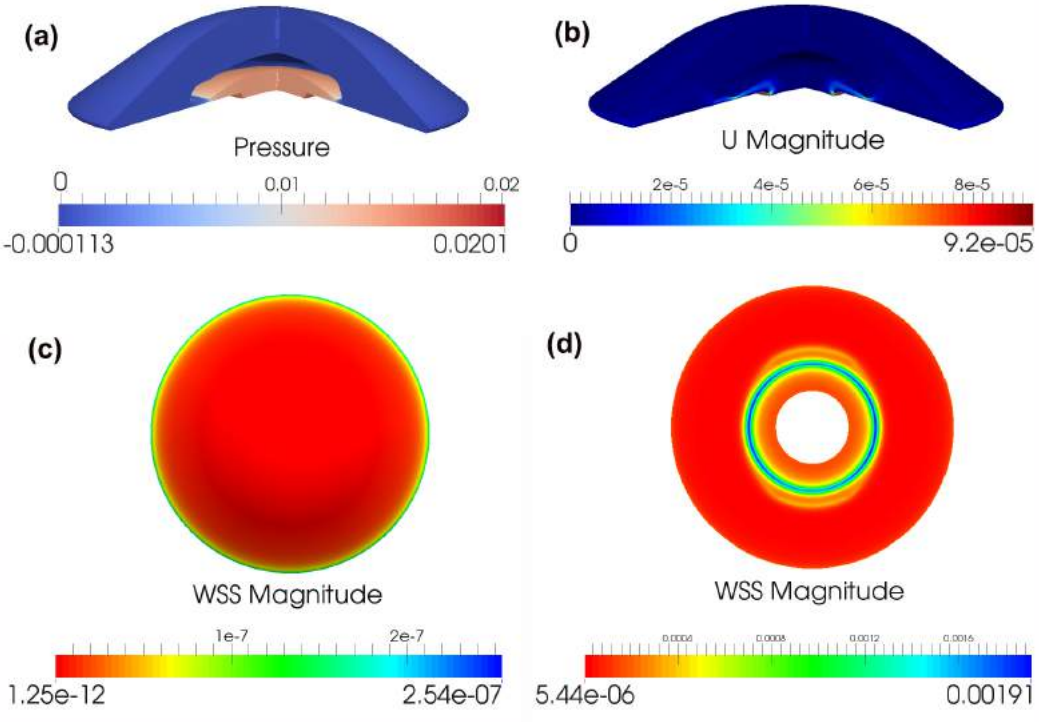

Figure 4.26: Pressure (a), velocity magnitude (b) and wall shear stress magnitude on the cornea (c) and iris (d) in the presence of the Artiflex when $H = 1.432$ mm. Maximum pressure: $p_{\max} = 2.01 \times 10^{-2}$ Pa. Maximum velocity magnitude: $u_{\max} = 9.2 \times 10^{-5}$ m/s. Maximum WSS magnitude on the cornea: $\mathrm{WSS}_{\max} = 2.54 \times 10^{-7}$ Pa. Maximum WSS magnitude on the iris: $\mathrm{WSS}_{\max} = 1.91 \times 10^{-3}$ Pa.

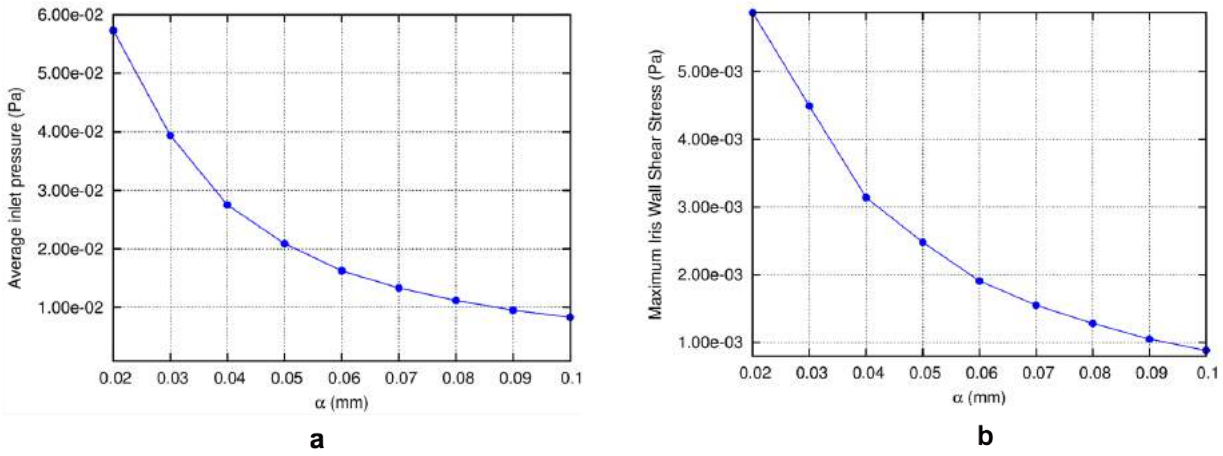

Figure 4.27: Variation of average inlet pressure (a) and maximum iris WSS magnitude (b) vs α.

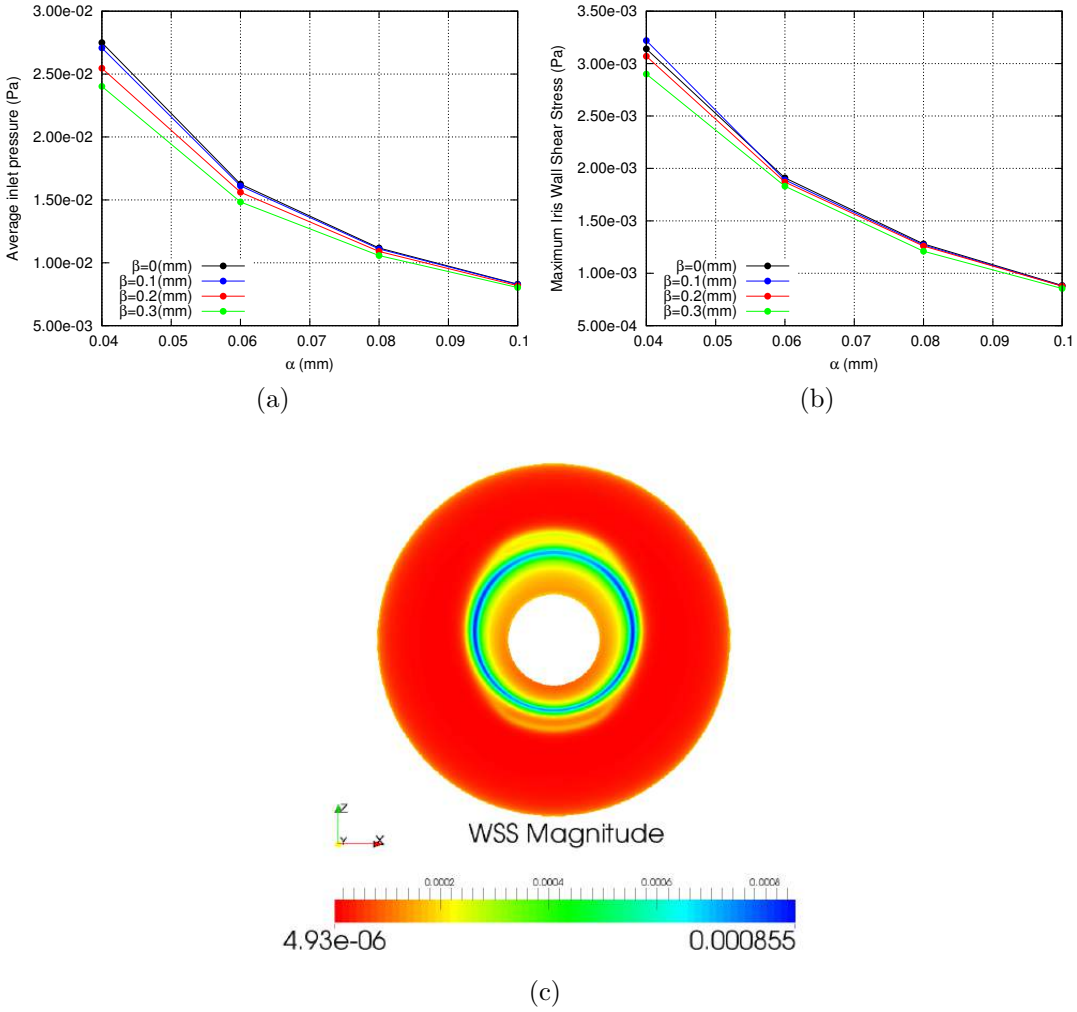

(a) (b)

(c)

Figure 4.28: Average inlet pressure (a), maximum WSS magnitude on the iris (b) for different values of α and β, and WSS magnitude on the iris for $\alpha = 0.1$ mm and $\beta = 0.3$ mm (c).

the Hydrophobic Artiflex. Particles in the central part of the domain and anterior to the lens move down. Fluid flow at the sides of the lens is mostly directed upwards and very little flow takes place behind the lens.

The three–dimensionality of the flow is clearly visible in figure 4.30 (c) by inspection of the flow streamlines. Furthermore, colour maps of velocity magnitude and temperature on various vertical planes are reported in figure 4.30 (a) and (d), respectively. The results confirm that most of the flow takes place in front and on the sides of the lens, while the flow behind the lens is quite weak.

In figure 4.31 the maximum WSS on the cornea and iris are shown for the case in which $H = 1.432$ mm ($\alpha = 0.06$ mm). On the cornea the maximum values are found in the central upper and lower regions, where the fluid velocity is high and where the distance between the lens and the cornea is smallest. On the iris the WSS pattern is different, with peaks being located in the upper and lower regions between the iris and the lens and also along the sides of the lens. The peak values occur in the two thin regions

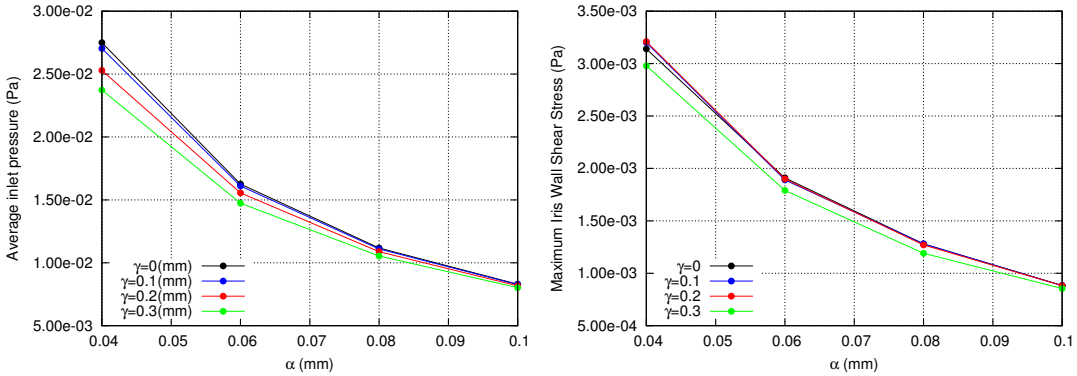

(a) (b)

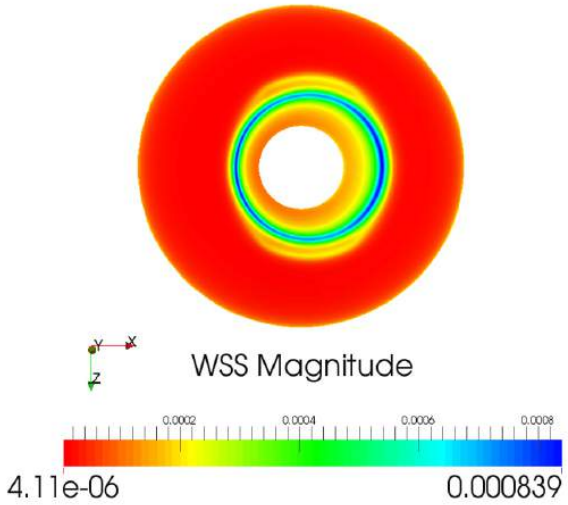

(c)

Figure 4.29: Average inlet pressure (a), maximum WSS magnitude on the iris (b) for different values of α and γ, and WSS magnitude on the iris for $\alpha = 0.1$ and $\gamma = 0.3$ mm (c).

where the minimum distance between the lens and the iris is found.

In figure 4.32 the maximum WSS magnitude on the iris is shown as a function of the axial distance between the lens and the cornea. The WSS increases as the value of α increases and this is due to the fact that the flow posterior to the Artiflex becomes more intense as the lens is moved away from the iris.

4.5.3.3 Flow induced by saccadic eye rotations

We also model saccadic rotations of 10–50 degs in the counterclockwise direction about the z-axis for the case of Artisan pIOL. In figures 4.33 we show contour plots of the velocity magnitude on a diametral cross–section of the anterior chamber with the presence of the Artiflex pIOL at different time steps for the saccadic motion of 10 degrees amplitude. Comparing directly with the results obtained in the case of Hydrophobic Artiflex lens,the results are very similar. Note that since the Artiflex pIOL is closed to the iris, less flow

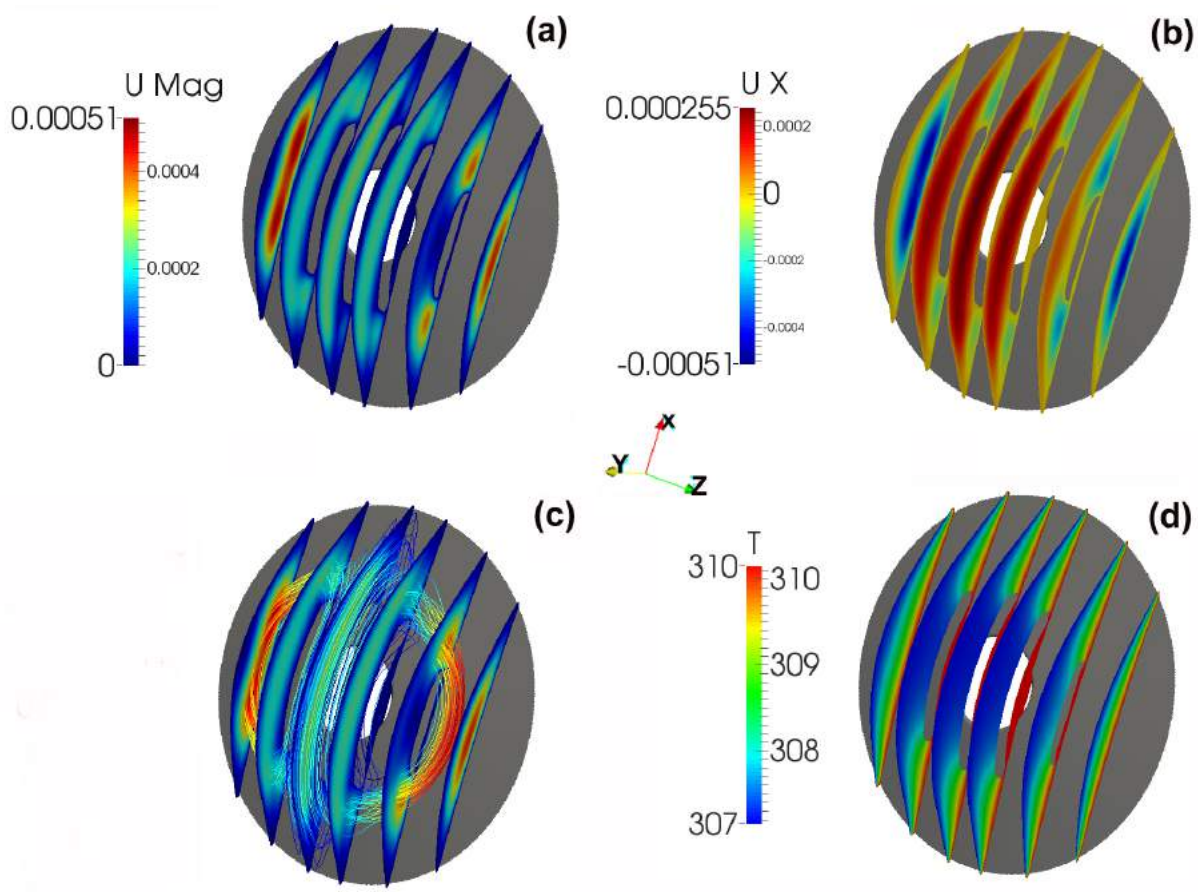

Figure 4.30: Colour maps of (a) velocity magnitude (b) the vertical velocity component (c) streamlines and velocity magnitude (d) temperature on various vertical cross–sections. Gravity in all images is in the negative x–direction and $H = 1.432$ mm ($\alpha = 0.06$ mm).

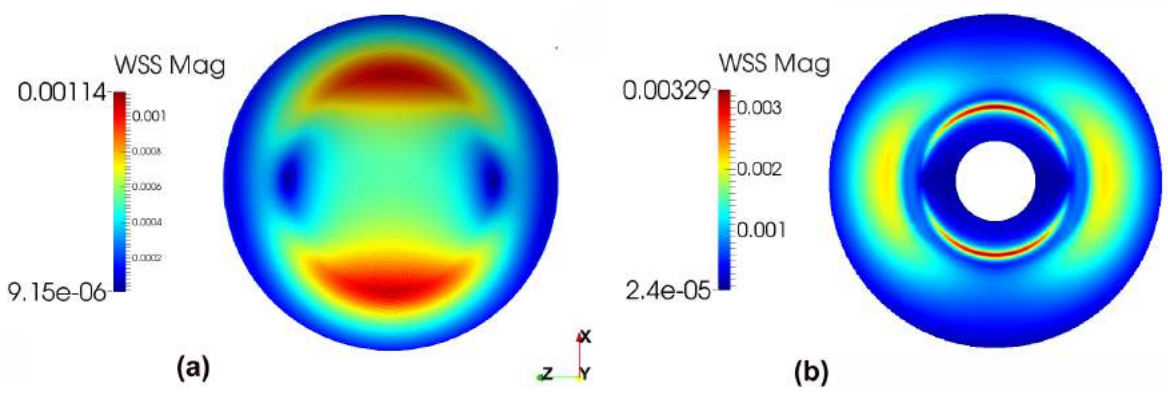

Figure 4.31: Colour map of the WSS on (a) the cornea, and (b) the iris for the case in which $H = 1.432$ mm ($\alpha = 0.06$ mm).

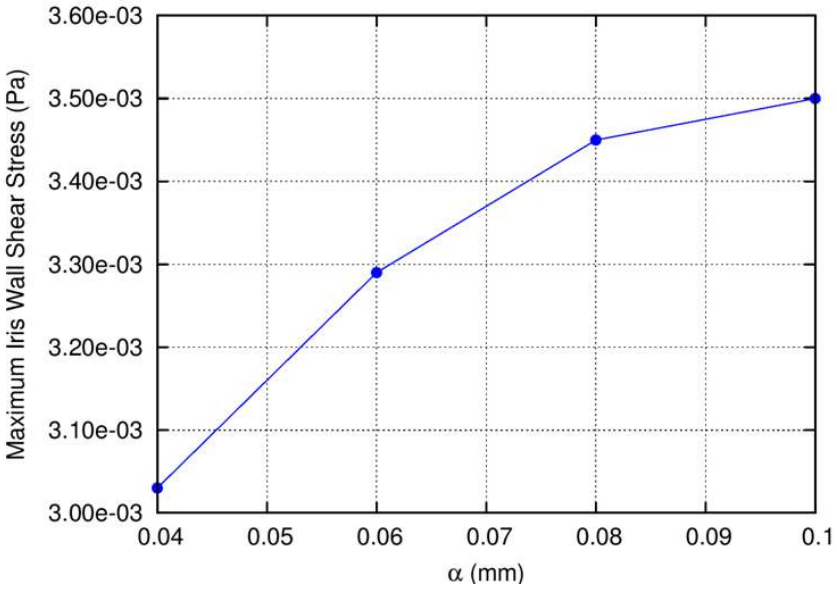

Figure 4.32: The maximum WSS on the iris as a function of the axial distance between the Artiflex lens and the cornea.

appears underneath of the lens.

In figure 4.34 we show the time evolution of the maximum (in space) WSS on the cornea for the different cases. For all rotations two peaks are found: the first during the initial acceleration phase and the second when the saccadic rotation ends. Which of the two peaks is larger depends on the angle of rotation. Interestingly, the maximum WSS does not depend significantly on the amplitude of the oscillations. This finding agrees with the experimental results obtained by Repetto et al. [118] for the case of motion of Newtonian fluid in the vitreous chamber.

The maximum WSS attains values that are very similar to those found in the absence of the iris-fixated lens and also in the presence of the Hydrophobic Artiflex.

The present simulations confirm that eye rotations are the mechanism that produces the most intense flow in the anterior chamber and also the highest values of the WSS on the cornea. Our findings show that implantation of an iris fixated lens (Hyrophobic Artiflex or Artiflex) does not increase the WSS on the cornea.

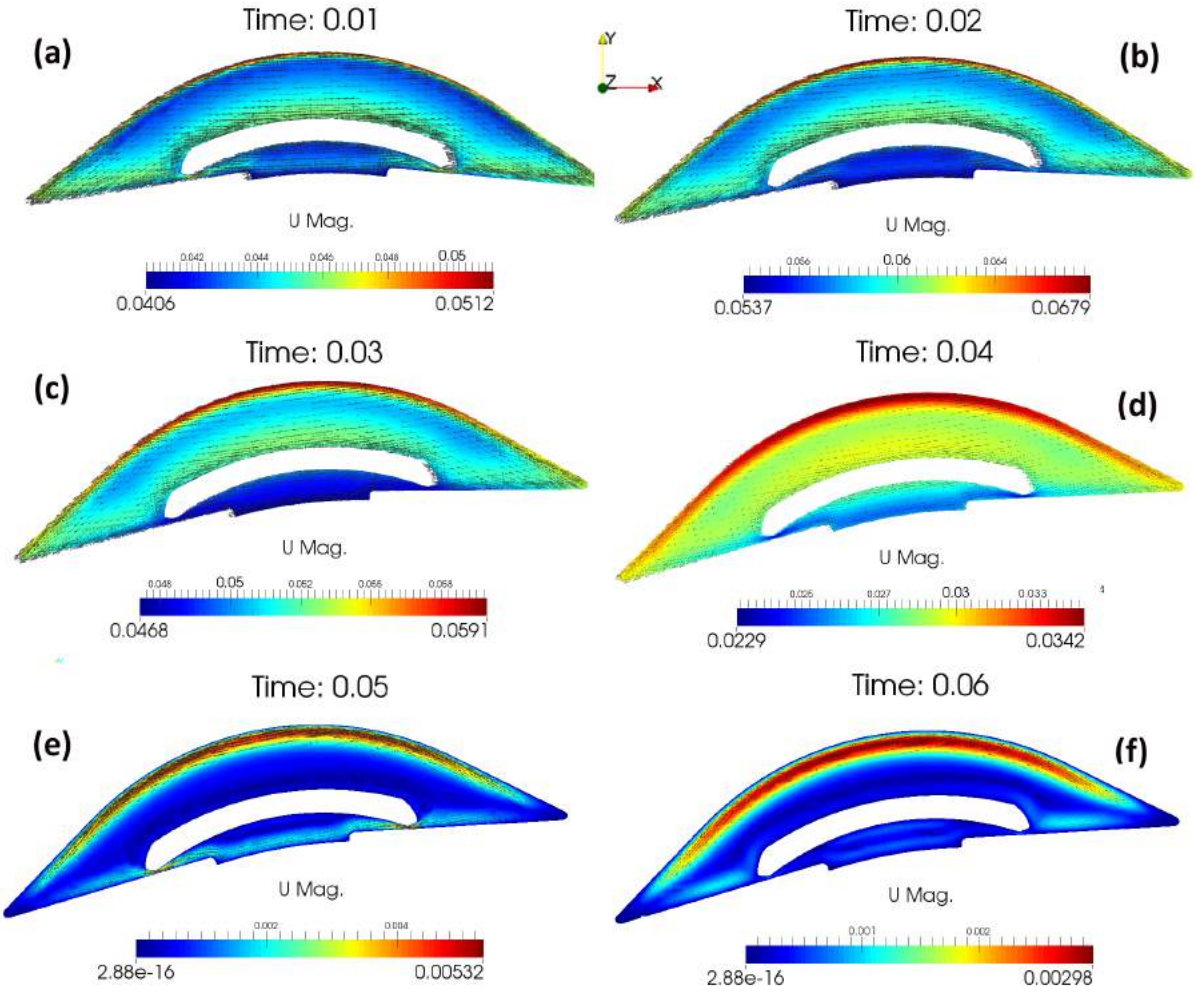

Figure 4.33: Velocity magnitude profile on a diametral cross–section of the anterior chamber with the presence of the Artiflex pIOL, for different time steps for the saccadic motion of 10 degrees amplitude. The arrows indicate the velocity vector fields.

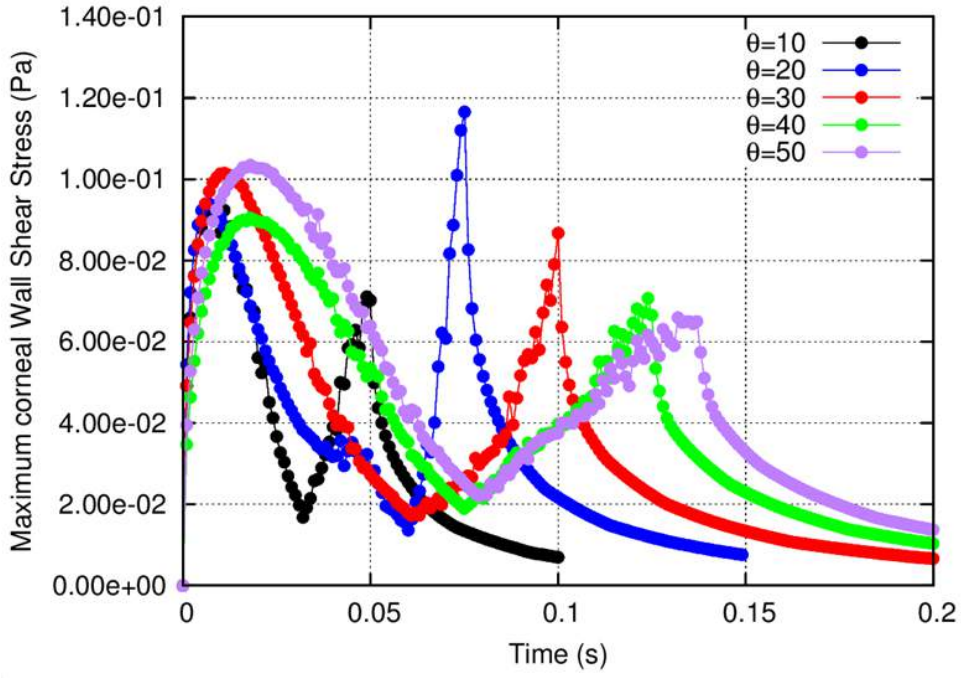

Figure 4.34: Maximum value of the WSS on the cornea as a function of time during saccadic motions of different amplitude θ.

4.6 Summary of the simulations

In this chapter we have described simulations of the flow in the anterior chamber with and without the presence of the Hydrophobic Artiflex and Artiflex pIOLs, provided by Ophtec BV. The aim of this chapter was to understand how and to what extent the implantation of an iris–fixated intraocular lens modifies the fluid dynamics of the anterior chamber. This is a problem of great clinical significance. In fact, among the possible complications associated with the implantation of an iris–fixated intraocular lens are i) loss of endothelial cells from the cornea and iris and ii) increase of the intraocular pressure [78]. It has been hypothesized that these complications might be related to changes in aqueous flow within the anterior chamber.

Since in–vivo measurements of aqueous flow are extremely challenging, a numerical approach seems to be the best option. As the Reynolds number of the flow is always relatively small, the flow is invariably laminar and, therefore, no turbulence models are required, which would require the need of adopting somewhat questionable assumptions.

We considered all the main mechanisms that induce flow in the anterior chamber, namely:

i) flow due to aqueous production at the ciliary processes and drainage at the trabecular meshwork;

ii) flow generated by contraction/expansion of the pupil (which was described in a highly simplified way in the present work);

iii) flow induced by thermal effects;

iv) flow generated by eye rotations.

The anterior chamber was modelled in a simplified, yet realistic, way as an axisymmetric domain. For all cases we run benchmark simulations of the flow in the anterior chamber in the absence of the intraocular lens and then considered the same cases accounting for the presence of the pIOLs. The pIOL geometry was also modified by drilling holes into its body. We considered both the case of a single central hole in the body of the pIOL and also the case of two lateral holes. A hole in the body of the lens could be a possible alternative to iridectomy. A perforation in the pIOL can also contribute to reduce the resistance to the aqueous flow. Perforated pIOL are already in use for lenses implanted in the posterior chamber of the eye.

4.7 Summary of the results

4.7.1 Bulk flow induced by aqueous production/drainage

The simulations show that the intraocular lens has a very little effect on the pressure drop within the anterior chamber. In order to induce a clinically significant increase of the pressure the lens should be located very close to the iris, at a distance of the order of less than a micron. This is well below the intended distance between the iris and the intraocular lens, when the latter is properly placed.

Implantation of iris fixated intraocular lenses is often associated with iridotomy, which is aimed at preventing an undesirable pressure growth. The present simulations suggest

that, at least as far as only the slow production/drainage aqueous flow is concerned, iridotomy is not required for keeping the pressure within physiologically acceptable limits. In the extreme case in which the passage between the pIOL and the iris gets blocked (either due to cell deposition or to the fact the iris progressively moves forward with ageing), a relatively small hole in the body of the pIOL is sufficient to keep the pressure within physiologically acceptable limits. However, we note that a pupillary block caused by implantation of an iris-fixated pIOL is an extremely unlikely event.

The most critical possible complication associated with implantation of iris-fixated intraocular lenses is related to an increased risk of cell loss from the corneal endothelium. In this respect, one could think that a hole in the body of the pIOL may increase the wall shear stress on certain regions of the cornea (in front of the jet exiting the hole) and thus increase the risk of cell detachment. This mechanism has been postulated for the case of holes in the iris generated with iridotomy. Our simulations showed that the wall shear stress grows in the central region of the cornea, but for all cases considered here, keeps values which are safely within physiologically acceptable limits. Furthermore in the case of the production–drainage flow the wall shear stress on all surfaces with the presence of pIOL is so small that it does not have clinical significance. Changing the axial distance between Artiflex pIOL and cornea and offset positioning with respect to the axial direction did not have a significant effect on pressure and wall shear stress to be considered clinically relevant.

Finally, we note that lens implantation modifies significantly the aqueous flow structure. In particular, the flow in proximity of the cornea is strongly damped.

4.7.2 Flow generated during contraction/expansion of the pupil

This flow is modelled in a highly simplified way, by keeping the geometry fixed and imposing that an unsteady jet enters the domain from the pupil. In this case both pressure and wall shear stress change in time. The maximum pressure is still much lower than what would be clinically relevant, if the lens is properly positioned. The wall shear stress on the iris can attain relatively high values which, however, are unlikely to produce detachment of pigment cells from the iris. We note that, if iridotomy were present, the wall shear stress on the iris would drop again to very low values.

As also suggested by Kaji et al. [69] and Yamamoto et al. [139], the present numerical simulations show that the wall shear stress on the cornea can locally increase quite severely when an iridotomy hole is produced.

4.7.3 Flow induced by buoyancy effects

The flow induced by thermal effects in the anterior chamber is much more intense than that due to the aqueous production–drainage. The present simulations show that the structure of the flow is strongly modified by the presence of the lens. However, the maximum wall shear stress on the cornea does not change significantly after the implantation of the lens. The wall shear stress on the iris also keeps within physiologically acceptable limits. similar to the aqueous production–drainage case altering the axial distance between Artiflex pIOL and cornea and the position with respect to the axial direction did not have a significant effect on pressure and wall shear stress.

4.7.4 Flow induced by eye rotations

Eye rotations produce the highest values of the shear stress on the cornea, among all mechanisms that generate aqueous humor flow. However, these values are not large enough to produce cell damage in normal conditions. The numerical simulations show that, after the implantation of an iris–fixated lens, the maximum wall shear stress on the cornea generated during a saccadic rotation is slightly smaller than that that would occur in the corresponding case in the absence of lens.

4.8 Conclusion

The numerical simulations conducted within this chapter allow us to understand how the fluid mechanics in the anterior chamber is modified by implantation of an iris–fixated lens.

The main conclusions of the work are as follows:

i) Lens implantation has negligible influence on the intraocular pressure, if the lens is properly placed.

ii) lens implantation does not produce an increase of the shear stress on the cornea.

iii) after lens implantation the iris is subjected to a higher than normal shear stress that, however, is not large enough to justify cell detachment from this tissue.

iv) a hole in the body of the pIOL has not a significant effect to be clinicaly important but can be a viable alternative to iridotomy to keep the pressure within safe values in the case in which the passage between the pIOL and the iris gets blocked.

The above results are encouraging, as they suggest that modifications of the fluid mechanics in the anterior chamber induced by lens placement are unlikely to increase the intraocular pressure and to cause endothelial cell detachment from the cornea.

It remains, therefore, open the question of what corneal cell detachment might be due to.

An obvious possible explanation is mechanical friction between the cornea and the intraocular lens in the case that the patient rubs her/his eyes, thus inducing a direct contact between the cornea and the lens.

An alternative possible mechanism that might deserves consideration and is considered in the next chapter can be related to lack of nutrient or oxygen delivery to the cornea after lens implantation. In order to test the feasibility of the above speculation the equations of motion for aqueous flow will be coupled with an advection–diffusion equation for metabolic species transport in chapter 5.

Chapter 5

Mathematical model of corneal metabolism

5.1 Introduction

Since the cornea is an avascular tissue it has to rely on oxygen and nutrient supply from the surrounding tissues or from the external environment. In the healthy cornea, oxygen is primarily supplied by air when the eyes are open and from blood circulation in the palbebral conjunctiva when the eyes are closed [35]. On the other hand, glucose primarily diffuses into the cornea from the aqueous humor [36]. The aim of the work presented in this chapter is to investigate if and how implantation of an iris-fixated, phakic intraocular lens (pIOL) modifies nutrient and oxygen availability of the cornea. Furthermore the effect of a central hole in the body of the lens will also be investigated.

Various experimental data exist on oxygen and glucose consumption and lactate production, their concentrations and the response of pH in hypoxia, in particular for the rabbit cornea [e.g. 130, 14, 122, 59, 95]. Several mathematical models have also been proposed, aimed at describing corneal metabolism. Taking advantage of the fact that the thickness of the cornea is much smaller that its lateral dimension, in the majority of cases one-dimensional models have been adopted, in which the transport of all species across the corneal wall was assumed much larger than in the other directions. Chhabra et al. [23] proposed a coupled reaction-diffusion model for nutrient and oxygen delivery to the cornea, which is the basis of the model used in this work, and has been described in chapter 3, section 3.3.

In all of these studies the effect of glucose transport through advection and diffusion in the aqueous humor has been lumped into a concentration boundary condition at the corneal endothelium. When the eyelids are open, due to the temperature gradient across the anterior chamber, a buoyancy driven aqueous flow is generated that is significantly more intense that the production/drainage flow (see chapter 4, sections 4.5.1). Eye movements are also capable of generating significant velocities in the aqueous (see chapter 4, subsection 4.5.1.3). As a consequence of relatively large velocities in the anterior chamber, it is reasonable to assume that when the eyes are open, the aqueous humor is well mixed in the anterior chamber and, therefore, that the concentration of oxygen and nutrients is constant. Thus, lumping the effect of nutrient transport across the anterior chamber into a boundary condition on the endothelium for solving the problem in the cornea is a sensible approach.

On the contrary, when the eyelids are closed, the temperature in the anterior chamber is approximately uniform and equal to the body temperature and, as a consequence, the thermal flow vanishes. In this case, the mechanisms that produce fluid flow will be restricted to: i) aqueous humor production at the ciliary processes and drainage at the the trabecular meshwork and ii) rapid eye movements (REM). However, we note that REM do not occur continuously during sleeping but, rather, at fairly regular intervals. Since the production/drainage flow is very slow we should not expect oxygen and nutrients concentrations to be constant throughout the anterior chamber in this case. Thus, in order to study nutrient delivery to the cornea in the case of closed eye lids, it is necessary to also account for transport within the aqueous humor.

In the present chapter, we use the model adopted by Chhabra et al. [23] which is further improved by considering a sigmoidal function for oxygen consumption, as proposed by Alvord et al. [3]. The mathematical models are described in detail in chapter 3, section 3.3.

5.2 Geometry

Figure 5.1 represents the idealized axisymmetric shape of the anterior chamber and the cornea. The anterior chamber has the same shape as considered in chapter 4, section 4.2 and, again, we neglect the flow in the posterior chamber. Hence the iris–lens channel represents the inlet section for the simulations related to closed eyelids. The cornea consists of the three layers: endothelium, stroma and epithelium, moving inside out (see the inset in figure 5.1). The Descmet's and Bowman's membranes are considered as part of the stroma, since they have similar transport properties. Geometrical characteristics of the cornea is given in table A.2 in the Appendix. The geometry of the anterior chamber is the same as the one, used in chapter 4.

We performed simulations, with and without an iris fixated pIOL. For the pIOL we considered the Hydrophobic Artiflex, which was also used in chapter 4, section 4.2. In all simulations we neglect the presence of the haptics, which were shown in Repetto et al. [115] to have a small influence on aqueous flow.

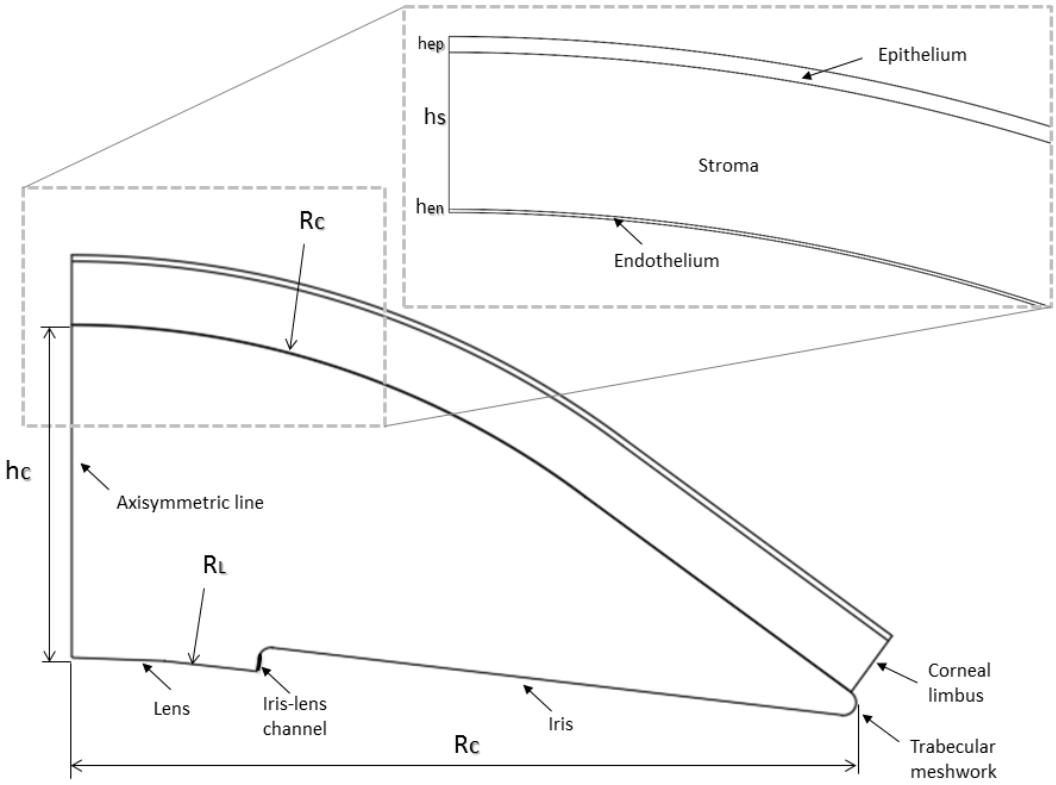

Figure 5.1: Cross-section of the idealized anterior chamber with corneal layers.

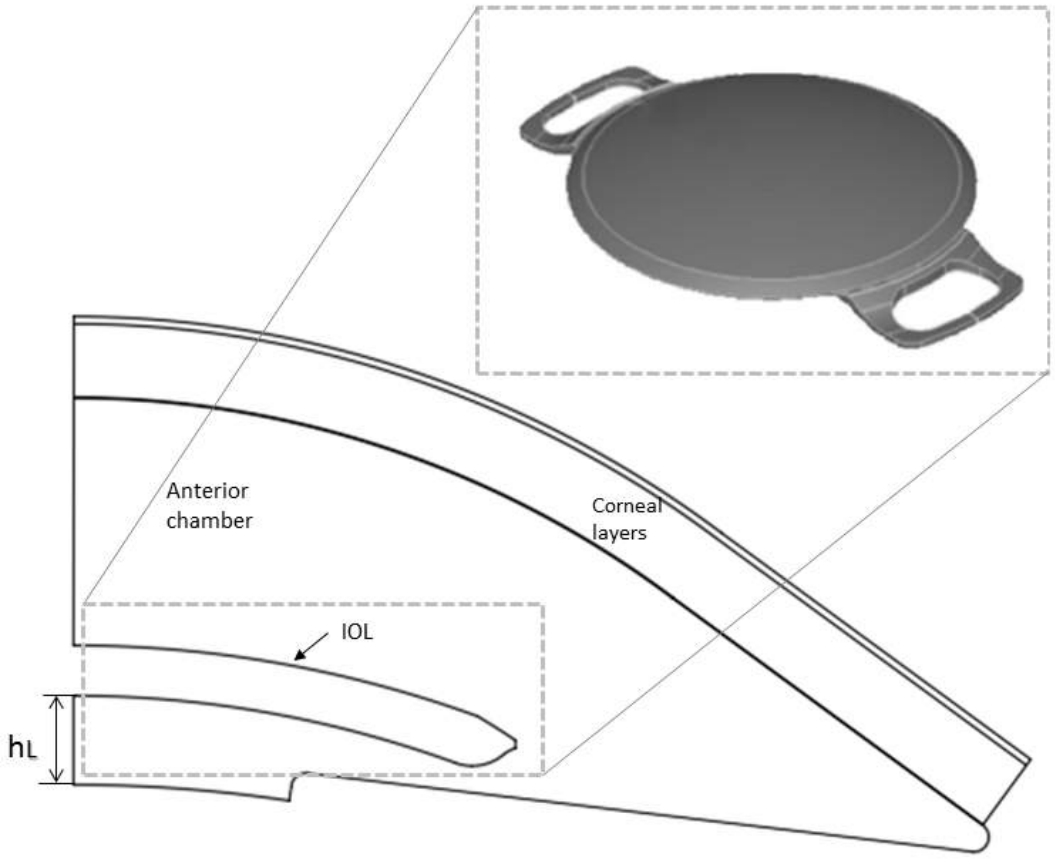

Figure 5.2: Cross-section of the idealized anterior chamber with the positioned pIOL without haptics.

5.3 Experimental data

One of the most important and delicate parts in the developed mathematical model of tissue metabolism consists in calibrating all model parameters. To this end one has to rely on experimental data, when available. In this section we mention the experimental works from which we obtained data to calibrate our model.

5.3.1 Oxygen

The measurement of oxygen tension in the anterior chamber is crucial for specifying the boundary conditions for our models. We mainly focus our attention on the work of Mclaren et al. [95]. The authors used a scanning ocular fluorometer and measured the oxygen tension through the depth of the anterior chamber. This experiment was repeated for different cases and we focus our attention on the measurement of oxygen tension obtained on the cornea in the case with a PMMA contact lens and when eye lids are closed. The reasons for this choice are given below.

The oxygen permeability of a PMMA lens is low, therefore a very small amount of oxygen can pass through it. Since the majority of oxygen is provided from the air when eyelids are open and from palbebral conjunctiva with closed lids, when a PMMA contact lens is used the cornea is deprived from these oxygen sources and we can in this situation consider that oxygen is mostly provided by the aqueous humor. Under these conditions Mclaren et al. [95] found that the oxygen tension close to the crystalline lens is approximately equal to 6 mmHg and it decreases to 3 mmHg in the central region of the anterior chamber. Following these observations we set the oxygen tension and the inlet channel to 6 mmHg.

When the eyelids are closed, the oxygen is mainly provided by the palbebral conjunctiva, which has an oxygen level of approximately one third of that present in the air [39]. According to Mclaren et al. [95] when the eyelids are closed, the oxygen tension in the mid-anterior chamber is around 10 mmHg after 20 min. Our model results are validated against this measurement.

5.3.2 Lactate

Langham et al. [80] showed that when rabbits eyelids are closed for 24 hours, the corneal lactate acid increases by 10% to 20% with respect to the open eyelid case. This shows that when the eyelids are closed, the corneal lactate concentration is higher than in the open eye case. Since lactate concentration in the posterior chamber is given by Reddy et al. [111], we use the value of 81 mg/dl or 4.5 mM of lactate concentration at the inlet and crystalline lens.

5.3.3 pH

In the case of open eyelids the corneal pH is about 7.6 but, when the eyelids are closed, it decreases to approximately 7.39 [14]. The pH value has an effect on the consumption rates of oxygen and glucose, which is accounted for in the model proposed by Chhabra et al. [23]. In the present work we also account for the increase in oxygen consumption during night time related to a decrease in pH with respect to day time conditions.

5.4 Description of the simulations

We performed two series of simulations, with open and closed eye lids. The open eyelids simulations are meant to validate the model since many clinical observations are available for this case.

5.4.1 Open eyelids

Following the discussion presented in section 5.1 we assume that in the case of open eye lids the thermal flow and the flow generated by eye rotations are intense enough as to suppress concentration gradients in the anterior chamber. This allows us to neglect the anterior chamber in our simulations and solve the transport equations only in the cornea, by imposing constant concentration conditions at the corneal endothelium. Thus in our model in the case of open eye lids the presence of the pIOL does not have any effect on oxygen and metabolic species concentrations in the cornea.

Since both the corneal geometry and the boundary conditions imposed are axisymmetric, the solution is also axisymmetric, which allows us to avoid complicated and numerically expensive three-dimensional simulations.

5.4.2 Closed eyelids

In this case the thermal flow and eye rotations (neglecting the role of REMs, which will be discussed later) are suppressed. Therefore, the flow is only generated by the production and drainage mechanism.

We solve for this flow and for oxygen and nutrient transport in the aqueous and couple the problem with the transport in the cornea. Again the problem is axisymmetric and, therefore, we only run axisymmetric simulations. In these simulations we consider the anterior chamber with and without the presence of a pIOL.

5.4.3 Boundary conditions

5.4.3.1 Open eyelids

At the interfaces between each layer, the three metabolic species should satisfy continuity of concentrations. Moreover, conservation of mass requires continuity of normal fluxes. Oxygen tension, glucose and lactate ion concentrations at the anterior chamber-endothelium interface are set equal to 24 mmHg, 6.9 mM, and 7.7 mM, respectively [23]. At the epithelium-tear film interface, oxygen concentration is assumed equal to 155 mmHg, which is equal to the atmospheric oxygen tension [23]. Glucose concentration in the tear film is about 40 times less than that in the anterior chamber. For this reason glucose flux is set to zero at this interface. Since the lactate concentration in the tear film is small, lactate flux is also set to zero at the epithelium-tear film interface. At the corneal limbus we consider a zero flux boundary condition for all metabolic species.

5.4.3.2 Closed eyelids

At the iris-lens channel (which is the aqueous humor inlet section) we impose oxygen tension, glucose and lactate concentration of 6 mmHg [95], 6.9 mM [23], and 4.5 mM [80],

respectively. For the iris and corneal limbus we impose zero flux for all metabolic species. At the epithelium-tear film interface the oxygen concentration is assumed equal to 61.5 mmHg, which is the oxygen tension in the palbebral conjunctiva. In analogy with the open eyelids case, the glucose and lactate fluxes are set to zero at the epithelium-tear film interface. At the trabecular meshwork an outflow boundary condition for all of metabolic species is imposed. For the aqueous flow, all of the boundary conditions are the same as adopted in chapter 4 section 4.4.1.

The imposed boundary conditions for both cases are summarized in table A.6 in the Appendix.

5.5 Results

5.5.1 Steady simulations

We first study the steady state solution of the problem described in chapter 3 section 3.3. In section 5.5.2 we will investigate the time required for this steady solution to be reached. For all cases considered we run a simulation without the pIOL and one with it. We also investigate the effect of a perforation in the pIOL on the transport of metabolic species in the anterior chamber and cornea.

Figure 5.3 shows the equilibrium concentration profiles of oxygen (a), lactate (b) and glucose (c) across the thickness of the axis of symmetry of the cornea. In the plots the x-axis represents a coordinate running outwards and with the origin in correspondence of the interface between the aqueous humor and the corneal endothelium. The vertical dashed lines mark the boundaries between the various corneal layers. The four curves correspond to the open eyelids case (blue), closed eyelids without pIOL (green), closed eyelids with pIOL (red) and closed eyelids with perforated pIOL (purple).

Let us consider the open eyelids case first. Moving from epithelium toward the anterior chamber, due to the consumption of oxygen by corneal layers, there is a decline in the oxygen tension. Moreover, since in our model glucose is solely provided by the aqueous humor and is consumed by the corneal layers, there is a decrease of glucose concentration towards the epithelium. As the consequence of glycosis, lactate concentration increases toward the epithelium.

In the case of closed eye lids we impose a lower oxygen pressure at the epithelium and also consider transport of species in the aqueous humor. The oxygen levels in the cornea are lower than when the eyes are closed and the minimum value, which occurs at the endothelium, drops from 24 to ≈ 13 mmHg. Since glucose is mainly provided by the aqueous humor and the flow is slower in the closed eyelids case, glucose concentration at the anterior chamber-endothelium interface is significantly lower than in the open eyelids case.

Finally we consider the results in the presence of the pIOL and the perforated one. In order to understand our findings, it is useful to consider the changes in aqueous flow that are generated by the pIOL, shown in figure 5.4 and figure 5.5. In figure 5.4 we plot a colour map of the velocity magnitude and also streamlines of the flow in the anterior chamber with and without the presence of pIOL. It appears that the pIOL forces fluid towards the periphery of the anterior chamber and a region of very slow motion forms anterior to the pIOL. In this region the flow is characterized by two extremely slow circulations with opposite signs. Since the flow anterior to the lens is so slow, glucose in the aqueous has

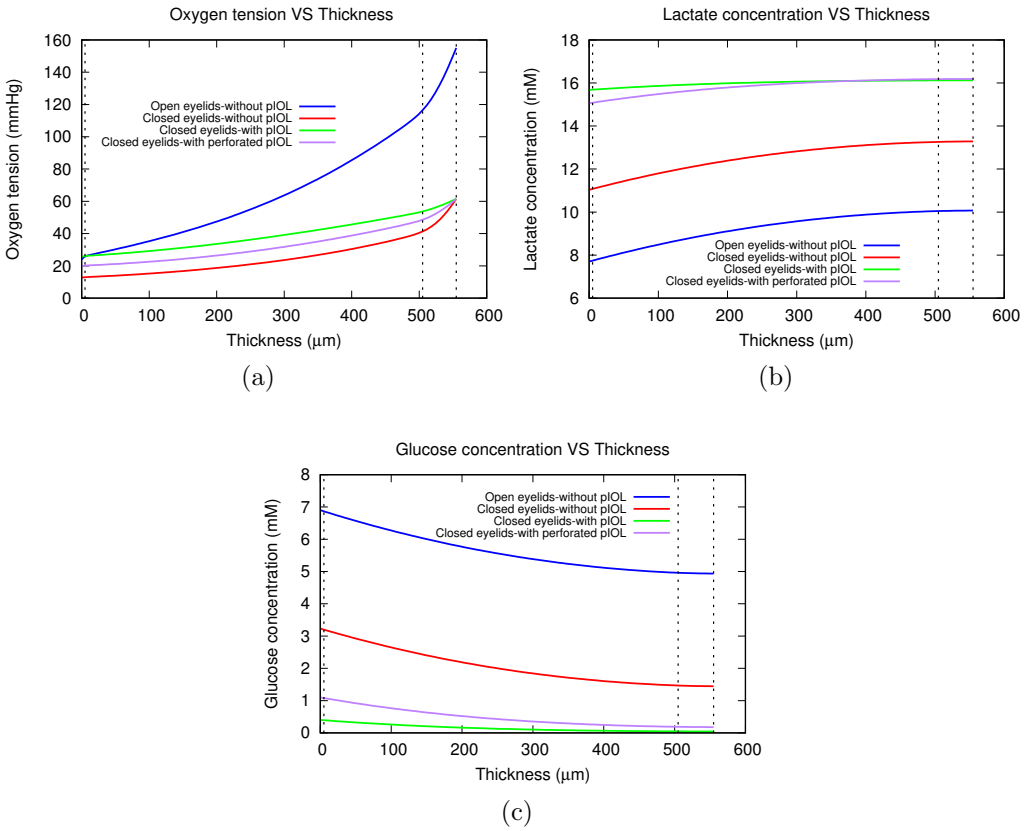

Figure 5.3: Equilibrium concentration profiles of oxygen (a), lactate (b) and glucose (c) across the thickness of the axis of symmetry of the cornea. The x-axis represents a coordinate running outwards and with the origin in correspondence of the interface between the aqueous humor and the corneal endothelium. The vertical dashed lines mark the boundaries between the various corneal layers. The four curves correspond to the open eyelids case (blue), closed eyelids without pIOL (green), closed eyelids with pIOL (red) and closed eyelids with perforated pIOL (purple).

to rely primarily on molecular diffusion in order to reach the central region of the cornea and, since diffusion is a very slow transport mechanism, we expect to find lower levels of glucose along the endothelium in this case.

This is confirmed by our results, as shown in figure 5.3 (c) (green curve). Indeed, in this case the glucose concentration drops to very low values throughout the thickness of the central cornea. As a consequence of the glucose drop, the oxygen partial pressure in the cornea is higher when the pIOL is present than in the reference case, a shown in figure 5.3 (a).

On the other hands, the presence of a hole at the center of the lens diverts part of the flow toward the central region of the cornea, (see figure 5.5). In figure 5.6 we show colour maps of equilibrium glucose concentration in the anterior chamber and cornea, with and without the perforated pIOL. As can be seen in this figure and considering the advective transport of aqueous flow toward the hole, the availability of glucose on the endotheliums is higher than without the perforation. Furthermore, as it is shown in figure 5.3 (c) (purple curve), throughout the corneal layers, the glucose concentration in the presence

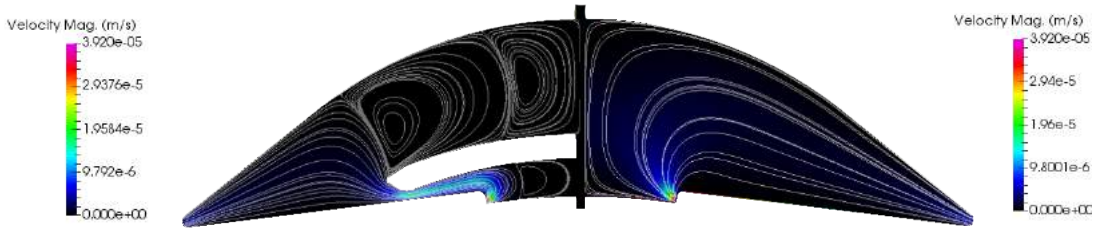

Figure 5.4: Velocity magnitude and flow streamlines in the anterior chamber with and without the pIOL.

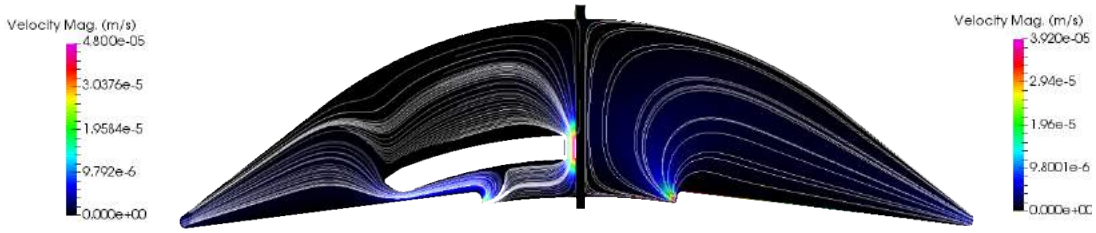

Figure 5.5: Velocity magnitude and flow streamlines in the anterior chamber and cornea with and without the perforated pIOL.

of the pIOL with a central hole is higher than the pIOL without any modification, even though still much lower that in the case without the pIOL.

In figure 5.6 we show colour maps of equilibrium glucose concentration in the anterior chamber and cornea, with and without pIOL. The figure shows that glucose distribution in the two cases is very different. This is essentially due to the advective transport induced by aqueous motion. In the case of implanted pIOL the glucose levels in the region anterior to the pIOL are much smaller, in agreement with the results shown in figure 5.3 (c).

In figures 5.8 and 5.10 we report the colour maps of oxygen and lactate, for the case of anterior chamber with and without the presence of the pIOL, respectively. Since with the pIOL the centre of cornea is at a lower glucose concentration the consumption of oxygen is lower than without the lens, leading to an increase of oxygen level. Moreover, owing to the lack of glucose (and in spite of the small increase of oxygen concentration in the cornea), the production rate of lactate increases in the case of implanted pIOL, which in turn increases lactate concentration.

Finally in figures 5.9 and 5.11, for the case of anterior chamber with and without the presence of the perforated pIOL, we show the colour maps of oxygen and lactate, respectively. Since oxygen is mainly provided from the epithelium side, the central hole at the lens body has a negligible effect in comparison to the case of the pIOL without the hole. On the other hand, due the increase in the glucose concentration, anterior to the perforated lens, the lactate concentration in this region decreases, which also decreases the risk of corneal acidification.

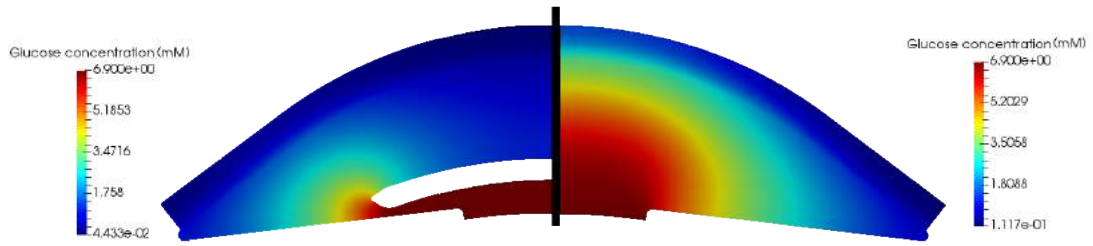

Figure 5.6: Glucose concentration in the anterior chamber and cornea with and without the pIOL.

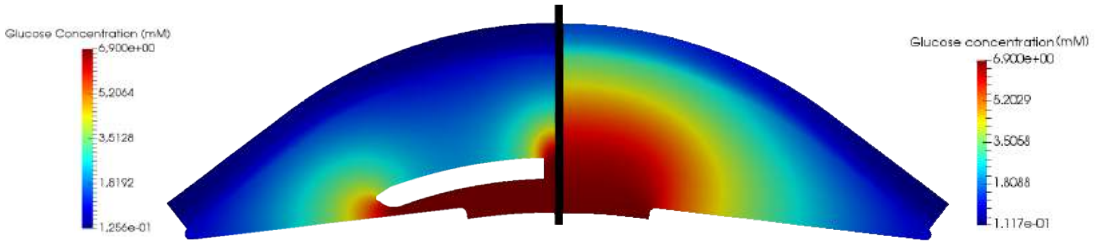

Figure 5.7: Glucose concentration in the anterior chamber and cornea with and without the perforated pIOL.

5.5.2 Unsteady simulations

In the previous section we discussed the steady state results of our model. Obviously, for steady state concentrations to be reached a certain time is required, and it is of interest to estimate it. This will allows us to verify whether the solutions described in the previous section can be reached in reality. We recall that we are assuming that during daytime aqueous humor is efficiently mixed by eye rotations and thermal flow. During sleeping, these sources of fluid motion are suppressed. However, we know that at relatively regular intervals REM occur during sleeping. On average, the first REM phase occurs approximately 80 min after falling asleep and then the following phases are separated by time intervals of approximately one hour and a half.

We show in this section results of unsteady simulations aimed at studying the time evolution of the concentration of all species. We note that the simulations are unsteady for the species concentrations but not for fluid flow. This implies that fluid velocity $\mathbf{u}$ and pressure p are solved for in steady conditions and equations 3.24 are then solved for the concentrations, keeping $\mathbf{u}$ constant in time.

In the unsteady simulations we assume the concentrations of all species in the anterior chamber to be initially uniform. For the glucose and lactate we use the values they assume in daytime conditions ($c_G = 6.9$ mM, $c_L = 7.7$ mM). The concentration of metabolic species in the cornea is assumed to be the same as calculated in 5.5.1 for the open eyelids case. With these initial conditions we run unsteady simulations using the same boundary conditions adopted in the previous section for the closed eyelids case.

In figure 5.12 we show the time evolution of the concentration of all species at the centre of the cornea. The blue curve corresponds to the case of absence of pIOL, the red one to the case in which a pIOL is present and the green one to the case in which a

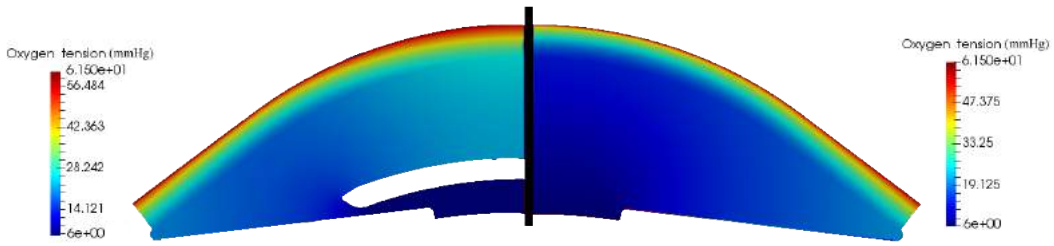

Figure 5.8: Oxygen concentration in the anterior chamber and cornea with and without the pIOL.

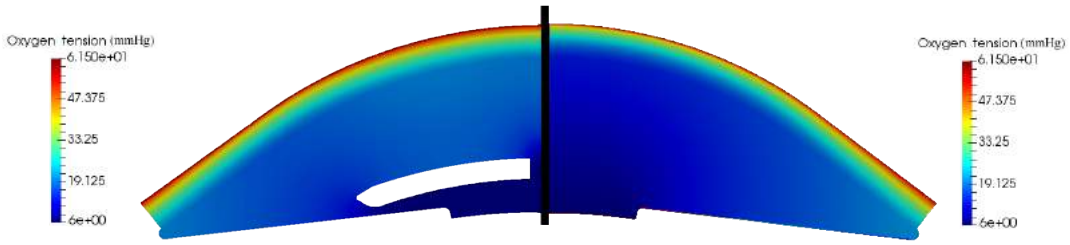

Figure 5.9: Oxygen tension in the anterior chamber and cornea with and without the perforated pIOL.

pIOL with a central hole is present. In the figure we also mark with a vertical dashed black line the time at which the first REM cycle is expected to occur. The figure shows that the time scale of evolution is of the order of some hours: the final steady state is reached in approximately four hours. Since, on average, REM occur approximately every 80 minutes, this final steady state is unlikely to be reached in normal conditions.

We find that when the first REM phase occurs the glucose concentration has reduced to 3.4 mM (with no pIOL) and to 2.18mM (with pIOL with hole) and 1.6 mM (with pIOL), respectively.

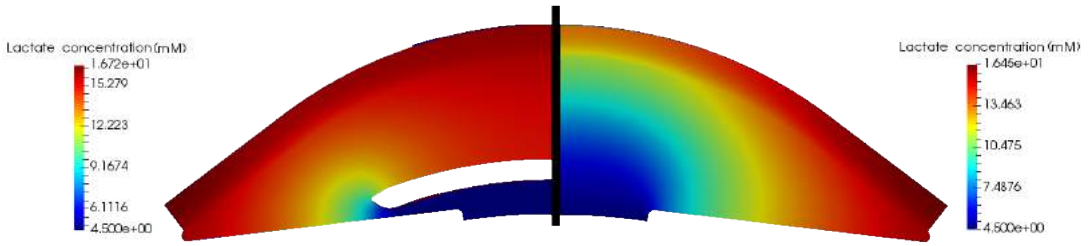

Figure 5.10: Lactate concentration in the anterior chamber and cornea with and without the pIOL.

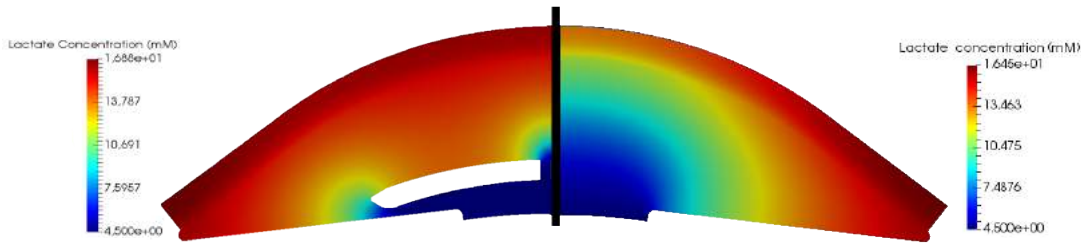

Figure 5.11: Lactate concentration in the anterior chamber and cornea with and without the perforated pIOL.

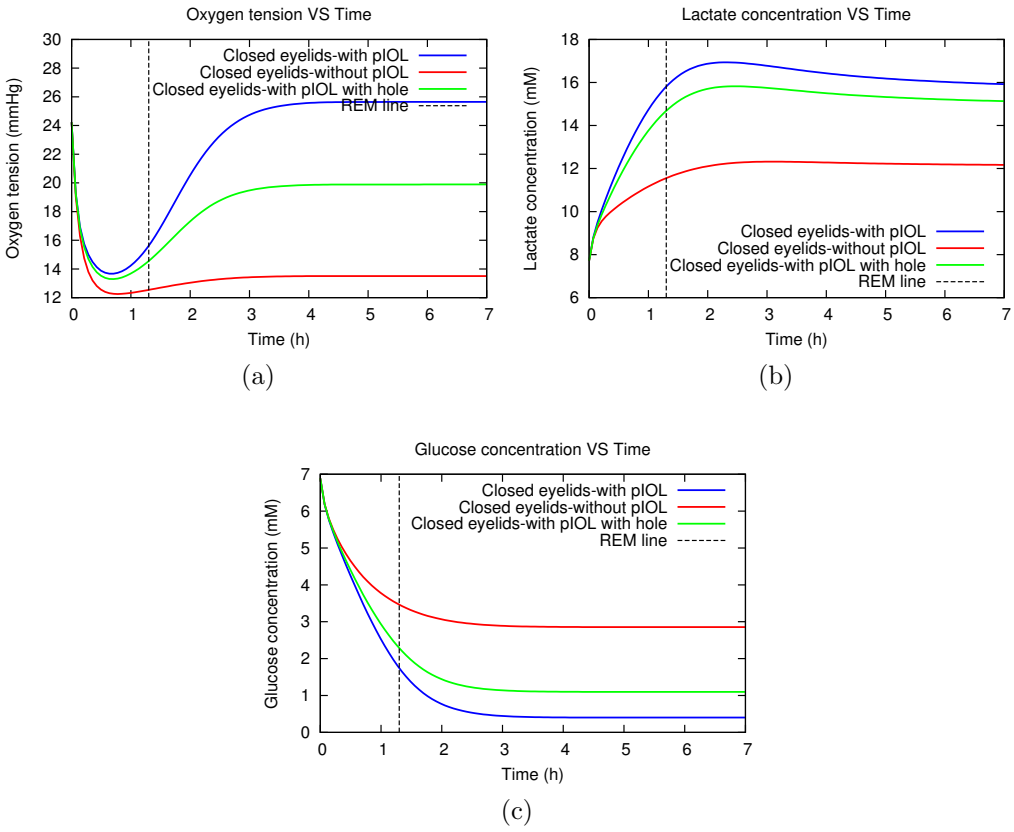

Figure 5.12: Time evolution of metabolic species concentration at the centre of cornea with and without the pIOL.

5.6 Summary of the simulations

In this chapter we have described simulations of the metabolic species delivery to the cornea considering aqueous flow in the anterior chamber with and without the presence of the Hydrophobic Artiflex. The aim of this chapter was to understand how and to what extent the implantation of an iris-fixated lens modifies the aqueous metabolic species delivery in the anterior chamber and cornea. This is a problem of clinically interest. As we mentioned in chapter 4 section 4.6, loss of endothelial cells from the cornea is among the possible complications associated with the implantation of an iris–fixated intraocular lens [78]. It has been hypothesized that these complications might be related to changes in the nutrient transport by the aqueous flow.

When the eyelids are open, due to buoyancy driven aqueous flow and eye movements, aqueous humor is well-mixed in the anterior chamber. Due to these reasons concentration of species are approximately constant in the anterior chamber. Therefore, in the case of open eyelids, we lumped the species transport across the anterior chamber into a boundary condition on the endothelium. On the contrary when the eyelids are closed, the temperature in the anterior chamber is approximately uniform and the mechanisms that produce fluid flow will be mainly bulk production/drainage flow. Being this flow very slow, for the closed eye lids we also account for transport of metabolic species within the aqueous humor.

The anterior chamber was modelled in a simplified, yet realistic axisymmetric way and three corneal layers (endothelium, stroma and epithelium) have been considered. Open eyelids simulations were mostly used to validate our model with the existing experiments in the literature. For the simulations with closed eye lids, we run steady and unsteady simulations of metabolic species delivery in the anterior chamber and cornea, with and without the presence of the Hydrophobic Artiflex pIOL. The unsteady simulations are aimed at studying time evolution of species concentrations. We also analysed the effect of perforation of the lens on the corneal metabolic species delivery.

5.7 Summary of the results

5.7.1 Steady simulations

When the eyelids are closed and no lens is implanted, our simulations suggest the oxygen and glucose levels at the corneal endothelium are lower (approximately half) than when the eyes are open. When the lens is implanted in the anterior chamber since the pIOL forces fluid towards the periphery of the anterior chamber, the region anterior to the pIOL is characterized by a very slow motion and glucose in the aqueous has to mainly rely on diffusion to reach the central region of the cornea. Diffusion is a very slow transport mechanism and our simulations suggest a much lower level of glucose along the endothelium is reached than in the case without pIOL. Lack of glucose also increases the lactate concentration in the central part of cornea.

5.7.2 Unsteady simulations

Our simulations suggest that the final steady state is reached in approximately four hours. Since rapid eye movements occur approximately every 80 minutes and their occurrence

produces fluid mixing, the final steady state is unlikely to be reached in normal conditions. However till the occurrence of the first REM phase, the glucose concentration is reduced to 3.4 mM (with no pIOL) and to 2.18 mM (with pIOL with hole) and 1.6 mM (with pIOL), respectively. The central hole in the body of the pIOL increases glucose concentration in the cornea in comparison to the case of lens without any perforation.

5.8 Conclusions

We propose a mathematical model for the transport of metabolic species in the cornea and the anterior chamber, considering aqueous flow when eyelids are closed. In comparison to all the previous studies, our model is more consistent with the experimental data discussed in section 5.3. To our knowledge, the effect of aqueous flow on the delivery of nutrients to the cornea was neglected in all previous works.

The steady state simulations showed that the presence of a pIOL has a strong influence on glucose availability on the cornea in sleeping conditions. When the pIOL is implanted, aqueous flow is diverted towards the periphery of the anterior chamber and glucose concentration decreases dramatically in the region anterior to the lens. However, we show that several hours are needed for this steady solution to be reached. Since during sleeping REM are expected to occur approximately every 80 minutes, the steady state solution predicted by our model is unlikely to be ever reached. Rather, the system is constantly in an unsteady state. Glucose concentration anterior to the lens progressively decreases until REM occur; these eye rotations mix up the aqueous humor and, then, glucose concentration in front of the pIOL increases again. We found that the minimum value of glucose that is expected to be reached in the presence of a pIOL is approximately half of that that would occur without pIOL. On the cornea, glucose and oxygen availability in the case of a perforated pIOL increases and lactate concentration decreases.

We note that we did not consider in our model the effect endogenous glycogen from the epithelium. Thus, variations of glucose concentration in the cornea in vivo may not be as strong as those shown in the results.

Summarising, our model suggests that implantation of a pIOL may produce a decrease in nutrient availability in the central region of the cornea during sleeping. It must be verified whether this has clinical relevance.

Chapter 6

Analysis of forces on the Artisan aphakia lens

6.1 Introduction

As mentioned in chapter 1, section 1.4, the two main types of cataract surgery are Extracapsular Cataract Extraction (**ECCE**) and Intracapsular Cataract Extraction (**ICCE**). In ECCE the lens is entirely removed and the elastic lens capsule remains intact. Then a cataract intraocular lens is placed in the capsule. On the other hand if the patient has a weak zonula, cataract intraocular lenses cannot be used and ICCE will be performed. ICCE requires removal of the natural lens and the surrounding lens capsule in one piece. When this happens, vitrectomy (a surgery to remove the vitreous gel from the vitreous chamber) is performed and the vitreous chamber is in direct contact with the anterior one and is filled by the aqueous humor. The surgeon then often chooses to use an iris fixated lens to recover the vision.

In this chapter we focus on the Artisan Aphakia +30.0 D lens (aIOL), designed by Ophtec BV., which is used in cataract surgery of patients with a weak zonula. What makes this aIOL special is that it can be implanted both on the anterior or the posterior side of the iris. This is possible as the lens optical properties remain unchanged upon reversal of the lens. Ophtec used to recommend implantation on the anterior surface of the iris (in the anterior chamber) and only recently the company has officially approved the implantation also on the back surface of the iris. Surgeons often chose to implant the lens in the posterior side of the iris since it is surgically more convenient.

As seen in chapter 4, section 4.5, there are many mechanisms inducing flow in the anterior chamber. Among those, flow induced by the eye movements creates higher velocities in the chamber and, consequently higher mechanical forces. Since the vitreous chamber is bigger in comparison to the anterior one, if an aIOL is attached to the posterior surface of the iris, in the case of vitrectomized eyes, the lens might experience significantly higher mechanical forces than when it is implanted in the anterior chamber.

The aim of this chapter is to investigate, from the mechanical point of view, whether one of the implantation options is preferable with respect to the other. The main observables of the numerical simulations will be the forces acting on the aIOL and the forces transmitted by the aIOL to the iris. We will consider the two cases of the aIOL implanted on the anterior and posterior surface of the iris, separately. We will only focus on the flow induced by the saccadic movements of eye since in chapter 4, section 4.5, we showed that

this is by far the mechanism that creates the most intense flow.

In section 6.2 we describe the geometry of the anterior chamber, vitreous chamber and the Artisan aphakia lens. In section 6.3 we discuss the boundary conditions and the solver that have been used to model the flow induced by the saccadic motion of the eye. Furthermore the force calculation procedure and the results of the simulations are discussed in sections 6.4 and 6.5, respectively and the comparison between the anterior and posterior placement of the aIOL is given in section 6.6. In section 6.7 and 6.8 we summarize the simulations and the results obtained in this chapter, respectively and finally conclusions are discussed in section 6.9.

6.2 Geometries

6.2.1 Geometry of the anterior chamber

In this work the geometry of the anterior chamber has been slightly modified with respect to that adopted in chapter 4, section 4.2. This is because the aIOL is thicker than the Artiflex Hydrophobic and the Artiflex pIOLs and, as shown in figure 6.1, it would intersect the iris if the original shape of the anterior chamber was adopted. To avoid this, we flattened the shape of the iris by increasing the iris-cornea angle. This is also physically plausible since, in this chapter, we are concerned with the case in which the natural lens has been removed and, in this case, that the iris would move posteriorly. The geometry of the anterior chamber is taken from Kapnisis et al. [70].

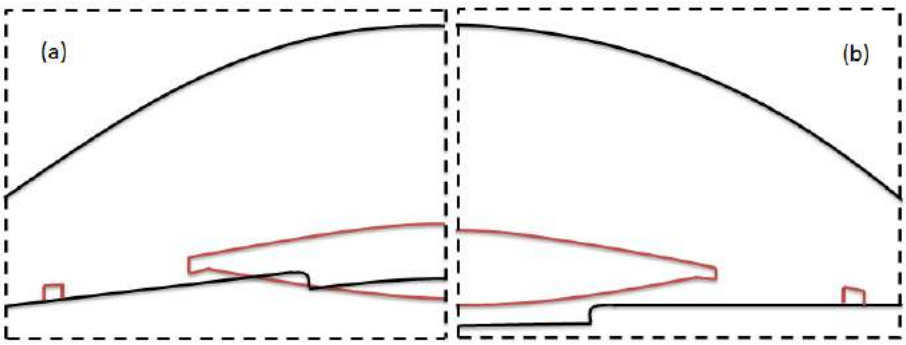

Figure 6.1: (a) Geometry of the anterior chamber adopted in 4 section 4.2. The aIOL intersects the iris. (b) Modified geometry obtained by increasing the iris-cornea angle.

6.2.2 Geometry of the vitreous chamber

We consider the vitreous geometry shown in figure 6.2 (b), which represents an idealisation of the real vitreous chamber. Specifically, we assume that the chamber is axisymmetric and we model the cross section shown in figure 6.2 (a), and smooth the joints between the different tissues. The geometry is based on Gesell et al [46], Woo et al. [136] and Pavlin et al. [105], and the iris is flattened to be consistent to the anterior chamber shape, discussed previously. The parameters shown in figure 6.2 (a) are given in table A.7 in the Appendix.

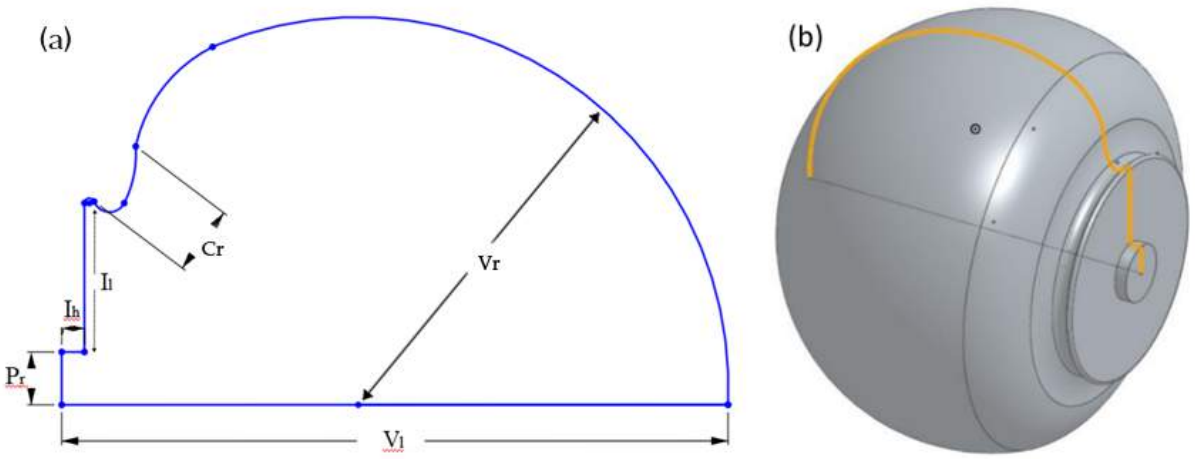

Figure 6.2: (a) Cross section of vitreous chamber. The parameters are given in table A.7 in the Appendix. (b) three dimensional model of vitreous chamber.

6.2.3 Lens geometry

In this study we consider the Artisan Aphakia lens (+30.0 D), including the haptics. The lens is shown in figure 6.3 (a). As mentioned before, this aIOL can be implanted both in the anterior and posterior side of the iris. The positioning in the anterior and vitreous chambers can be seen in 6.3 (b) and 6.3 (c), respectively. The lens is thicker than the Artiflex Hydrophobic and the Artiflex pIOLs. Furthermore unlike these two pIOLs, the haptics embrace the Artisan Aphakia body. Since we mainly focus on the analysis of mechanical forces on the aIOL, in our analysis the haptics are also considered since they might have major influence on the forces.

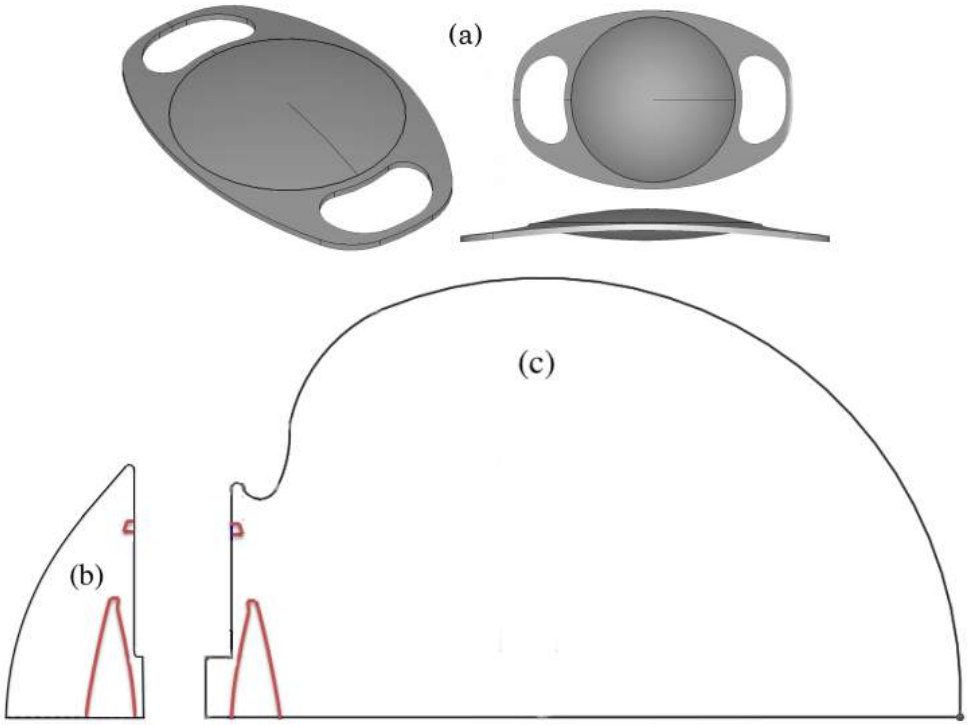

Figure 6.3: Artisan Aphakia Lens with top and side views (a), lens positioning in the anterior chamber (b) and vitreous chamber (c).

6.3 Boundary conditions and solver

On all suraface we impose the no slip condition with the exception of the boundaries marked in blue in Figure 6.4, where we impose the slip velocity, since the fluid is not in contact with a solid wall. Although the boundary conditions on the aIOL and chambers are identical, for the purpose of post processing of the forces of the aIOL, we keep them separate. For the simulations regarding saccadic eye rotations, we thus impose the following boundary conditions:

- **Slip surface.** We used a slip velocity boundary condition. This is corresponding with a zero normal component of the velocity and zero velocity gradient in the tangential direction.
- **All other surfaces.** On all other surfaces we impose the no slip condition, i.e. the boundary velocity associated to the saccadic motion discussed in chapter 4, subsection 4.5.1.3.

Similarly to what was done in chapter 4, the aqueous humor is modelled as a Newtonian incompressible fluid. The equations of motion (Navier-Stokes equations) are solved numerically using the *pimpleDyMFoam* solver in OpenFOAM (see chapter 3, section 3.2.1).

As for the cases discussed in chapter 4, we first performed mesh independence analysis. For the results presented in this chapter, a mesh of 2.5 million volumes has been used. Moreover, the time step was fixed to a value of 5×10^{-6} s, with the corresponding maximum Courant number of 10^{-2}. For all simulations, discretisation methods corresponding to

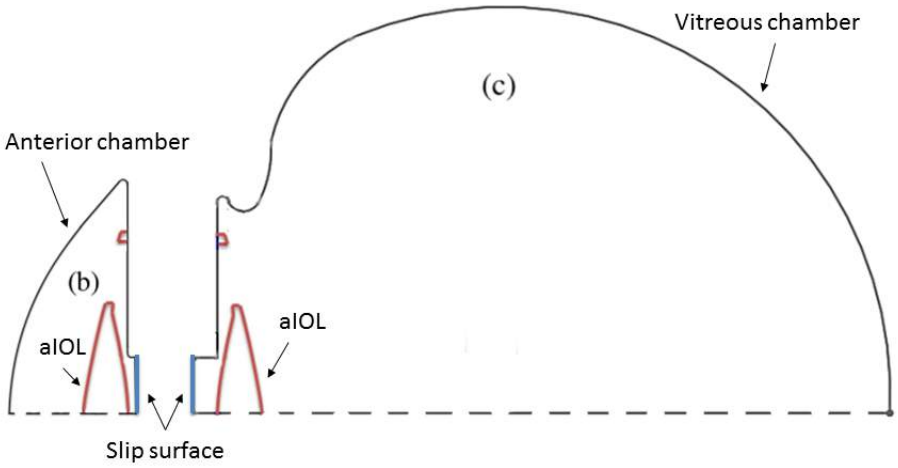

Figure 6.4: the surface names for (a) the anterior and (b) vitreous chamber: (red) for Artisan Aphakia aIOL, (blue) is the slip surface and (black) for all other surfaces. The dashed line represents the axisymmetric line.

second order accuracy in time and space have been considered. The simulations were performed using 16 processors and each solution was computed in approximately 6 days.

6.4 Force calculation procedure

The hydrodynamic forces (pressure and viscous forces) on the lens are computed using OpenFOAM force function object utility. The hydrodynamic force is computed as

$$\mathbf{F}_{\text{hydrodynamic}} = \iint_S \mathbf{t}\ dS, \tag{6.1}$$

where $\mathbf{t}$ is the stress vector and S the surface of the aIOL. The stress vector on a given surface with normal $\mathbf{n}$ is calculated using the stress tensor $\boldsymbol{\sigma}$ according to the following equation

$$\mathbf{t} = \boldsymbol{\sigma}\mathbf{n} = (-p\mathbf{I} + \mathbf{d})\mathbf{n}, \tag{6.2}$$

where p is the pressure, $\mathbf{I}$ is the identity tensor and $\mathbf{d}$ is the deviatoric part of the stress tensor. Substituting equation (6.2) in equation (6.1) we obtain

$$\mathbf{F} = \iint_S -p\ \mathbf{n}\ dS + \iint_S d\ \mathbf{n}\ dS. \tag{6.3}$$

In the above expression we denote the first integral as $\mathbf{F}_{\text{pressure}}$ and the second as $\mathbf{F}_{\text{viscous}}$. Since we wish to calculate the force exerted by the aIOL on the iris, we also need to account for the fictitious forces on the lens due to the acceleration of the domain. These forces are calculated analytically as follows

$$\mathbf{F}_{\text{fictitious}} = -m\boldsymbol{\Omega} \times (\boldsymbol{\Omega} \times \mathbf{r}) - m\frac{d\boldsymbol{\Omega}}{dt} \times \mathbf{r}, \tag{6.4}$$

where m is the mass of the lens, $\mathbf{r}$ is the distance of the centre of mass from the axis of rotation and $\boldsymbol{\Omega}$ is the angular velocity and $\frac{d\boldsymbol{\Omega}}{dt}$ is the angular acceleration of the domain.

6.5 Results

In this section we present the results obtained for the 10°, 20° and 30° saccadic rotations of the eye, in the presence of the Artisan Aphakia lens. We divide the section into two subsections: simulations in the anterior (a) and vitreous chambers (b). We later compare these two simulations with each other in section 6.6.

6.5.1 Simulations in the anterior chamber

6.5.1.1 Velocity and pressure fields

In this part we report the results obtained with the aIOL implanted in the anterior chamber. Figure 6.5 shows a cross-section of the domain; in the figure the region occupied by the aqueous humor is shown in dark grey and we also report the coordinate system adopted in the simulations. The axis of rotation is the z-axis (pointing up out of the page) and the saccadic rotation always has a counter clockwise direction.

The governing equations are solved with respect to a fixed reference frame, in terms of absolute velocity. However, results will be presented with respect to a coordinate system that follows the rotation of the domain. In other words, at all times, the y-axis passes through the axis of symmetry of the anterior chamber.

Figure 6.5: Cross section of the anterior chamber with aIOL and system of coordinates.

Here we will describe in detail the results of velocity and pressure distribution obtained in the case of a 10° saccadic rotation. The corresponding results, in terms of forces on the lens for 10°, 20° and 30° saccadic rotations are discussed in 6.5.1.2.

In figure 6.6 we show various snapshots of the pressure distribution in the anterior chamber, taken at different times. Notice that, as shown in figure 4.13 the angular velocity of the domain peaks at $0.0225s$ and the saccadic rotation has a duration of $0.05s$. At the initial times the pressure has a maximum on the right side of the domain, owing to the fact that the domain is subjected to an angular acceleration in the counter clockwise direction (thus accelerates from right to left). When the angular acceleration changes sign, the pressure gradient also reverses and the maximum of the pressure is localized on the left side of the domain (see figure 6.6 (c), corresponding to $t = 0.03s$).

The corresponding distribution of the velocity magnitude is shown in figure 6.7, again at different times. The figures show that a thin boundary layer forms at the wall, the thickness of which grows in time, owing to viscous diffusion of momentum. After the domain ceases to move ($t \geq 0.05s$) some fluid motion still occurs in the anterior chamber, due to fluid inertia. Much care has been taken to properly resolve with the numerical discretisation of the thin boundary layer at the wall. This is important since the motion within the boundary layer at the aIOL surface affects the shear stress exerted on the surface of the lens.

6.5.1.2 Forces on the aIOL

In this part we consider the force acting on the aIOL. In particular the total hydrodynamic force $\mathbf{F}_{\text{hydrodynamic}}$ can be written as the sum of two components, the contribution due to pressure ($\mathbf{F}_{\text{pressure}}$) and the viscous contribution ($\mathbf{F}_{\text{viscous}}$), so that $\mathbf{F}_{\text{hydrodynamic}} = \mathbf{F}_{\text{pressure}} + \mathbf{F}_{\text{viscous}}$. Moreover, we define $\mathbf{F}_{\text{total}}$ as the sum of the hydrodynamic forces and the fictitious forces acting of the lens as a consequence of the acceleration of the domain (see section 6.4). Thus, $\mathbf{F}_{\text{total}}$ effectively represents the force that the lens transmits to the iris, which is the main observable of the present work.

In figure 6.8 we report the force on the aIOL versus time for the saccades of 10°, 20° and 30°. In figure 6.8(a,b) we plot the x and y-components of $\mathbf{F}_{\text{pressure}}$, in (c,d) the x and y-components of $\mathbf{F}_{\text{viscous}}$ and, finally, in (e,f) the x and y-components of the total force $\mathbf{F}_{\text{total}}$. The results show that the force due to the pressure distribution on the aIOL is larger than the viscous one for all saccades. However, the fictitious force acting on the aIOL is almost opposite to the force induced by the pressure distribution (see figure 6.9), so that the sum of the two turns out to be comparable to the viscous force. The x-component of the pressure and the viscous forces is significantly larger than the y-

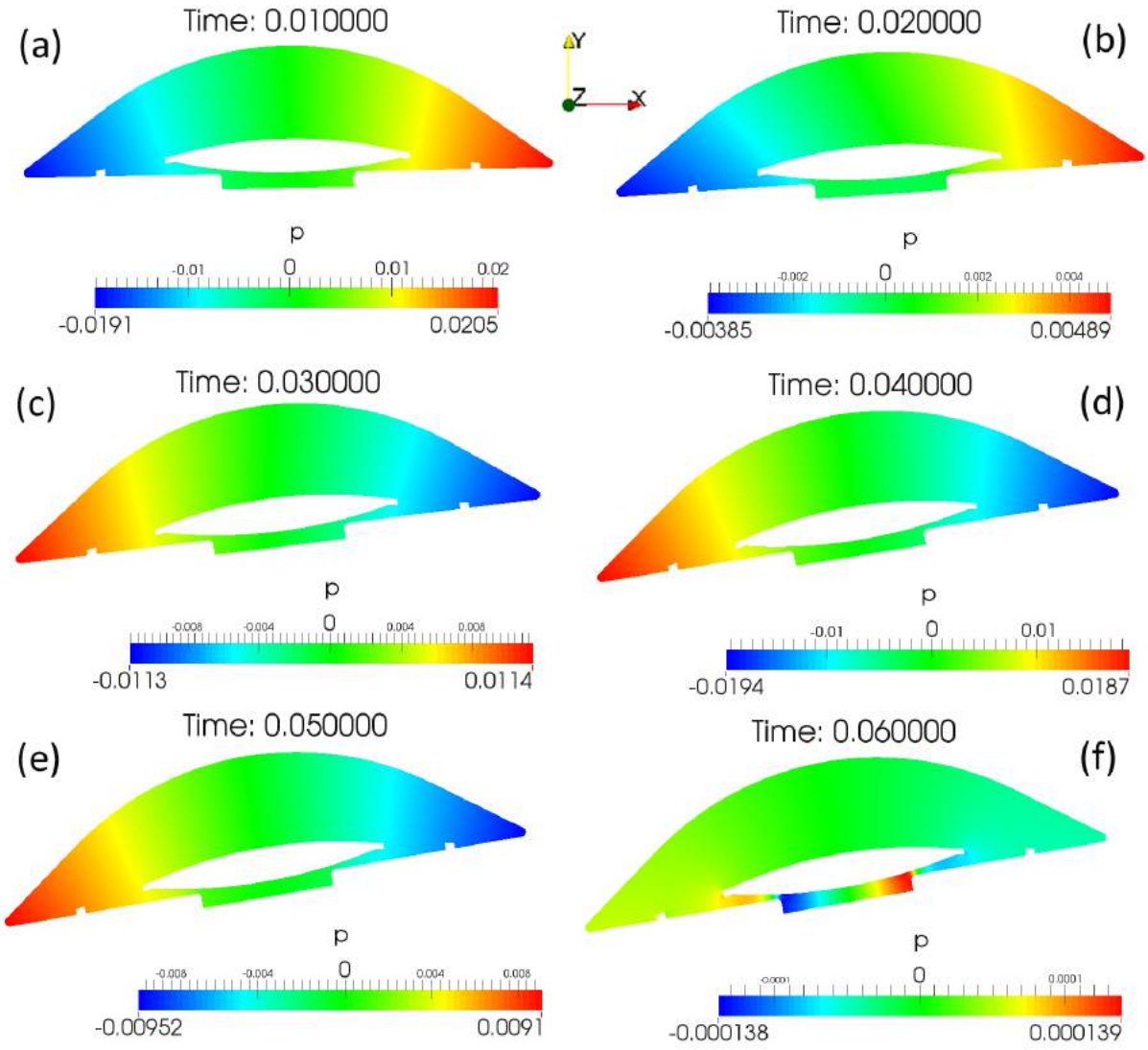

Figure 6.6: Maps of the pressure distribution in the anterior chamber at different times. Saccade with an amplitude of 10°.

component for all saccades (by more than an order on magnitude). Correspondingly, also the x-component of $\mathbf{F}_{\text{total}}$ is larger than its y-component for all saccades.

We also observe that the maximum and the minimum value of the x-components of forces decreases and increases from the saccades of 10° to 30°, respectively. This is completely vice versa for the y-components of pressure and viscous forces that is the the minimum decreases from the saccades of 10° to 20°. However considering the contribution of the y-components of fictitious forces, the maximum value of the y components of total force decreases from the saccades of 10° to 30°.

In agreement with the pressure distribution shown in figure 6.6, $F_{\text{pressure } x}$ for the saccade of 10°, changes sign in time, being negative during the initial phase of motion (force from right to left) and positive when the angular acceleration changes sign. The y-component of the viscous stress ($F_{\text{viscous } y}$) has a qualitatively similar behaviour. This can be also observe for the other amplitudes. As can be seen in figure 6.8(a,b) the sign

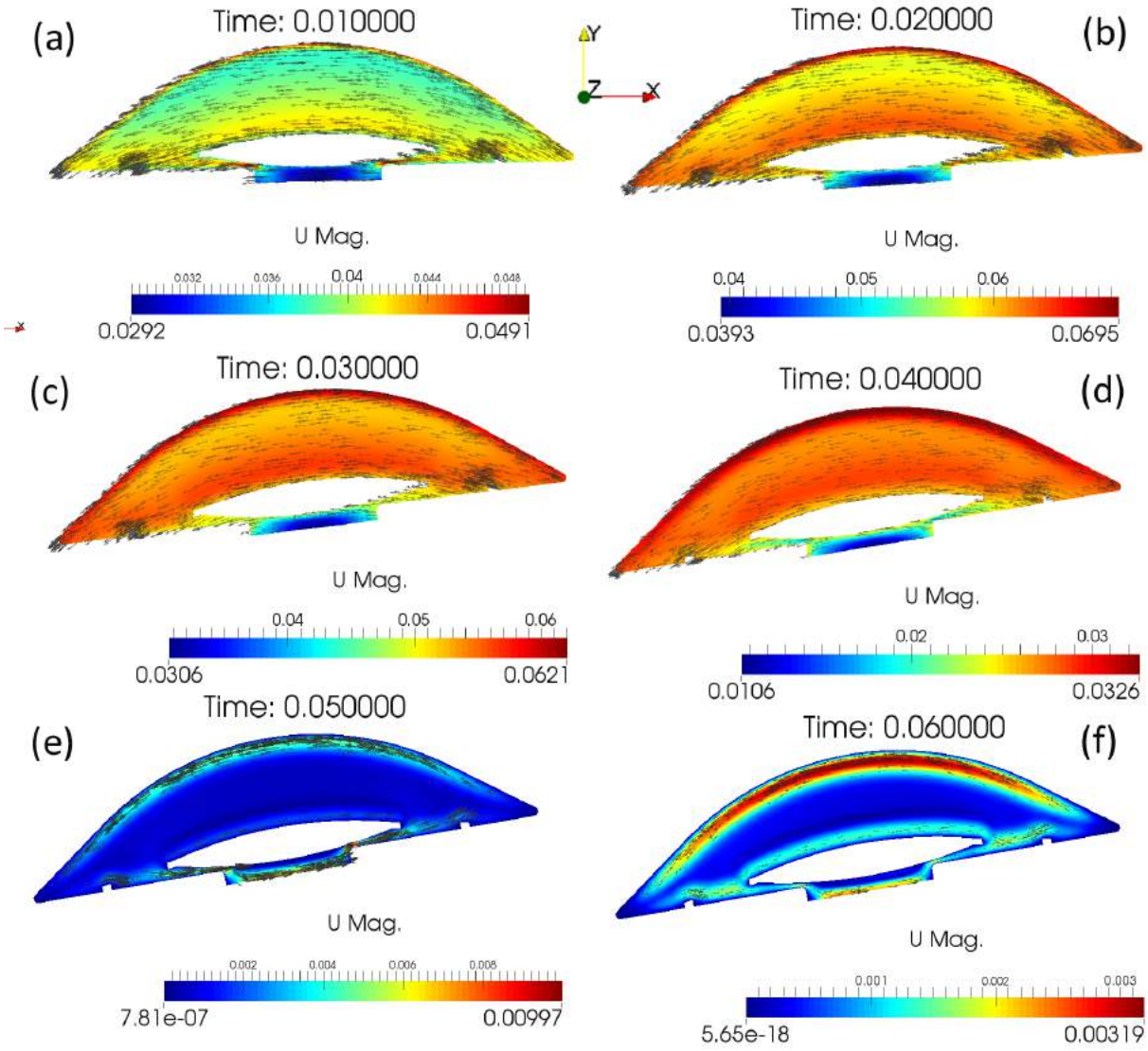

Figure 6.7: Maps of the velocity magnitude and velocity vectors in the anterior chamber at different times. Saccade with an amplitude of 10°.

of $F_{\text{pressure } x}$ will change at $t = 0.03s$ for saccades 20°, which is in agreement with the experiments of Repetto et al. [118]. As the amplitude of the saccadic rotation increases, the components of the forces are also stretched in time which is due to the increase in the duration of saccades from 10° to 30°.

6.5.2 Simulations in the vitreous chamber

6.5.2.1 Velocity and pressure fields

We now discuss the results obtained for the case when the aIOL is implanted on the posterior surface of the iris. We recall that, in this case we assume that the natural lens and capsule have been removed and vitrectomy has been performed. Thus, the lens is effectively placed in the vitreous chamber. A cross-section of the domain is shown in figure 6.10 along with the adopted coordinate system. As for the case described in

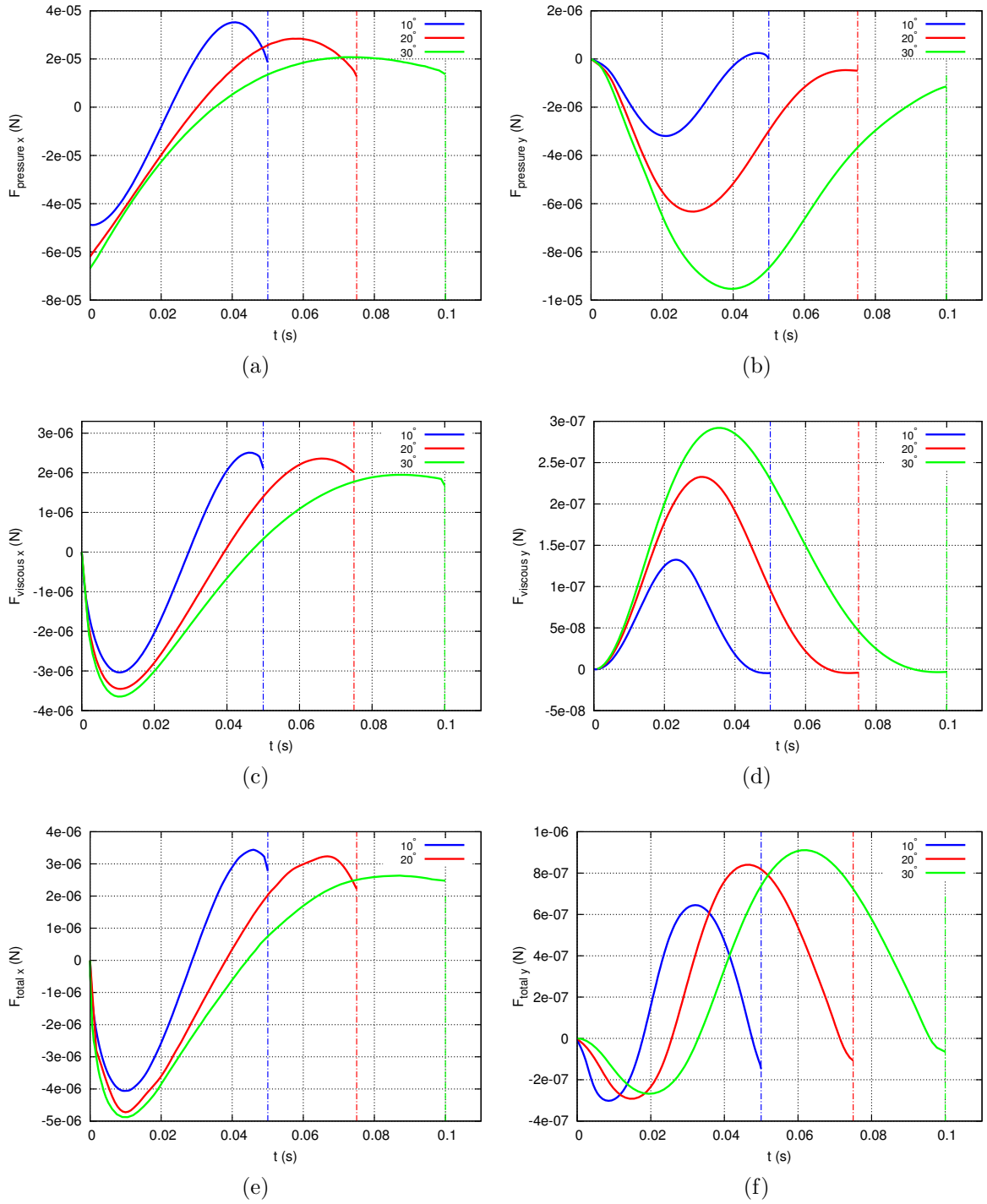

Figure 6.8: The aIOL is placed on the anterior surface of the iris. Force on the aIOL versus time. (a) x-component of the force due to pressure; (b) y-component of the force due to pressure; (c) x-component of the viscous force; (d) y-component of the viscous force; (e) x-component of the total force (including fictitious forces acting on the aIOL); (f) y-component of the total force (including fictitious forces acting on the aIOL). Saccade with an amplitude of 10°, 20° and 30°.

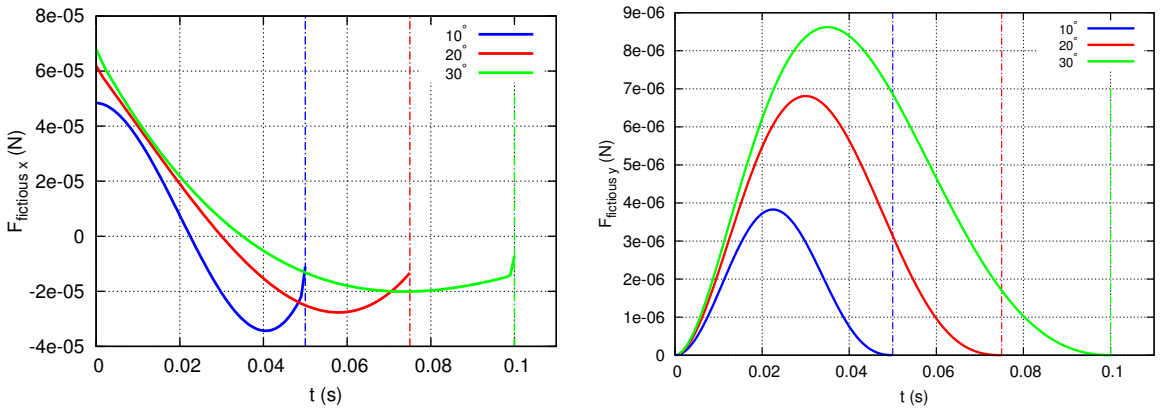

(a) (b)

Figure 6.9: The aIOL is placed on the anterior surface of the iris. The fictitious force on the aIOL versus time for the saccades of 10°, 20° and 30°. (a) x-component of the fictitious forces and (b) y-component of the fictitious forces.

6.5.1.1, the domain rotates about the z-axis in the counter clockwise direction and the y-axis coincides with the antero-posterior symmetry axis of the domain. Moreover, the system of coordinates rotates with the domain.

We note that in the present case the domain is very different with respect to that considered in section 6.5.1: the vitreous chamber can be thought of as a deformed sphere, whereas the anterior chamber is a thin domain. As a consequence, the characteristics of the flow field are expected to be very different.

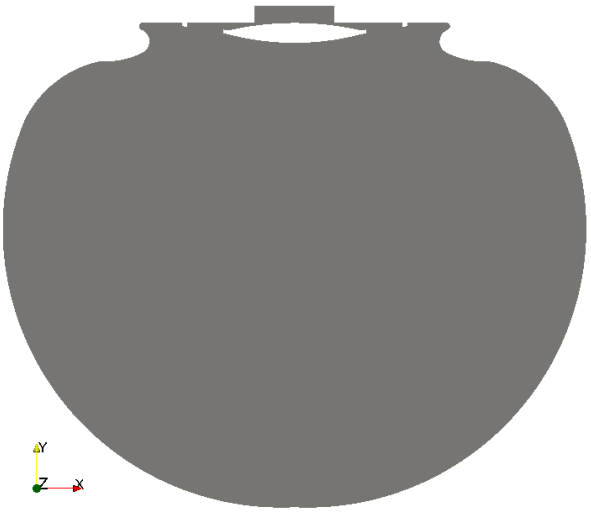

Figure 6.10: Cross section of the vitreous chamber with aIOL and system of coordinates.

Similar to what we did in section 6.5.1 we describe here the velocity and pressure distribution results obtained with a saccadic rotation of 10° and in subsection 6.5.2.2 we report the results, in terms of forces on the aIOL, relative to rotations with an amplitude of 10°, 20° and 30°.

In figure 6.11 we report various snapshots of the pressure distribution taken at different times during the saccadic eye rotation of 10°. As a consequence of the "quasi spherical" shape of the domain the pressure is almost zero in the core of the domain and attains relatively large values only in the region close to the wall, where the wall velocity has a significant component in the direction normal to the wall; specifically in the anterior part of the domain. The sign of the pressure is essentially dictated by the sign of the angular acceleration. As a consequence of fluid motion, relatively large pressures occur in the narrow region between the aIOL and the iris, even when the domain has come to rest (see for instance the snapshot at $t = 0.06$).

Figure 6.12 show the distribution of the velocity magnitude at different times. It clearly appears that in this case the motion remains confined into a narrow boundary layer at the wall, the velocity out of this thin layer being very small at all times. In fact the thickness δ of the boundary layer at the wall generated during a rotation of duration D is expected to be of order $\sqrt{\nu D}$, with ν being fluid kinematic viscosity [67]. Assuming that the vitreous chamber is filled with aqueous that approximately has the same viscosity as water ($\nu = 7.5 \times 10^{-7}$ m/s^2) and for $D = 0.05s$ one finds $\delta \approx 1.93 \times 10^{-4}$ m, which is consistent with our findings. Much care has been taken to properly resolve the boundary layer at the wall in the numerical discretisation.

A closer inspection of the flow field in the anterior region of the domain shows more complexity (see figure 6.13). A circulation is generated close to the lens, along with further circulations in the vicinity of the ciliary body. The generation of the large circulation behind the aIOL is consistent with the experimental observations of Stocchino et al. [129] and with the theoretical predictions of Repetto et al. [117]. Indeed, the authors also observed the existence of a circulation in the vitreous chamber, induced by the change of curvature of the domain produced the natural lens.

6.5.2.2 Forces on the lens

In this section we report results analogous to those shown in section 6.5.1.2, i.e. the time evolution of the pressure, viscous and total force on the aIOL versus time (both x and y-components) for the sacades of 10°, 20° and 30°. In this case the x and y components of pressure force are comparable in magnitude and also have a similar trend in time for all sacades (see figure 6.14 (a,b)). However, for all saccades, the y component of viscous force is significantly smaller that the y component. Similarly to what we observed in section 6.5.1, also in this case the x-component of all forces is larger than the corresponding y-component.

Similar to the anterior case, the contribution of fictitious forces, shown in figure 6.15, has also been considered in the calculation of total force (see figure 6.14 (e,f)).

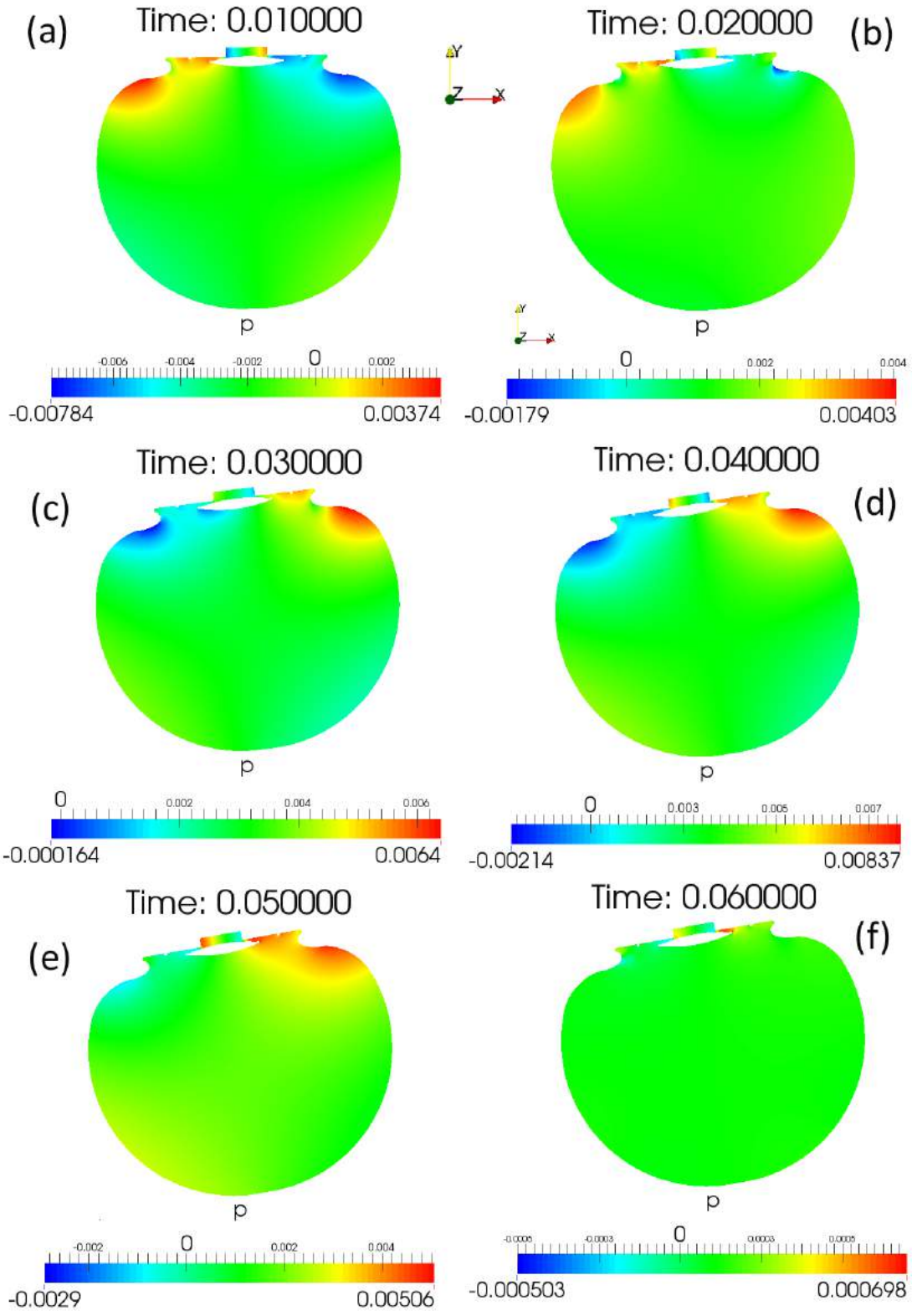

Figure 6.11: Maps of the pressure distribution in the anterior chamber at different times. Saccade with an amplitude of 10°.

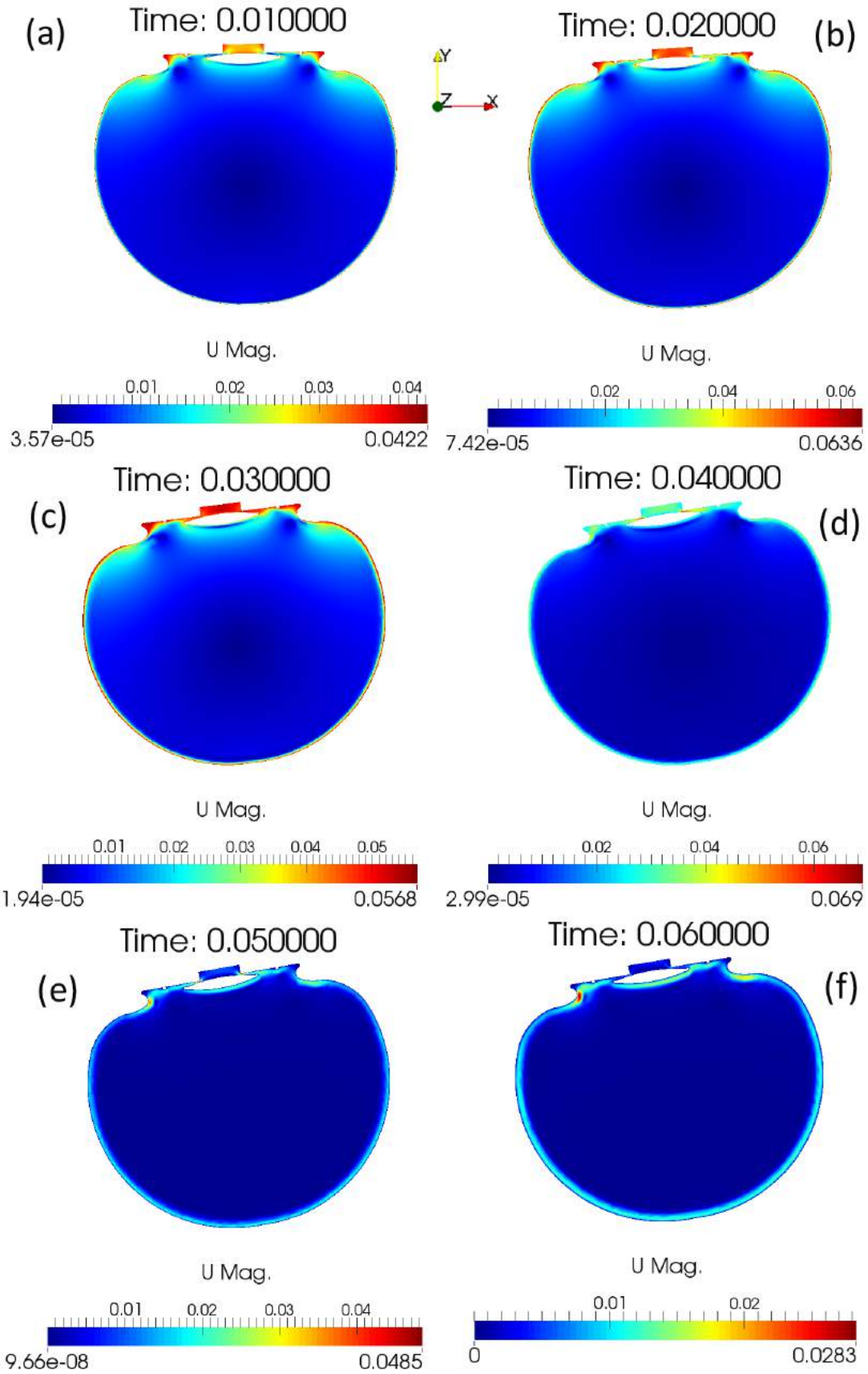

Figure 6.12: Maps of the velocity magnitude and velocity vectors in the anterior chamber at different times. Saccade with an amplitude of 10°.

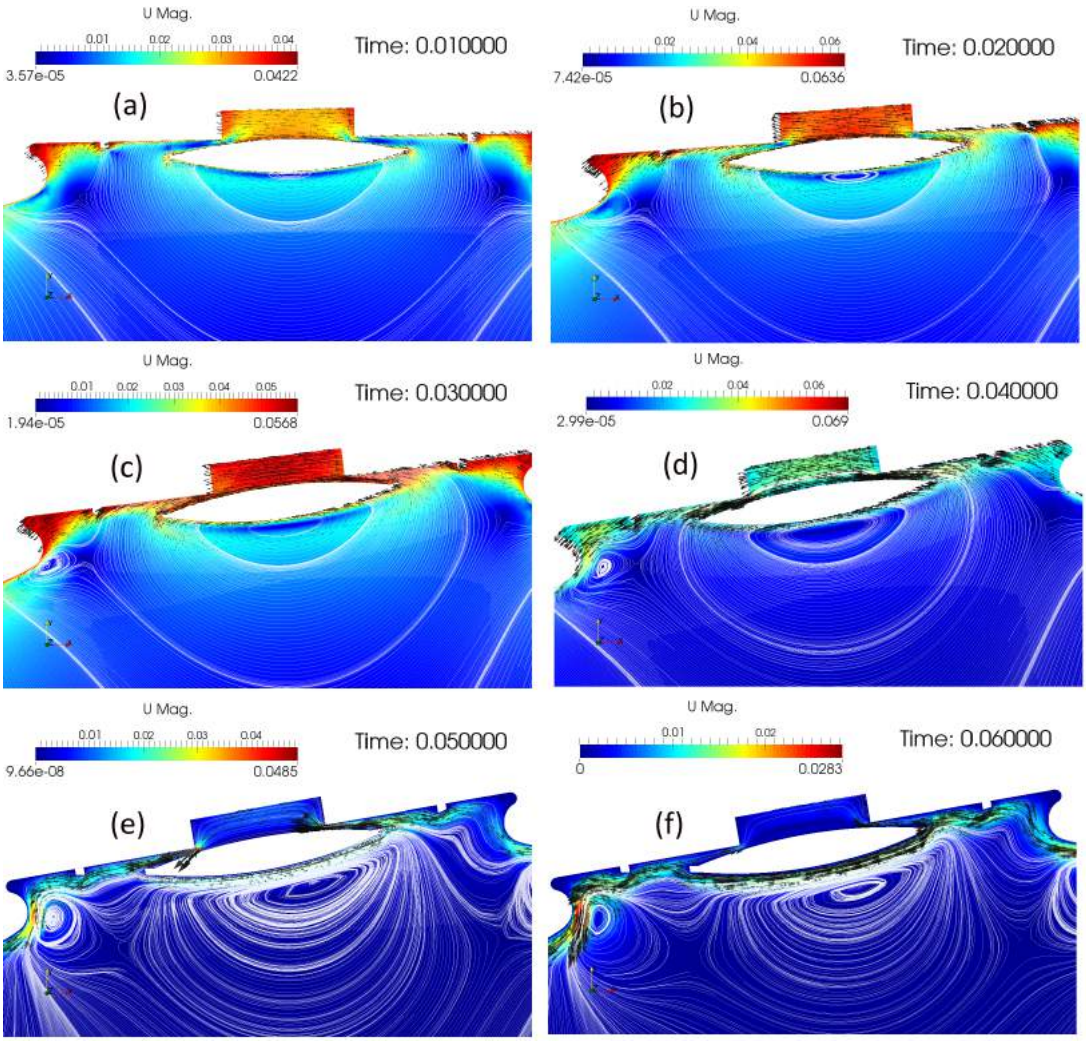

Figure 6.13: Maps of the velocity magnitude and velocity vectors in the anterior chamber at different times. Saccade with an amplitude of 10°.

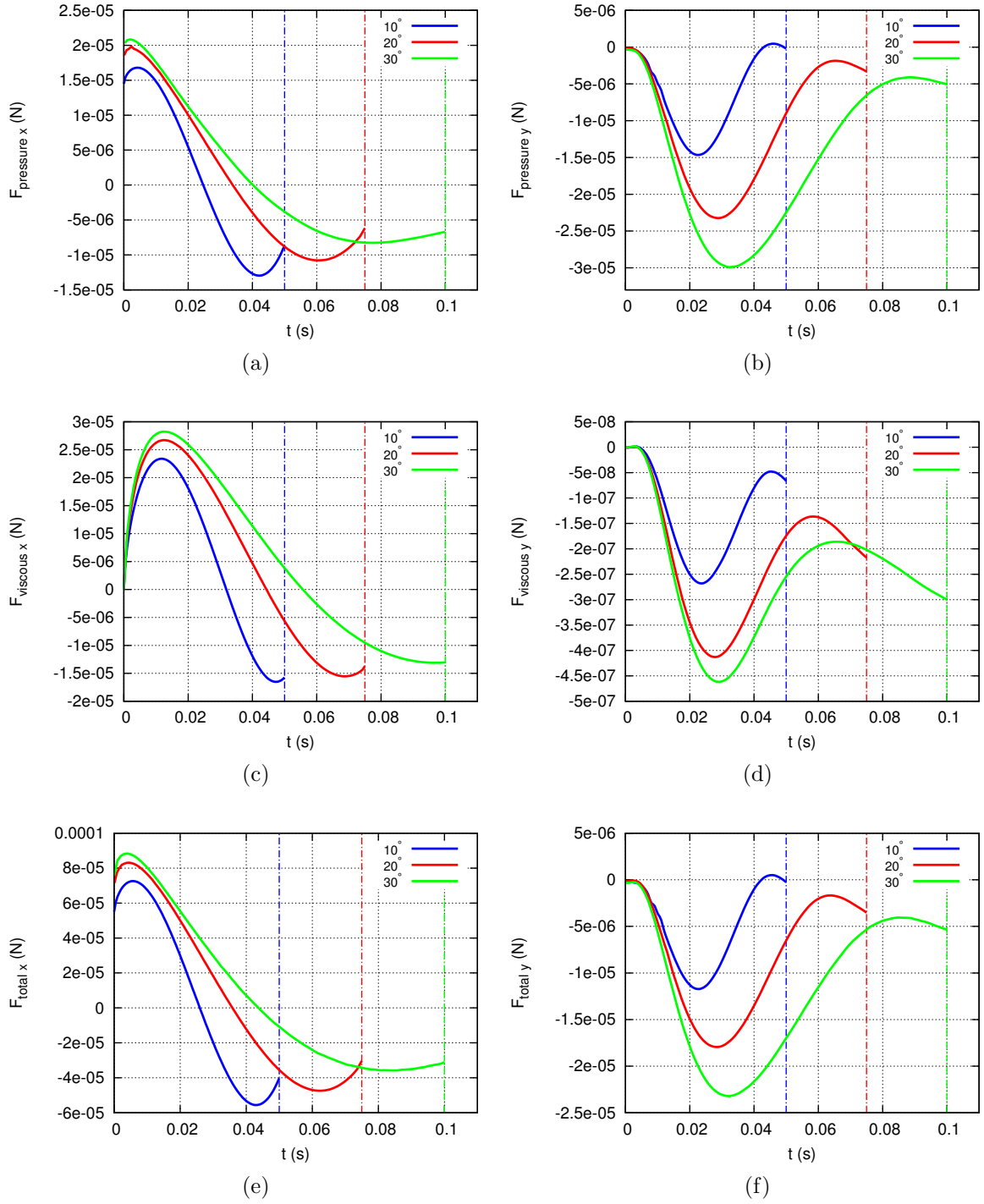

Figure 6.14: The aIOL is placed on the posterior surface of the iris. Force on the aIOL versus time. (a) x-component of the force due to pressure; (b) y-component of the force due to pressure; (c) x-component of the viscous force; (d) y-component of the viscous force; (e) x-component of the total force (including fictitious forces acting on the aIOL); (f) y-component of the total force (including fictitious forces acting on the aIOL). Saccade with an amplitude of 10°, 20° and 30°.

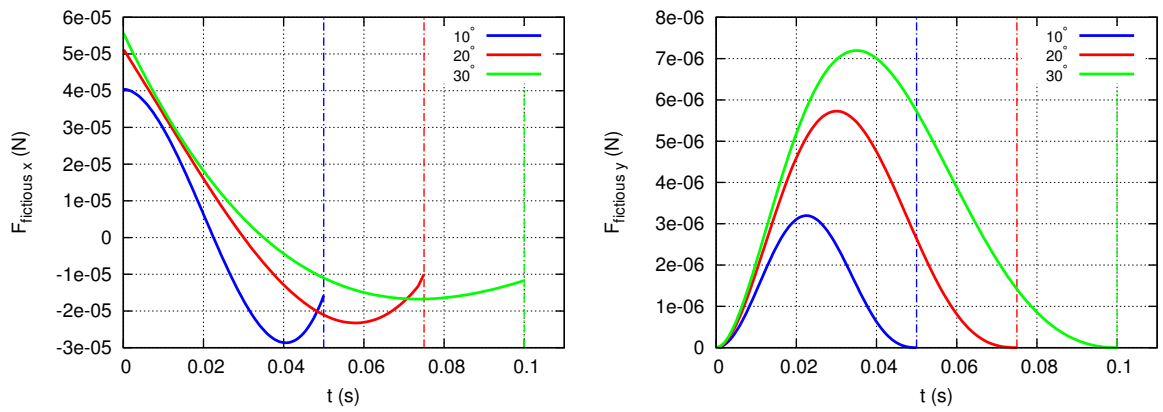

(a) (b)

Figure 6.15: The aIOL is placed on the posterior surface of the iris. Fictitious forces on the aIOL versus time. (a) x-component of the fictitious forces and (b) y-component of the fictitious forces. Saccade with an amplitude of 10°, 20° and 30°.

6.6 Comparison between the anterior and posterior placement of the aIOL

In section 6.5.1 and 6.5.2 we studied the flow characteristics and forces on the aIOL that are generated during eye rotations, when the lens is mounted on the anterior and posterior surface of the iris, respectively. We now compare the forces exerted on the lens in the two cases. Specifically, we compare the values attained by total force $\mathbf{F}_{\text{total}}$, which is the force transmitted by the aIOL to the iris (it includes both the hydrodynamic and fictitious forces on the lens). This is an important physical quantity since it is likely associated with the risk of lens dislocation/luxation (the two terms will be used interchangeably in the following).

We note that the force in the x-direction can always contribute to lens dislocation, whereas the force in the y-direction (i.e. in the direction approximately orthogonal to the surface of the iris) can do so only if it tends to pull the aIOL away from the iris. This means that, as far as lens dislocation is concerned, we only need to consider positive values of $F_{\text{total } y}$ when the lens is placed in the anterior chamber and negative values when it is placed behind the iris.

In figure 6.16 we plot the time evolution of the x and y-components of $\mathbf{F}_{\text{total}}$ ($F_{\text{total } x}$ left and $F_{\text{total } y}$) for the two cases. The three rows correspond to the three different amplitudes that have been investigated (10°, 20° and 30°). Inspection of the figure clearly shows that both $F_{\text{total } x}$ and $F_{\text{total } y}$ attain significantly larger values when the aIOL is implanted posteriorly to the iris. In fact the maximum force is invariably at least an order of magnitude larger, when the lens sits on the posterior surface of the iris.

In figure 6.17 we show how the maximum detaching force (in the x and y-directions) depends on the saccade amplitude. As one might expect, the force grows with the saccade amplitude, the dependency being, however, quite small. This is somehow consistent with the experimental findings of Repetto et al. [118]. The authors showed that the shear stress on the retina only slightly grows with the amplitude of saccades and postulated that small amplitude eye rotations, being much more frequent, could actually be responsible to the possible occurrence of retinal damages.

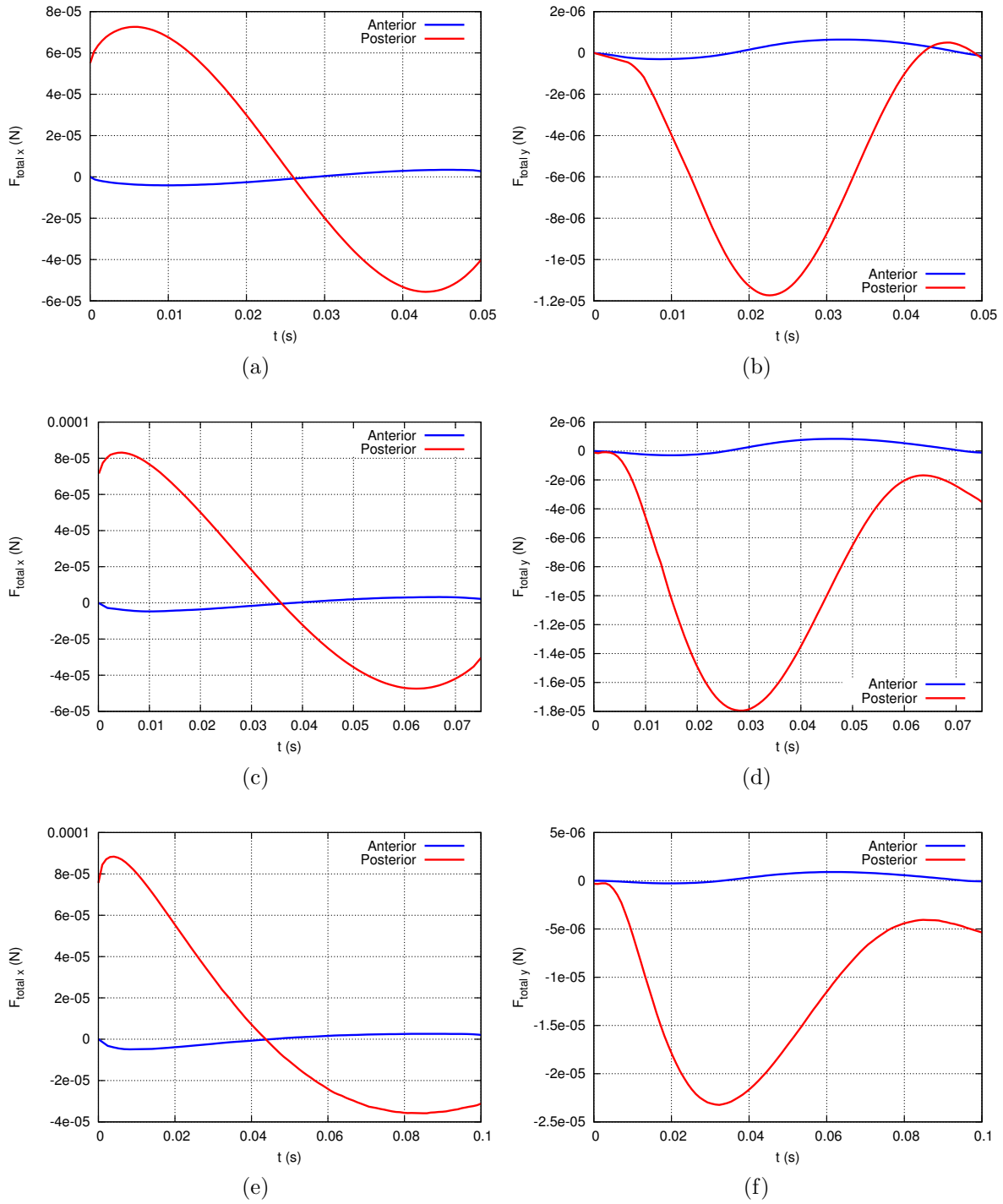

Figure 6.16: Total force on the aIOL versus time. (a) rotation of 10°, x-component of the force; (b) rotation of 10°, y-component of the force; (c) rotation of 20°, x-component of the force; (d) rotation of 20°, y-component of the force; (e) rotation of 30°, x-component of the force; (f) rotation of 30°, y-component of the force.

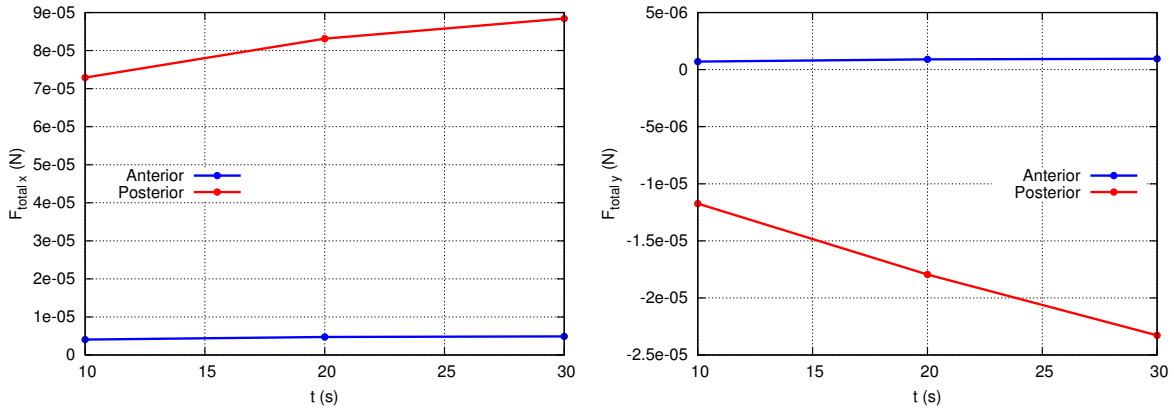

Figure 6.17: Maximum force in the x (a) and y (b) directions as a function of the saccade amplitude. For the x component of the force we consider the maximum of the absolute value of $F_{\text{total } x}$, for the y direction we consider the maximum positive value for the blue line and the maximum negative value for the red line.

6.7 Summary of the simulations

In this work we considered the mechanical hydrodynamic forces exerted on the Artisan Aphakia lens +30.0 D (aIOL). Specifically we compared two cases of the lens either implanted on the anterior or the posterior surface of the iris. Both surgeries are possible and normally employed. To our knowledge, no studies exist comparing the outcomes of the two procedures, specifically as far as the risk of lens dislocation is concerned. However, from a purely mechanical point of view, it is reasonable to expect hydrodynamic forces on the aIOL that are potentially very different in the two cases.

Among all possible mechanisms that can generate aqueous flow in the eye we only considered eye rotations and, specifically, saccades since in chapter 4, we showed that eye rotations generate velocities (and consequently forces on the lens) larger than any other mechanism. The aim of this chapter was to investigate, from the mechanical point of view, whether one of the implantation options is preferable with respect to the other.

We considered separately the following two different cases.

- *aIOL implanted on the anterior surface of the iris*

  In this case the computational domain is the anterior chamber of the eye. We slightly modified the shape of the anterior chamber with respect to that used in chapter 4, since, owing to the removal of the natural lens the iris displaces backwards and the anterior chamber becomes a bit thicker.

- *aIOL implanted on the posterior surface of the iris*

  In this case we consider that the lens and capsule have been completely removed and vitrectomy performed. Thus, the domain of calculation is delimited anteriorly by the iris and posteriorly by the retinal surface and it essentially coincides with the vitreous chamber of the eye.

In both cases we assumed that the fluid has the properties of aqueous humor used also in chapter 4.

We performed numerical simulations of the flow induced by 10°, 20° and 30° saccadic rotation of the anterior and vitreous chamber with the presence of an aIOL. Using OpenFOAM we solved the problem of fluid motion numerically and computed the hydrodynamic forces acting on the aIOL and the force that the aIOL transmits on the iris.

6.8 Summary of the results

In section 6.5 we studied the the hydrodynamic and fictitious forces on the Artisan aphakia lens, implanted on the anterior and posterior side of the iris separately. For all saccades, we observed that the x-component of all hydrodynamic (pressure and viscous) and fictitious forces is significantly larger than the corresponding y-component. The sum of all these forces provides us with the total force transmitted by the aIOL to the iris. This force is an important quantity since it is likely associated with the risk of lens dislocation/luxation. We observed that as we increase the amplitude of saccades from 10° to 30°, the maximum value of the total force on the lens increases too.

6.9 Conclusions

Our results show that, when the aIOL is mounted on the posterior surface of the iris, it transmits forces on it that are much larger than when the aIOL is implanted in the anterior chamber.

In order to understand whether the computed forces are potentially of clinical interest it is quite natural to compare them with the submerged weight W of the aIOL, which is the force the aIOL transmits to the iris in static conditions. This force is not zero, since the lens is not neutrally buoyant and its magnitude can be computed as follows

$$W = g(m_{\text{aIOL}} - \rho V_{\text{aIOL}}), \tag{6.5}$$

where g is the acceleration of gravity, m_{aIOL} the mass of the aIOL (12×10^{-6} kg, information from Ophtec BV), ρ aqueous density and V_{aIOL} the aIOL volume ($V_{\text{aIOL}} \approx 1.0378 \times 10^{-8}$ m^3). With the above numbers we obtain $W = 1.59 \times 10^{-5}$ N.

Comparing the above value with the forces reported in figure 6.17 it appears that W is significantly larger than the forces the aIOL is subjected to, when it is placed in the anterior chamber (blue curve in the figure). On the other hand, when the lens is implanted on the posterior surface of the iris, the dynamic forces generated on the iris during eye rotations are significantly larger than the lens weight W (red curves in the figure). This means that eye rotations certainly have a significant role in the possible dislocation of the lens.

Summarising the results of this chapter, we may say that our simulations suggest that implantation of the aIOL on the posterior surface of the iris is potentially associated with a higher risk of lens dislocation. It would be extremely interesting to verify whether these theoretical predictions are supported by clinical observations. We note that several authors have observed relatively high rates of dilsocation/luxation in the case of posterior iris-claw aIOL implantation (e.g. 8.7% in Gonnermann et al.[52]; 10% in Rufer et al. [123]; 13% in Gonnermann et al. [53]).

Chapter 7

Validation of the implantation of direction-splitting method with immersed boundary treatment

7.1 Introduction

In this chapter we introduce a direction splitting method with an immersed boundary treatment (IBM) which is very useful method for many CFD applications and can deal with many of the traditional numerical methods difficulties for solving the Navier–Stokes equations. Here we summarize some of the benefits of this method.

- Due to the discretization methods used in this approach, the method is second order accurate in time and space.
- Due to the design of the direction splitting solver, the numerical method is much faster that the traditional projection methods, since the resulting solver is one–dimensional, non iterative and linear.
- The complexity of the direction splitting solver for parallelization is less that the traditional methods.
- The simulation will be ran over a fixed Cartesian mesh (Eulerian points). Due to the IBM method, used in this approach, geometries are treated as the Lagrangian variables, defined on a curvilinear mesh that moves freely through the fixed Cartesian mesh without being constrained to adapt to it. This will decrease the computational time for moving or deformable geometries.

In this chapter we discuss about the in–house code, developed for solving the Navier–Stokes equations using a direction splitting method with an IBM. The chapter is organized as follow. In section 7.2 we discuss about the motivation of our code development. In section 7.3 we describe the mathematical equations and the numerical approach of this method. In section 7.4 we introduce series of benchmark cases and we compare the result of our code with OpenFOAM and other numerical works. Since our code is written in serial mode, we also run the OpenFOAM simulations with one processors to compare the computational performance of our code. Finally in section 7.6 we discuss about the conclusions of this work.

7.2 Motivation

As we discussed in the previous section, the method that we describe in this chapter is very useful for many CFD applications. This method can also be usefully employed to study flows in the human eye and in the following we provide examples of the possible applications that motivated the work. In this section we discuss about the applications that this method can be used in the mathematical modeling of flow in the eye. We summarized some of these applications as follow

- As discussed in chapter 4, simulations regarding saccadic rotations are in general computationally expensive. As an example, for the simulations of chapter 4, subsection 4.5.1.3, we used 15 processors and the each simulation lasted over a week with a maximum Courant number of 0.01. The simulations of saccadic rotations are sensitive to mesh design particularly near to the walls and for the present simulations we used meshes consisting of almost 2 million elements. Using this method, we can decrease the computational time with even higher number of elements over lower number of processors, as we show in section 7.4. In general eye movement simulations are very time consuming and by introducing this method, these simulations can be performed with a lower computational time.

- As discussed in chapter 4, section 4.5.2.2, we simplified miosis by considering a time–dependent velocity profile at the inlet surface of the anterior chamber and keeping the shape of the domain fixed. In reality miosis should be modeled considering iris motion. As mentioned in previous section, deformation of the geometry leads to mesh deformation and leads to very time consuming and complicated simulations. However, with the method that we describe in this chapter, the deformation of geometry will not affect the fixed–Cartesian mesh, leading to lower computational time. There are many interesting topics in the eye that needs the deformation of a structure in the eye. As an example, one interesting topic could be modeling of saccadic rotation in the eye with retinal tear. This will help researcher to know how the retinal tear will be developed to form a complete detached retina. Another topic could be the deformation of iridotomy hole. This could give indication to surgeons for the size of the hole to not create any aqueous jet toward endothelium cells on the cornea.

- Using the IBM method that will discuss in subsection 7.3.1, we are able to calculate the forces on the surfaces in the domain of interest. One application of this could be the analysis of forces mentioned in chapter 6.

We note that in the course of the present PhD work, we did not get to apply the method to the above applications. In this chapter we discuss the application of the numerical model to benchmark cases to validate it.

7.3 Numerical tools and modeling

7.3.1 Direction Splitting Algorithm with Immersed Boundary Treatment

The pressure correction in traditional pressure-correction algorithms for large size problems and large Reynolds numbers is very costly. Furthermore the parallelization of the Poisson equation that appears in these algorithms is complex on very large numbers of computer processors. In the following we introduce a direction splitting method for solving incompressible Navier–Stokes equations to deal with these complexities [56].

If we consider the time-dependent incompressible Navier–Stokes equations (3.2a) and (3.2b) in the non-dimensional form in the dimensionless box, $\Omega = [0, L_x]\times[0, L_y]\times[0, L_z] \subset \mathbb{R}^3$, we obtain:

$$\begin{cases} \frac{\partial \mathbf{u}}{\partial t} + (\mathbf{u}\cdot\nabla)\mathbf{u} + \nabla p - \frac{1}{Re}\nabla^2\mathbf{u} - \mathbf{f} = \mathbf{0} & in\ \Omega\times[0,T], \\ \nabla\cdot\mathbf{u} = 0 & in\ \Omega\times[0,T], \\ \mathbf{u}|_{\partial\Omega} = \mathbf{a} & in\ \partial\Omega\times[0,T], \\ \mathbf{u}|_{t=t_0} = \mathbf{u}_0 & in\ \Omega, \end{cases} \tag{7.1}$$

where $\mathbf{a}$ is the boundary data, and $\mathbf{u_0}$ is the initial condition and Re is the Reynolds number.

It is well known that most of the incremental pressure-correction algorithms, (see e.g. [110]), are semi-discrete versions of the following singular perturbation of the linearized version of equations in (7.1)

$$\begin{cases} \frac{\partial \mathbf{u}_\epsilon}{\partial t} + \nabla p_\epsilon - \frac{1}{Re}\nabla^2\mathbf{u}_\epsilon - \mathbf{f} = \mathbf{0} & in\ \Omega\times[0,T],\ \ \mathbf{u}_\epsilon|_{\partial\Omega\times(0,T]} = \mathbf{a},\ \mathbf{u}_\epsilon|_{t=t_0} = \mathbf{0}, \\ -\Delta t\Delta\phi_\epsilon + \nabla\cdot\mathbf{u}_\epsilon = 0 & in\ \Omega\times[0,T],\ \ \frac{\partial\phi_\epsilon}{\partial n}|_{\partial\Omega\times(0,T]} = 0, \\ \Delta t\frac{\partial p_\epsilon}{\partial t} = \phi_\epsilon - \frac{\chi}{Re}\nabla\cdot\mathbf{u}_\epsilon, & p_\epsilon|_{t=t_0} = p_0, \end{cases} \tag{7.2}$$

where $p_0 = p|_{t=t_0}$, $\chi \in (0, 1]$ is an adjustable parameter and $\Delta t = \epsilon$ is the perturbation parameter. The convergence properties of the system of equations (7.2) have been analyzed by Guermond et al. [57, 55] and it has been shown that $\mathbf{u}_\epsilon$ is a $\mathcal{O}(\Delta t^2)$ perturbation of $\mathbf{u}$ in the L^2-norm and a $\mathcal{O}(\Delta t^{\frac{3}{2}})$ in the H^1-norm for all $\chi \in (0, 1]$. In the traditional pressure-correction algorithms, the main idea is to uncouple the velocity and pressure in the Navier–Stokes equation which is done by solving the system of equations (7.2).

The system of equations (7.2) can be generalized for direction splitting by considering the following alternative

$$\begin{cases} \frac{\partial \mathbf{u}_\epsilon}{\partial t} + \nabla p_\epsilon - \frac{1}{Re}\nabla^2\mathbf{u}_\epsilon - \mathbf{f} = \mathbf{0} & in\ \Omega\times[0,T],\ \ \mathbf{u}_\epsilon|_{\partial\Omega\times(0,T]} = \mathbf{a},\ \mathbf{u}_\epsilon|_{t=t_0} = \mathbf{0}, \\ \Delta t\mathbf{A}\phi_\epsilon + \nabla\cdot\mathbf{u}_\epsilon = \mathbf{0} & in\ \Omega\times[0,T],\ \ \phi_\epsilon \in D(\mathbf{A}), \\ \Delta t\frac{\partial p_\epsilon}{\partial t} = \phi_\epsilon - \frac{\chi}{Re}\nabla\cdot\mathbf{u}_\epsilon & p_\epsilon|_{t=t_0} = p_0, \end{cases} \tag{7.3}$$

where the operator A and its domain $D(A)$ are such that the bilinear form $a(p, q) = \int_\Omega q\ A\ p\ dx$ is symmetric and satisfies the following condition:

$$\|\nabla q\|^2_{\mathbf{L^2}} \leq a(q,q) \quad \forall q \in D(A), \tag{7.4}$$

Guermond et al.[57],[55] has shown that this new singular perturbation has similar approximation properties as (7.2) provided that the limit solution is smooth enough. For the direction splitting algorithm, in the work of Guermond et al. [55], $A := (1-\partial_{xx})(1-\partial_{yy})(1-\partial_{zz})$ has been used which under appropriate boundary conditions satisfies the symmetric and (7.4) conditions. The momentum equation is solved by means of the second-order accurate direction splitting of Douglas [31] and using this operator, the pressure correction is computed.

The algorithm is as follows

- **Pressure predictor**: the initialization is done by considering $p^{-\frac{1}{2}} = p_0$ and $\phi^{-\frac{1}{2}} = 0$. The pressure predictor is calculated as:

$$p^{*,n+\frac{1}{2}} = p^{n-\frac{1}{2}} + \phi^{n-\frac{1}{2}} \quad \forall n \geq 0. \tag{7.5}$$

- **Velocity update**: the initialization of velocity field is done by considering $\mathbf{u}^0 = \mathbf{u}_0$. $\forall n \geq 0$ the velocity update is computed by solving the following series of one-dimensional problems

$$\begin{cases} \frac{\boldsymbol{\xi}^{n+1}-\mathbf{u}^n}{\Delta t} - \frac{1}{Re}\Delta\mathbf{u}^n + \nabla\, p^{*,n+\frac{1}{2}} + \frac{3}{2}(\mathbf{u}^n\cdot\nabla)\mathbf{u}^n - \frac{1}{2}(\mathbf{u}^{n-1}\cdot\nabla)\mathbf{u}^{n-1} = \mathbf{0} & \boldsymbol{\xi}^{n+1}|_{\partial\Omega} = \mathbf{a}, \\ \frac{\boldsymbol{\eta}^{n+1}-\boldsymbol{\xi}^{n+1}}{\Delta t} - \frac{1}{2Re}\partial_{xx}(\boldsymbol{\eta}^{n+1}-\mathbf{u}^n) = \mathbf{0} & \boldsymbol{\eta}^{n+1}|_{x=0,L_x} = \mathbf{a}, \\ \frac{\boldsymbol{\zeta}^{n+1}-\boldsymbol{\eta}^{n+1}}{\Delta t} - \frac{1}{2Re}\partial_{yy}(\boldsymbol{\zeta}^{n+1}-\mathbf{u}^n) = \mathbf{0} & \boldsymbol{\zeta}^{n+1}|_{x=0,L_y} = \mathbf{a}, \\ \frac{\mathbf{u}^{n+1}-\boldsymbol{\zeta}^{n+1}}{\Delta t} - \frac{1}{2Re}\partial_{zz}(\mathbf{u}^{n+1}-\mathbf{u}^n) = \mathbf{0} & \mathbf{u}^{n+1}|_{x=0,L_z} = \mathbf{a}. \end{cases} \tag{7.6}$$

- **Penalty step**: $\forall n \geq 0$ the pressure increment $\phi^{n+\frac{1}{2}}$ is computed by the following one-dimensional problems:

$$\begin{cases} \psi - \partial_{xx}\psi = -\frac{1}{\Delta t}\nabla\cdot\mathbf{u}^{n+1} & \partial_x\psi|_{x=0,L_x} = 0, \\ \varphi - \partial_{yy}\varphi = \psi & \partial_y\varphi|_{y=0,L_y} = 0, \\ \phi^{n+\frac{1}{2}} - \partial_{zz}\phi^{n+\frac{1}{2}} = \varphi & \partial_z\phi^{n+\frac{1}{2}}|_{z=0,L_z} = 0. \end{cases} \tag{7.7}$$

- **Pressure update**: finally we update the pressure as follows:

$$p^{n+\frac{1}{2}} = p^{n-\frac{1}{2}} + \phi^{n+\frac{1}{2}} - \frac{\chi}{Re}\nabla\cdot(\frac{1}{2}(\mathbf{u}^{n+1}+\mathbf{u}^n)). \tag{7.8}$$

This scheme is unconditionally stable in the Stokes regime [56]. This algorithm only requires solving one-dimensional problems. The main difficulty of this methods is that it is limited to simple Cartesian geometries which for this reason we introduce an immersed boundary method to deal with this limitation.

In order to consider complex geometries in the direction–splitting algorithm, we use a mean least squares (MLS) immersed boundary method (IBM) proposed by De tulio et al. [28]. The immersed boundary method was first introduced to study flow patterns around heart valves and has evolved into a generally useful method for problems of fluid–structure

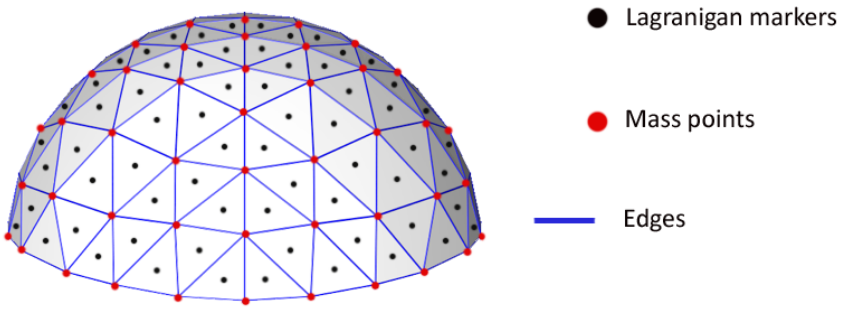

Figure 7.1: Discretization of a geometry to triangular elements. The centriods of elements are the Lagrangian markers.

interaction [106]. In the immersed boundary method, the fluid is represented in the Eulerian framework and the structure is represented in the Lagrangian framework. The Eulerian variables are defined on a fixed Cartesian mesh and the Lagrangian variables are defined on a curvilinear mesh that moves freely through the fixed Cartesian mesh without being constrained to adapt the Eulerian mesh. In summary there is no deformation of the Eulerian mesh due to the motion of the body.

In the present method, a direct-forcing function should be built that will enforce the proper imposed boundary conditions on all the Eulerian grid nodes influenced by the immersed body. The forcing function on the Lagrangian markers should be computed and then transfer it to the Eulerian grid nodes. The transfer operators are constructed using MLS shape functions with compact support. For this reason the geometry is discretized to N_t triangular elements and the centriods of the elements are the Lagrangian markers (see figure 7.1).

For a given Lagrangian marker, we first find the nearest Eulerian marker, centered in a cell with dimension Δx_i in the i-th direction. Then as it is shown in figure 7.2, a support centered on the Lagrangian marker with the dimension of $\pm r_i = \pm 1.5\Delta x_i$ is created. A volume $\Delta V_l = A_l h_l$ is also associated to the marker, where A_l is the l-th triangle area and h_l its local thickness, equal to the average mesh size at the marker location, which will be discussed later.

Initially the intermediate velocity $\widehat{\mathbf{u}}$ is calculated over Eulerian markers as shown in the system of equations (7.6). We can now define the transfer operator that will enable to build a transfer function between the Eulerian and Lagrangian grids as follow

– On the Lagrangian grid point l, the velocity on the Lagrangian grid point $\widehat{U}_i$ is calculated using the MLS approach which in the support domain can be approximated as follow

$$\widehat{U}_i(\mathbf{x}) = \mathbf{p}^T(\mathbf{x})\mathbf{a}(\mathbf{x}), \tag{7.9}$$

where in our work $\mathbf{p}(\mathbf{x}) = [1, x, y, z]$ is a linear basis function vector with dimension 4 and $\mathbf{a}(\mathbf{x})$ is a vector of coefficients and $\mathbf{x}$ is the Lagrangian point coordinates. The coefficient vector $\mathbf{a}(\mathbf{x})$ is then obtained by minimizing the weighted L2-norm defined as:

$$\mathbf{J} = \sum_{k=1}^{N_e} \mathbf{W}(\mathbf{x} - \mathbf{x}^k)\left[\mathbf{p}^T(\mathbf{x}^k)\mathbf{a}(\mathbf{x}) - \widehat{u}_i^k\right]^2, \tag{7.10}$$

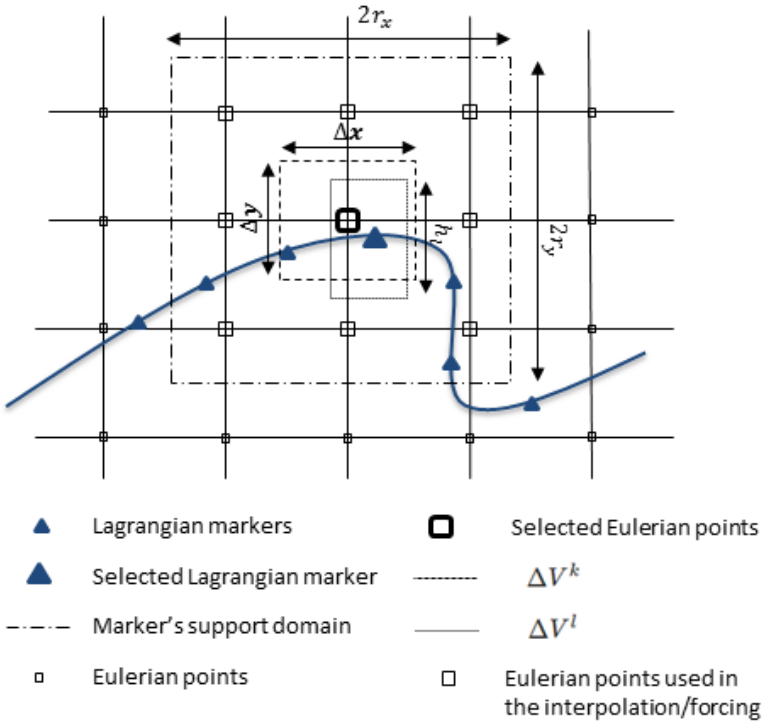

Figure 7.2: Support domain of a Lagrangian marker and the Eulerian points involved in the interpolation of the variables at it.

where $\widehat{u}_i^k$ and $\mathbf{x}^k$ are the intermediate velocity component and position vector, respectively, at Eulerian point k in the support domain and $\mathbf{W}(\mathbf{x}-\mathbf{x}^k)$ is a given weight function. Minimizing $\mathbf{J}$ with respect to $\mathbf{a}(\mathbf{x})$ leads to the following equation

$$\mathbf{A}(\mathbf{x})\mathbf{a}(\mathbf{x}) = \mathbf{B}(\mathbf{x})\widehat{\mathbf{u}}_i, \tag{7.11}$$

where

$$\mathbf{A}(\mathbf{x}) = \sum_{k=1}^{N_e} \mathbf{W}(\mathbf{x}-\mathbf{x}^k)\mathbf{p}(\mathbf{x}^k)\mathbf{p}^T(\mathbf{x}^k), \tag{7.12}$$

$$\mathbf{B}(\mathbf{x}) = \left[\mathbf{W}(\mathbf{x}-\mathbf{x}^1)\mathbf{p}(\mathbf{x}^1)...\mathbf{W}(\mathbf{x}-\mathbf{x}^{N_e})\mathbf{p}(\mathbf{x}^{N_e})\right], \tag{7.13}$$

and

$$\widehat{\mathbf{u}}_i = \left[\widehat{u}_i^1...\widehat{u}_i^{N_e}\right]^T. \tag{7.14}$$

Let us define $\mathbf{\Phi} = \mathbf{p}^T(\mathbf{x})\mathbf{A}^{-1}(\mathbf{x})\mathbf{B}(\mathbf{x})$ as the transfer operator containing the shape function values for marker point l, then using equation (7.9) we obtain

$$\widehat{U}_i(\mathbf{x}) = \mathbf{\Phi}^T(\mathbf{x})\widehat{\mathbf{u}}_i, \tag{7.15}$$

For the weight function the following exponential function has been used

$$\mathbf{W}(\mathbf{x}-\mathbf{x}^k) = \begin{cases} e^{-(\frac{|\mathbf{x}-\mathbf{x}^k|}{0.3r_i})^2} & \text{if } \frac{|\mathbf{x}-\mathbf{x}^k|}{r_i} \leq 1, \\ 0 & \text{otherwise.} \end{cases} \tag{7.16}$$

– At all Lagrangian grid points we then calculate the volume force component F_i

$$F_i = \frac{V_i^b - \widehat{U}_i}{\Delta t}, \tag{7.17}$$

where V_i^b is the velocity component that should be imposed as a boundary condition at the marker.

– We then transfer back F_i to the N_e Eulerian grid points associated with each Lagrangian marker, using the same shape functions employed in the interpolation procedure and imposing that the total force acting on the fluid is not changed by the transfer. Consequently the i-th component of the volume force in the Eulerian point k can evaluate as

$$f_i^k = \sum_{l=1}^{N_l} c_l \Phi_k^l F_i^l, \tag{7.18}$$

where N_l indicates the number of Lagrangian points associated with the Eulerian point k. Since the total force acting on the fluid is not changed by the transfer we have

$$\sum_{k=1}^{N_{e,t}} f_i^k \Delta V^k = \sum_{k=1}^{N_{e,t}} F_i^l \Delta V^l, \tag{7.19}$$

where $N_{e,t}$ is the total number of forced Eulerian grid points and $\Delta V^k = \Delta x^k \times \Delta y^k \times \Delta z^k$ is the volume associated with the Eulerian grid point k. h_l in ΔV^k can now be defined as $h_l = 1/3 \sum_{k=1}^{N_e} \phi_k^l (\Delta x^k + \Delta y^k + \Delta z^k)$. Using equation (7.18) in (7.19) and rearranging terms we have

$$c_l = \frac{\Delta V^l}{\sum_{k=1}^{N_e} \phi_k^l \Delta V^k}. \tag{7.20}$$

– Using equation (7.18) we correct the intermediate velocity with respect to the boundary condition on the immersed body which is given as

$$\mathbf{u}^* = \widehat{\mathbf{u}} + \Delta t \mathbf{f}. \tag{7.21}$$

Given the triangular discretization of the surface, the local force contribution is evaluated for each triangular element. The local hydrodynamic force per unit area on a surface element is

$$f_i^{Hyd} = \Big[-p\delta_{ij} + \mu \big(\frac{\partial u_i}{\partial x_j} + \frac{\partial u_j}{\partial x_i}\big)\Big] n_j, \tag{7.22}$$

where f_i^{Hyd} is the hydrodynamic surface force in the x_i direction, n_j is the direction cosine of the normal unit vector in the x_j direction and μ is the dynamic viscosity. In order to use this equation we need to calculate p and velocity derivatives on the Lagrangian markers. For this purpose, for each Lagrangian marker, a normal probe is created by locating an external point e, at a distance, h_n(which is proportional to the local grid spacing), from the surface. Using the same MLS formulation, pressure and velocity are evaluated at the probe location. The pressure at the Lagrangian marker can be calculated as

$$p_l = p_e + h_l \frac{D\mathbf{u}_l}{Dt} \cdot \mathbf{n}_l, \tag{7.23}$$

where p_e is the pressure at the probe and $\frac{D\mathbf{u}_l}{Dt}$ comes from the evaluation of the pressure gradient in the normal direction by the momentum equation [141].

The velocity derivatives, $\frac{\partial \widehat{\mathbf{U}}_i}{\partial x_j}$ at the location e for each Lagrangian marker are computed by differentiating equation (7.15) and is given as

$$\frac{\partial \widehat{\mathbf{U}}_i}{\partial x_j} = \sum_{k=1}^{N_e} \frac{\partial \phi_k}{\partial x_j} u_i, \tag{7.24}$$

where $\frac{\partial \phi_k}{\partial x_j}$ comes from the solution of an additional system of equations similar to equation (7.11) [141]. If we assume a linear variation of the velocity near the body, then $\frac{\partial \widehat{U}_i}{\partial x_j}$ is a good approximation of $\frac{\partial \widehat{u}_i}{\partial x_j}$, at the surface.

7.4 Benchmark simulations

In this section we evaluate the performance of the method described in section 7.3. In particular we perform series of benchmark cases using this method and compare our results with other research works and OpenFOAM simulations.

7.4.1 Lid-driven flow in a cavity

The lid-driven flow in a cavity problem has long been used as validation case for CFD codes. The geometry and boundary conditions of the problem are simple and in general two-dimensional. In the standard case fluid contained in a square domain with Dirichlet boundary conditions on all sides, and with a non-zero tangential velocity boundary condition on one lid and zero velocity to the other sides. Since our code is three-dimensional, we extend this case to a cube.

7.4.1.1 Geometry, boundary conditions and solvers

Figure 7.3 (a) shows the three-dimensional geometry of the model. Figure 7.3 (b) shows the mid cross section of the domain. The side the cube has length d. For the simulations we used parameter values proposed by of Ding et al. [29] and ku et al. [76]. Thus $d = 1m$, $U_0 = 1\ m/s$. The viscosity in both papers was defined based on three Reynolds number:$R_e = 100, 400, 1000$. Since the flow in the eye in general has low Reynolds number, we just compare our simulations for $R_e = 100$.

In the simulations we used the following boundary conditions

- **Purple surface**. The x–component of the velocity vector takes a non zero uniform value of $U_0 = 1\ m/s$. The other components are zero.

- **Other surfaces**. We considered zero velocity boundary condition for other surfaces.

The time step Δt and spatial resolution, Δx, Δy, and Δz, are set to be 0.0001 s and 0.006 m. This corresponds to ≈ 4.45 million points.

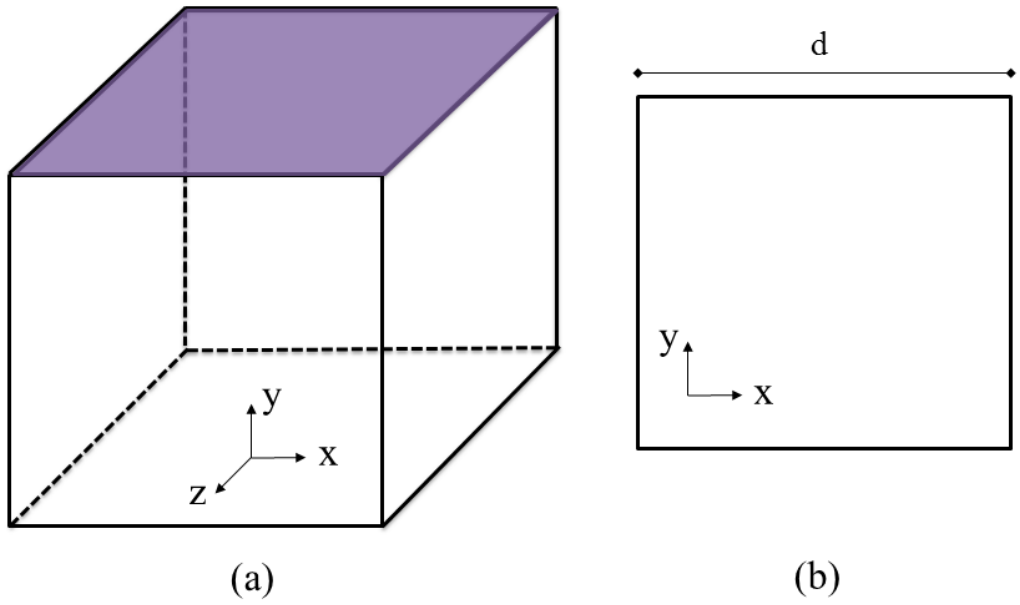

Figure 7.3: (a) three-dimensional view of the lid-driven flow in the cavity and (b) the mid $y-z$ cross section of it. here the side length of the cube is $d = 1m$.

7.4.1.2 Results

Figure 7.6 shows the velocity magnitude (a) and pressure distribution (b) of the flow at the mid cross section of the domain. At this Reynolds number, a unique vortex develops near the top and gradually holds the whole domain, up to a stable steady state. Nonlinear effects of Navier-Stokes equations can be seen in Figure 7.6 (a) which is mainly due to the convection of the vortex, resulting in an asymmetric flow.

Figure 7.5 (c) shows the probe lines that has been used in order to compare the obtained results with the works of Ding et al. [29] and ku et al. [76]. The first (u) and second (v) components of the velocity are sampled over the blue and red prob line and presented in the Figure 7.6 (a) and (b), respectively. As can be seen in these two figures, our results are very similar to those obtained in the works of Ding et al. [29] and ku et al. [76].

7.4.2 Lid-driven flow in a cavity with treatment of boundary condition

The non–zero velocity boundary condition at the lid and zero velocity boundary condition at the walls, creates singularities around the corners (see two top corner in figure 7.6). This is a very common problem in lid–cavity models. In order to deal with these singularities, we modify the boundary condition at the lid to a polynomial function of order 18. This velocity profile is suggested in the work of Leriche [84]. We adopted this velocity profile and in our simulations the following boundary condition at the lid has been used

$$u = U_0\left(1 - (\frac{x-h}{h})^n\right)^2\left(1 - (\frac{z-h}{h})^n\right)^2, \tag{7.25}$$

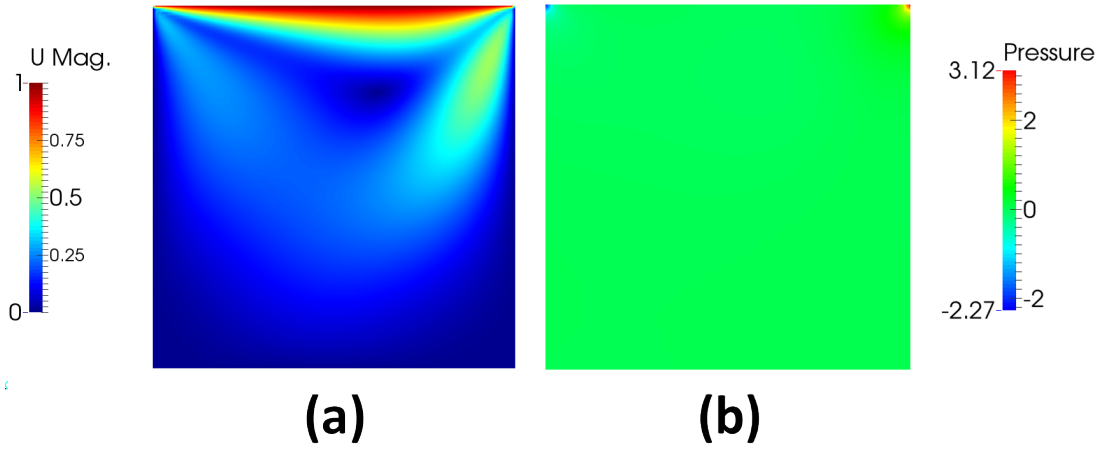

Figure 7.4: Velocity magnitude (a) and pressure distribution of the flow at the mid $y-z$ cross section of the domain at $t = 1.5\ s$.

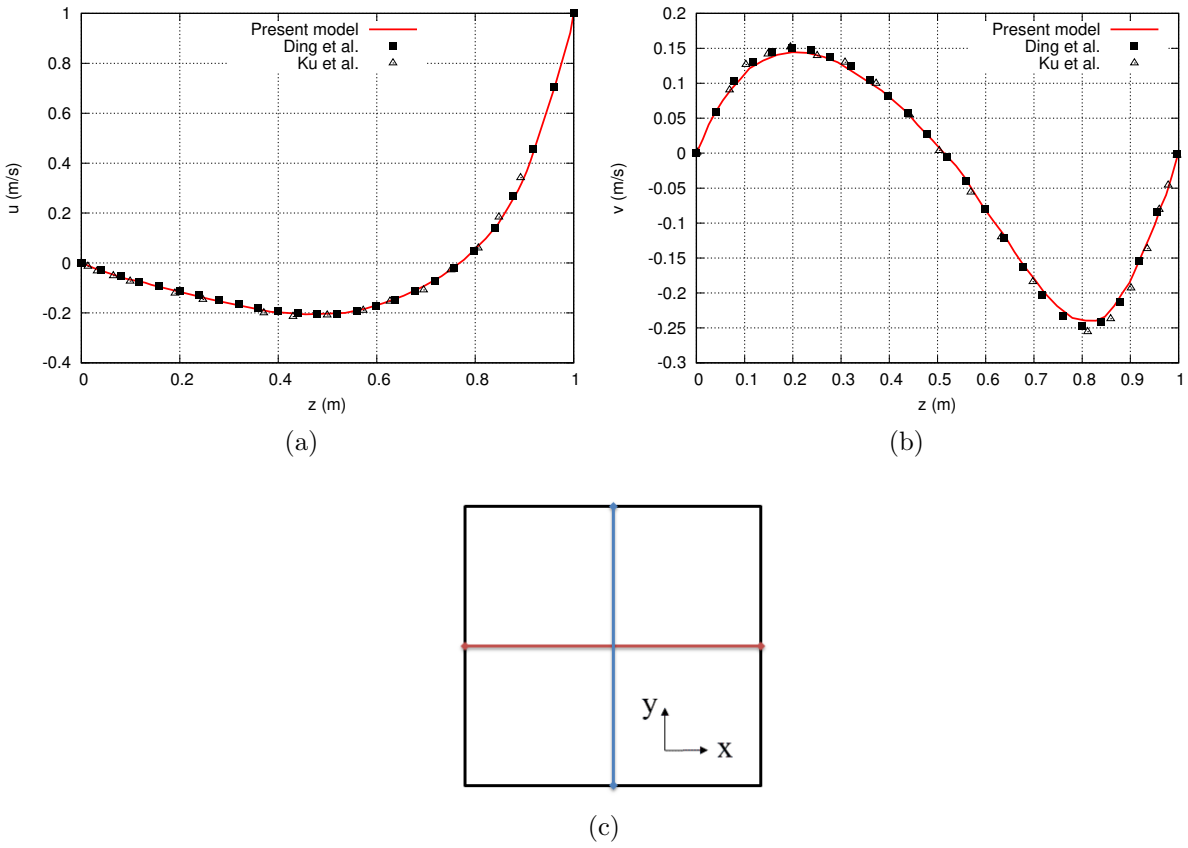

Figure 7.5: Results obtain for u (a) in the blue prob line in the mid $y-z$ cross section (c) and v (b) in the red prob line in the mid cross section (c). In figures (a,b) red line represents the our simulation results, square and triangle points are the results of numerical simulations of Ding et al. [29] and ku et al. [76], respectively. The Reynolds number in these simulations is 100.

where $n = 18$ and $h = d/2$. Figure 7.6 shows the velocity profile on the lid surface, obtained by using equation (7.25).

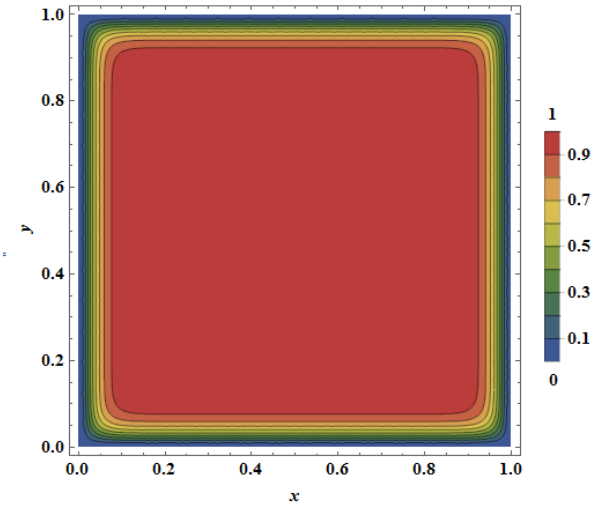

Figure 7.6: Velocity profile on the lid surface, obtained by using equation (7.25) .

The simulations for this case were also performed by OpenFOAM for comparison. In OpenFOAM we also used second order accuracy in time and space discretization methods and the solver was pimpleFOAM, discussed in chapter 3, section 3.2.1. The mesh is generated using blockMesh utility of OpenFOAM with $\approx$ 2.5 million cells. Here the Reynolds number is 100. We ran these simulations on 15 processors.

7.4.2.1 Results

Figure 7.7 shows the velocity magnitude (a,b) and pressure distribution (c,d) of the flow at the mid $y - z$ cross section of the domain, calculated by OpenFOAM (left) and by the in-house code (right), at $t = 1.5\ s$. As it can be seen in all figures, the solutions are almost identical and the the solution at the corners of the lid is more smooth and singularities are not presented.

Figure 7.8 shows the pressure (a,b), first component (c,d) and second (e,f) components of the velocity vector in the domain at $t = 10\ s$. The left and right figures are the results calculated on the blue and red line probes, shown in figure 7.5 (c). In all plots the results, obtained by in–house code are almost identical to the ones calculated by OpenFOAM.

In figure 7.9, we show the streamlines of the flow in the domain, taken at different times. As time evolves, the vortex near to the lid is affected by the convection of the vortex, resulting in an asymmetric flow. This effect has also been observed in the work of Leblond et al. [83]. They observed that isocontours of the velocity streamfunction for the Stokes flow are axysimetric and the nonlinear effect of the Navier–Stokes flow shifts this vortex.

We also ran the OpenFOAM simulations using one processor to compare with our code in the sense of computational time. The computational time for each time step in the serial case for OpenFOAM and in–house code was $\approx 10\ s$ and $\approx 2.5\ s$, respectively.

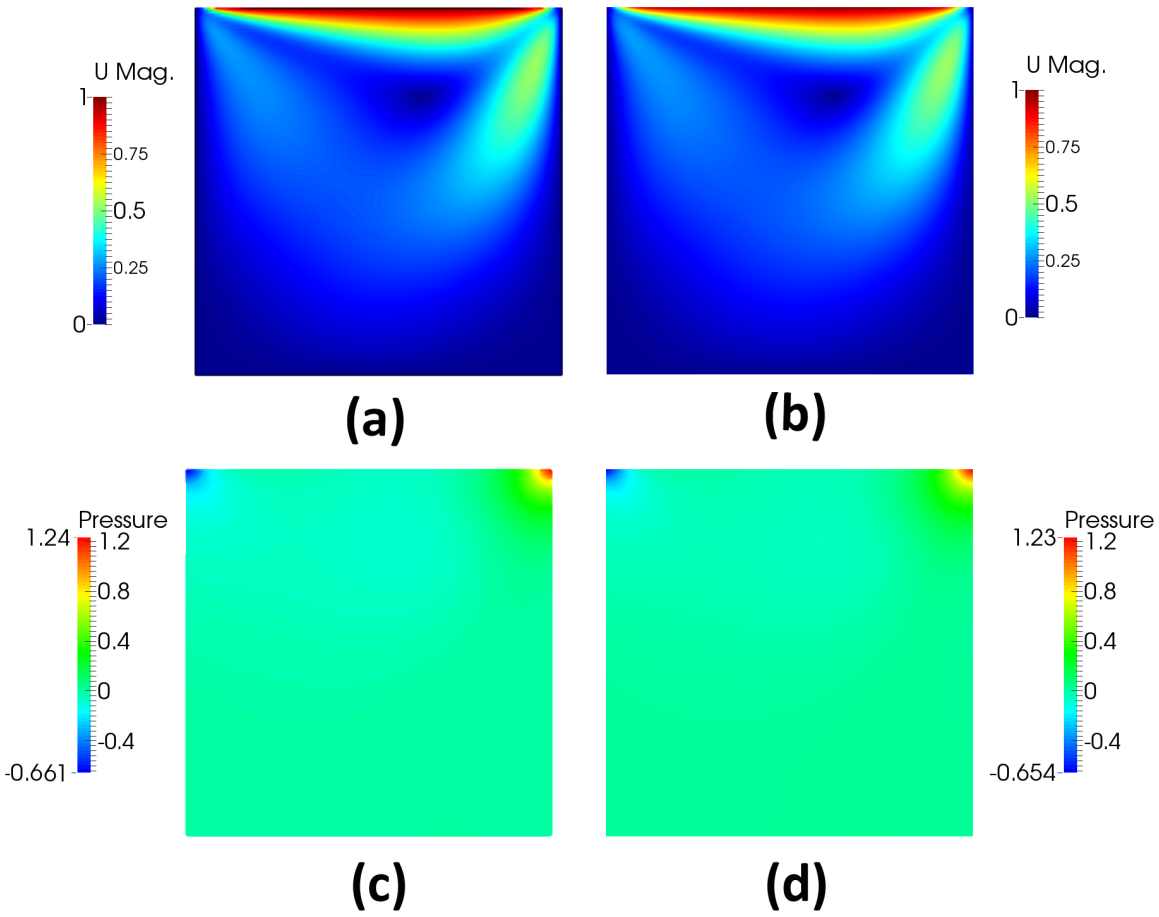

Figure 7.7: Velocity magnitude (a,b) and pressure distribution (c,d) of the flow at the mid $y-z$ cross section of the domain, calculated with OpenFOAM (right) and in–house code (left) at $t = 1.5\ s$. Here we used equation (7.25) for the lid velocity profile. The Reynolds number is 100.

7.4.3 Lid-driven flow in a cavity with a sphere inside

In order to assess the IBM performance, we perform a simulation with a sphere in a cube. The flow is still produced by the motion of the upper wall.

7.4.3.1 Geometry, boundary conditions and solvers

Figure 7.10 shows the three–dimensional view (a) and the mid $y-z$ cross section of the domain (b). The center of sphere is positioned in the center of the cube. The radius of the sphere is $r = 0.25\ m$.

In these simulations we used the following boundary conditions

- **Red surface**. The x–component of the velocity vector, u, is described by the equation (7.25). The other components are zero.
- **Other surfaces**. We considered zero velocity boundary condition for other surfaces, including the surface of the sphere.

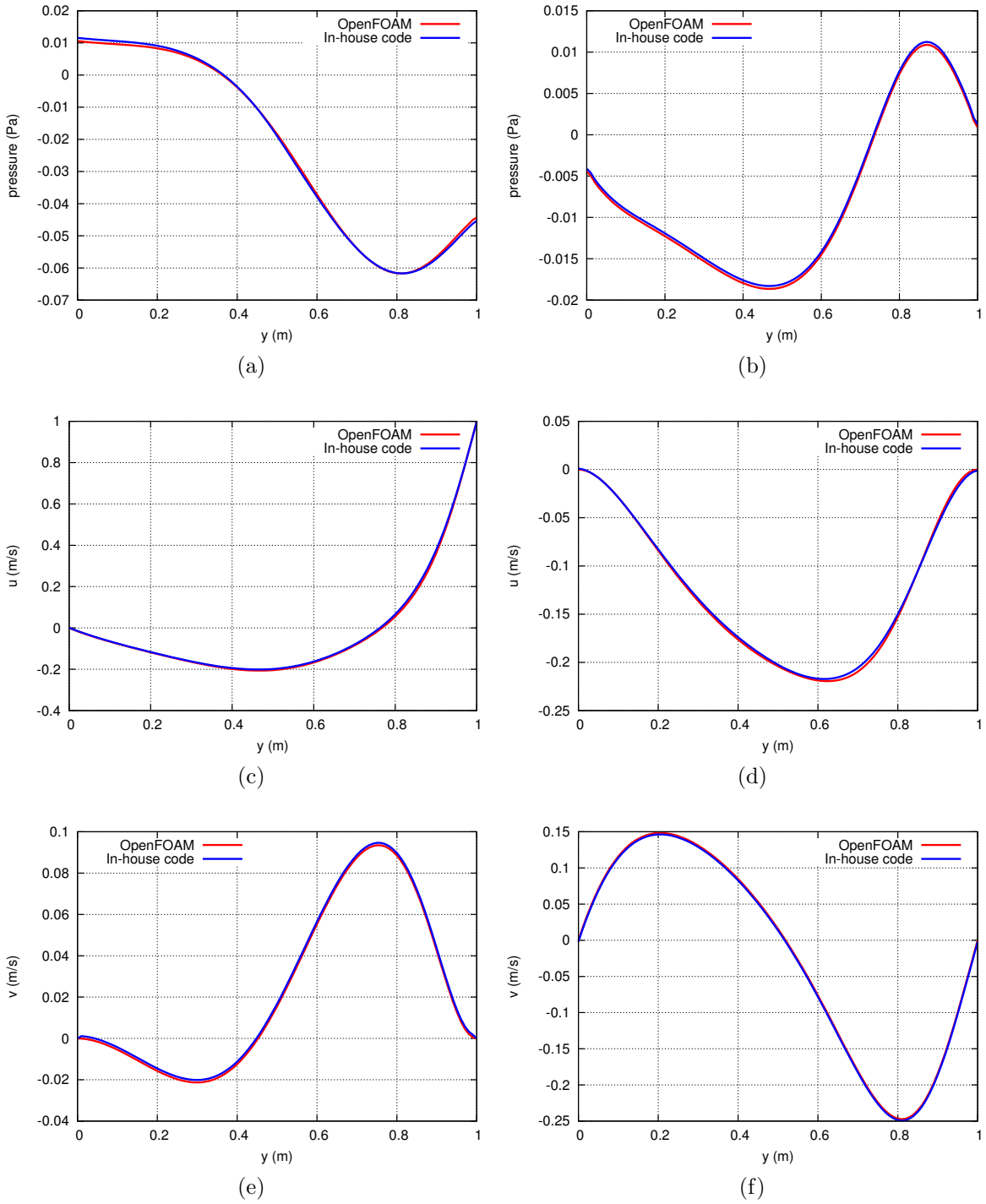

Figure 7.8: Pressure (a,b), first component (c,d) and second (e,f) components of the velocity vector at $t = 10\ s$, calculated along the blue (right) and red (left) line probes. The Reynolds number is 100.

The time step Δt and spatial resolution Δx for each direction are set to be 0.0001 s and 0.002 m, which corresponds to a mesh with $\approx$ 8 million points. Similar to the previous benchmark case, we compare our results with OpenFOAM, with the same setup

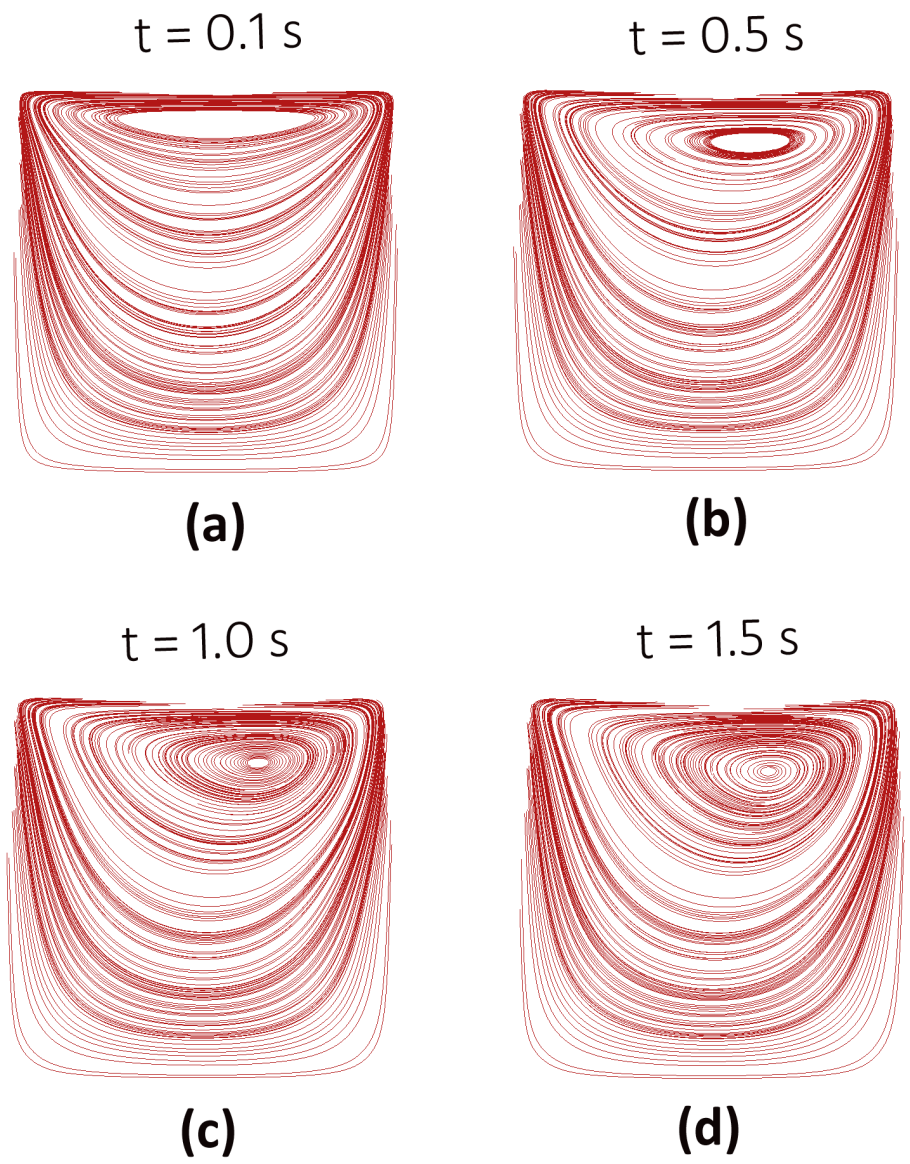

Figure 7.9: Streamlines of the flow at the mid $y-z$ cross section of the domain, evolving in time.

of solver and discretization methods, described in subsection 7.4.2. The mesh is generated using cfMesh software. The number of elements in this mesh is approximately 2.5 million cells. We ran these simulations on 15 processors.

7.4.3.2 Results

Figure 7.12 shows the velocity magnitude (a) and pressure distribution (b) at the mid $y-z$ cross section of the domain, calculated by the in–house code. The IBM effects clearly can be seen in these figures. In order to have a better comparison with OpenFOAM we remove the sphere from these plots and show these results in figure 7.12.

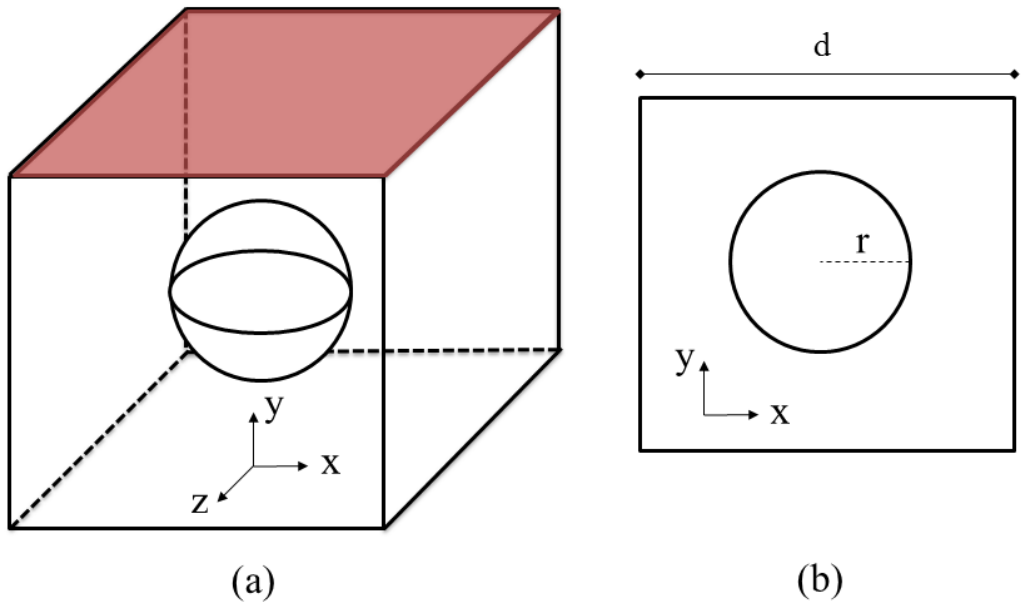

Figure 7.10: (a) three-dimensional view of the lid-driven flow in a cavity with a sphere inside and (b) the mid $y-z$ cross section of it. Here the length of the cube is $d = 1m$ and radius of sphere is $r = 0.25\ m$. The Reynolds number is 100.

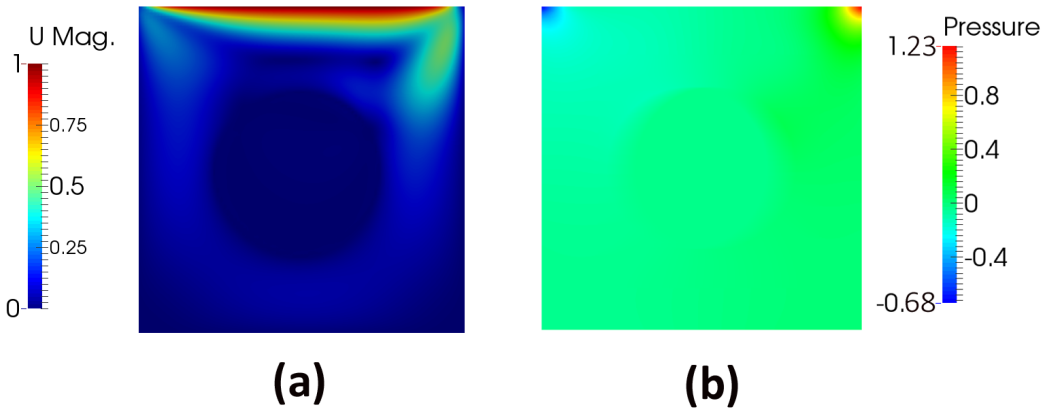

Figure 7.11: Velocity magnitude (a) and pressure distribution of the flow at the mid $y-z$ cross section of the domain at $t = 1.5\ s$.

Figure 7.12 shows the velocity magnitude (a,b) and pressure distribution (c,d) of the flow at the mid cross section of the domain, calculated by OpenFOAM (right) and the in-house code (left) at $t = 1.5\ s$. Again, similarly to what was discussed in the previous section, the results show the solutions are almost identical.

In figure 7.13, we show the streamlines of the flow in the domain, at different times. Comparing this with figure 7.9, it appears that the vortex near to lid is affected by the the presence of the sphere. As time evolves, the streamlines near to the vortex start to change direction and make the flow three dimensional.

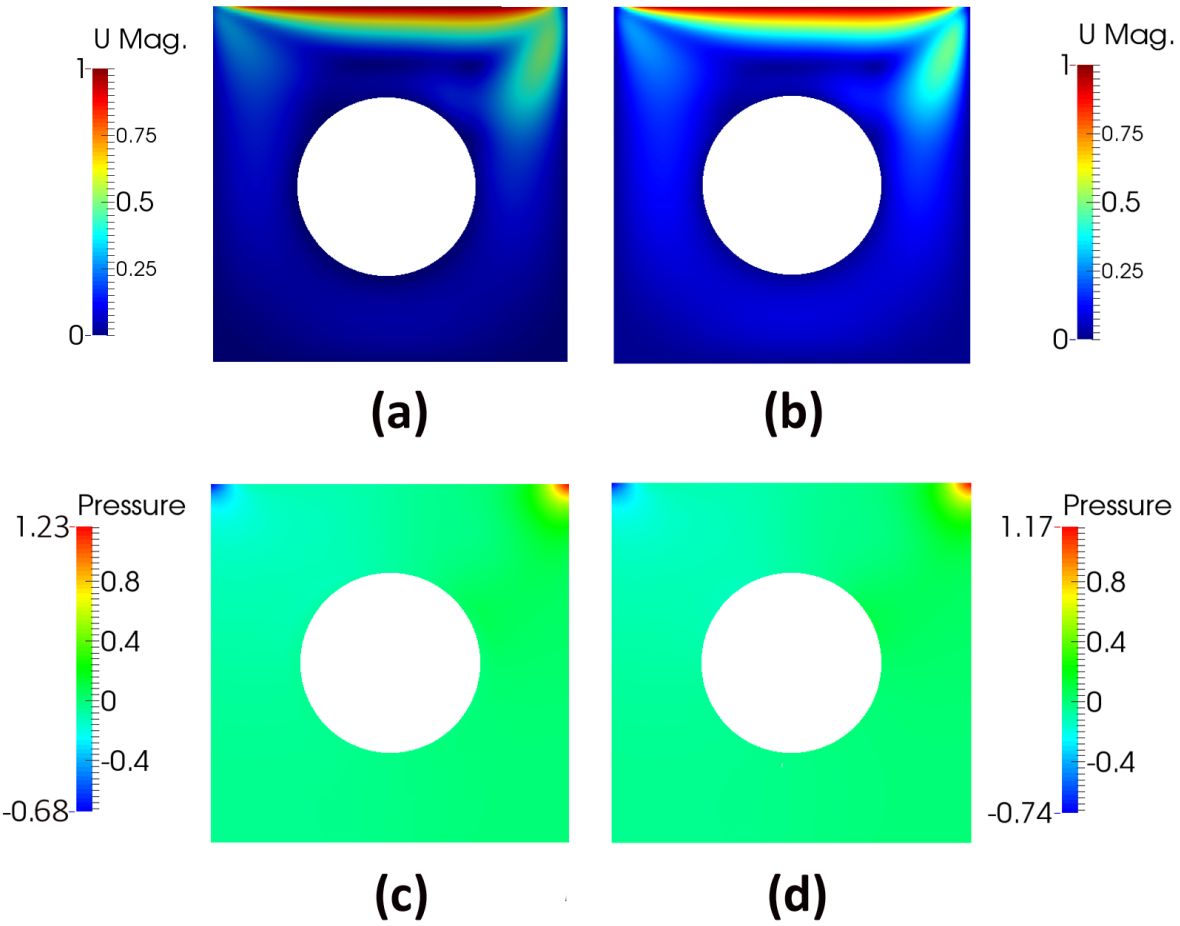

Figure 7.12: Velocity magnitude (a,b) and pressure distribution (c,d) of the flow at the mid $y-z$ cross section of the domain, calculated with OpenFOAM (right) and in–house code (left) at $t = 1.5\ s$. Here we used equation (7.25) for the lid velocity profile. The Reynolds number is 100.

Similar to the previous benchmark case we present the pressure and velocity components in the probes, calculated both with OpenFOAM and in–house code, in figure 7.14. The grey region in this figure refers to the region that sphere is presented.

The computational time for each time step in the serial mode for OpenFOAM and in–house code was $\approx 10\ s$ and $\approx 4\ s$, respectively.

7.4.4 Moving sphere inside a cube

In this part, we study the flow in a cube induced by the motion of a sphere inside it.

7.4.4.1 Geometry, boundary conditions and solvers

Figure 7.15 shows the three-dimensional view (a) and the mid $y-z$ cross section of the domain (b). At the initial time the center of the sphere is positioned at the center of cube with length $d = 1\ m$ and the sphere velocity vector of $(0, -2, 0)\ m/s$. The radius of the

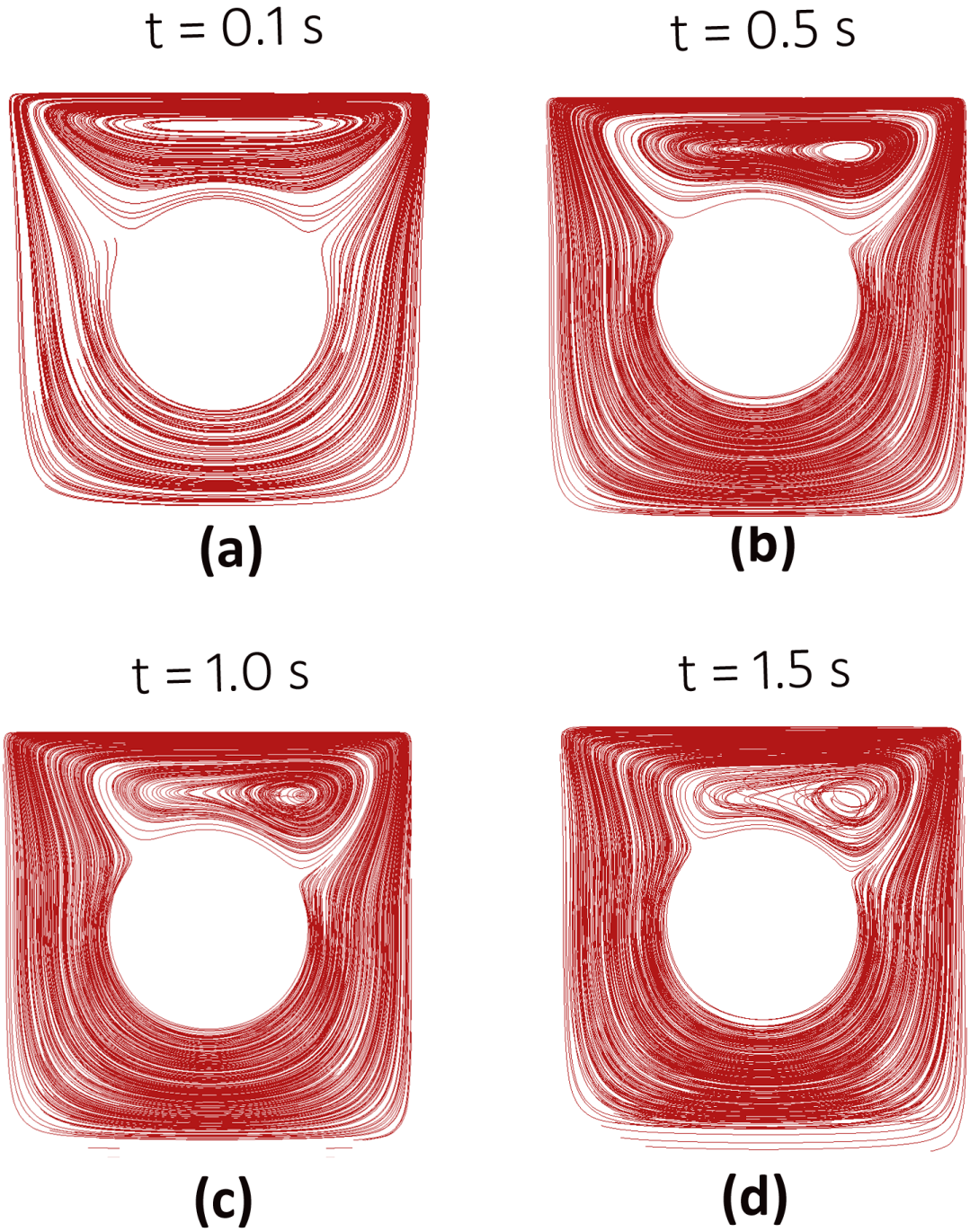

Figure 7.13: Streamlines of the flow at the mid cross section of the domain, evolving in time.

sphere is $r = 0.1\ m$. The viscosity of the fluid is $\nu = 2 \times 10^{-3}$. Figure 7.15 (c) shows a probe (dashed line) passing through the center of sphere at $t = 0.1\ s$. We sketch our solution over this probe for the comparison with OpenFOAM.

In the simulations we used the following boundary conditions

– **Sphere surface**. We considered a rigid motion of the sphere, with the velocity

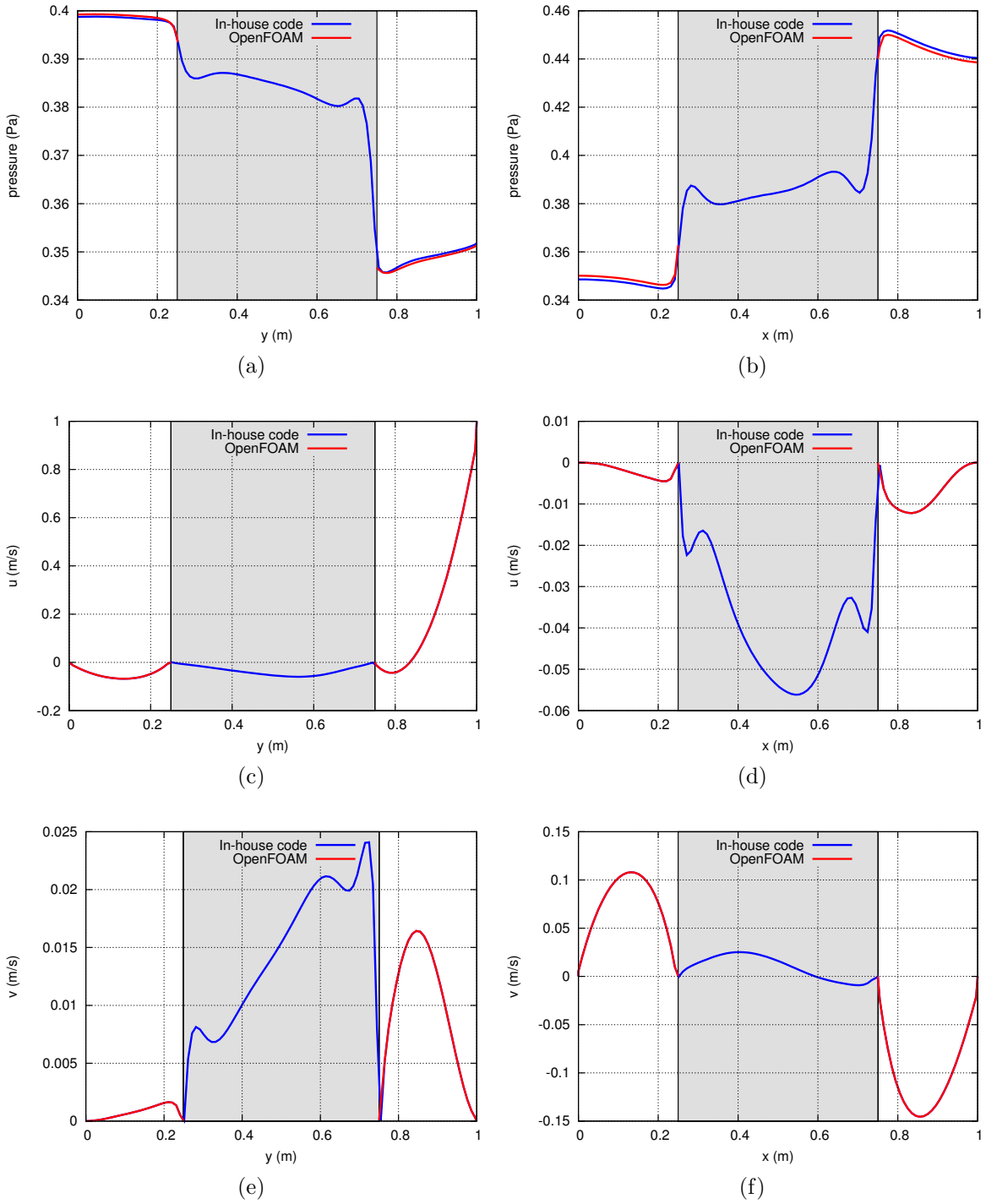

Figure 7.14: Pressure (a,b), first component (c,d) and second (e,f) components of the velocity vector at $t = 10\ s$, calculated on the blue (right) and red (left) line probes. The Reynolds number is 100. The grey region refers to the region occupied by sphere.

vector of $(0, -2, 0)\ m/s$.

– **Cube surfaces**. We considered a zero velocity boundary condition for all surfaces on the cube.

The corresponding Reynolds number can be calculated as $Re = 2rU/\nu = 100$, where $U = 2\ m/s$. The time step Δt and spatial resolution Δx are the same as in the simulation of subsection 7.4.3.

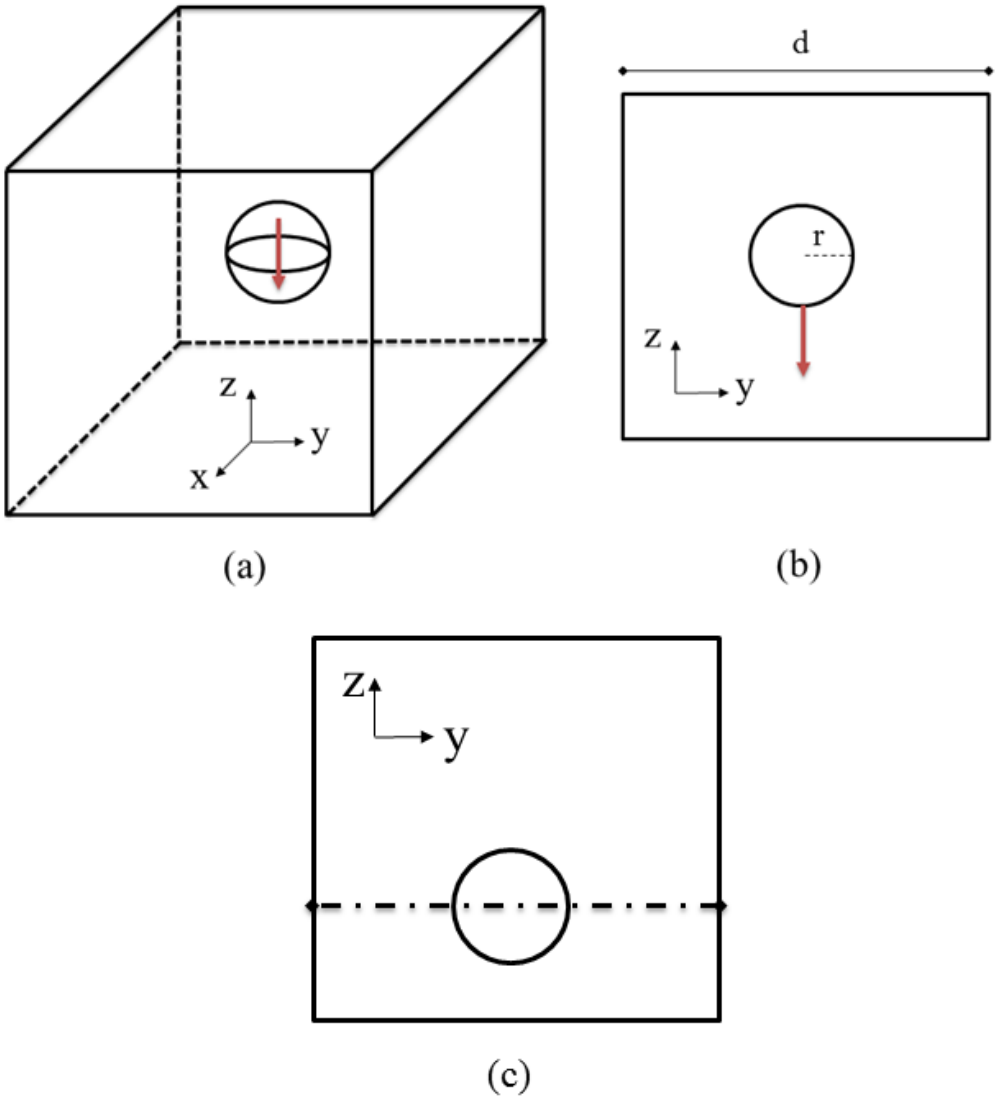

Figure 7.15: (a) three-dimensional view of a cube with a sphere inside and (b) the mid $y - z$ cross section of the domain. The sphere is moving to the bottom of the cube at the speed of 2 m/s in the negative z–direction. Here the length of the sides of the cube is $d = 1m$ and radius of the sphere is $r = 0.1\ m$. (c) the dashed line is the probe that we sketch the solution over it at $t = 0.1\ s$. The probe is passing through the center of sphere.

Similar to subsection 7.4.3, we compare our results with those obtained from OpenFOAM, using the same setup of discretization methods as described in subsection 7.4.2. The solver in this case is PimpleDyMFoam, discussed in chapter 3. The number of elements in this mesh is approximately 2.5 million cells and we ran these simulations on 15 processors.

7.4.4.2 Results

Figure 7.16 shows the velocity magnitude and flow streamlines at $y-z$ mid cross section of the domain for different times. In each sub–figure, right and left figures correspond to the results obtained by OpenFOAM and the in–house code, respectively. Similarly in figure 7.17 we show the pressure distribution in the domain at different times. As can be seen in these figures the results obtained are in excellent agreement.

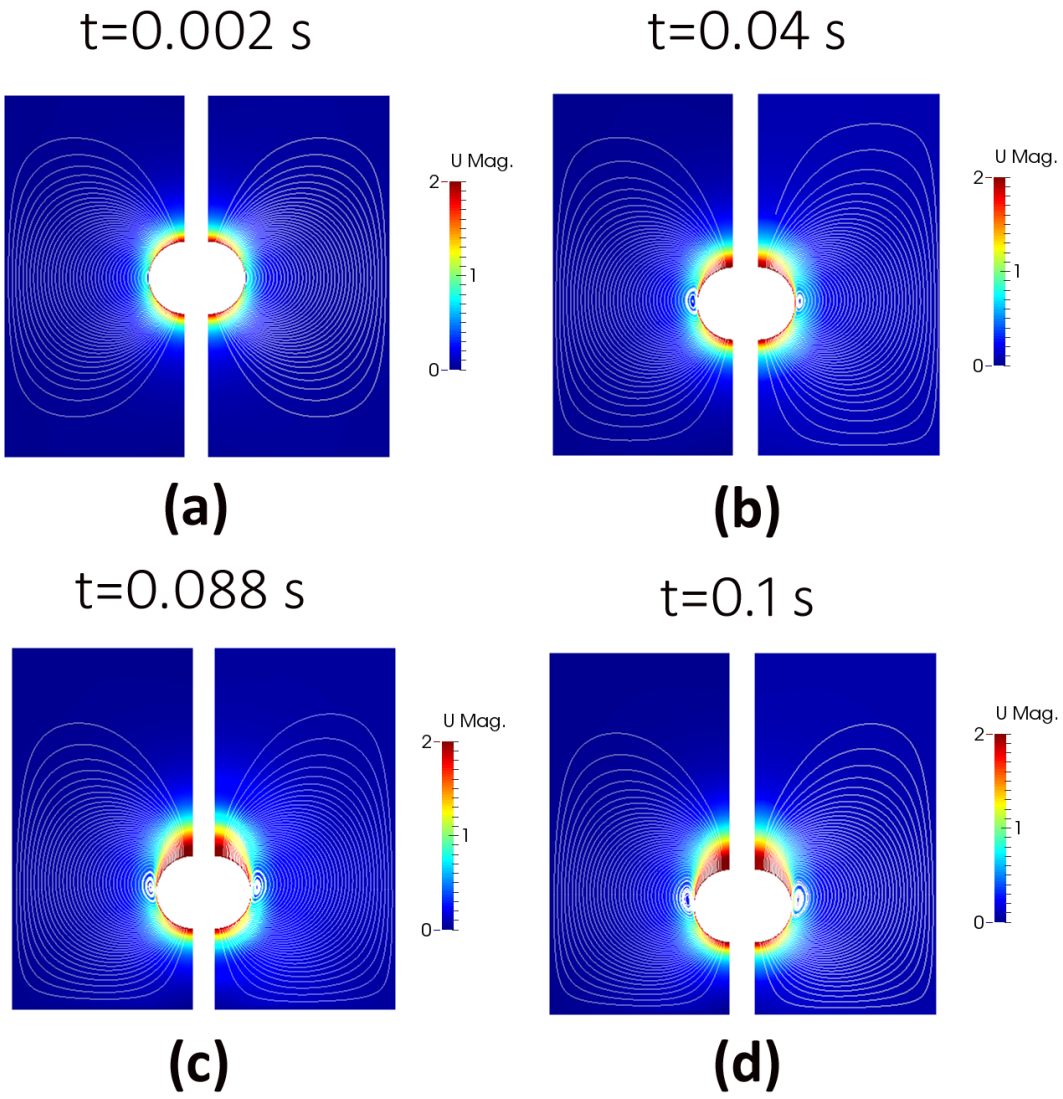

Figure 7.16: The velocity magnitude and flow streamlines at the mid $y-z$ cross section of the domain for different times. The right and left sub–figures are the results obtained by OpenFOAM and the in–house code, respectively.

Figure 7.18 shows u (a), v (b) and w (c) components of velocity vector, and pressure (d) of the flow at the probe (see figure 7.15 (c)), calculated by OpenFOAM and the in-house code at $t = 0.1\ s$. Again, similarly to what was discussed in the previous section, the results show the solutions are almost identical.

We also ran the OpenFOAM simulations using one processor to compare with our

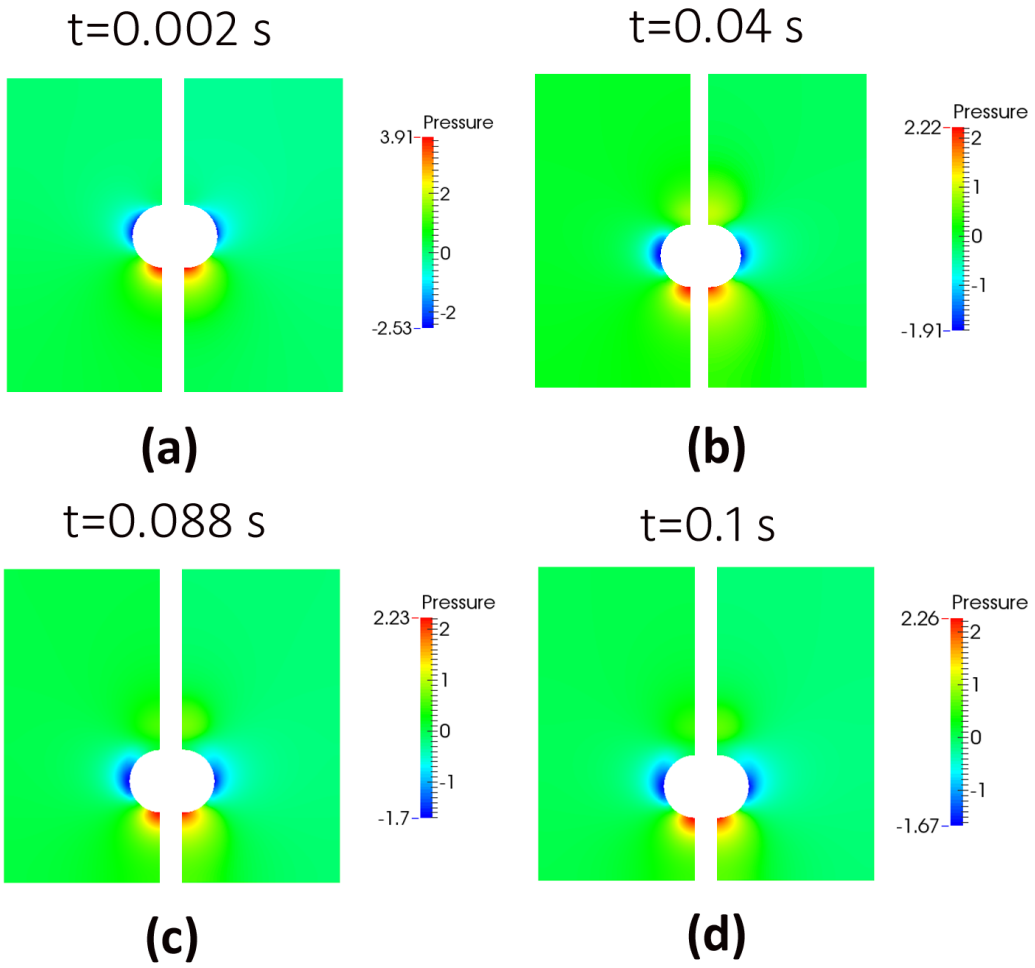

Figure 7.17: The pressure distribution at the mid $y-z$ cross section of the domain for different time steps. The right and left sub–figures are the results obtained by OpenFOAM and the in–house code, respectively.

code in the sense of computational time. The computational time for each time step in the serial mode for OpenFOAM and in–house code was $\approx 16\ s$ and $\approx 4\ s$, respectively. The computational time in OpenFOAM for this case is increased, since at each time step, OpenFOAM need to additionally solve an an equation corresponding to the mesh motion after some iterations, there is a mesh refinement in order to not have highly skewed elements in the mesh after deformation. Indeed this is not the case for the in–house code since, as explained at the beginning of the chapter, the mesh of the sphere does not conform with the Cartesian mesh and is treated by IBM.

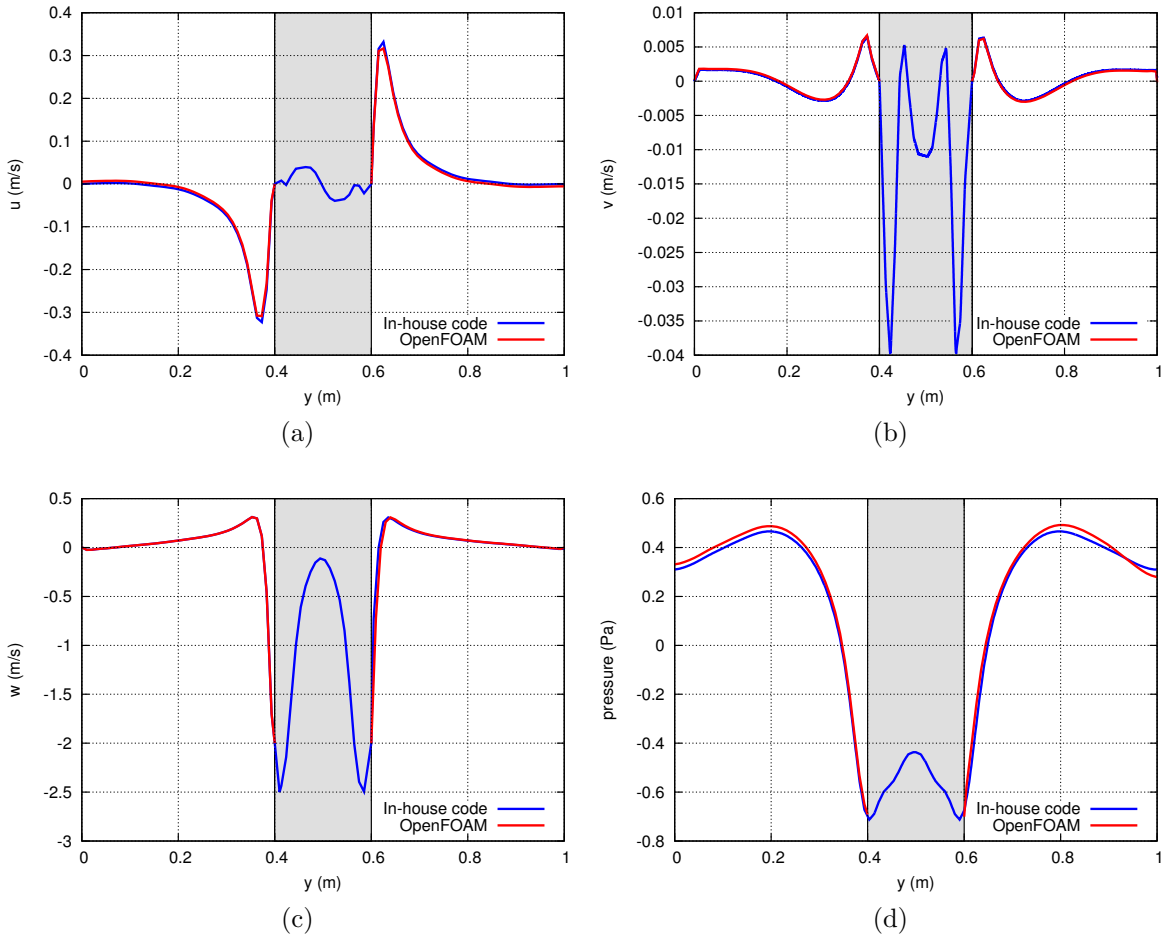

Figure 7.18: u (a), v (b) and w (c) components of velocity vector, and pressure (d), calculated on the probe line (see figure 7.15 (c)). The Reynolds number is 100. The grey region refers to the region occupied by sphere.

7.5 Summary of simulations and results

In this chapter we showed results from a code based on the direction–splitting method with an immersed boundary treatment, described in section 7.3. The numerical method is second order accurate in time and space and, due to its algorithm, it is faster that the traditional Navier–Stokes solvers. We designed a series of benchmark cases in order to evaluate the performance of the method. For each case, we first described the geometry and the boundary conditions that have been used and then we showed the results. We summarize the simulations of the models as follows

7.5.1 Lid-driven flow in a cavity

In subsection 7.4.1 we described the simulation related to the so–called lid-driven flow in a cavity for which the Reynolds number was 100, corresponding to the maximum Courant number of 0.0167. We considered two probes at the mid $y-z$ cross section of the domain in the x- and y–directions, and we showed the u and v components of the velocity, and

pressure on these probes. We compared our results with the works of Ding et al. [29] and ku et al. [76], and the agreement was excellent.

7.5.2 Lid-driven flow in a cavity with treatment of lid boundary conditions

In subsection 7.4.2 we described the lid-driven flow in a cavity with a boundary condition described in the work of Leriche [84]. This boundary condition removes the singularity at the corners of the cube, in contact with the moving lid. The parameters in this part are identical to those described in subsection 7.4.1. We also performed numerical simulations of this model, using OpenFOAM for comparison. We found that the solution obtained with the in–house code is almost identical to that obtained by OpenFOAM. We also observed that the flow is asymmetric due to the non–linear effects of Navier–Stokes equations (seen also in Leblond et al. [83]).

7.5.3 Lid-driven flow in a cavity with a sphere inside

In subsection 7.4.3 we described a lid-driven cavity simulation, with the same parameters described in subsection 7.4.2, and a sphere with radius of 0.25 at the center of the cube. The boundary conditions for the cube are the same as those used in the simulations presented in subsection 7.4.3 and we imposed a zero velocity boundary condition at the sphere which was treated by IBM. We also performed numerical simulations of the this case, using OpenFOAM for the comparison which the agreement was excellent. Similar to the previous case, as time evolves, a vortex near to the lid is created, however it appears that it is affected by the the presence of the sphere and stretched along the top of the side sphere, near to the lid.

7.5.4 Moving sphere inside a cube

In section 7.4.4 we performed simulations of a moving sphere with radius of 0.1 m inside a cube with length of 1 m. The center of sphere is positioned at the center of cube. At the surfaces of the cube, we considered zero velocity boundary conditions. At the surface of sphere, we imposed a velocity vector of $\mathbf{u}_{sp} = (0, -2, 0)\ m/s$. We also performed numerical simulations of the this model, using OpenFOAM for the comparison.

7.5.5 Computational time comparisons

Since at the moment the in–house code is written in serial, for the benchmark cases that we compare our results with OpenFOAM, we also preformed OpenFOAM simulations in one processor. This gives us an indication about the computational time performance of the code. In table 7.1 we show the computational time required for one time–step in both OpenFOAM and the in–house code. Indeed in all benchmark cases, the in–house code is faster than to OpenFOAM, particularly in the case moving sphere inside a cube.

Benchmark case	In–house code	OpenFOAM
Lid–driven flow in a cavity with treatment of lid BC.	$\approx 2.5\ s$	$\approx 10\ s$
Lid-driven flow in a cavity with a sphere inside	$\approx 4\ s$	$\approx 10\ s$
Moving sphere inside a cube	$\approx 4\ s$	$\approx 16\ s$

Table 7.1: Computational time required for one time–step in OpenFOAM and in–house code for different benchmark cases.

7.6 Conclusions

The motivation for the development of an in–house code based on the direction–splitting method with immersed boundary treatment was related to possible CFD applications in the human eye, such as flow induced by eye movements and miosis (see section 7.1). In this chapter we proposed benchmark cases to test the current state of the code. Each benchmark case was designed for a purpose. The **lid-cavity** models are used to verify the accuracy and the performance of the *direction–splitting method*. In this case we also compared our results with other research work, showing very good agreement. The **lid–driven flow with a sphere inside** was used to verify the performance of the *immersed boundary method*, which we compared with results obtained by OpenFOAM. Our results show that the in–house code is faster than OpenFOAM in serial. The case of **a moving sphere inside a cube** was used, since there are many applications in eye that involves motion of domains and boundaries e.g. iris motion. If the motion of the iris is known, this can be easily implemented in this code. Also in this case we compared our results with OpenFOAM and the simulation with the in–house code was much faster. This is because in OpenFOAM mesh movement has to be taken into account and an additional solver describing the motion of the mesh points is required. Furthermore, at some iterations, additional refinement has to be used to avoid skewed elements in the mesh.

7.7 Acknowledgement

The development of the in–house code is under the collaboration of Dr. Jean-Luc Guermond (Texas A&M University) and Dr. Franco Auteri (Polytechnic University of Milan). There are also the following contributors in this work: Dr. Marco Donato de Tullio (Polytechnic University of Bari), Dr. Anna Pandolfi (Polytechnic University of Milan), Dr. Jan Oscar Pralits (University of Genoa) and Dr. Rodolfo Repetto (University of Genoa).

Chapter 8

Summary and conclusions

The main objectives of this thesis were to contribute, through the use of mathematical models, to improve our understanding of:

i) the characteristics of aqueous flow in the anterior chamber of the human eye, with and without the presence of an iris–fixated intraocular lens;

ii) metabolic species transport to the cornea, with and without the presence of an iris–fixated intraocular lens;

iii) the mechanical implications of implanting an iris–fixated cataract lens on the anterior or posterior surface of the iris.

The first two objectives were defined to investigate the possible roles of mechanics and fluid flow on the main two complications of i) loss of endothelial cells from the cornea and iris and ii) increase of the intraocular pressure. These complications have indeed been assumed to be related to changes in the aqueous flow within the anterior chamber due to the presence of iris–fixated intraocular lenses.

The last objective was to analyse the risk of aIOL dislocation and luxation, which is one of the complications associated with the implantation of these cataract lenses on the iris. In particular we investigate if such risk is higher in one of the two possible implantation options: on the anterior or posterior side of the iris.

The work related with the above objectives are described in chapter 4, 5 and 6, respectively.

8.1 Conclusions of chapter 4

The main conclusions of this chapter are summarized in the following:

i) In the case of flow induced by aqueous production/drainage, in the absence of the pIOL, fluid can reach to all parts of the the anterior chamber almost uniformly. On the other hand the implantation of the pIOLs forces the fluid towards the periphery of the anterior chamber and a region of very slow motion forms anterior to the pIOL. The presence of one or more holes in the pIOL can divert part of the flow towards the central region of the cornea, thus leading to a flow pattern more similar to the physiological one.

ii) The implantation of a pIOL has a negligible influence on the intraocular pressure, if the lens is properly placed i.e. if there is sufficient clearance between the pIOL and the iris.

iii) After pIOL implantation, the wall shear stress (WSS) distribution on the iris and cornea changes in comparison to the case without the lens. However, the WSS is not large enough to justify cell detachment from these tissues.

iv) Holes in the body of the Hydrophobic Artiflex pIOL have not a significant effect on the WSS on the cornea and iris. However, the results suggest that a perforation in the pIOL is very effective in avoiding excessive pressure growth in the case that the passage between the pIOL and the iris gets blocked. Thus a perforation in the pIOL may represent a variable alternative to iridotomy, i.e. a hole surgically created in the iris, which is now invariably associated to the implantation of an iris–fixated pIOL.

8.2 Conclusions of chapter 5

In chapter 5 we investigate whether implantation of a pIOL can change nutrient delivery to the cornea. This is a sensible assumption since metabolic species such as, in particular, glucose are transported to the cornea by the aqueous humor, the cornea being an avascular tissue. Since implantation of a pIOL significantly modifies flow patterns in the anterior chamber, transport processes will also be significantly modified, since they strongly rely on advection.

For our analysis, we considered two main cases, metabolic species transport to the cornea when the eyelids are open (a) and closed (b). This is because when the eyelids are open, the thermal flow and the flow generated by eye rotations are intense and we postulated that the aqueous humor is well-mixed in the anterior chamber. For this reason we lumped the effect of species transport across the anterior chamber into a boundary condition on the endothelium–anterior chamber interface. On the other hand when the eyelids are closed, the mechanisms that produce fluid flow will be mainly the bulk production/drainage flow. Since this flow is very slow, for this case we also account for transport of metabolic species within the aqueous humor. We also considered a central hole on the body of the pIOL to investigate its effect on the transport of metabolic species to the cornea.

The model was solved numerically using COMSOL Multiphysics. The main conclusions for chapter 4 are summarized below.

i) Steady state simulations showed that glucose concentration at the center of the corneal endothelium layer when the eyelids are closed is approximately half in comparison to the open eyelids case.

ii) Steady state simulations also showed that the presence of a pIOL leads to a decreased glucose availability in the region anterior to the lens on the cornea in sleeping conditions. However, we show that several hours are needed for this steady solution to be reached and since during sleeping, rapid eye movements (REM) occur at regular interval of about 80 minutes, the steady state solution is unlikely to be ever reached.

iii) In the unsteady state simulations, glucose concentration anterior to the lens progressively decreases until REM occurs and the minimum value of glucose in the presence of a pIOL is about half in comparison to the case without pIOL.

iv) The presence of a hole in the lens body mitigates the above effects. The decrease in glucose concentration with respect to the physiological case is smaller that when the hole is not present.

Summarising, our model suggests that the presence of a pIOL in the anterior chamber may decrease glucose availability in the central region of the cornea during sleeping. This might be an explanation for the loss of corneal cells that some patients experience after pIOL implantation. Obviously, the clinical implications of these findings must be verified on the basis of data from patients.

8.3 Conclusions of chapter 6

In chapter 6 we pursued the third objective mentioned above.

When the natural lens capsule gets broken during cataract surgery, one of the few options the surgeon has is to adopt an iris–fixated aphakic lens. The most used of such lenses is the Artisan Aphakia lens. This lens can be implanted either on the anterior or posterior surface of the iris. No indications exist on which choice is better. In chapter 6 we have considered the problem from the mechanical point of view, in particular computing the force that the attachment points between the lens and the iris experience during eye rotations. This is because such forces are associated to the lens dislocation, which is one of the complications of the surgery. This analysis is relative to the case when cataract surgery and vitrectomy are performed, the vitreous gel is replaced by the aqueous humor and we assume that both the anterior and the vitreous chambers contains aqueous humor.

The model was then solved numerically using OpenFAOM. Using the force function object utility of OpenFOAM we calculated the the hydrodynamic force on the aIOL and using an analytical approach we also considered the contribution of fictitious forces on the aIOL due to the acceleration of the domains.

The main conclusions of chapter 6 are summarized below.

i) In all considered cases, the total force on the lens is much higher in the nasal–temporal direction than the anteroposterior one (for a rotation around a vertical axis).

ii) We invariably found that the lens experiences much bigger forces when it is implanted on the posterior surface of the iris. This is essentially because there is more flow in the vitreous chamber than in the anterior one.

Summarising the results of this part, our simulations suggest that implantation of the aIOL on the posterior surface of the iris is potentially associated with a higher risk of lens dislocation. It would be interesting to verify whether these theoretical predictions are supported by clinical observations.

8.4 Conclusion of chapter 7

Numerical methods are essential for solving Navier–Stokes equations. However they are associated to some difficulties, such as high computational resources and time consuming simulations. In this chapter we developed an in–house code based on direction–splitting method with immersed boundary treatment. This method has lots of benefits over the traditional Navier–Stokes solvers, in particular in terms of computational time. The motivation of development of such a code was a lean toward numerical modeling of some applications in the human eye such as simulations of flow induced by eye movements, which in general are very time consuming. In this chapter we validate our numerical model against published data and simulations with OpenFOAM considering various benchmark simulations cases.

The main conclusions of chapter 7 are summarized below.

i) In all considered models, the results of the in–house code were in a very good agreement with numerical results of some research works and OpenFOAM.

ii) Running in serial mode, we invariably found that the in–house code is faster than OpenFOAM, particularly when mesh motion in the simulations is involved.

Appendix A

Appendix

All numerical simulations have been run adopting the parameter values listed in the following tables.

Aqueous properties			
Density	ρ	1000 kg/m^3	
Aqueous flux	Q	3 μl/min $= 5 \cdot 10^{-11}$ m^3/s	[18, 19]
Kinematic viscosity	ν	$7.5 \cdot 10^{-7}$ m^2/s	[13]
Specific heat at constant pressure	c_p	$4.178 \cdot 10^3$ J kg^{-1}K^{-1} (water at 37°)	[8]
Thermal conductivity	k	0.578 W m^{-1}K^{-1}	[109]
Thermal expansion coefficient	α	$3 \cdot 10^{-4}$ K^{-1} (water at 30°)	[8]
Geometrical characteristics of the anterior chamber			
Diameter	D_c	11.8 mm	[70]
Maximum height	h_C	3.15 mm	[70]
Minimum radius of curvature of the cornea	R_C	6.8 mm	ISO-11979-3 [63]
Radius of curvature of the natural lens	R_L	10 mm	
Height of the iris-lens channel		0.1 mm	
Angle between cornea and iris		30°	

Table A.1: Parameter values used for the simulations of chapter 4.

Geometrical characteristics of the cornea		
Endothelium thickness	0.005 mm	[107]
Stroma thickness	0.5 mm	[107]
Epithelium thickness	0.05 mm	[107]

Table A.2: Geometrical Parameter values of the cornea used for the simulations of chapter 5.

Diffusion Coefficients of metabolic species in aqueous humor			
Oxygen diffusion Coefficient	D_O^{aq}	$2.9 \cdot 10^{-5}$ cm^2/s	[22]
Glucose diffusion Coefficient	D_G^{aq}	$9.3 \cdot 10^{-6}$ cm^2/s	[22]
Lactate diffusion Coefficient	D_L^{aq}	$1.45 \cdot 10^{-5}$ cm^2/s	[22]

Table A.3: Diffusion Coefficients of metabolic species in aqueous humor, used in chapter 5.

Corneal properties 2			
p_{crit}	p_{crit}	40.9 mmHg	[3]
R	R	13 mmHg	[3]
Corneal pH (Open eyelids)	pH	7.6	[59]
Corneal pH (Closed eyelids)	pH	7.39	[59]
Corneal pH (Closed eyelids)	K_{pH}	0.1	[23]
K_O^O	K_O^O	2.2 mmHg	[23]
K_O^L	K_O^L	2.2 mmHg	[23]
K_G^O	K_G^O	0.4 mM	[23]
K_G^L	K_G^L	0.4 mM	[23]

Table A.4: Parameter values used in the metabolic species equations of chapter 5.

Corneal properties 1				
Parameter	Units	Endothelium	Stroma	Epithelium
$D_O k_O$	Barrer	5.3	29.5	18.8
D_G	10^{-6} cm^2/s	3.0	3.0	3.0
D_L	10^{-6} cm^2/s	4.4	4.4	4.4
Q_{Omax}	10^{-5} mLO_2/mL/s	47.78	2.29	25.9
Q_{Lmin}	10^{-6} mol/mL/h	4.7	23.4	28.1

Table A.5: Parameter values used in the metabolic species equations of chapter 5. The values are from Pisnky [107].

Corneal properties 3		
Open eyelids		
Oxygen tension at endothelim-AC interface	24 mmHg	[107]
Oxygen tension at epitheluim-air interface	155 mmHg	[107]
Glucose concentration at Endo-AC interface	6.9 mM	[107]
Lactate concentration at Endo-AC interface	7.7 mM	[107]
Closed eyelids		
Oxygen tension at epitheluim-air interface	61.5 mmHg	[107]
Inlet and natural lens oxygen tension	6 mmHg	[95]
Inlet and natural lens glucose concentration	6.9 mmHg	[107]
Inlet and natural lens lactate concentration	4.5 mmHg	[80]

Table A.6: Boundary condition values used for the simulations of chapter 5. Here AC and Endo are the abbreviations of anterior chamber and endothelium, respectively.

Geometrical parameter values of vitreous chamber			
Clliary body's length	C_r	2 mm	[46]
Vitreous chamber radius	V_r	11 mm	[46]
Vitreous chamber length	V_l	19.5 mm	[46]
Pupil radius	P_r	1.5 mm	[114]
Iris length	I_l	5.72 mm	[136]

Table A.7: Geometrical parameter values of vitreous chamber used in the simulations of chapter 6.

Bibliography

[1] O. Abouali, A. Modareszadeh, A. Ghaffarieh, and J. Tu. Investigation of saccadic eye movement effects on the fluid dynamic in the anterior chamber. *Journal of biomechanical engineering*, 134(2):021002, Feb. 2012. PMID: 22482669.

[2] O. Abouali, A. Modareszadeh, A. Ghaffariyeh, and J. Tu. Numerical simulation of the fluid dynamics in vitreous cavity due to saccadic eye movement. *Medical Engineering & Physics*, 34(6):681–692, July 2012.

[3] L. A. Alvord, W. J. Hall, L. D. Keyes, C. F. Morgan, and L. C. Winterton. Corneal oxygen distribution with contact lens wear. *Cornea*, 26(6):654–664, 2007.

[4] E. Amara. Numerical investigations on thermal effects of laser-ocular media interaction. *International Journal of Heat and Mass Transfer*, 38(13):2479–2488, 1995.

[5] M. H. Assaad, G. Baerveldt, and E. J. Rockwood. Glaucoma drainage devices: pros and cons. *Current opinion in ophthalmology*, 10(2):147–153, 1999.

[6] D. A. Atchison, G. Smith, and G. Smith. Optics of the human eye. 2000.

[7] R. K. Balachandran. *Computational modeling of drug transport in the posterior eye*. University of Minnesota, 2010.

[8] G. K. Batchelor. *An Introduction to Fluid Dynamics*. Cambridge University Press, 1967.

[9] G. K. Batchelor. *An introduction to fluid dynamics*. Cambridge university press, 2000.

[10] W. Becker. Metrics. In R. Wurtz and M. Goldberg, editors, *The neurobiology of saccadic eye movements*. Elsevier Science Publisher BV (Biomedical Division), 1989.

[11] J. Bergmanson, J. Johnsson, P. G. Söderberg, and B. T. Philipson. Lactate levels in the rabbit cornea and aqueous humor subsequent to non-gas permeable contact lens wear. *Cornea*, 4(3):173–176, 1984.

[12] O. Bessey and S. Wolbach. Vascularization of the cornea of the rat in riboflavin deficiency, with a note on corneal vascularization in vitamin a deficiency. *The Journal of experimental medicine*, 69(1):1, 1939.

[13] J. A. Beswick and C. McCulloch. Effect of hyaluronidase on the viscosity of the aqueous humour. *Br. J. Ophthamol.*, 40:545–548, 1956.

[14] J. Bonanno and K. Polse. Corneal acidosis during contact lens wear: effects of hypoxia and co2. *Investigative ophthalmology & visual science*, 28(9):1514–1520, 1987.

[15] J. A. Bonanno, T. Stickel, T. Nguyen, T. Biehl, D. Carter, W. J. Benjamin, and P. S. Soni. Estimation of human corneal oxygen consumption by noninvasive measurement of tear oxygen tension while wearing hydrogel lenses. *Investigative ophthalmology & visual science*, 43(2):371–376, 2002.

[16] A. Bonfiglio, A. Lagazzo, R. Repetto, and A. Stocchino. An experimental model of vitreous motion induced by eye rotations. *Eye and Vision*, 2(1):10, 2015.

[17] N. A. Brennan. Corneal oxygenation during contact lens wear: comparison of diffusion and eop-based flux models. *Clinical and Experimental Optometry*, 88(2):103–108, 2005.

[18] R. F. Brubaker. Measurement of aqueous flow by fluorophotometry. In *The Glaucomas*. Mosby (St. Louis), 1989.

[19] R. F. Brubaker. Flow of aqueous humor in humans [the friedenwald lecture]. *Investigative Ophthalmology and Visual Science*, 32(13):3145–3166, 1991. PMID: 1748546.

[20] C. R. Canning, M. J. Greaney, J. N. Dewynne, and A. Fitt. Fluid flow in the anterior chamber of a human eye. *IMA Journal of Mathematics Applied in Medicine and Biology*, 19:31–60, 2002.

[21] https://www.northamptoneye.com/our-services/cataract/cataract-surgery-what-to-expect/.

[22] M. Chhabra. *Oxygen transport through soft contact lens and cornea: Lens characterization and metabolic modeling*. ProQuest, 2007.

[23] M. Chhabra, J. M. Prausnitz, and C. J. Radke. Modeling corneal metabolism and oxygen transport during contact lens wear. *Optometry & Vision Science*, 86(5):454–466, 2009.

[24] http://drlakosha.ca/corneal-cross-linking-cxl/.

[25] T. David, S. Smye, T. Dabbs, and T. James. A model for the fluid motion of vitreous humour of the human eye during saccadic movement. *Phys. Med. Biol.*, 43:1385–1399, 1998.

[26] H. Davson. *Physiology of the Eye*. Elsevier, 2012.

[27] A. de ROETTH Jr. Respiration of the cornea. *AMA archives of ophthalmology*, 44(5):666, 1950.

[28] M. D. de Tullio and G. Pascazio. A moving-least-squares immersed boundary method for simulating the fluid–structure interaction of elastic bodies with arbitrary thickness. *Journal of Computational Physics*, 325:201–225, 2016.

[29] H. Ding, C. Shu, K. Yeo, and D. Xu. Numerical computation of three-dimensional incompressible viscous flows in the primitive variable form by local multiquadric differential quadrature method. *Computer Methods in Applied Mechanics and Engineering*, 195(7):516–533, 2006.

[30] S. Dorairaj, J. M. Liebmann, C. Tello, V. Barocas, and R. Ritch. Posterior chamber volume does not change significantly during dilation. *British Journal of Ophthalmology*, 93(11):1514–1517, 2009.

[31] J. Douglas. Alternating direction methods for three space variables. *Numerische Mathematik*, 4(1):41–63, 1962.

[32] M. Dvoriashyna, R. Repetto, M. Romano, and J. Tweedy. Aqueous humour flow in the posterior chamber of the eye and its modifications due to pupillary block and iridotomy. *Mathematical medicine and biology: a journal of the IMA*, 2017.

[33] P. Ehrlich. Ueber provocirte fluorescenzerscheinungen am auge. *DMW-Deutsche Medizinische Wochenschrift*, 8(02):21–22, 1882.

[34] http://anatomyid.com/eye-diagram-and-function/eye-diagram-and-function-human-eye-diagram-labeled-health-medicine-and-anatomy-reference/.

[35] I. Fatt. Steady-state distribution of oxygen and carbon dioxide in the in vivo cornea: Ii. the open eye in nitrogen and the covered eye. *Experimental eye research*, 7(3):413–430, 1968.

[36] I. Fatt and M. T. Bieber. The steady-state distribution of oxygen and carbon dioxide in the in vivo cornea: I. the open eye in air and the closed eye. *Experimental eye research*, 7(1):103–112, 1968.

[37] I. Fatt, R. Freeman, and D. Lin. Oxygen tension distributions in the cornea: a re-examination. *Experimental eye research*, 18(4):357–365, 1974.

[38] I. Fatt and D. Lin. Spatial distribution of oxygen in the cornea of a closed eye hearing a gas permeable contact lens. *Current eye research*, 4(6):723–724, 1985.

[39] I. Fatt and B. A. Weissman. *Physiology of the eye: an introduction to the vegetative functions*. Butterworth-Heinemann, 2013.

[40] J. I. Fernández-Vigo, A. Macarro-Merino, J. Fernández-Francos, L. De-Pablo-Gómez-de Liaño, J. M. Martínez-de-la Casa, J. García-Feijóo, and J. Á. Fernández-Vigo. Computational study of aqueous humor dynamics assessing the vault and the pupil diameter in two posterior-chamber phakic lensesaqueous humor dynamics study in phakic lenses. *Investigative ophthalmology & visual science*, 57(11):4625–4631, 2016.

[41] F. Fischer. Ueber den gasaustausch der hornhaut mit der luft. *Arch. f. Augenh.*, 102:146, 1930.

[42] A. D. Fitt and G. Gonzalez. Fluid mechanics of the human eye: Aqueous humour flow in the anterior chamber. *Bulletin of Mathematical Biology*, 68(1):53–71, 2006.

[43] R. D. Freeman. Oxygen consumption by the component layers of the cornea. *The Journal of physiology*, 225(1):15, 1972.

[44] R. D. Freeman and I. Fatt. Oxygen permeability of the limiting layers of the cornea. *Biophysical journal*, 12(3):237–247, 1972.

[45] A. B. Friedland. A hydrodynamic model of aqueous flow in the posterior chamber of the eye. *Bulletin of mathematical biology*, 40(2):223–235, 1978.

[46] T. F. Gesell, J. W. Hopewell, M. W. Lantz, J. W. Osborne, B. R. Scott, S. M. Seltzer, R. E. Shore, and B. V. Worgul. Biological effects and exposure limits for'hot particles,'. *National Council on Radiation Protection and Measurements Bethesda MD NCRP Report 130*, 1999.

[47] M. Goel, R. G. Picciani, R. K. Lee, and S. K. Bhattacharya. Aqueous humor dynamics: a review. *The open ophthalmology journal*, 4:52, 2010.

[48] H. Goldmann. Abfluss des kammerwassers beim menschen. *Ophthalmologica*, 111:146, 1946.

[49] H. Goldmann. Weitere mitteilung uber der abfluss des kammerwassers beim menschen. *Ophthalmologica*, 112:344, 1946.

[50] H. Goldmann. Enthalten die kammerwasservenen kammerwasser? *Ophthalmologica*, 117:240, 1949.

[51] H. Goldmann. Abflussdruck, minutenvolumen und widerstand der kammerwasser stromung des menschen. *Doc Ophthalmol*, 5-6:278, 1951.

[52] J. Gonnermann, M. K. Klamann, A.-K. Maier, J. Rjasanow, A. M. Joussen, E. Bertelmann, P. W. Rieck, and N. Torun. Visual outcome and complications after posterior iris-claw aphakic intraocular lens implantation. *Journal of Cataract & Refractive Surgery*, 38(12):2139–2143, 2012.

[53] J. Gonnermann, N. Torun, M. K. Klamann, A.-K. B. Maier, C. v. Sonnleithner, A. M. Joussen, P. W. Rieck, and E. Bertelmann. Visual outcomes and complications following posterior iris-claw aphakic intraocular lens implantation combined with penetrating keratoplasty. *Graefe's Archive for Clinical and Experimental Ophthalmology*, 251(4):1151–1156, 2013.

[54] M. Grüb and J. Mielke. Aqueous humor dynamics. *Der Ophthalmologe: Zeitschrift der Deutschen Ophthalmologischen Gesellschaft*, 101(4):357–365, 2004.

[55] J. Guermond and P. Minev. Start-up flow in a three-dimensional lid-driven cavity by means of a massively parallel direction splitting algorithm. *International Journal for Numerical Methods in Fluids*, 68(7):856–871, 2012.

[56] J.-L. Guermond and P. D. Minev. A new class of fractional step techniques for the incompressible navier–stokes equations using direction splitting. *Comptes Rendus Mathematique*, 348(9-10):581–585, 2010.

[57] J.-L. Guermond and J. Shen. Velocity-correction projection methods for incompressible flows. *SIAM Journal on Numerical Analysis*, 41(1):112–134, 2003.

[58] H. Hamano, M. Hori, T. Hamano, H. Kawabe, M. Mikami, and S. Mitsunaga. Effects of contact lens wear on mitosis of corneal epithelium and lactate content in aqueous humor of rabbit. *Japanese journal of ophthalmology*, 27(3):451–458, 1982.

[59] D. M. Harvitt and J. A. Bonanno. ph dependence of corneal oxygen consumption. *Investigative ophthalmology & visual science*, 39(13):2778–2781, 1998.

[60] D. M. Harvitt and J. A. Bonanno. ph dependence of corneal oxygen consumption. *Investigative ophthalmology & visual science*, 39(13):2778–2781, 1998.

[61] D. M. Harvitt and J. A. Bonanno. Re-evaluation of the oxygen diffusion model for predicting minimum contact lens dk/t values needed to avoid corneal anoxia. *Optometry & Vision Science*, 76(10):712–719, 1999.

[62] K. Heald and M. E. Langham. Permeability of the cornea and the blood-aqueous barrier to oxygen. *The British journal of ophthalmology*, 40(12):705, 1956.

[63] H. v. Helmholtz. *Handbuch der physiologischen Optik*. University of Michigan Library, third edition, 1909.

[64] J. J. Heys and V. H. Barocas. A Boussinesq model of natural convection in the human eye and formation of krunberg's spindle. *Annals of Biomedical Engineering*, 30:392–401, 2002.

[65] J. J. Heys, V. H. Barocas, and M. J. Taravella. Modeling passive mechanical interaction between aqueous humor and iris. *Transactions of the ASME*, 123:540–547, December 2001.

[66] R. M. Hill and I. Fatt. Oxygen uptake from a reservoir of limited volume by the human cornea in vivo. *Science*, 142(3597):1295–1297, 1963.

[67] K. Isakova, J. O. Pralits, R. Repetto, and M. R. Romano. A model for the linear stability of the interface between aqueous humor and vitreous substitutes after vitreoretinal surgery. *Physics of Fluids*, 26(12):124101, 2014.

[68] R. I. Issa. Solution of the implicitly discretised fluid flow equations by operator-splitting. *Journal of computational physics*, 62(1):40–65, 1986.

[69] Y. Kaji, T. Oshika, T. Usui, and J. Sakakibara. Effect of shear stress on attachment of corneal endothelial cells in association with corneal endothelial cell loss after laser iridotomy. *Cornea*, 24(8):S55–S58, 2005.

[70] K. Kapnisis, M. Van Doormaal, and C. R. Ethier. Modeling aqueous humor collection from the human eye. *Journal of biomechanics*, 42(15):2454–2457, 2009.

[71] V. J. Katsanevaki and S. J. Tuft. Refractive surgery: what patients need to know. *British medical bulletin*, 83(1):325–339, 2007.

[72] T. Kawamorita, H. Uozato, and K. Shimizu. Fluid dynamics simulation of aqueous humour in a posterior-chamber phakic intraocular lens with a central perforation. *Graefe's archive for clinical and experimental ophthalmology*, 250(6):935–939, 2012.

[73] P. D. Khongar, J. O. Pralits, P. Soleri, and R. Repetto. Aqueous flow in the presence of a perforated iris-fixated intraocular lens. *Meccanica*, 52(3):577–586, 2017.

[74] A. Kleineller, D. M. Fambrough, D. J. Benos, and M. M. Civan. *The Eye's Aqueous Humor: From Secretion to Glaucoma*, volume 45. Academic Press, 1997.

[75] T. Koskela and R. Brubaker. The nocturnal suppression of aqueous humor flow in humans is not blocked by bright light. *Investigative ophthalmology & visual science*, 32(9):2504–2506, 1991.

[76] H. C. Ku, R. S. Hirsh, and T. D. Taylor. A pseudospectral method for solution of the three-dimensional incompressible navier-stokes equations. *Journal of Computational Physics*, 70(2):439–462, 1987.

[77] S. Kwitko and A. P. Stolz. Iris-claw (artisan®/artiflex®) phakic intraocular lenses for high myopia and high hyperopia. *Expert Review of Ophthalmology*, 6(5):505–512, 2011.

[78] S. Kwitko and A. P. Stolz. Iris-claw (Artisan®/Artiflex®) phakic intraocular lenses for high myopia and high hyperopia. *Expert Review of Ophthalmology*, 6(5):505–512, 2011.

[79] J. Lagendijk. A mathematical model to calculate temperature distributions in human and rabbit eyes during hyperthermic treatment. *Physics in medicine and biology*, 27(11):1301, 1982.

[80] M. Langham. Utilization of oxygen by the component layers of the living cornea. *The Journal of physiology*, 117(4):461–470, 1952.

[81] X. Larrea, C. De Courten, V. Feingold, J. Burger, and P. Buechler. Oxygen and glucose distribution after intracorneal lens implantation. *Optometry & Vision Science*, 84(12):1074–1081, 2007.

[82] A. B. Laursen and S. Lorentzen. Glucose, pyruvate, l-lactate, and citrate concentrations in the aqueous humour of fasting rabbits in relation to age. *Acta ophthalmologica*, 53(4):553–562, 1975.

[83] C. Leblond and C. Allery. A priori space–time separated representation for the reduced order modeling of low reynolds number flows. *Computer Methods in Applied Mechanics and Engineering*, 274:264–288, 2014.

[84] E. Leriche. Direct numerical simulation in a lid-driven cubical cavity at high reynolds number by a chebyshev spectral method. *Journal of Scientific Computing*, 27(1):335–345, 2006.

[85] B. K. Leung, J. A. Bonanno, and C. J. Radke. Oxygen-deficient metabolism and corneal edema. *Progress in retinal and eye research*, 30(6):471–492, 2011.

[86] R. J. LeVeque. *Finite volume methods for hyperbolic problems*, volume 31. Cambridge university press, 2002.

[87] H. Liu, S. Fan, V. Gulati, L. J. Camras, G. Zhan, D. Ghate, C. B. Camras, and C. B. Toris. Aqueous humor dynamics during the day and night in healthy mature volunteers. *Archives of ophthalmology*, 129(3):269–275, 2011.

[88] A. Logg, K.-A. Mardal, and G. Wells. *Automated solution of differential equations by the finite element method: The FEniCS book*, volume 84. Springer Science & Business Media, 2012.

[89] C. F. Lovisolo and D. Z. Reinstein. Phakic intraocular lenses. *Survey of ophthalmology*, 50(6):549–587, 2005.

[90] L. Mangani and C. Bianchini. Heat transfer applications in turbomachinery. In *Proceedings of the OpenFOAM International Conference*, 2007.

[91] D. Maurice. Nutritional aspects of corneal grafts and prostheses. In *Corneo-Plastic Surgery: Proceedings of the Second International Corneo-Plastic Conference*, pages 197–207. Pergamon Press, Elmsford, NY, 1969.

[92] D. M. Maurice. The cornea and sclera. In *Vegetative Physiology and Biochemistry*, pages 289–368. Elsevier, 1962.

[93] C. A. McCannel, S. R. Heinrich, and R. F. Brubaker. Acetazolamide but not timolol lowers aqueous humor flow in sleeping humans. *Graefe's archive for clinical and experimental ophthalmology*, 230(6):518–520, 1992.

[94] B. E. McCarey and F. H. Schmidt. Modeling glucose distribution in the cornea. *Current eye research*, 9(11):1025–1039, 1990.

[95] J. W. McLaren, S. Dinslage, J. P. Dillon, J. E. Roberts, and R. F. Brubaker. Measuring oxygen tension in the anterior chamber of rabbits. *Investigative ophthalmology & visual science*, 39(10):1899–1909, 1998.

[96] K. M. Meek and C. Knupp. Corneal structure and transparency. *Progress in retinal and eye research*, 49:1–16, 2015.

[97] A. Modarreszadeh and O. Abouali. Numerical simulation for unsteady motions of the human vitreous humor as a viscoelastic substance in linear and non-linear regimes. *Journal of Non-Newtonian Fluid Mechanics*, 204:22–31, 2014.

[98] D. Myung, K. Derr, P. Huie, J. Noolandi, K. P. Ta, and C. N. Ta. Glucose permeability of human, bovine, and porcine corneas in vitro. *Ophthalmic research*, 38(3):158–163, 2006.

[99] M. Niazi, A. Esteghamatian, O. Abouali, A. Ghaffariyeh, and G. Ahmadi. Numerical study of natural convection in the anterior chamber of human eye with implanted intraocular lens. In *ASME 2012 Heat Transfer Summer Conference collocated with the ASME 2012 Fluids Engineering Division Summer Meeting and the ASME 2012 10th International Conference on Nanochannels, Microchannels, and Minichannels*, pages 1007–1012. American Society of Mechanical Engineers, 2012.

[100] T. Okuno. Thermal effect of infra-red radiation on the eye: a study based on a model. *The Annals of occupational hygiene*, 35(1):1–12, 1991.

[101] Y. Onishi, T. Utsumi, T. Hashimoto, and K. Namba. Pupillary dynamics under open-loop photic stimulus, variations in age and sex. *Folia Ophthalmol Jpn*, 30:921–926, 1979.

[102] http://openfoam.com.

[103] W. H. Organization et al. Global data on visual impairments 2010. *Geneva: World Health Organization Organization*, 2012.

[104] S. Patankar. *Numerical heat transfer and fluid flow*. CRC press, 1980.

[105] C. J. Pavlin, K. Harasiewicz, and F. S. Foster. Ultrasound biomicroscopy of anterior segment structures in normal and glaucomatous eyes. *American journal of ophthalmology*, 113(4):381–389, 1992.

[106] C. S. Peskin. Flow patterns around heart valves: a numerical method. *Journal of computational physics*, 10(2):252–271, 1972.

[107] P. M. Pinsky. Three-dimensional modeling of metabolic species transport in the cornea with a hydrogel intrastromal inlay3d modeling of metabolic species transport. *Investigative ophthalmology & visual science*, 55(5):3093–3106, 2014.

[108] M. Pop and Y. Payette. Risk factors for night vision complaints after lasik for myopia. *Ophthalmology*, 111(1):3–10, 2004.

[109] H. F. Poppendiek, R. Randall, J. A. Breeden, J. E. Chambers, and J. R. Murphy. Thermal conductivity measurements and predictions for biological fluids and tissues. *Cryobiology*, 3(4):318–327, 1967.

[110] R. Rannacher. On chorins projection method for the incompressible navier-stokes equations. *Lecture notes in mathematics*, 1530:167–183, 1992.

[111] D. Reddy and V. Kinsey. Composition of the vitreous humor in relation to that of plasma and aqueous humors. *AMA Archives of Ophthalmology*, 63(4):715–720, 1960.

[112] G. Reiss, D. Lee, J. Topper, and R. Brubaker. Aqueous humor flow during sleep. *Investigative ophthalmology & visual science*, 25(6):776–778, 1984.

[113] R. Repetto. An analytical model of the dynamics of the liquefied vitreous induced by saccadic eye movements. *Meccanica*, 41:101–117, 2006.

[114] R. Repetto, J. O. Pralits, J. H. Siggers, and P. Soleri. Phakic iris-fixated intraocular lens placement in the anterior chamber: Effects on aqueous flowphakic iris-fixated intraocular lens placement. *Investigative ophthalmology & visual science*, 56(5):3061–3068, 2015.

[115] R. Repetto, J. O. Pralits, J. H. Siggers, and P. Soleri. Phakic iris-fixated intraocular lens placement in the anterior chamber: effects on aqueous flowphakic iris-fixated intraocular lens placement. *Investigative ophthalmology & visual science*, 56(5):3061–3068, 2015.

[116] R. Repetto, J. Siggers, and A. Stocchino. Mathematical model of flow in the vitreous humor induced by saccadic eye rotations: effect of geometry. *Biomechanics and modeling in mechanobiology*, 9(1):65–76, 2010.

[117] R. Repetto, J. H. Siggers, and A. Stocchino. Mathematical model of flow in the vitreous humor induced by saccadic eye rotations: effect of geometry. *Biomechanics and Modeling in Mechanobiology*, 9(1):65–76, 2010.

[118] R. Repetto, A. Stocchino, and C. Cafferata. Experimental investigation of vitreous humour motion within a human eye model. *Phys. Med. Biol.*, 50:4729–4743, 2005.

[119] M. Riley. Glucose and oxygen utilization by the rabbit cornea. *Experimental eye research*, 8(2):193–200, 1969.

[120] M. Riley. Intraocular dynamics of lactic acid in the rabbit. *Investigative Ophthalmology & Visual Science*, 11(7):600–607, 1972.

[121] W. Robbie, P. Leinfelder, and T. Duane. Cyanide inhibition of corneal respiration. *American journal of ophthalmology*, 30(11):1381–1386, 1947.

[122] C. M. Ruben and Y.-Y. Zhu. Occlusion of the cornea with contact lens and anterior chamber lactate levels. *Acta ophthalmologica*, 65(3):287–292, 1987.

[123] F. Rüfer, M. Saeger, B. Nölle, and J. Roider. Implantation of retropupillar iris claw lenses with and without combined penetrating keratoplasty. *Graefe's Archive for Clinical and Experimental Ophthalmology*, 247(4):457, 2009.

[124] D. R. Sanders and J. A. Vukich. Comparison of implantable contact lens and laser assisted in situ keratomileusis for moderate to high myopia. *Cornea*, 22(4):324–331, 2003.

[125] J. A. Scott. A finite element model of the heat transport in the human eye. *Phys. Med. Biol.*, 33(2):227–241, 1988.

[126] E. Seidel. Uber der abfluss des kammerwassers aus der vorderen augenkammer. *Graefes Arch Clin Exp Ophthalmol*, 104:357, 1921.

[127] E. Seidel. Uber der manometrischen nachweis des physiologischen druckgefalles zwishen vorderkammer und schlemmschen canal. *Graefes Arch Clin Exp Ophthalmol*, 107:101, 1921.

[128] L. M. Shanyfelt. *ArF excimer laser corneal ablation: Effects of laser repetition rate and fundamental laser-tissue coupling*. University of Florida, 2008.

[129] A. Stocchino, R. Repetto, and C. Cafferata. Eye rotation induced dynamics of a newtonian fluid within the vitreous cavity: the effect of the chamber shape. *Phys. Med. Biol.*, 52:2021–2034, 2007.

[130] G. H. Takahashi and I. Fatt. The diffusion of oxygen in the cornea. *Experimental eye research*, 4(1):4–12, 1965.

[131] J. E. Topper and R. F. Brubaker. Effects of timolol, epinephrine, and acetazolamide on aqueous flow during sleep. *Investigative ophthalmology & visual science*, 26(10):1315–1319, 1985.

[132] S. Türk. Untersuchungen über eine strömung in der vorderen augenkammer. *Albrecht von Graefes Archiv für Ophthalmologie*, 64(3):481–501, 1906.

[133] A. Villamarin, S. Roy, R. Hasballa, O. Vardoulis, P. Reymond, and N. Stergiopulos. 3d simulation of the aqueous flow in the human eye. *Medical engineering & physics*, 34(10):1462–1470, 2012.

[134] B. A. Weissman and D. T. Fazio. Human corneal oxygen flux under soft contact lenses. *Optometry & Vision Science*, 59(8):635–638, 1982.

[135] S. E. Wilson and J.-W. Hong. Bowman's layer structure and function: critical or dispensable to corneal function? a hypothesis. *Cornea*, 19(4):417–420, 2000.

[136] S. L. Woo, A. Kobayashi, C. Lawrence, and W. Schlegel. Mathematical model of the corneo-scleral shell as applied to intraocular pressure-volume relations and applanation tonometry. *Annals of Biomedical Engineering*, 1(1):87–98, 1972.

[137] J. Worst. Iris claw lens. *Journal-American Intra-Ocular Implant Society*, 6(2):166, 1980.

[138] H. J. WYATT. Ocular pharmacokinetics and convectional flow: evidence from spatio-temporal analysis of mydriasis. *Journal of ocular pharmacology and therapeutics*, 12(4):441–459, 1996.

[139] Y. Yamamoto, T. Uno, T. Joko, A. Shiraishi, and Y. Ohashi. Effect of anterior chamber depth on shear stress exerted on corneal endothelial cells by altered aqueous flow after laser iridotomy. *Investigative ophthalmology & visual science*, 51(4):1956–1964, 2010.

[140] Y. Yamamoto, T. Uno, K. Shisida, L. Xue, A. Shiraishi, X. Zheng, and Y. Ohashi. Demonstration of aqueous streaming through a laser iridotomy window against the corneal endothelium. *Archives of ophthalmology*, 124(3):387–393, 2006.

[141] J. Yang and E. Balaras. An embedded-boundary formulation for large-eddy simulation of turbulent flows interacting with moving boundaries. *Journal of Computational Physics*, 215(1):12–40, 2006.

[142] A. Yeslin and P. Shurrager. Temperature gradients in the rabbit eye. *Psychonomic Science*, 4(1):39–40, 1966.

[143] O. C. Zienkiewicz, R. L. Taylor, O. C. Zienkiewicz, and R. L. Taylor. *The finite element method*, volume 3. McGraw-hill London, 1977.

[144] C. A. Zurawski, B. E. McCarey, and F. H. Schmidt. Glucose consumption in cultured corneal cells. *Current eye research*, 8(4):349–355, 1989.